High Pressure Fluid

Phase Equilibria

By

Marlie du Rand

Thesis presented in partial fulfilment of the requirements for the degree of Master of Science in Engineering (Chemical Engineering) at the University of Stellenbosch.

Supervisor: Prof. Izak Nieuwoudt

December 2000

Declaration

I, the undersigned, hereby declare that the work contained in this thesis is my own original work and that I have not previously in its entirety or in part submitted it at any university for a degree.

Marlie du Rand

10 October 2000

Acknowledgements

I would like to express my gratitude towards all the people who supported me throughout this project.

I would especially like to thank Prof. I. Nieuwoudt, my supervisor, for his guidance and support over the past two years, and to Mr. J.C. Crause, for his advice and help with the computer modelling programs.

I would also like to thank all the staff from the technical workshop at the Department of Chemical Engineering at the University of Stellenbosch, for all their effort and time spent on the construction of the view cell.

Lastly, I would like to thank Schümann Sasol International AG and the National Research Foundation for their financial support of this project.

ABSTRACT

Supercritical extraction is being investigated as a possible alternative to the processes currently used in the fractionation of paraffinic waxes. By removing the lighter carbon fractions from the wax, the wax hardness will be improved and its melting temperature range reduced, hence improving the performance of the wax product in certain applications. In order to evaluate and operate such an extraction process optimally, it is necessary to have a thermodynamic model that accurately represents the process system. There are, however, currently no predictive models available for these systems. In order to fit present models to the systems, accurate phase equilibrium data of the supercritical solvent – n-alkane systems are needed. Unfortunately, the amount of reliable published data on these systems in the required operating range is very limited.

A view cell was designed and developed with which these high pressure equilibria could be studied. The binary phase equilibria of supercritical CO_2 with n-C_{12}, n-C_{16}, n-C_{20}, n-C_{24}, n-C_{28} and n-C_{36} and of supercritical ethane with n-C_{16}, n-C_{24} and n-C_{28} were measured in the temperature range $313 - 367$ K. It was found that the systems with these two solvents have very different types of phase behaviour. The n-alkane solubility is much higher in ethane, but supercritical CO_2 will provide a much better degree of control over the selectivity achieved in an extraction process.

Of the various equations of state investigated, it was found that the Patel Teja equation of state provided the best fit of the CO_2 – n-alkane systems and that the Soave-Redlich-Kwong equation fitted the ethane – n-alkane systems the best. The interaction parameters of both these equations of state display a functional relationship with temperature and n-alkane acentric factor, making it possible to determine parameter values for application at other operating temperatures and with other n-alkane systems.

It was found that the current equations of state were not able to represent the phase equilibria accurately over the entire range of operating conditions. The poor performance of the equations of state can be attributed to inherent flaws in the existing equations of state.

OPSOMMING

Superkritiese ekstraksie word tans ondersoek as 'n moontlike alternatief vir die prosesse wat huidiglik gebruik word om paraffiese wasse te fraksioneer. Die ligter koolstofwasse word verwyder om die washardheid te verhoog en die temperatuurgebied waaroor die was smelt te verklein. Dit verbeter dan die was se kwaliteit en werkverrigting. Modelle wat die superkritiese ekstraksie proses akkuraat kan voorstel word egter benodig om die ekstraksie proses te kan evalueer en optimaal te bedryf. Daar is tans geen modelle beskikbaar wat die proses direk kan voorstel nie. Akkurate fase-ewewigsdata word benodig om bestaande modelle aan te pas vir gebruik in hierdie sisteme. Daar is egter baie min betroubare fase-ewewigsdata vir die superkritiese oplosmiddel – n-alkaan sisteme beskikbaar in die literatuur.

'n Sig-sel, waarmee hierdie hoë druk data gemeet kan word, is ontwerp en ontwikkel. Die volgende binêre fase ewewigte is in die temperatuur gebied 313 – 367 K gemeet: superkritiese CO_2 met n-C_{12}, n-C_{16}, n-C_{20}, n-C_{24}, n-C_{28} en n-C_{36}, en superkritiese Etaan met n-C_{16}, n-C_{24} en n-C_{28}. Daar is gevind dat hierdie twee superkritiese oplosmiddelsisteme verskillende tipes fase-ewewigsgedragte openbaar. Die n-alkane het 'n baie hoër oplosbaarheid in Etaan, maar deur superkritiese CO_2 in 'n ekstraksie kolom te gebruik, sal tot beheer oor die selektiwiteit van die ekstraksieproses lei.

Uit die verskillende toestandsvergelykings wat ondersoek is, is daar gevind dat die Patel-Teja vergelyking die CO_2 sisteme die beste kon beskryf en dat die Soave-Redlich-Kwong vergelyking die beste vergelyking was om die Etaan sisteme mee te modelleer. Beide die toestandsvergelykings se interaksie parameters het 'n funksionele verband met temperatuur en die n-alkaan asentrise faktor getoon. Dit is dus moontlik om waardes vir die parameters vir sisteme by ander temperature en met ander n-alkaan tipes te bepaal.

Daar was gevind dat die bestaande toestandsvergelykings nie die die fase-ewewigte oor die hele eksperimenele gebied akkuraat kon voorstel nie. Dit kan toegeskryf word aan foute wat inherent is aan die vergelykings.

Table of Contents

List of Figures

List of Graphs

List of Tables

1   SUPERCRITICAL FLUID PROCESSING

Since the first discovery of the critical point of a substance by Baron Cagniard de la Tour in 1822 (McHugh & Krukonis, 1994), and the first report of the ability of supercritical fluids to dissolve low vapour-pressure solids by Hannay and Hogarth in 1879, supercritical fluid processing has been approached with varying levels of enthusiasm (Krukonis et al., 1994).

The research in and use of supercritical fluid technology seems to have been split between the European and American continents. In the early 1980's there was, especially in the United States of America, a great degree of interest in the use of supercritical extraction as a more energy efficient alternative to traditional separation processes (Krukonis et al., 1994; McHugh & Krukonis, 1994). Unfortunately, many of these claims were overrated and the excitement waned towards the mid '80 's. On the other hand, in Europe, due to legislative rulings that prohibited the use of certain fluids in the decaffeination of coffee, the focus was shifted to using supercritical CO_2 as solvent for the caffeine. This lead to the development of large extraction plants using supercritical fluids in coffee and tea decaffeination and in the extraction of hops and other spices (Krukonis et al., 1994). These plants are mainly located in Europe and Asia, with only three hops extraction plants and one large coffee decaffeination plant in the USA (Chordia & Robey, 2000).

Krukonis (Krukonis et al., 1994) reports that there has been a renewed interest in supercritical fluid processes since the early 1990. The main driving forces behind the development of supercritical fluid technology have been identified as the following (Krukonis, 1988):

- Energy or other cost considerations. In some processes, supercritical technology might be a more cost effective alternative.
- Solvents: There is an increasing scrutiny of solvent residues in foodstuffs. Supercritical extraction does not have this problem.
- Environmental legislation and protection. Supercritical technologies are in many cases more environmentally friendly, not producing large waste streams, or requiring the use of hazardous solvents.

1

- Product performance. Using supercritical technology may in some cases result in an actual improvement in the product, such as a better volatility or colour etc. In other instances, supercritical processes may only be perceived as being an improvement over current processes by the market, for example using CO_2 instead of hexane in the processing of a food product appears more attractive, even though the product quality achieved by both processes is the same.

Although most of the large plants today use supercritical fluid technology in extraction and separation technologies, there are many other varied fields of application for this technology. Examples of these applications are the cleaning of semiconductors, optic fibres, missile gyroscopes etc. (Chordia & Robey, 2000; Krukonis et al., 1994), the use of supercritical fluids in particle formation in the pharmaceutical industry (Chordia & Robey, 2000), or as a reactive medium where the use of supercritical water seems to generate a lot of interest. In fact, the application field of supercritical fluids is so broad that it is not possible to cover all the aspects of it in this overview.

The use of supercritical fluids as extraction media has several advantages (Brunner, 1990; Humphrey et al., 1984):

- Supercritical fluids have liquid like densities, but have transport properties, viscosities and diffusivities, comparable to gaseous substances.

- Compressed supercritical gases have good solvent powers.
- The solvent density is the decisive parameter in the solute solubility. The solute can easily be recovered by manipulating the solvent density by changing the system temperature or pressure.

- The temperature of supercritical gas extraction is dependent on the solvent critical temperature. This temperature is normally well below the non-volatile component boiling temperature, which makes this system ideal for the separation of temperature sensitive materials.

- The energy requirements of supercritical extraction are in some cases also much lower than for conventional liquid-liquid extraction processes.

- The replacement of the liquid solvents with gaseous solvents that are easily recovered from the extract is a significant advantage, as it eliminates the problems of residual solvent contaminating the final product.

Some of the disadvantages of supercritical fluid extraction are the high operating pressures, and hence the high capital costs of the equipment compared with standard separation equipment, and the poor understanding of the high-pressure phase equilibrium behaviour (Brunner, 1990; McHugh & Krukonis, 1994).

As this project entails the study of the solubility of components in supercritical fluids for primarily the application in supercritical fluid fractionation, the following section will give a brief background of this application.

1.1 APPLICATION IN HEAVY MOLECULAR WEIGHT SEPARATIONS

McHugh and Krukonis (1994) state that the earliest patent they were able to locate referring to the use of supercritical CO_2 to separate hydrocarbons was a patent brought out by Pilat and Godlewic in 1940 titled the "Method of separating high molecular weight mixtures" (Pilat & Godlewicz, 1940).

The practical application of supercritical fractionation and separation in the petroleum industry and in heavy molecular weight separation are of particular interest in this study, because of the nature of the systems investigated in this work.

Propane De-asphalting

Propane-de-asphalting is the first commercial application that utilized the change in a liquid's solvent power with temperature and pressure in the field of petroleum processing. (1936). This process is still in use today in the refining of lubricant base oils (McHugh & Krukonis, 1994; Sequeira Jr., 1994). It is not strictly speaking a supercritical fluid extraction process because the extraction step is carried below the critical temperature of the solvent.

Compressed liquid propane at 50 °C is used to dissolve all the compounds in the lubricant oil feedstock except for the asphalt fraction. The asphalt is separated from the mixture and recovered. The next step in the process is the de-waxing of the mixture. By evaporating a portion of the propane in the mixture, the mixture is cooled to 4 °C. At this temperature, the wax precipitates from the solution and is removed. Then, by heating the solution to temperatures above 100 °C, the solubility of the components in the mixture is decreased,

3

and the stepwise precipitation and recovery of the resins, heavy ends and naphthalenic constituents is possible. Only the lightest paraffins remain in solution (McHugh & Krukonis, 1994).

ROSE Process

The Residuum Oil Supercritical Extraction, or ROSE, process was developed by Kerr-McGee in the 1950's. It is an improved de-asphalting process, and was first applied commercially in 1976 (Nieuwoudt, 1994). This process, similarly to the propane de-asphalting process, is also not entirely a supercritical fluid extraction process. It derives its supercriticality from the final step in the process.

The residuum oil is mixed with compressed liquid or pentane solvent. Similarly to the propane-de-asphalting process, all the components except the asphaltene fraction dissolve in the liquid phase. After the removal of the asphalt, the mixture consists of the solvent, resin and light oils. The resin is precipitated and removed by heating the solution, isobarically, to a temperature just below the solvent critical temperature. At this temperature, the solvent power of the liquid is not sufficient to keep the resin in solution.

In the final step of the ROSE process, the mixture, which now contains the solvent and light oils, is heated to a temperature slightly above the solvent critical temperature. At this stage, the solvent power is significantly reduced and the light oils are precipitated from the solution. By employing the properties of a supercritical solvent the final step in the ROSE process, the recovery of the light oils is achieved with a minimum heat input (McHugh & Krukonis, 1994; Humphrey et al., 1984).

DEMEX and Solvahl-Asvahl Processes

These two processes are similar to the ROSE process discussed above, employing light hydrocarbon solvents near their critical point to extract light oils and resins from vacuum residuum and heavy crudes and separating it into different fractions.

These processes have low utility consumptions and produce clean demetalised oils that can be used in lube oils or as feedstock for fluid catalytic cracking (Nieuwoudt, 1994).

4

SOLEXOL Process

The SOLEXOL process is another classic near-supercritical extraction process. It was developed in 1946 by the M.W. Kellogg Company (McHugh & Krukonis, 1994). It is similar to the propane de-asphalting process and uses propane as selective solvent to concentrate the poly-unsaturated triglycerides in vegetable oils and extract vitamin-A from fish oils.

At room temperature, propane dissolves all the triglycerides, but heating the propane diminishes its solvent power for the unsaturated triglycerides relative to its solvent power for the saturated triglycerides. Similarly to the propane de-asphalting system, by operating at conditions close to the propane critical point, it is possible to precipitate the various oil fractions through successive temperature increases (McHugh & Krukonis, 1994).

Other Studies in Heavy Molecular Weight Separation

One of the areas of research in supercritical fluid processing is the investigation of the use of supercritical fluid extraction in the fractionation of waxes.

Via et al. (Via & Taylor, 1994) investigated the use of CO_2 and propane in the fractionation of high-density polyethylene wax in order to generate polymeric materials with a narrower molecular weight distribution than can be achieved with the current techniques. They found that propane had a greater solvating strength than the CO_2, but that it did not have the same degree of selectivity. By using a 20 vol% mixture of propane and CO_2, they were able to achieve much higher solubilities with almost the same degree of selectivity achieved by using pure CO_2.

Hickey et al (Hickey et al.) investigated the ability of the ROSE-SR process to separate the Fischer-Tropsch catalyst wax from the catalyst-wax mixture. The ROSE-SR process, or the Residuum Oil Supercritical Extraction – Solids Rejection process, is a derivative of the ROSE process discussed above. They found that it was possible to generate a wax product with a catalyst content lower than 0.1 wt %

De Haan and De Graaw (de Haan & de Graaw, 1991) investigated the fractionation of alkanes with supercritical CO_2. They found that although it was possible to separate the

alkanes, the cost of such a separation plant compared to a standard vacuum distillation plant does not justify the use of the process.

Nieuwoudt (Nieuwoudt, 1994) also investigated the use of supercritical fluid technology to produce high molecular weight n-alkane fractions with low polydispersities. He used propane, iso-butane and n-butane as supercritical solvents, and concluded that the profitability of the process would be better than that of short path fractionation if the required product polydispersity were lower than what can be achieved with one short path distillation unit.

1.2 THE NEED FOR HIGH QUALITY EQUILIBRIUM DATA AND THERMODYNAMIC MODELS

In the supercritical extraction process, as in the case of any other solution or extraction process, the driving force for mass transfer is the system deviation from the thermodynamic equilibrium at the specific operating conditions.

The equilibrium state of a system provides the following information important for the development and operation of a supercritical extraction process (Brunner, 1994):

- The capacity of the supercritical solvent. This provides information on the maximum amount of substance that can be dissolved into the solvent.
- The amount of solvent dissolved in the heavy, solute, phase.
- The selectivity of the solvent. The ability of the solvent to selectively dissolve one or more components from a mixture of compounds.
- The dependence of the solvent properties on the system pressure and temperature.
- The extent of the two-phase area. This area delimits the operating range of an extraction process.

If the capacity and selectivity of a supercritical solvent are known for a specific system, it will be possible to make a first estimate on whether the desired separation can be achieved with supercritical extraction and also on the what the mode of operation of such an extraction system should be (Brunner, 1994). The equilibrium information is also applied in determining the optimal conditions, such as the temperature, pressure and degree of reflux, at which the extraction process must be operated. It enables the designer to

determine the degree of performance of the column, such as the HETP of an extraction column, and to make changes in the process to meet different operating requirements.

The measurement of accurate high-pressure phase equilibrium data is very costly and time consuming, and the possible range of conditions and systems so vast, that it is impossible to determine experimentally the phase equilibrium data for all the possible conditions and systems. Accurate thermodynamic models are therefore needed to correlate and extend the experimental data.

1.3 OBJECTIVES OF THIS STUDY

Supercritical extraction is currently being investigated as a means to deoil waxes (Crause & Nieuwoudt, 2000; Crause, 2000). Removing the lighter molecular weight fractions from a wax the oil content of the wax is lowered, reducing the wax sweating, improving the wax hardness and resulting in a narrower wax melting point temperature range. Current processes used to fractionate the waxes are sweating processes, recrystallisation process, warm-up and spray deoiling, liquid-liquid extraction and more recently short path distillation techniques. In order to operate and evaluate a supercritical fractionation plant optimally, accurate models of the extraction process are needed.

As discussed in section 1.2 above, accurate thermodynamic models are needed to represent the high-pressure phase equilibrium data of the extraction system. However, the development of a mathematical model to represent the phase equilibria has been hindered by several factors. Problems such as the lack of understanding of the phase equilibrium behaviour of systems at high pressures, especially near the critical region of mixtures, and the accurate mathematical representation of the interaction forces between the molecules at high pressures and of different sizes, shapes and polarities, have resulted in the fact that there are no thermodynamic models available today to predict the high-pressure phase equilibria (McHugh & Krukonis, 1994; Nieuwoudt, 1994).

The existing thermodynamic models can however be forced to represent the high-pressure equilibrium data of a system. This is achieved by fitting the model to the data by modifying adjustable parameters within the model. To do this, accurate phase equilibrium data are needed. However, there is a very limited amount of reliable published phase

7

equilibrium data available for supercritical solvent– n-alkane systems in the operating region of interest.

The objectives of this study were:

- To design and develop an equilibrium cell with which the high-pressure phase equilibria of binary mixtures could be studied.
- To study the phase equilibria of supercritical solvents with paraffinic waxes.
- To investigate the ability of some existing models to represent the experimentally determined high-pressure phase equilibrium data.

8

2 HIGH PRESSURE PHASE EQUILIBRIUM CELL DESIGN

2.1 BACKGROUND: EXPERIMENTAL METHODS

A wide variety of experimental methods to study high-pressure phase equilibria has been used in the past. These methods have been lumped into several categories by different authors. The experimental techniques in this work are discussed according to the classification by Fornari (Fornari et al., 1990) where the techniques are classified according to the method employed to determine the equilibrium compositions. The two main categories are the analytical or direct sampling techniques and synthetic or indirect techniques.

The analytic techniques require the taking of samples that need to be analysed further. The synthetic techniques on the other hand, use indirect methods to determine the equilibrium compositions.

2.1.1 Analytical techniques.

Analytical methods involve the determination of the compositions of the phases in equilibrium. This can be done by taking samples from the phases and analysing them at normal atmospheric pressure, or by using physiochemical analysis methods, such as spectroscopic methods, inside the cell at the equilibrium pressure (Dohrn & Brunner, 1995). The analytical techniques can be subdivided according to the methods used to reach equilibrium.

Static Method

The static method is theoretically the simplest method to determine the phase equilibrium. The components are placed in a closed cell, and the contents mixed until pressure and temperature equilibrium has been reached. The mixing is then stopped and the phases allowed to separate. Samples can then be drawn from the various phases and be analysed.

The cells may be of a constant-volume type, where the pressure in the cell is adjusted by changing the amount of volatile component in the cell, or of a variable-volume type where the cell volume is changed. In the past the volume change was accomplished by injecting

9

mercury into the cell, but more recently cells have been designed were the cell volume can be varied by moving a piston into and out of it.

The sampling procedure is the critical operation in the static technique. The experimental errors with this method are usually in the determination of the equilibrium concentration, and are caused by the following:

- Non-equilibrium at the moment of sampling.
- Changes in composition during sampling.
- Insufficient phase separation.

A major problem with this technique is that there is a drop in pressure in the cell when a sample is taken. This pressure drop results in a disturbance in the equilibrium condition within the cell. To overcome this problem researchers have reduced the sample size. However, the near the critical point the mixtures are very sensitive to a small drop in pressure.

In the region near the mixture critical point the physical properties, such as the densities of the various phases present, are very similar. This then results in poor separation of the phases and makes the sampling of the phases extremely difficult in this region. The static analytic technique is therefore unsuitable for work in the mixture critical region.

Circulation Method

There are several variations of the circulation method employed in experimental designs (Fornari et al., 1990).

With single-pass flow or pure gas circulation methods, a continuous high-pressure gas stream is passed through the liquid phase. Once equilibrium has been reached, the effluent gas stream is sampled and analysed. Samples can also be taken from the liquid phase to determine the gas phase solubility in the liquid. This system is ideal for the study of mixtures with high concentrations of volatile components. The possible lack of attainment of equilibrium is however a problem with this system (Fornari et al., 1990; Dohrn & Brunner, 1995).

10

In order to promote the attainment of equilibrium within the cell, either the liquid or vapour or both phases are continuously recirculated. This increases the contact area between the phases and reduces the time needed for the phases to reach equilibrium.

The recirculation loops may also be used as sampling loops for the individual phases. This will eliminate the problem of the pressure drop during sampling. However good phase separation in the cell and no entrainment of the different the phases in the sampling loops must first be ensured, before a sample can be taken.

Continuous Flow Method

Researchers have employed several different experimental methods involving the continuous flow of phases in their study of high-pressure phase equilibria.

The first method is one in which both the heavier and lighter phases are continually fed to a mixing cell where they come into contact and reach equilibrium. Downstream from the cell the phases are separated and expanded individually. Four samples, of which the composition can be determined individually, are produced in this manner. This setup has the advantage that the residence times in the cell for both phases are very short. It makes this technique ideal for use in situations where high temperature data is needed from temperature sensitive materials. Large quantities of samples can also be produced. However, the separation of the phases may be problematic in the near critical region, and the possibility of phase entrainment also exists.

Another similar experimental technique is one in which the heavier phase or solute has been immobilized in a packed column. The high-pressure solvent, or lighter phase, is brought into contact with the heavier phase by pumping it through the column. After passing through the column the stream is expanded and the heavier components collected in a cold trap. The flow rate of the solvent through the column must be controlled to be such that there is sufficient contact time in the column to ensure equilibrium with the heavier component.

This method has the following disadvantages:

- The exact flow rates of the streams need to be known in order to determine the equilibrium compositions accurately.

- Due to the short contact time there is always a risk that equilibrium conditions have not been obtained.

- Density inversions in the phases may cause problems.

- Undetected phase changes can occur in the column.

- Only the lighter phase is sampled, and the solubility of the lighter phase in the heavy phase is unknown.

- Care must be taken with multi-component mixtures, not to deplete one of the components during the experiment.

- Possible entrainment of the liquid solute at high solvent flow rates.

2.1.2 Synthetic Techniques

With synthetic methods no sampling of the phases are necessary. The problems inherent with sample taking are thus avoided. These techniques can be used where analytical methods fail, e.g. at points where the phases separation is poor, i.e. near the critical point, or in barotropic systems where at certain conditions the phases have the same density.

Indirect methods are used to determine the phase boundary, i.e. the points where the transition from one phase to another occurs. Visual or other physical properties are monitored to detect the phase transition. With binary systems, with two degrees of freedom, the composition of the phases are fixed when the temperature and pressure of the system are known. However with multi-component systems, this technique will only provide information on the existence of the phase envelope, it will still be necessary to take samples in order to determine the phase compositions and the tie lines. Synthetic method cells may however be designed to facilitate the taking of samples if necessary.

The synthetic method requires that accurate quantities of the components be loaded into the cell. The pressure in the cell is then varied at a constant temperature, or the temperature varied at a constant pressure, until the disappearance or appearance of a phase in the cell can be detected. Since it is easy to vary the pressure in the cell by simply changing its

volume at constant temperature, constant temperature, variable volume cells are used in most cases. The temperature, pressure and composition (in the case of a binary system) at which the phase transition is observed form a point on the phase boundary line.

The phase transition can be detected directly by visual observation. The point at which the formation of the first vapour bubble in the cell can be observed as the pressure is reduced, is defined as the bubble point of the system. The dew point is defined as that point at which the first liquid droplets or dew can be detected as the pressure is reduced.

With iso-optic systems, where the phases have approximately the same refractive index, the visual observation technique cannot be used. However, changes in other physical properties of the system can also be monitored to determine a phase transition. At the phase boundary, the compressibility of a system changes (Brunner, 1994). A phase transition can therefore also be detected by monitoring the pressure-volume relationship of a system. Over the range of the experiments there is a linear relationship between the pressure and change in volume of the system, however when a phase transition occurs in the system the slope of the pressure – volume relationship will change. Usually the change in the slope of the line is gradual and both lines have to be extrapolated to find the intersection point of the lines. This intersect is at the phase boundary conditions. Dohrn (Dohrn & Brunner, 1995) reports other techniques to detect the phase transition by monitoring the change in system physical properties such as the use of microwaves to monitor changes in dielectric properties.

The advantages of the use of the synthetic method are as follows:

- If there is no sampling an infinite number of data points at a constant composition, but at different temperatures and pressures can be obtained without having to reload the cell.

- When the phase transitions are determined visually the presence of an additional phase will be observed, and density inversions can be easily detected.

- Heavy solids, liquids and polymers can be studied with this method.

- Small samples are required for the experiment.

Due to the nature of the experimental method used to determine the phase equilibria, inaccuracies in the experimental data are usually caused by the inaccurate determination of

13

the total composition of the cell content and by the inaccurate measurement of the equilibrium pressure.

The total cell composition is determined by the careful weighing of the components before loading.

The equilibrium pressure is taken at the point where the first formation of gas or liquid droplets can be observed. However the phase boundary is, by definition, that point at which there is zero amount of a phase present. This inaccuracy is at its most pronounced in the regions where the system is highly sensitive to pressure, in regions close to the mixture critical point or in supercritical gas extraction systems.

The synthetic method is unsuitable for use in systems with low concentrations of the heavier components. There is too little of the condensable component present to detect the formation of an additional phase visually or by a change in a mixture physical property.

2.1.3   Other Techniques

Besides the analytical and synthetic methods to determine the phase equilibria, other techniques such as chromatographic and spectroscopic methods can also be employed.

Bruno (Bruno & Ely, 1991) reports on the use of Supercritical Fluid Chromatography, SFC, instrumentation in the study of high-pressure phase equilibria, and how the instrumentation may be adapted to perform these solubility measurements. This technique is able to produce rapid measurements on a wide range of solid samples, but is of little value for heavy liquid samples. A major drawback of the use of SFC is the cost of the experimental equipment. Thin layer chromatography, TLC, has also been used to carry out the solubility measurements. This technique is, however, not suitable for high accuracy solubility measurements, but is useful for determining the threshold solubility pressures.

Various spectroscopic methods are also being employed in the investigation of high-pressure phase equilibria. Fourier-transform infrared spectroscopy has been used to determine the concentration of the solute in the solvent. A solid solute is loaded into a cell, which is then purged and pressurised by the solvent. After sufficient time has been allowed for the system to reach equilibrium, the concentration of the solute that has dissolved can be determined by measuring the absorbance of a characteristic property of the solute. For

example if a supercritical CO_2 – hydrocarbon system was being investigated, the absorbance of a strong band such as the C-H stretching frequency could be measured, and by using the Beer-Lambert law the concentration of the dissolved hydrocarbon could be calculated. Similarly, nuclear magnetic resonance (NMR) spectroscopy has been used in the investigation of high-pressure solubility. Here the signal from the solution can be distinguished from the solid by the large difference in the spin-spin relaxation times. The spectroscopy techniques are mostly suited to very dilute mixtures, and the study of solid-supercritical fluid equilibria (Bruno & Ely, 1991; McHugh & Krukonis, 1994).

Other techniques to determine the partial molar volume have also been developed, e.g. measuring the density using vibrating tube densitometers. The major uncertainties with this technique lie with the temperature control of the system (McHugh & Krukonis, 1994).

2.2 CELL DESIGN

2.2.1 Experimental Method

This project entails the measurement of high-pressure equilibrium data of supercritical solvents and alkanes. The system has the following key characteristics that had to be taken into account when an experimental method for studying the equilibria was decided upon.

- The alkanes have a high melting point.
- The alkane components used in the study are expensive.
- The phase equilibria under investigation are in the mixture critical region.

Furthermore, any proposed experimental set-up had to be of a simple design so that it could be manufactured in-house, or had to be reasonably priced if it had to be purchased.

The high melting point of the alkanes will be problematic during sampling. Once the system pressure is reduced, the heavy paraffinic components will immediately precipitate. This may cause problems with the clogging of the sample tubes and valves. It will also make the accurate analysis of the samples extremely difficult since all the precipitated heavy components will first have to be recovered from the sampling system before it can be analysed. This problem can be solved by taking large samples, thus reducing the experimental inaccuracies as a result of irrecoverable solute in the sampling system.

However, as mentioned in section 2.1.1, the taking of large samples in a static experimental method will disturb the phase equilibrium in the cell, resulting in inaccurate data. The other analytical techniques such as circulation and continuous flow methods do not have the problem of pressure drop during sampling, but they require the use of large quantities of the components. Because of the high cost of the alkanes, these flow methods were deemed impractical.

Techniques that incorporate chromatography and spectroscopy were unsuitable because of the high cost of the experimental equipment and the complicated method of operation.

Analytical techniques were thus found to be unsuitable to study the high-pressure phase equilibria in this work. This finding is also supported by the fact that the project involves the study of phase equilibria in the mixture critical point. As has been mentioned earlier, the phase densities are very similar in this region, making phase separation before sampling very difficult.

It was therefore decided to use a synthetic technique to study the phase equilibria.

2.2.2   Experimental Design

As discussed in section 2.2.1, it was decided to study the phase equilibria by a synthetic method, using a change in the physical properties of the system to detect a phase transition within the equilibrium cell. The simplest method to observe this phase transition is to visually observe the appearance or disappearance of a phase. Changes in other physical properties, such as the overall system density, may also be used to detect a phase transition. It was decided to develop a cell incorporating both the visual technique and the monitoring of system density.

The cell design had to meet the following requirements:

- The cell volume had to be large enough to ensure that the experimental inaccuracies during the loading of the cell will have a negligible effect on the overall cell composition. The cell was designed to have a volume of roughly 130 cm^3. In conducting the experiments, depending on the system to be studied, between 50 g and 120 g of material was loaded into the cell. The components were weighed on a scale

with a 0.01 g accuracy. A 0.02 g error during the loading will therefore only result in a 0.04 % error in the cell composition.

- A maximum volume of the cell chamber had to be visible. This will enable the operator to easily observe a phase boundary. It will also reduce the risk of an additional phase present in the system going undetected. In future modifications of the cell, the large visible volume will aid in the sampling of the various phases. The operator will be able to identify the various phase interfaces and observe when complete phase separation has been attained.

- The temperature and pressure within the cell have to be accurately controlled, in order to ensure accurate experimental data.

- The cell design had to be such that future modifications of the cell are possible. McHugh (McHugh & Krukonis, 1994) describes how the measurement of the mixture viscosity can be incorporated into a view cell apparatus. A circulation section with a vertical tube is incorporated into the cell design. The cell content is forced into a single phase and then circulated through the vertical tube. After sufficient time has been allowed for the mixing of the cell content, the circulation section is shut off and the time it takes a spherical weight to fall through the solution in the vertical tube, measured. By calibrating the weight's fall time with a fluid of known viscosity the mixture viscosity can be determined. Other possible modifications of the cell design are the addition of circulation loops and sampling ports, to enable the investigation of multi component systems.

The experimental set-up used in this study is as follows:
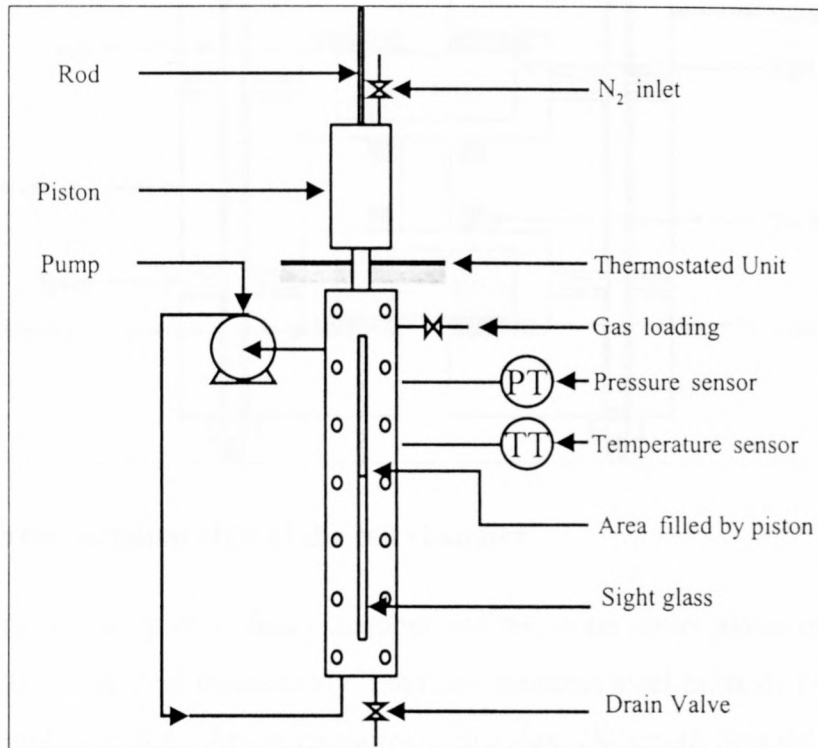
Figure 2-1 High Pressure Variable Volume View Cell

It consists of three sections, the main cell chamber, the circulation section and the piston unit.

Cell Chamber

The chamber design is based on a design by Roebers and Thies (1990). They developed an equilibrium view cell for use in a continuous flow apparatus. The cell is conceptually based a liquid level gauge such as the Jerguson Model T-40 (Jerguson Gage and Valve Co.).

18
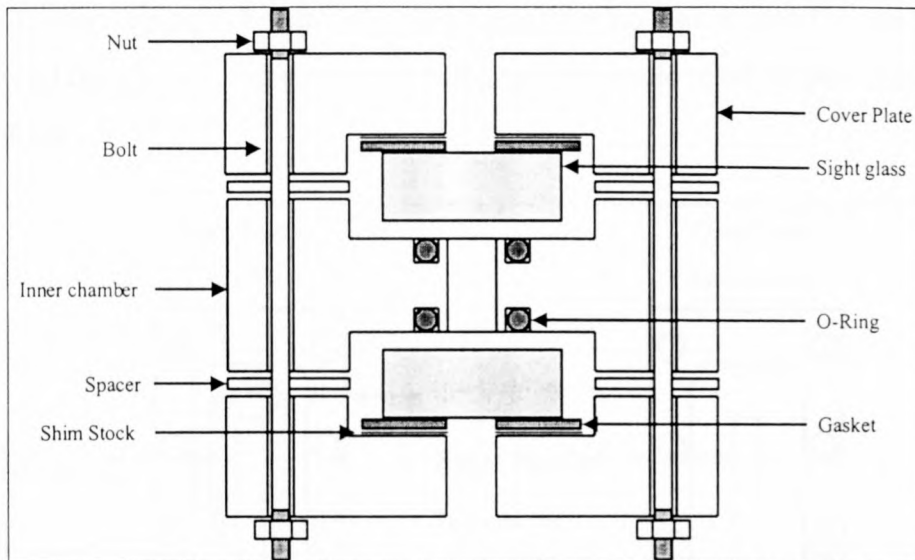
Figure 2-2 Cross sectional view of the cell chamber

The cell body is made up of an inner chamber and two outer cover plates machined out of 316 and 304 stainless steel respectively. Fourteen stainless steel bolts of 14 mm diameter hold the cell body together. Armoured borosilicate glass (Macbeth Brand Gage Glass), as used in high-pressure liquid level gauges, is used as the sight glass. This sight glass is the controlling factor in determining the maximum operating pressure and temperature of the system. The manufacturer's maximum recommended working pressure for the glass is 344 bar at 338 K. The maximum temperature at which experimental work will be done with this cell is 353.15 K, it is therefore advisable to work at a lower maximum operating pressure. The cell has been repeatedly tested up to operating pressures of 280 bar, with the maximum pressure set at 300 bar.

The sealing of the cell against the sight glass at the high operating pressures proved problematic. As a first attempt, Viton o-rings were used to provide this seal. Viton was selected as the material because a temperature resistant material was required at the higher operating temperatures of up to 353 K. However, during the experiments it was found that the o-ring material was not resistant to the supercritical CO_2. The CO_2 would permeate into the o-rings at high pressure, and then as the pressure in the cell is reduced, they would rupture as a result of the pressure difference between the gas trapped inside the o-rings and that outside it. A CO_2 resistant material was therefore required to provide the sealing.

Teflon o-rings were finally found to able to provide sealing under the system operating conditions. However, Teflon exhibits creep when placed under mechanical stress and it is

necessary to store the equilibrium cell under pressure when not in use. This prevents the o-rings from relaxing and moving out of position, which would result in poor sealing around the sight glass.
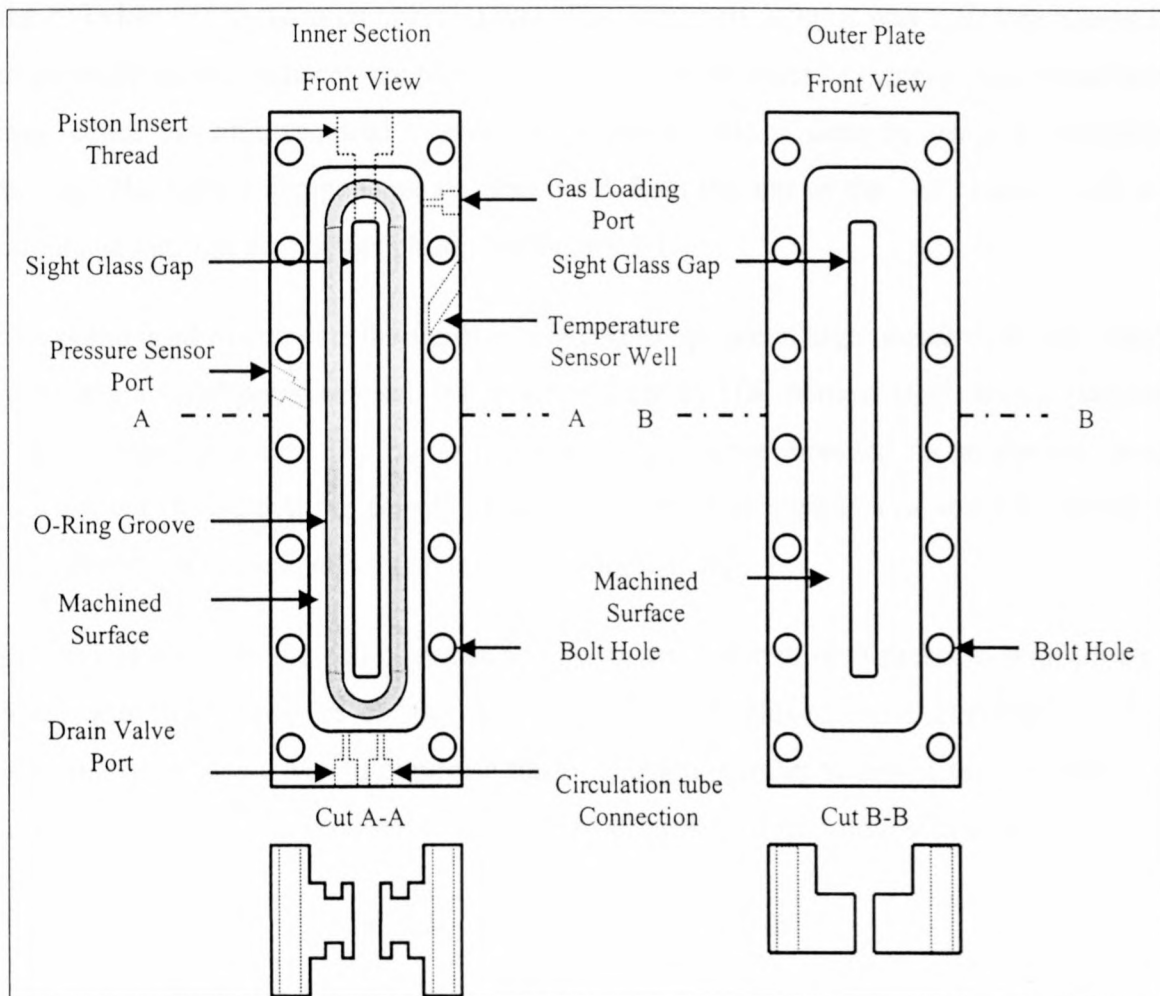
Figure 2-3 Cell Body View. Inner Section Outer Section

The cell had to be manufactured to very tight tolerances in order to prevent direct contact between the sight glass and the metal. The cell dimensions were designed in such a way that once the bolts have been tightened there would always be a fixed gap of 0.05 mm between the glass and the metal. The o-ring grooves or housings were designed to accommodate a 6.0 mm thick o-ring. When the bolts are tightened, the o-ring will be compressed, providing the necessary sealing. The sight glass is protected from contact with the outer cover plate by using KlingRit gasket material.

Circulation Unit

Because of the geometry of the main cell chamber, there is only a small area of contact between the various phases present in the cell. As a result, the time required for a system in the cell chamber to reach equilibrium would be extremely long. It was therefore necessary to promote mixing between the phases within the cell in order to increase the contact area and reduce the time required to reach equilibrium. This is done by using a circulation stream. The lighter components are drawn off from the top of the cell chamber and are circulated through the heavier phase. See Figure 2-1.

The pump used to circulate the fluids is required to operate at high pressure but only needs to deliver a small pressure head. It is machined out of 316 stainless steel, with a magnetic Teflon coated impeller. The pump is driven by a magnet mounted on an electric motor shaft. It was found that the density of the lighter phase at pressures of about a 100 bar, is such that it can be pumped by this relatively simple pump.

The tubing between the cell chamber and pump are 1/4 inch high pressure stainless steel tubes with high pressure fittings from Autoclave Engineers. The circulation unit is constructed in such a way to minimise the tube length in order to reduce the hold-up in the circulation unit and the required pressure head as a result of friction losses in the system.
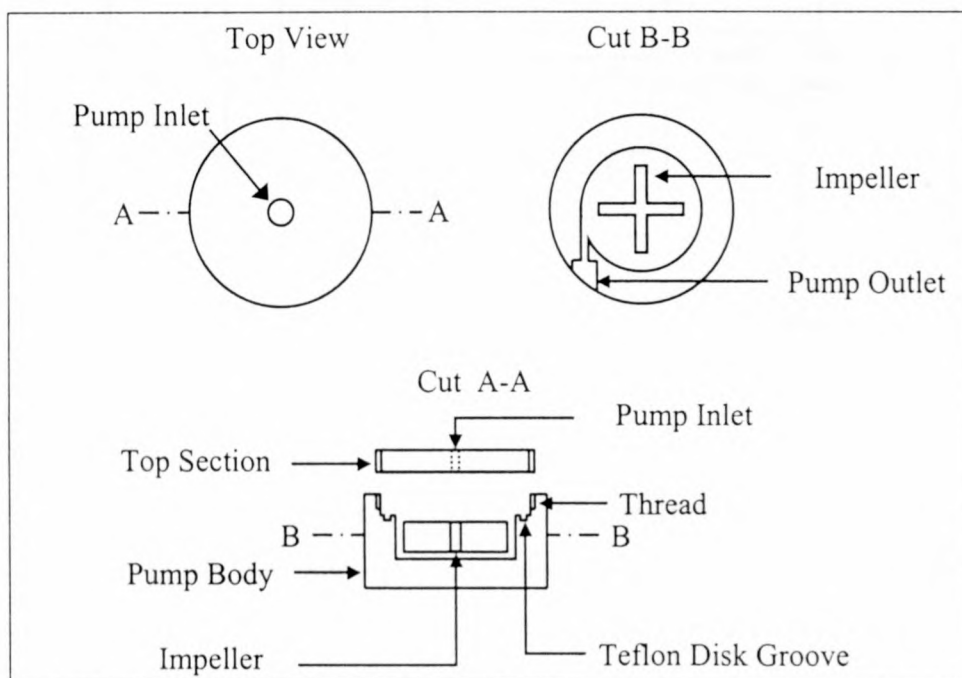
Figure 2-4 Simple Diagram of the Pump Design

It was found that the Teflon coated impeller experiences swelling when it has been in contact with supercritical CO_2 for a long time. It was therefore necessary to reduce the impeller dimensions in order to accommodate the swelling during operation, otherwise the impeller would get too large for the pump housing, and get stuck. However, the clearance between the impeller and the pump walls could not be too large, since this would reduce the pump's performance. An optimum size for the impellor had to be found, this was done by trial and error.

A similar problem with the rupturing of Viton o-rings as was described in the previous section was experienced in the pump. The pump housing was finally designed in such a way that the sealing is done against a flat Teflon disk. See Figure 2-4.

Piston Unit

The pressure in the cell is controlled by moving a piston in and out of the cell chamber. This changes the cell volume, and hence increases or reduces the cell pressure.
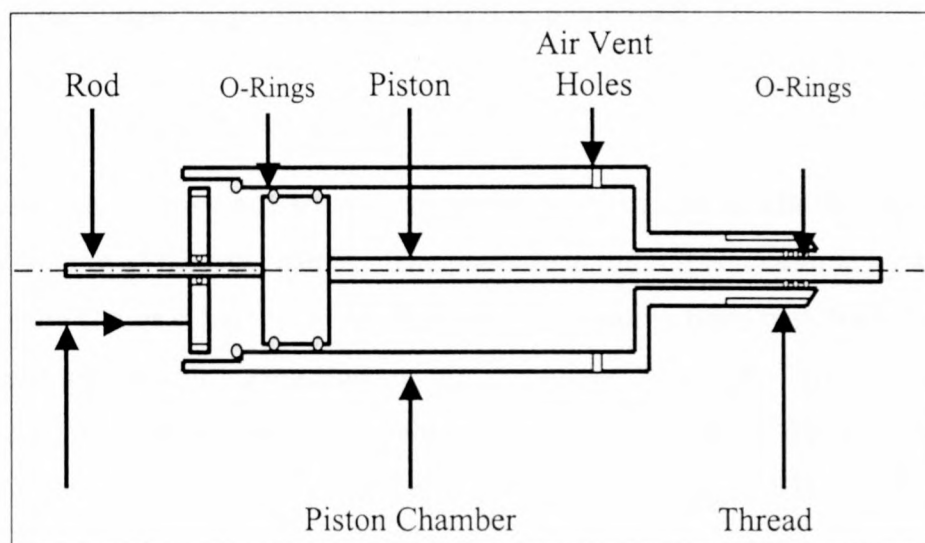
Figure 2-5 Piston Unit

The piston inserted into the chamber has a diameter of 16.5 mm and can cause a 33 % volume reduction at the maximum piston displacement. The piston has an area ratio of 20:1, and nitrogen from a standard gas cylinder is used to exert the pressure on it. A pressure regulator on the cylinder and a vent valve in the nitrogen feed line are used to control the nitrogen pressure. The nitrogen feed line also contains a pressure relief valve as

a safety measure. The relief valve is set to prevent the piston unit from exerting a pressure greater than the maximum allowable operating pressure of the cell chamber.

A stainless steel rod has been attached to the piston. By measuring the change in the length of the rod protruding from the piston chamber, the displacement of the piston into the cell, and the hence the change in cell volume can be determined. If the cell volume and the mass loaded into the cell are known, it is a trivial operation to calculate the overall system density.

The piston unit is screwed into the top of the cell chamber. See Figure 2-3. Sealing between the cell chamber and the piston is accomplished by placing a precision Teflon collar around the piston before screwing it into the cell chamber. The collar is then compressed as the piston unit is tightened, providing the seal between the cell chamber and the movable piston. There are three additional o-rings situated in the piston neck, they serve as a backup to the Teflon collar. These o-rings are not normally exposed to the cell contents and are made out of Viton. Since all the other o-rings in the piston unit are not exposed to the system temperatures, standard o-rings are used.

Temperature and Pressure control

As discussed in the previous section, the pressure in the cell is adjusted by moving the piston in and out of the cell chamber. The pressure in the cell is measured by a ISI Digital Melt Pressure Gauge (Model 0251A). The pressure sensor is filled with NaK, which serves as the pressure-transmitting medium within the sensor. The NaK, however, experiences thermal expansion at temperatures above ambient. To compensate for this expansion the pressure sensor was calibrated in the temperature operating range of 313.15 K to 343.15 K with a dead weight pressure gauge. The calibration of the pressure sensor is accurate to within 0.4 bar. See Appendix E for the calibration data and curves for the pressure sensor.

The temperature control in the cell is achieved by placing the cell in a thermostated water bath. The water bath has two transparent Lexan windows. The cell sight glasses are lined up with these windows to enable to operator to see the cell contents. The water bath has an additional purpose in that is serves as a safety measure in case of cell failure under pressure. The large mass of water in the bath will absorb some of the explosive force if a catastrophic cell failure occurs. The bath temperature is controlled by a Julabo MD heating

circulator with a temperature stability of $\pm$ 0.02 °C. The cell temperature is monitored by a high accuracy 4 wire PT-100 probe, which is placed in a temperature sensor well in the cell chamber wall. The probe has been calibrated by the SABS and has an error smaller than 0.1 K in the operating temperature range.

2.3 PHASE EQUILIBRIUM CELL OPERATING PROCEDURE

2.3.1 Loading Procedure

The synthetic or indirect method used to determine the phase equilibria, requires that the exact composition of the mixture loaded into the cell must be known.

A known mass of the n-alkane is loaded into the cell chamber through the piston insert opening at the top of the cell. To ensure that the presence of dissolved gases in the waxes does not influence the equilibrium measurements, the alkanes must be thoroughly degassed during each loading. This is done by evacuating the cell to a pressure of 80 Pa using a multistage vacuum pump once the wax is loaded into the cell. The cell and content is then left under these vacuum conditions for 30 min, with the vacuum pump continually drawing off any gas that may have come out of solution. Afterwards the cell is pressurised with the solvent to be used. The pressure is then released and the solvent allowed to escape, taking care not to entrain any of the heavy component. At room temperature conditions the cell is pressurized to 40 bar with CO_2 as solvent and to 25 bar when ethane is used as the solvent. Under these conditions the solubility of the heavy alkanes in the solvents is negligible. The flushing procedure is repeated three times to ensure the complete removal of all the air from the cell.

The solvent is loaded into the cell by using a gas bomb with a 300 cm^3 volume. The bomb is flushed three times with the solvent, before loading it. It is then connected to the cell at the gas loading port, and the connecting lines between the bomb and the cell evacuated using a vacuum pump. The solvent is forced from the bomb into the cell by heating it to a temperature higher than that of the cell chamber. The exact amount of solvent loaded into the cell is determined by weighing the gas bomb before and after the loading of the cell.

2.3.2   *Operating Procedure*

The loaded cell is placed into the thermostatically heated water bath. Due to the weight of the phase equilibrium cell a motor driven hoist system is used to lift and lower the cell. The water level in the bath should be sufficient to cover the cell entire chamber. See Figure 2-1. Due to the large mass of material that has to be heated, it is advisable to preheat the water bath to the desired operating temperature prior to the actual experiments, since this will to reduce the time taken for the entire system to reach thermal equilibrium.

As soon as the heavy alkane has melted, if it was in the solid phase, the circulation unit must be switched on and the pressure in the cell increased until the cell contents have been forced into a single phase. This will ensure that the composition in the cell remains constant even if there are small leaks in the system.

Once thermal equilibrium has been reached, the pressure in the cell can be gradually reduced until the formation of a second phase is observed. The phase boundary is located in the pressure interval between the points where it is possible to distinguish between a single or a two-phase state. The size of this pressure interval is reduced by alternately increasing and decreasing the pressure a number of times, each time observing the phase changes in the cell. It was found that with this experimental set-up the phase transition could be observed within an interval of 0.1 bar.

The phase boundary at the specific operating temperature is taken at the pressure at which the formation of the first liquid droplet or vapour bubble can be observed. The composition of the primary phase is taken to be that of the total composition loaded into the cell.

Besides improving the mixing within the cell, the use of a circulation stream has an added advantage in that it aids in the detection of the formation and disappearance of a second phase. The circulation is so turbulent that very good mixing of the two phases can be achieved. The cell contents appear opaque because of the dispersion of the small liquid of vapour droplets in the primary phase, however, as soon as only one phase is present the cell contents become clear.

The phase transition can also be detected by monitoring the change in the overall density of the cell contents. The system density is monitored by measuring the piston rod length at various pressures in the single and two phase regions. This data can then be used to

determine the phase boundary point as discussed in section 2.1.2. During experimentation, it was found that the phase boundary pressure detected by monitoring the change in volume in the cell is about 0.5 bar lower than the pressure determined by visually observing the phase transition. See Appendix C. As the technique monitoring the density change of the system requires the extrapolation of the data, it was deemed less accurate. Because a definite phase transition could be seen at all times in this work, only this technique was used to determine the phase boundaries.

Using both methods concurrently provides a check for the accuracy of the phase boundary determination. It also enables the operator to determine the molar volumes or densities of the phases on the phase boundary line.

A whole range of data points can be measured at various temperatures without having to reload the cell. Once a specific data point has been determined satisfactorily, the system can simply be heated to the next operating temperature. Whenever the operator is not actively busy determining a phase boundary, the cell contents must be kept in the single-phase region. As mentioned previously this will ensure that the overall cell composition remains constant, even if there is a loss of material as a result of small leaks in the system. In such a case only the density data will be inaccurate.

2.3.3 *Unloading, Cleaning and Storage*

During the unloading of the cell the operator must wear the necessary protective eyewear and heat resistant gloves.

The cell must be unloaded at temperatures well above the melting point of the paraffinic wax in the cell. Because of the high melting temperatures of the waxes and the temperature drop associated with a reduction in pressure, there is the possibility of the drain valves and circulation lines becoming clogged with solidified heavy product during unloading. If the cell temperature is high enough during unloading, the extent of this problem is greatly reduced.

The phase equilibrium cell must be removed from the water bath and dried completely. This is necessary to prevent the possible contamination of the wax with water from the cell exterior during unloading. The drain valve must be slowly opened and the wax collected.

Because of the high cost of the waxes it is necessary that as much wax as possible be recovered for reuse. If the valve becomes clogged by solidified wax, a hot air gun may be used to heat the valve and melt the product. The unloading must be done slowly to prevent the excessive cooling of the product and cell. A sudden reduction in the cell pressure and temperature may cause the sight glass to shatter or the o-rings to rupture.

Once the pressure has been released and the majority of the wax recovered, the piston unit may be removed. The cell must be washed with a suitable solvent, such as toluene, while it is still warm. This will increase the solubility of the heavy alkane in the solvent. It is necessary to drain the circulation lines and force solvent through the circulation system to clean it. The washing procedure is repeated three times.

Once the cell has cooled down all the traces of the solvent used to wash the cell must be removed from it. This is done by rinsing the cell with a volatile liquid such as pentane. Pentane has the added advantage that it is also able to dissolve any trace amounts of the heavy alkane that may have been left behind in the cell. The cell is rinsed three times to ensure the complete removal of the solvent. The volatile liquid that remained behind in the cell after rinsing is then evaporated by forcing compressed air through the cell for an hour.

If the cell is going to be out of operation for an extended period it is necessary to store it under pressure. The cell must be partially filled with liquid CO_2. This will prevent the Teflon o-rings and seals from relaxing and creeping out of position, causing leaks in the cell. CO_2 is used because it is non-toxic and inflammable. It would therefore not cause a hazardous situation if the cell were to start leaking over time. Partially filling the cell with liquid CO_2 ensures that the pressure will be maintained in the cell over an extended period of time, even if there is a small leak in the system.

Due to safety considerations the cell contents must never be viewed directly when it is under pressure. In this experimental set-up a mirror was used to view the contents during loading, unloading and operation.

2.4 FUTURE DESIGN MODIFICATIONS

In order to eliminate the need for the phase equilibrium cell to be stored under pressure, the sealing system should be redesigned. By using Teflon o-rings that completely fill their o-ring housings the seal would be placed under constant mechanical strain, once the chamber bolts and nuts have been tightened, and therefore eliminating the need for a high cell pressure to provide the force on the o-rings.

If the scope of the experimental work is expanded to include multi-component systems, the circulation system could be modified in such way to facilitate the sampling of the various phases present. Two circulation streams could be used to circulate the two phases individually. The circulation lines could be modified to include sampling bombs, which could be shut off from the system, providing a way to take samples without disturbing the equilibrium within the cell.

The circulation lines could also be modified to incorporate the measurement of other physical properties of the cell contents. For example, by incorporating a vertical tube and falling ball into the circulation system the mixture viscosity can be determined (McHugh & Krukonis, 1994).

3 HIGH PRESSURE PHASE EQUILIBRIUM MEASUREMENTS

3.1 BINARY PHASE EQUILIBRIA

This work entails the measurement of the phase equilibria of binary mixtures of supercritical solvents, CO_2 and ethane, with paraffinic alkanes, n-C_{12}, n-C_{16}, n-C_{20}, n-C_{24}, n-C_{28} and n-C_{36} at operating conditions of between 318 and 373 K, and in the pressure range of 70 – 300 bar. The phase boundaries were determined by using a synthetic variable volume view cell.

To use the data optimally it is first necessary to know and understand the type of phase behaviour the system displays and where the measured data fit into the overall binary phase equilibrium diagram.

It was found that virtually all the possible binary phase equilibrium systems could schematically be represented with six P-T diagrams (McHugh & Krukonis, 1994). Of these, the first five diagrams could be qualitatively modelled by using certain a and b parameters in the Van der Waals equation of state (Brunner, 1994). The sixth type can only be predicted by angle-dependent potential functions and not by the Van der Waals equation. However, this form of phase equilibrium is not very common.

Before going into the detail of the phase diagrams it will be helpful to take note of the phase rule:

$$F = n - p + 2 \tag{3.1.1}$$

In equation 3.1.1 F represents the degrees of freedom, n the number of components and p the number of phases present in a closed system. Zero degrees of freedom will be represented as a point on a P-T-x diagram, one, as a line, and three as a volume. For a binary system it is possible to have up to four phases in equilibrium, forming a point on the P-T-x diagram.

29

3.1.1 Vapour Liquid Phase Diagrams

Type I

This is simplest possible phase behaviour for a binary mixture. It is characterised by complete miscibility of the light and heavy components in the liquid phase. Only a single liquid phase is therefore present throughout the phase diagram. A continuous mixture critical curve runs from the heavy to light component critical points.
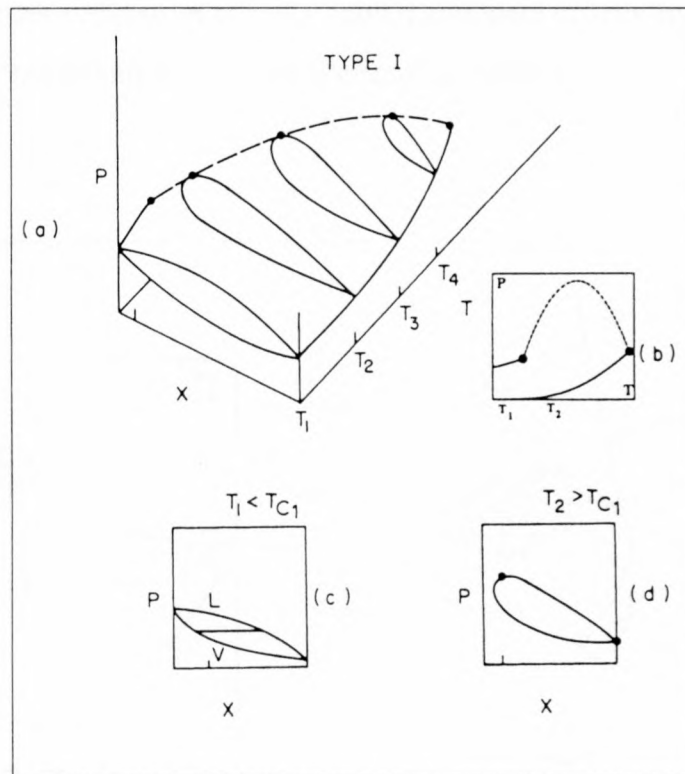
Figure 3-1 Type I Phase Boundary behaviour. (a) P-T-x (b) P-T (c, d) P-x projections at different temperatures (McHugh & Krukonis, 1994).

This phase behaviour is usually found with mixtures from a particular homologous series, such as n-alkanes, where the size difference between the components does not exceed a certain value.

Below the critical points, the P-x diagram has the familiar cigar-shape of binary equilibria. Figure 3-1(c). At pressures above the light component critical point the vapour-liquid envelope does not reach a mixture composition of x = 0 as the light component vapour pressure curve is never crossed. Figure 3-1(d)

The mixture critical curve runs from the heavy component critical point to the light component critical point. At temperatures between these points, the curve passes through the maximum of the vapour-liquid curves, or in other words the point on the phase boundary where slope is equal to zero. (dP/dx = 0). It is important to note that the mixture critical curve represented in Figure 3-1(a) and (b) is only one possible representation of the curve. Other systems may have a linear mixture critical line between the critical points or have pressure minimums or azeotropes at some points in the curve.

The ethane – n-alkane systems up to n-C_{17} exhibit complete miscibility of the components in the liquid phase and belong to this type (Peters et al., 1991).

Type II
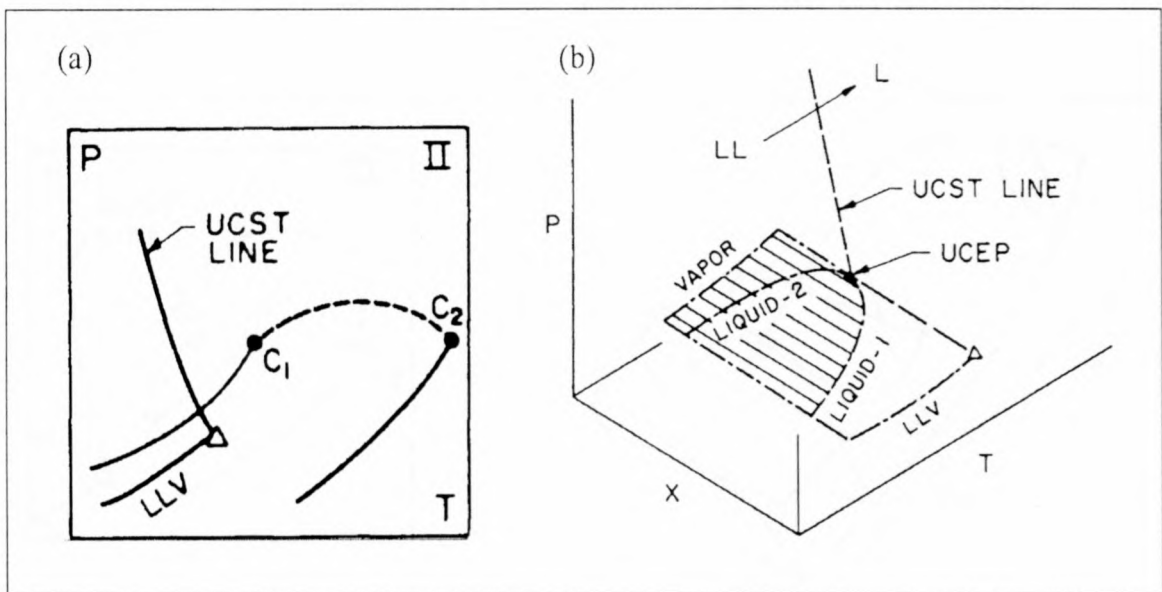
Figure 3-2 Type II Phase Boundary behaviour. (a) P-T (b) P-T-x (McHugh & Krukonis, 1994; Brunner, 1994)

This type of phase behaviour is similar to type I behaviour, except for the existence of liquid immiscibility at lower temperatures. The liquid phase splits into two liquid phases, resulting in the three-phase liquid-liquid-vapour, LLV, equilibrium line. At the liquid-liquid critical point the two liquid phases become critically identical and beyond this point no differentiation can be made between the two liquid phases, only a vapour-liquid equilibrium exists. Critical opalescence can be observed at this critical point. The upper critical solution temperature line (UCST line) is the line that connects the critical points

31

where the liquid phases merge. Only one liquid phase is present if the system temperature is increased beyond this temperature. The upper critical end point (UCEP) is the point of intersection between the LLV area and the UCST line. Depending on the type of binary system the UCST line may have a positive or negative slope.

With this type of phase behaviour the mixture critical curve is still a continuous curve between the heavy and light component critical points.

With alkanes, the heptane CO_2 system, is the first alkane CO_2 system that system displays liquid-liquid immiscibility (Charoensombut-Amon et al., 1986; McHugh, 1994). The type II behaviour continues for the various CO_2 – n-alkane systems up to n-C_{12} (Elliott & Lira, 1999).

Type III
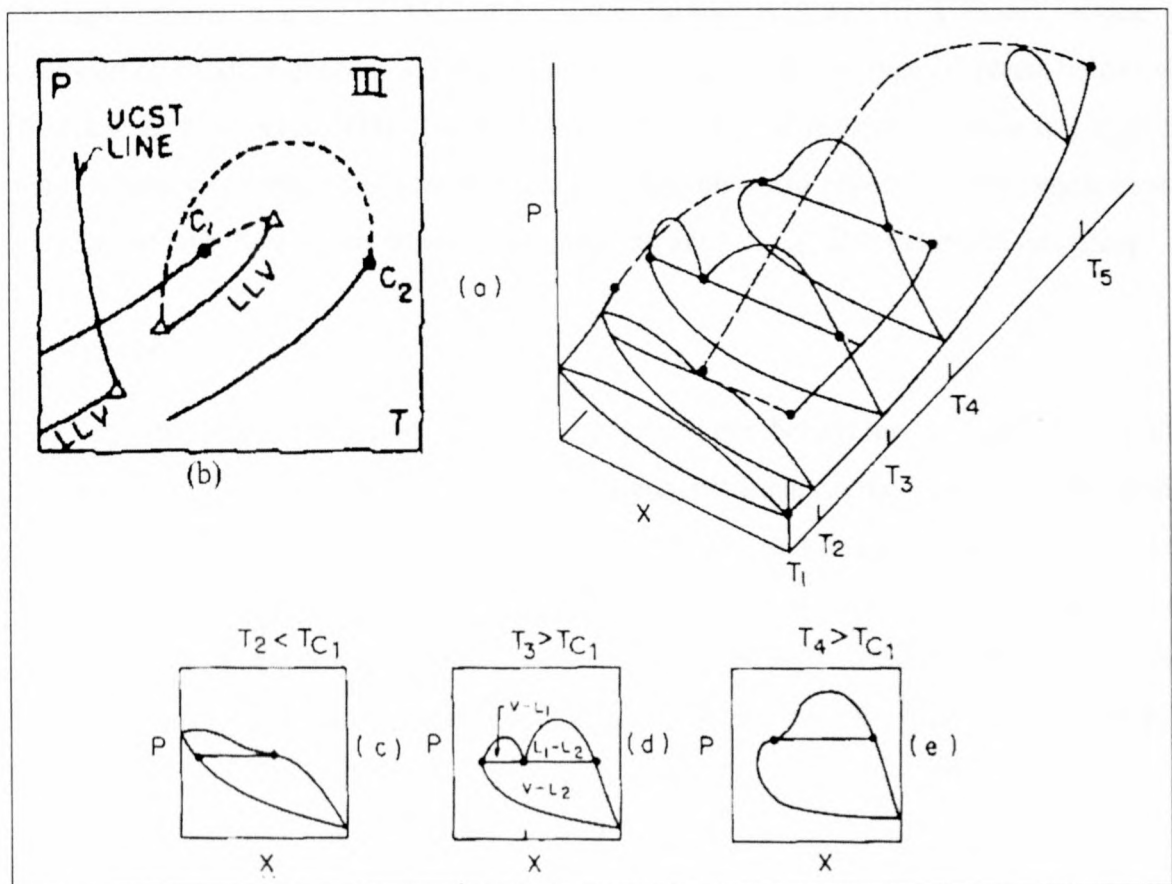
Figure 3-3 Type III Phase behaviour, (a) P-T-x (b) P-T (c, d, e) P-x projections at different temperatures (McHugh & Krukonis, 1994).

This type of phase behaviour is characterised by the existence of primary LLV equilibrium area near the light component critical point, in addition the secondary liquid immiscibility at the lower system temperatures. Two mixture critical lines can be observed. The first line runs from the heavy component critical point and intersects the primary LLV line at the lower temperature. This point is called the upper critical solution temperature, UCST. The second critical line runs between the light component critical point and the lower critical solution temperature, the LCST. The LCST is located at a temperature above the light component critical point.

Below the primary UCST near the light component critical point, the phase behaviour is similar to that of a type II binary system, with the secondary LLV line. Above the first LLV line the phase behaviour resembles that of a type I system with a vapour liquid equilibrium envelope that does not intersect the x=0 line.

McHugh reports that when the ratio of the carbon numbers of a binary ethane – hydrocarbon mixture exceeds 9.5 the systems will start to exhibit type III phase behaviour (McHugh & Krukonis, 1994). The system ethane –n-C_{19} will therefore have this type of phase behaviour. Peters et al reported that although the solid phase partially obscures the phase behaviour the systems ethane – n-C_{24} and ethane – n-C_{25} also belong to this group.

Type IV

This type of phase behaviour is an extension of the behaviour of type III. As the differences in the critical properties of the components increase the LLV line will extend over a larger temperature range. The UCEP will move to a higher temperature and the branch of the critical mixture curve that originates at the low volatility component critical point will tend towards higher temperatures, until it extends to temperatures above the highly volatile component critical point. It does not intersect the LLV line in the P-T diagram.
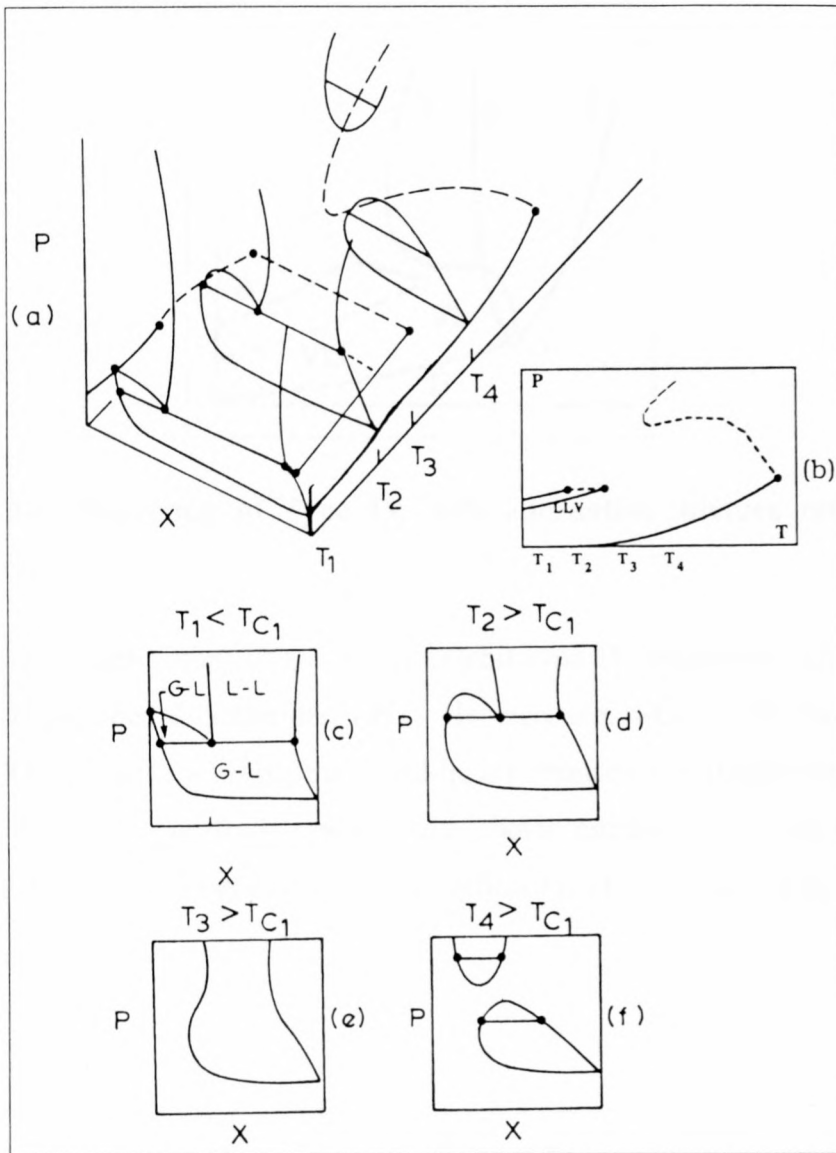
Figure 3-4 Type IV Phase Boundary behaviour. (a) P-T-x (b) P-T (c, d, e, f) P-x projections at different temperatures (McHugh & Krukonis, 1994).

In Figure 3-4 the critical curve has a temperature minimum. As the system pressure is increased the temperature decreases until it reaches a minimum value, after which it will increase with a further increase in the system pressure. This type of phase behaviour indicates that two vapour-liquid hyperbolic domes exist. It is important to note that the mixture critical curve does not have to have a temperature minimum, and may have slopes similar to curves 1,2 or 3 in Figure 3-5.

34
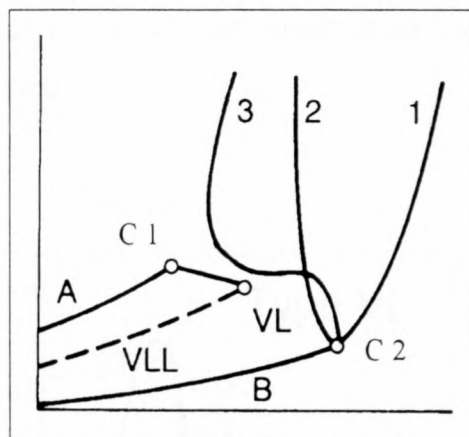
Figure 3-5 P-T Projection of Type IV with alternative mixture critical curves. (Brunner, 1994).

CO_2 – n-alkane systems from CO_2 – $n\text{-}C_{14}$ exhibit type IV behaviour (Charoensombut-Amon et al., 1986; Spee & Schneider, 1991). Heneicosane, $n\text{-}C_{21}$, is the longest n-alkane with which CO_2 will have a visible the liquid-liquid immiscibility (Charoensombut-Amon et al., 1986). For CO_2 – n-alkane systems with alkane numbers higher that 21 the LLV equilibria will be obscured because of the solidification of the alkane (Fall et al., 1985). See section 3.1.2.

Type V
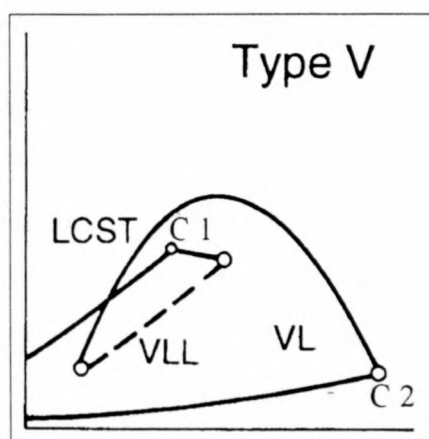
Figure 3-6 Type V P-T Projection (Brunner, 1994)

The fifth type of phase behaviour is very similar to type III. The mixture critical curve split into two sections, the one extending from the heavy component critical point to the LCST and the other from the light component critical point to the UCST. The only difference between the two types is that, in the case of type V behaviour, the crystallisation or

35

solidification temperature of the heavy component is so high that the secondary LLV equilibrium cannot be observed.

Type VI
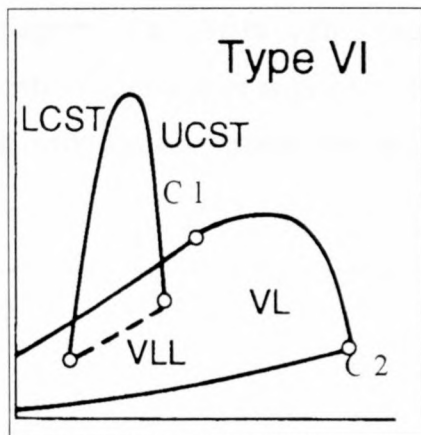
Figure 3-7 Type VI P-x Projection (Brunner, 1994)

At low temperatures, liquid-liquid immiscibility may be observed in systems that otherwise exhibit type I phase behaviour, these systems belong to the type VI. This type of phase boundary behaviour is usually only found with systems where both components have strong self-associating characteristics.

3.1.2 Solid-Supercritical Fluid Phase Diagrams

The six types of phase behaviour discussed in section 3.1.1 can be clearly seen in systems where the heavy component melting point is lower than the light component critical point. However, the all systems under investigation in this work, with the exception of the n-C_{12}-CO_2, n-C_{16}-CO_2 and n-C_{16}-ethane systems, involve heavy components with melting points above the solute critical temperature. In these cases, not all the phase behaviour phenomena can be detected, because the solidification of the n-alkanes at the lower system temperatures obscures the normal expected phase behaviour. As mentioned earlier, for CO_2 – n-alkane binary equilibrium systems, the CO_2 – n-C_{21} system is the highest carbon number system where a liquid-liquid equilibrium can be detected near the CO_2 critical point. The liquid-liquid immiscibility will be hidden by the formation of a solid n-alkane phase in systems with a higher carbon number n-alkane (Fall et al., 1985).

The existence of a solid phase complicates the phase equilibrium diagrams. Three types of such phase diagrams are discussed below.

Simple Phase Diagram

The simplest binary phase diagram of a system with a heavy component melting point above the liquid component critical temperature is given in Figure 3-8. This type of phase behaviour is normally found with systems where the two components are chemically similar.
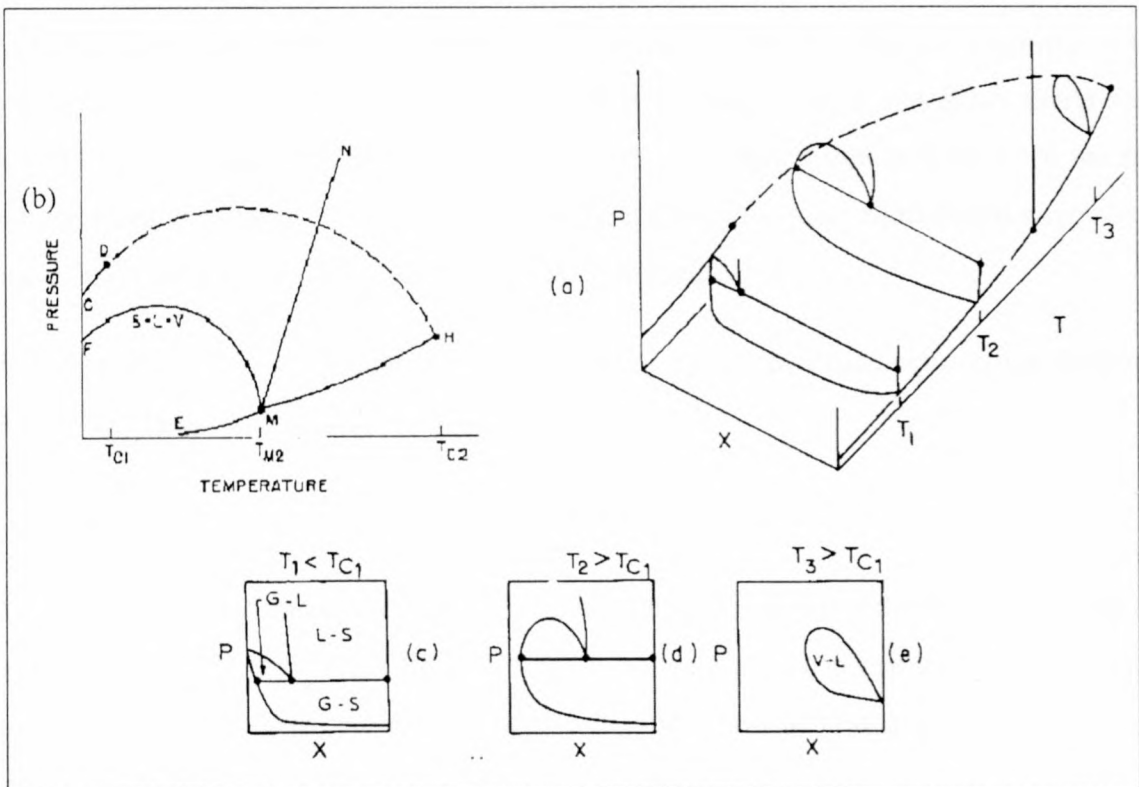
Figure 3-8 Simple Solid-Fluid Phase Diagram (a) P-T-x, (b) P-T, (c, d, e) P-x projections at various temperatures (McHugh & Krukonis, 1994).

In Figure 3-8 (b) the line EM represents the pure heavy component sublimation line, line MH, the heavy component vapour pressure curve, and line MN, the pure component melting curve. Line CD is the light component vapour pressure curve.

The solid-vapour-liquid, SVL, equilibrium line originates at the pure heavy component triple point. It then curves backwards towards lower temperatures as the pressure is increased. For this binary system the melting point of the pure component is decreased as a

result of the presence of the more volatile substance. As the pressure is increased, more of the volatile component dissolves in the liquid phase and hence the temperature needed to freeze the heavy component decreases drastically.

At temperatures below the light component critical point the P-x diagram, depicted in Figure 3-8 (c), indicates the existence of a vapour-solid equilibrium at low pressures. At higher pressures, either a liquid-solid or a liquid -vapour equilibrium can be observed, depending on the overall concentration of the mixture. The vapour –liquid equilibrium extends up to the x=0 concentration, where the mixture contains no heavy component.

At temperatures above the light component critical point, the P-x diagram is similar to the one discussed above, with vapour-solid equilibria at low pressures and either liquid-solid or liquid-vapour equilibria at higher temperatures. The only differences between the two temperatures are that at the higher temperature the liquid-vapour equilibrium envelope is much larger, and it does not extend up to x=0. See Figure 3-8 (d).

At temperatures above the pure component melting point, the phase equilibrium diagrams will be similar to those discussed in section 3.1.1.

Complicated Phase Diagrams

A more complicated phase diagram is formed when there is a big difference between the two components in the system. The SLV line is not continuous, but splits into two sections one at low temperatures, around the light component critical temperature, and the other near the pure heavy component triple point temperature.

At temperatures below the light component critical temperature, a vapour-solid equilibrium exists at low pressures, and depending on the total mixture composition either liquid-solid or liquid-vapour equilibria at higher pressures. See Figure 3-9. At temperatures above the volatile component critical point, the vapour-liquid envelope moves away from the x=0 line and decreases in size with increasing temperature, until it completely disappears at the lower critical end point, LCEP. The one section of the mixture critical curve runs from the light component critical temperature, through the pressure maximums in the vapour-liquid equilibrium curves and ends in the LCEP.

The second SLV equilibrium curve originates at the pure heavy component melting point, at x=1. In the presence of the lighter component, the melting point of the solid decreases with the increase in system pressure and the SLV curve on the P-T diagram will have a negative slope. The curve terminates in the upper critical end point, UCEP, where it intercepts the mixture critical curve from the heavy component critical point.
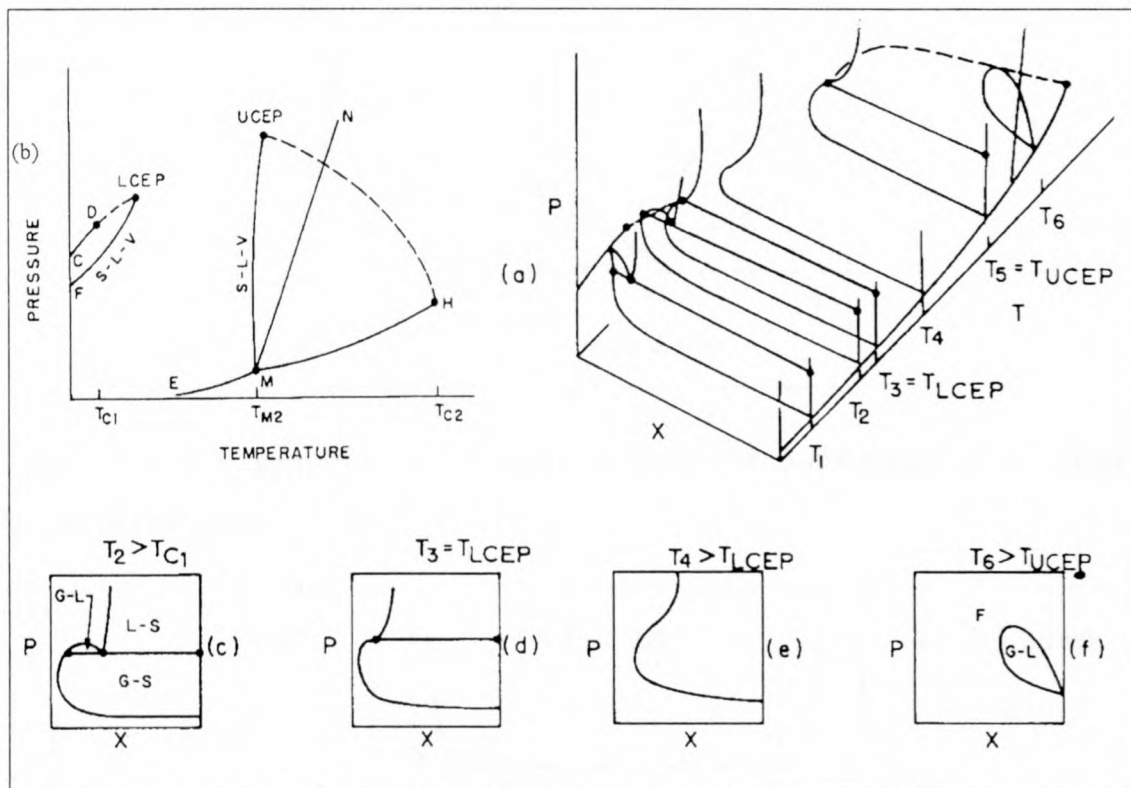
Figure 3-9 Complicated Solid-Fluid Phase Diagram (a) P-T-x, (b) P-T, (c, d, e) P-x projections at various temperatures (McHugh & Krukonis, 1994).

The P-x diagram of the phase behaviour is shown in Figure 3-9 (c)-(f). At temperatures above the UCEP phase boundaries exist similar to those in Figure 3-9 (c) at temperatures below the LCEP. The vapour liquid envelope will decrease in size with a decrease in temperature until it disappears at the UCEP. Between the LCEP and UCEP temperatures, only vapour-solid equilibria exist. At temperatures above the pure component melting point vapour-liquid phase behaviour similar to types I to VI exist.

The SLV curve that originates at the pure heavy component melting point does not always have a negative slope. In some systems, the curve goes through a temperature minimum after which the heavy component melting point will start to increase again. This results in a more complicated P-T-x diagram, since the SVL equilibrium will be intersected twice at

certain temperatures. The following P-x diagrams depict the binary phase behaviour in this region.
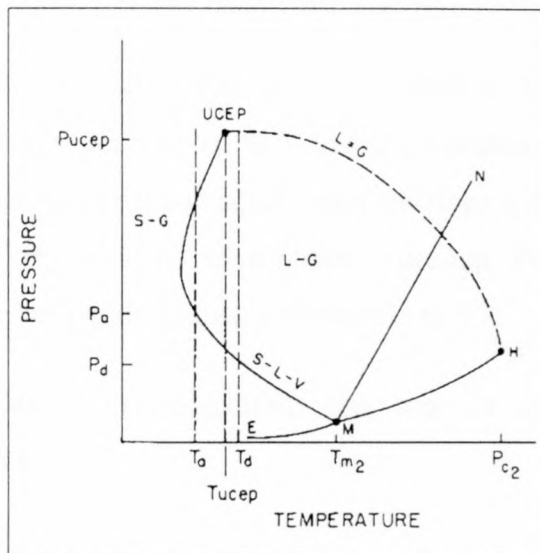
Figure 3-10 P-T projection of a more complicated Solid-Fluid phase diagram (McHugh & Krukonis, 1994).
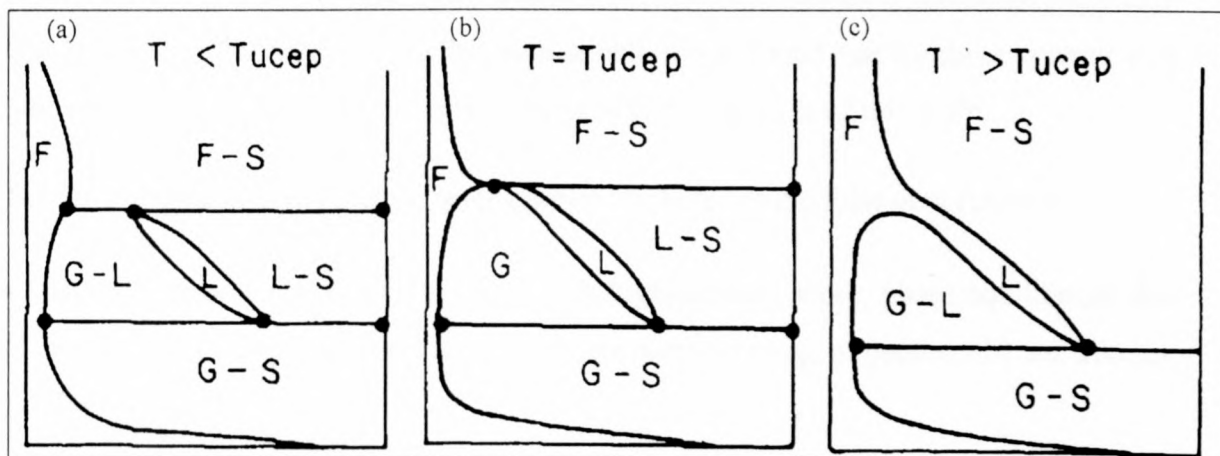
Figure 3-11 P-x projection at various temperatures of binary phase behaviour in Figure 3-10 (McHugh & Krukonis, 1994).

At a temperature smaller than the UCEP (Figure 3-11 (a)), a solid-vapour equilibrium exists at low pressures. With an increase in pressure, the isotherm will intersect the SLV equilibrium line. At this stage either a vapour-liquid, liquid or liquid-solid equilibria can exist, depending on the overall mixture composition. By increasing the pressure further the SLV line will be intersected again, in this region there will be no liquid phase present and only a fluid-solid equilibrium will exist.

At the UCEP temperature and pressure (Figure 3-11 (b)) a vapour-liquid equilibrium exists in the presence of a solid phase. The solid-liquid equilibrium curve intersects the gas-liquid envelope precisely at the binary liquid-vapour critical point.

At temperatures above the UCEP (Figure 3-11 (c)) there is no region of vapour-solid equilibrium at high pressures, because the SLV line is not intersected a second time. With increasing temperature the vapour-liquid equilibrium envelope will increase in size, until at the pure component melting point no solid phase is present. From this point the phase behaviour will be similar behaviour discussed for types I to VI.

The octacosane-CO_2 binary mixture exhibits this type of solid-liquid-vapour phase behaviour (McHugh, 1984).

3.2 PUBLISHED PHASE EQUILIBRIUM DATA FOR ALKANE SYSTEMS

The aim of this study was to investigate the binary liquid-vapour phase equilibria of supercritical solvents CO_2 and ethane with some paraffinic alkanes in the range n-C_{12} to n-C_{36}. However, after an extensive literature search, it was found that for these systems very little published data exist in the temperature and pressure range of this work.

The lack of data in the operating range may be attributed to the following reasons:

- Due to the practical difficulties involving high-pressure work, phase equilibrium data were mostly generated in the more moderate pressure range of between 10 and 100 bar. See Table 3-1.

System	Phases Studied	Temperature Range [K]	Pressure Range [Bar]	Source
$CO_2 - $ n-C_{16}	V+L V	293 – 553 323 – 573	Up to 55 Up to 50	(Breman et al., 1994) (Huang et al., 1988 a)
$CO_2 - $ n-C_{20}	L L	323 – 423 373 – 573	Up to 96 10 – 50	(Gasem & Robinson, 1985) (Tsai et al., 1988)
$CO_2 - $ n-C_{28}	L V+L V+L V+L	323 – 423 293 – 553 373 – 573 373 – 573	Up to 96 Up to 55 10 – 50 10 – 50	(Gasem & Robinson, 1985) (Breman et al., 1994) (Huang et al., 1988 b) (Tsai et al., 1988)
$CO_2 - $ n-C_{36}	L V+L	323 – 423 373 – 573	Up to 96 10 – 50	(Gasem & Robinson, 1985) (Tsai et al., 1988)
Ethane – n-C_{16}	V V+L V	323 – 448 293 – 553 323 – 573	9 – 80 Up to 55 Up to 50	(Kaul & Prausnitz, 1978) (Breman et al., 1994) (Huang et al., 1988 a)
Ethane – n-C_{20}	V V+L	438 – 543 373 – 573	9 – 80 10 – 40	(Kaul & Prausnitz, 1978) (Tsai et al., 1988)
Ethane – n-C_{28}	V+L V+L V+L	293 – 553 373 – 573 373 – 573	Up to 55 10 – 50 10 – 50	(Breman et al., 1994) (Huang et al., 1988 b) (Tsai et al., 1988)
Ethane – n-C_{36}	V+L	373 – 573	10 – 50	(Tsai et al., 1988)

Table 3-1 Published data for CO_2 and ethane – n-alkane systems at moderate pressures

- Many researchers investigated only the vapour phase composition with the aim of studying the systems for the use in supercritical extraction. It was often also the solid-vapour equilibria that were studied and not the liquid-vapour systems. Schmitt and Reid measured only the solubilities of the alkanes n-C_{18} through to n-C_{24} in supercritical carbon dioxide, while the solubility of the solvent in the heavy alkane remains unknown (Schmitt & Reid, 1988). Yao and Tsai investigated the solubilities of solid n-C_{24}, n-C_{28}, and n-C_{36} in CO_2 (Yao & Tsai, 1993).

- Another motivation for the study of the paraffin – supercritical solvent equilibria was the investigation of the phase behaviour and the appearance of the system P-T-x diagram. These operating regions do not fall in the scope of this study. Peters et al. studied the three phase equilibria of the ethane n-C_{20} system (Peters et al., 1991). Peters, Van der Kooi and De Swaan Arons investigated the phase behaviour of the ethane – nC_{24} system (Peters et al., 1987). McHugh et al. studied the high-pressure fluid phase behaviour of the CO_2 n-C_{24} system, and determined the LCEP of this system (McHugh, 1984). Huie, Luks and Kohn studied the CO_2 n-C_{20} system for vapour-liquid, solid-liquid-vapour and liquid-liquid-vapour systems (Huie et al., 1973).

Charoensombut-Amon et al. measured CO_2 n-C_{12} data in the temperature and pressure range of this work (Charoensombut-Amon et al., 1986). However, it is suspected that there may be some type of typographical error in some of the data tables, published in the referenced article, since even on first inspection some of the data appears to exhibit unrealistic trends. The data published by D'Souza, Patrick and Teja fall in the same range as the data points determined experimentally in this work (D'Souza et al., 1988). These data were used to test the validity of the experimental technique.

3.3   THERMODYNAMIC CONSISTENCY

In the cases where very few or no published data exist, the quality of the data must be determined by doing thermodynamic tests on them. Various techniques exist to check for the thermodynamic consistency of experimental data at low pressures. The most common techniques involve the use of the Gibbs-Duhem equation (Nieuwoudt, 1994).

$$x_1 d\left(\ln f_1\right) + x_2 d\left(\ln f_2\right) = \frac{v^l}{RT} dP \tag{3.2.1}$$

By simplifying and integrating this equation, the following equality can be determined:

$$\int_{x_{2,i}}^{x_{2,e}} \ln\left(\frac{\phi_2}{\phi_1}\right) dx_2 + \int_{x_{2,i}}^{x_{2,e}} \ln\left(\frac{K_2}{K_1}\right) dx_2 + \int_{P_i}^{P_e} \frac{v^l}{RT} dP = \left[\ln K_1 + \ln(\phi_1 P) + x_2\left(\ln\frac{\phi_2}{\phi_1} + \ln\frac{K_2}{K_1}\right)\right]_{x_{2,e},P_e}$$
$$-\left[\ln K_1 + \ln(\phi_1 P) + x_2\left(\ln\frac{\phi_2}{\phi_1} + \ln\frac{K_2}{K_1}\right)\right]_{x_{2,i},P_i} \tag{3.2.2}$$

43

The subscript 2 refers to the more volatile component, and the i and e refer to the upper and lower limits of the measurements.

The fugacities determined from the experimental data is compared to values calculated through the use of the Gibbs-Duhem equation. The differences between these values, the residuals, give an indication of the disparity in the data. An absolute average deviation of less than 0.03 indicates that the data have a high degree of consistency.

However, with high pressure work the determination of the fugacities is complicated, and must be calculated from the constant composition volumetric data:

$$RTd(\ln f_i) = \bar{v}_i dP \qquad (3.2.3)$$

It is an immense task to generate the volumetric data necessary to calculate the fugacities. In order to overcome this problem, researchers employed equations of state in their fugacity calculations. Bertucco employed the Soave-Redlich-Kwong equation of state with the Huron Vidal mixing rules in a thermodynamic test of vapour-liquid equilibrium data at high pressures (Bertucco et al., 1997). However, it is important that the equation of state fits the data accurately, else it will introduce a degree of inconsistency in the test. It is impossible to determine whether inconsistency determined by the test is introduced by the equation of state or the experimental data.

Due to the lack of a suitable test, it was not possible to check the experimental data in this work for thermodynamic consistency.

3.4   EXPERIMENTAL PHASE EQUILIBRIA MEASUREMENTS

3.4.1   *Operating Range*

The objective of the phase equilibria measurements was to determine the vapour-liquid equilibrium of supercritical solvents CO_2 and ethane with paraffinic alkanes, n-C_{12} to n-C_{36}.

The maximum pressure up to which the phase behaviour of the various systems could be studied was determined by the maximum operating pressure of the phase equilibrium cell. As discussed in section 2.2.2 the view cell has a maximum operating pressure of 280 bar.

Due to the low alkane solubilities in the supercritical CO_2 a different high pressure cell with a higher maximum operating pressure of 310 bar was used to study the $CO_2 - n\text{-}C_{20}$ to $CO_2 - n\text{-}C_{36}$ systems. A full description of the high pressure phase equilibrium cell is given in Appendix B. Throughout this work the variable volume cell discussed in section 2 will be referred to as the view cell and the second cell used to obtain the high pressures, as the high-pressure cell.

All the phase equilibria were measured at temperatures above the heavy component melting point, with the exception of the lowest temperature in the $CO_2\text{-}n\text{-}C_{36}$ system. The complicated solid-liquid-vapour equilibrium systems were therefore avoided. As the primary application for the data is to fit equations of state to for the application in a liquid-supercritical extraction column, information on the phase behaviour in the presence of a solid phase is not necessary.

The temperature control of the view cell is achieved by placing it in a thermostatted water bath (section 2.2.2). The maximum bath temperature therefore determined the maximum temperature at which the equilibria could be studied at with the view cell. Phase equilibria were determined up to 353 K with the view cell and 368 K with the high-pressure cell.

3.4.2 *Experimental Set-up and Operating Procedure*

The experimental set-up and operating procedure of the view cell is discussed in detail in sections 2.2.2 and 2.3, and the experimental set-up of the high pressure cell in Appendix B. The operating procedure for the high-pressure cell is the same as that of the view cell.

3.4.3 *Materials*

The alkanes used in the experiments are listed in **Table 3-2**. These chemicals were used without any further purification

COMPONENT	SOURCE	PURITY	T_{MELT} [K]
Dodecane n-C_{12}	Aldrich	> 99 %	264
Hexadecane n-C_{16}	Aldrich	99 %	291[*]
Eicosane n-C_{20}	Sigma	99 %	310
Tetracosane n-C_{24}	Sigma Fluka	≈ 99 % > 99 %	322-324[*]
Octacosane n-C_{28}	Fluka	≥ 98 %	330-335[*]
Hexatriacontane n-C_{36}	Fluka Humphry Chemical Company	98 % 99 %	349

[*]supplier specifications

Table 3-2 n-Alkanes used in the experiments

Liquid carbon dioxide was supplied by Afrox, and had a purity of 99.95 %. The ethane was supplied in the gaseous form, and liquid ethane was withdrawn from the cylinder by turning it upside-down. The ethane was supplied by Messr-Griesheim and had a purity of 99.5%. Normal low-grade nitrogen was used in the pressure control. The N_2 was supplied by Afrox.

3.4.4 *Experimental Results*

Comparison with Published Data

In order to verify the experimental method, the measured data must be compared with published results. The following graph contains experimental data measured for the CO_2 – n-C_{16} system at 313 K and published data by D'Souza et al. (D'Souza et al., 1988) for the same system but at 314 K. The 1 K difference in the datasets was considered small enough to enable meaningful direct comparison of the data.
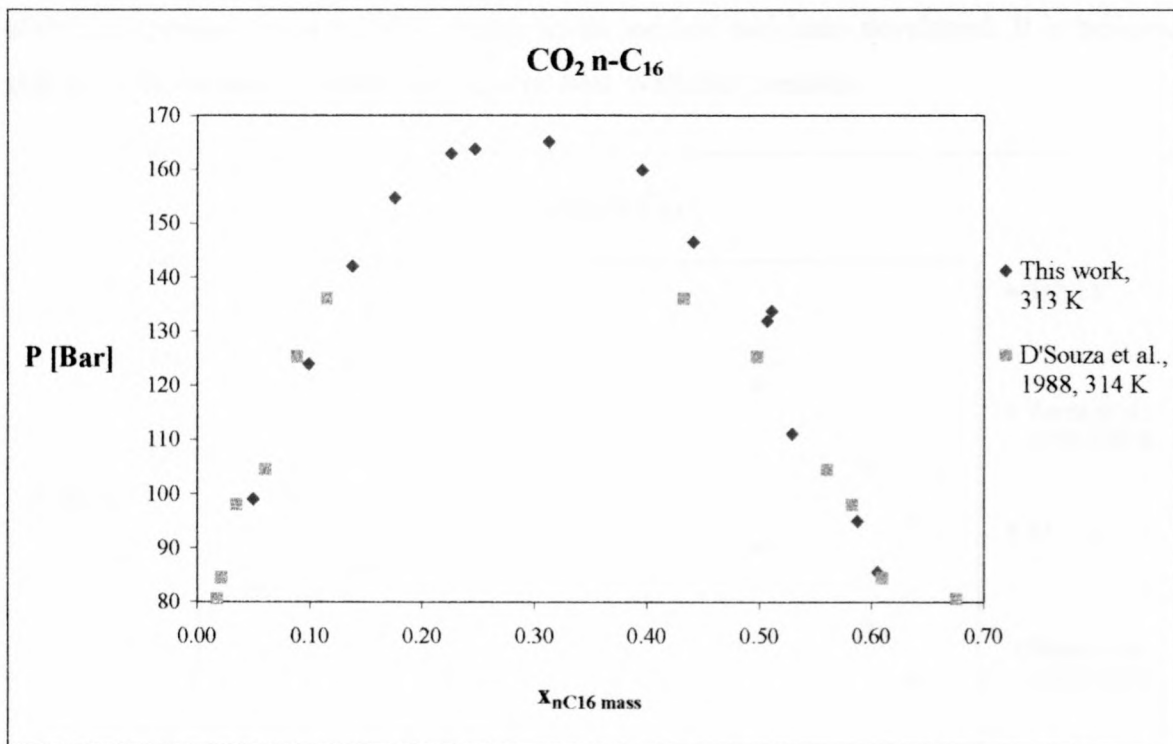
CO_2 n-C_{16}

Graph 3-1 Comparison of the published (D'Souza et al., 1988) and experimentally determined data for the system CO_2 – n-C_{16} at 313 K and 314 K respectively.

In regions away from the mixture critical point the experimental and published data in Graph 3-1 compare favourably, however the published liquid phase data have slightly lower heavy component fractions. D'Souza et al. (D'Souza et al., 1988) used a sampling technique to determine the phase compositions. As discussed in section 2.1.1, there are several problems with using a direct sampling method to determine the phase composition. There may have been some inaccuracy in the determination of the phase equilibrium composition of the data reported by D'Souza.

The experimental data of the ethane – n-C_{24} system ware also measured with the view cell. If it is taken into consideration that the published data are reported for temperatures 2 degrees lower than the measured data, it appears as if the experimental and measured pressures compare favourably.

As discussed in section 3.2 very few reliable phase equilibrium datasets have been published in the operating range of this work. Due to the lack of data it is impossible to test the validity of the other datasets. However, from the comparison with the limited data sets,

47

above, it appears that a suitable experimental method had been developed. It is believed that the date measured in this work are the best available presently.
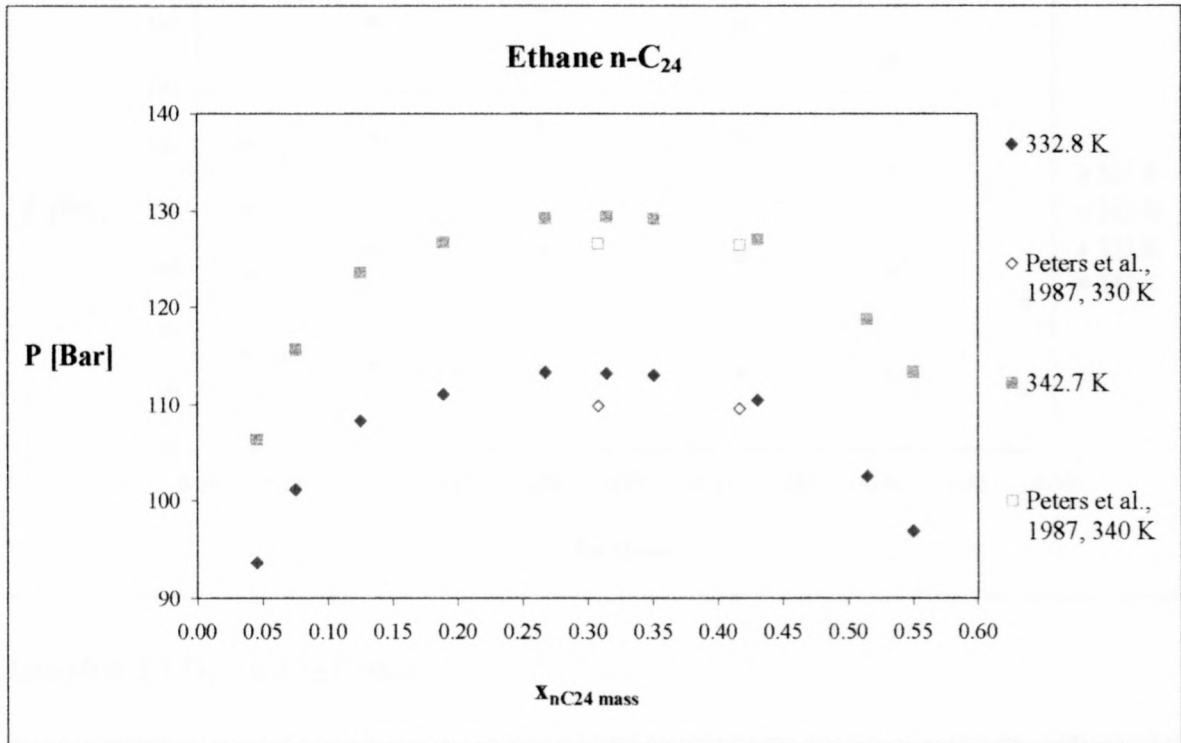
Graph 3-2 Comparison of the published (Peters et al., 1987) and experimentally determined data for the system ethane – n-C$_{24}$.

CO$_2$ – n-Alkane Phase Diagrams

The following graphs contain the CO$_2$ – n-alkane liquid vapour phase boundary plots.
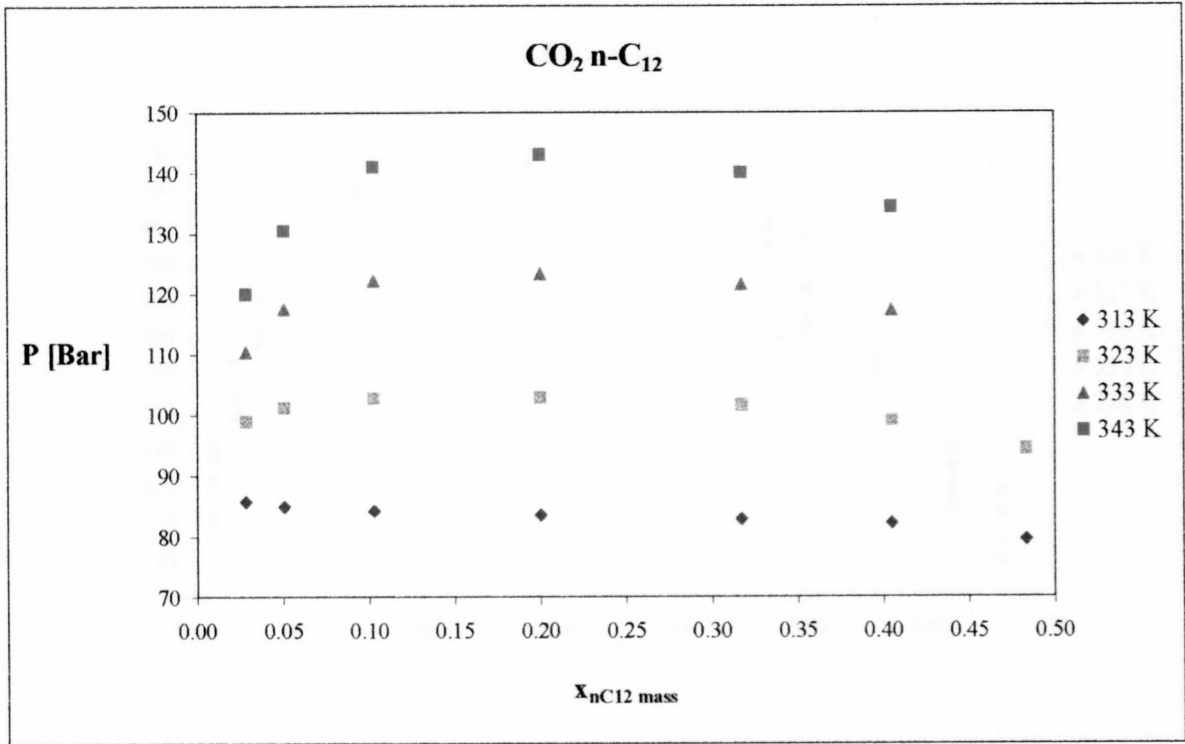
Graph 3-3 CO_2 – n-C_{12} System
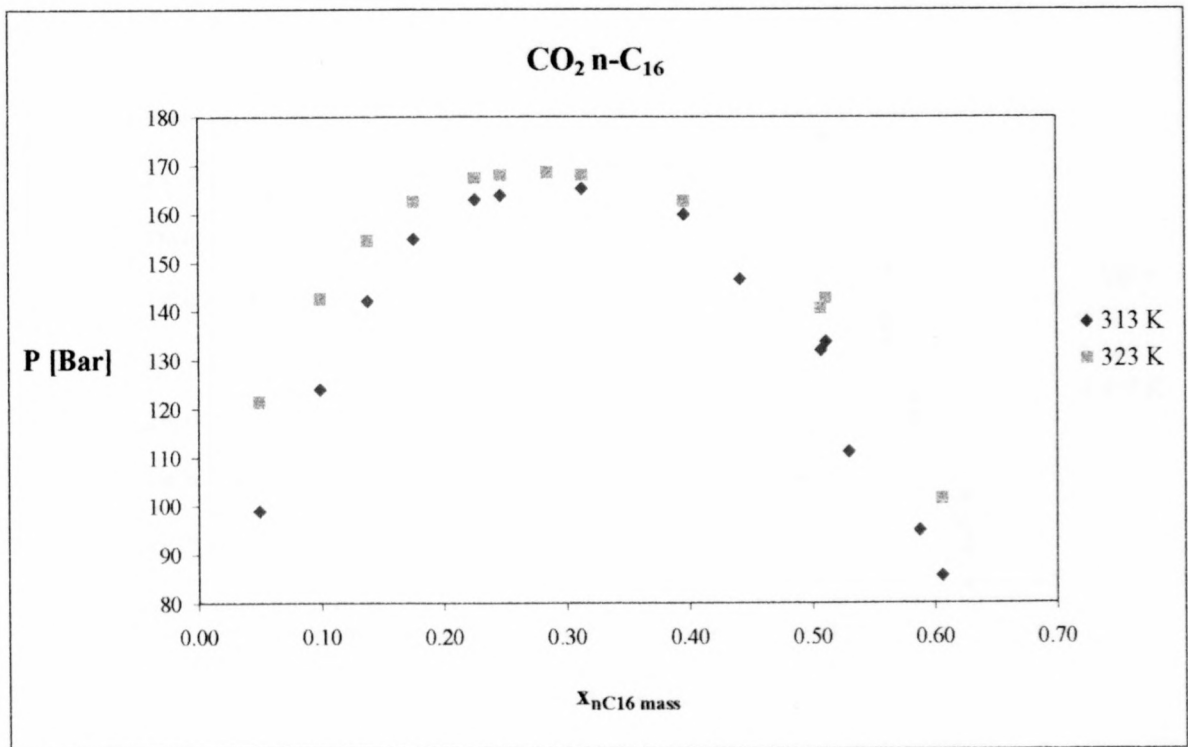
Graph 3-4 CO_2 – n-C_{16} System

49
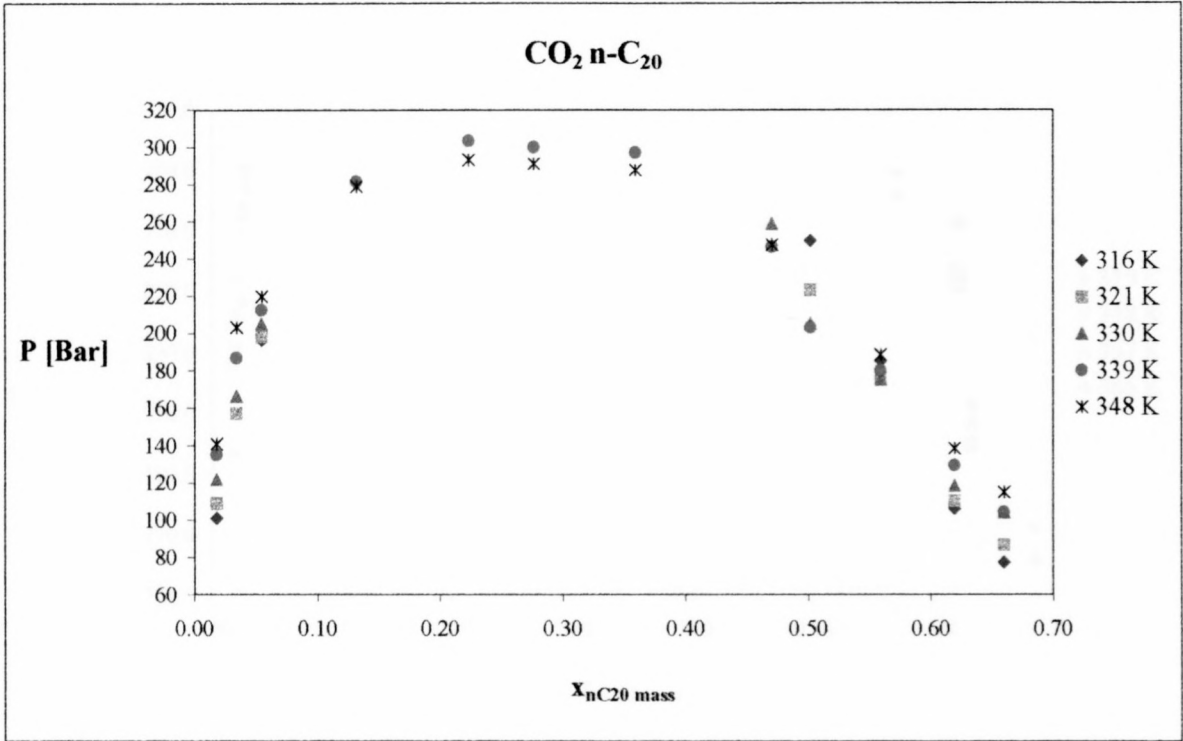
Graph 3-5 CO$_2$ – n-C$_{20}$ System
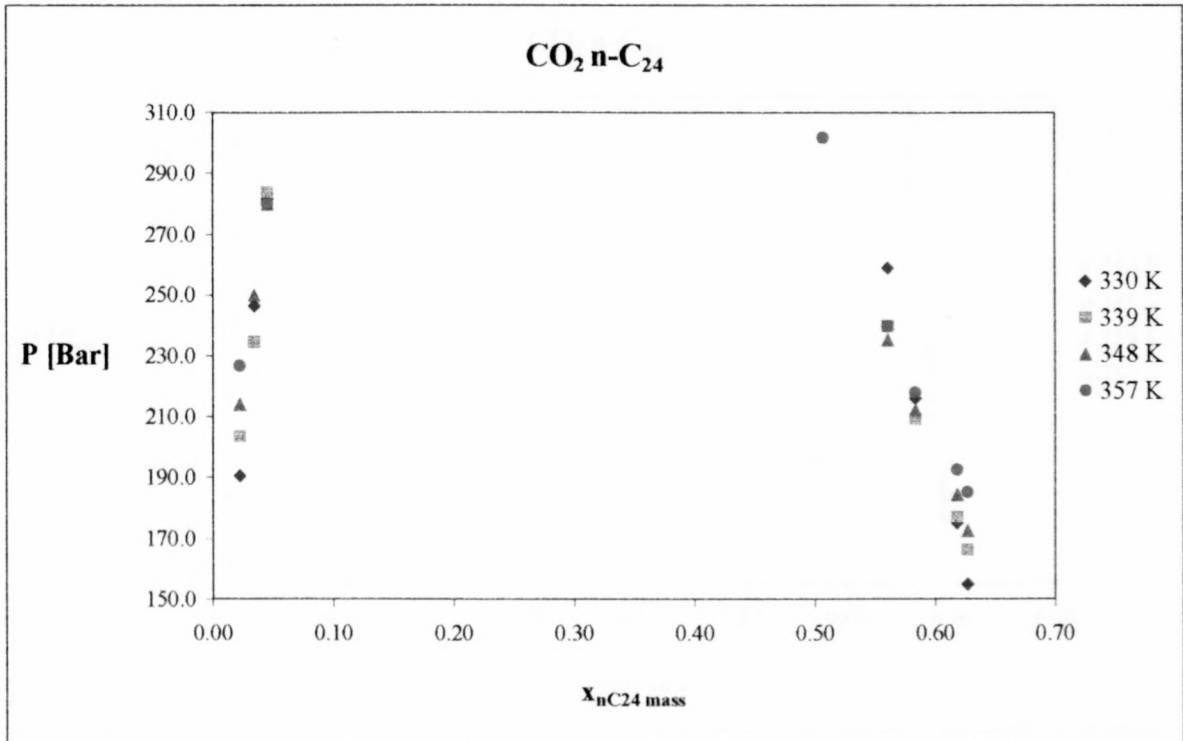
Graph 3-6 CO$_2$ – n-C$_{24}$ System

50
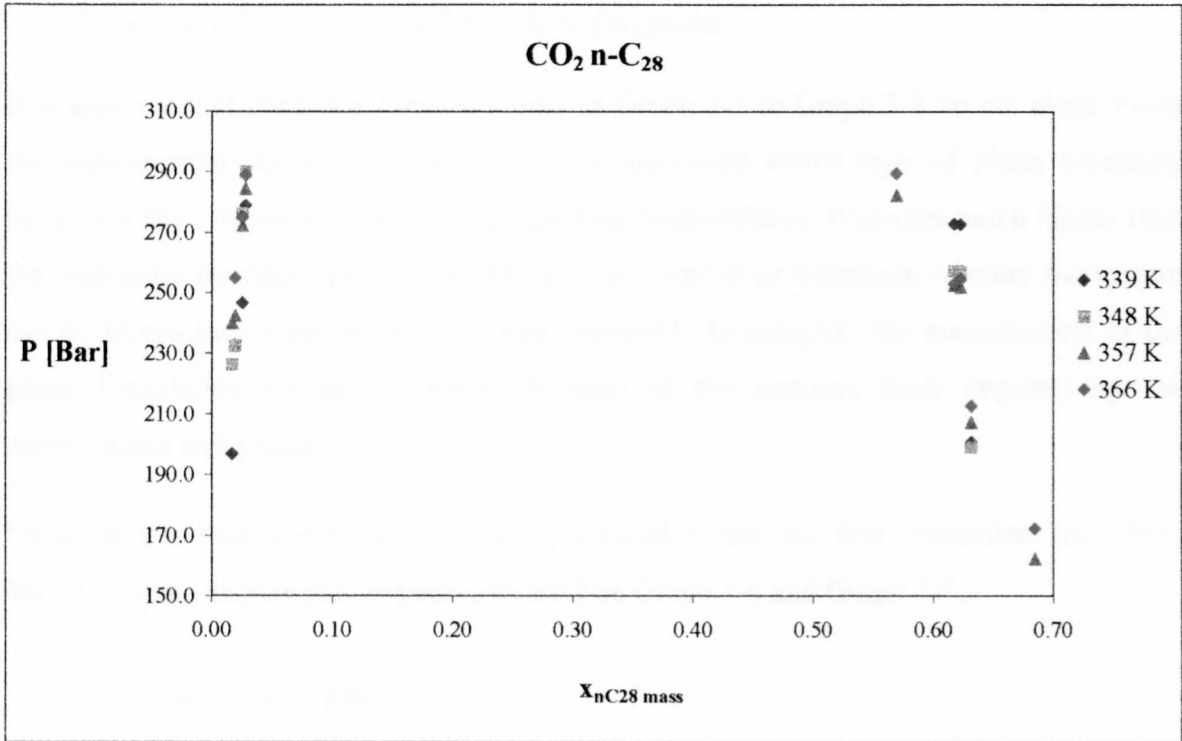
Graph 3-7 CO_2 – n-C_{28} System

Graph 3-8 CO_2 – n-C_{36} System

51

Stellenbosch University http://scholar.sun.ac.za
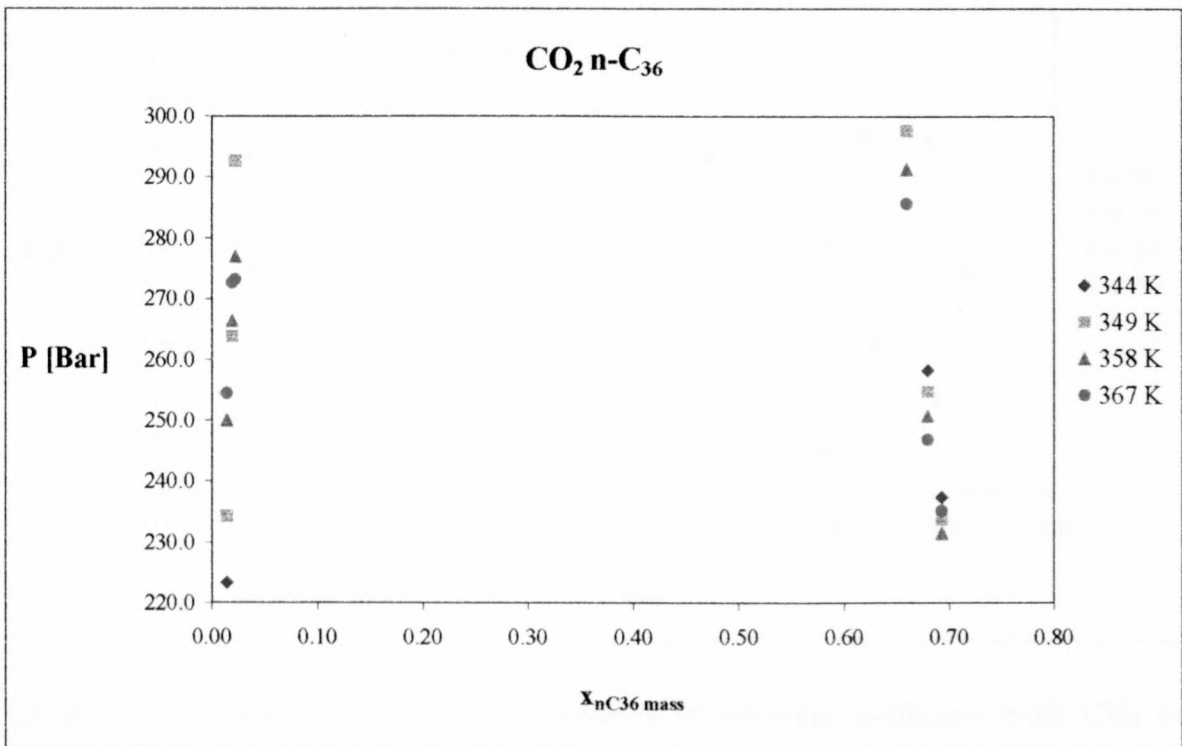
Discussion of the CO₂ – n-Alkane Phase Diagrams

It is apparent that the phase boundary lines in Graph 3-5 to Graph 3-8 do not close. From the experimental results, it is impossible to determine which type of phase boundary behaviour the systems exhibit at these operating temperatures. Pressures much higher than the maximum operating pressure of 310 bar, are needed to determine whether the system can be forced into a single phase. It was impossible to complete the measurement of the phase boundaries for these datasets because of the pressure limit imposed by the experimental equipment.

Some of the data points have been reproduced where on first inspection the phase boundary lines displayed unexpected trends See Graph 3-4 and Graph 3-7.

- *Carbon-Number Effect*
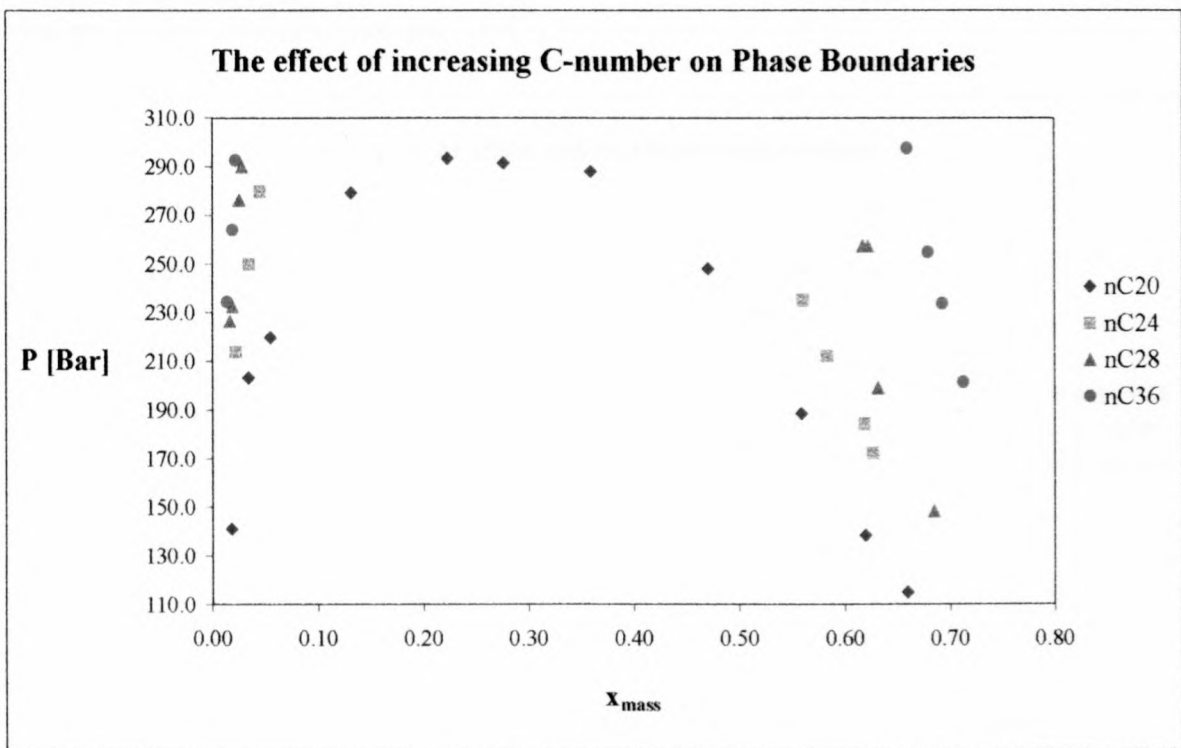
Graph 3-9 Comparison of phase boundaries of different n-alkanes with CO₂ as solvent at 348 K

When studying Graph 3-3 through to Graph 3-8, the first observation that can be made is the dramatic decrease in the solubility of the n-alkane in the supercritical carbon dioxide

52

solvent as the carbon number increases. This is apparent when studying Graph 3-9 which shows the effect of the increasing carbon-number more clearly.

- *The Effect of Temperature*

When the P-T relationship of the isopleths, the constant composition lines, for the system $CO_2 - n-C_{12}$ is plotted, it appears that the there is a linear relationship between the pressure and temperature. See Graph 3-10. This characteristic can be used to interpolate between the data points to determine the phase behaviour at conditions that have not been studied experimentally. It is also possible to extrapolate the curves to determine phase boundaries outside the scope of the experimental range, however, this must be done with care. Nieuwoudt (Nieuwoudt, 1994) reported a similar linear relationship for the system n-Butane – n-Tetrapentacontane. Peters (Peters et al., 1987, and Peters et al., 1988) fitted a low degree polynomial through the isopleths to interpolate his experimental data for the systems ethane – $n-C_{24}$ and ethane – $n-C_{22}$.
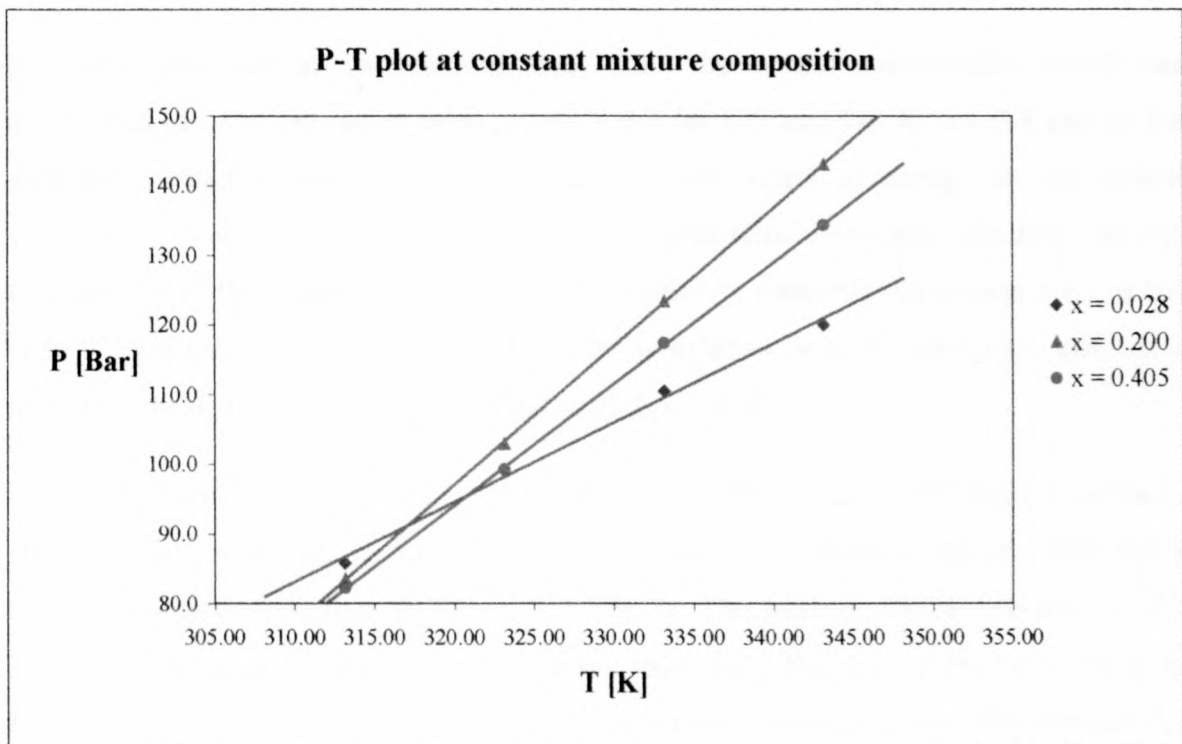
Graph 3-10 P-T plot of the CO_2- nC_{12} system, where x represents $x_{nC12\ mass}$

Care should however be taken in applying this characteristic blindly. It was found that the isopleth P-T plots of the binary mixtures of carbon dioxide and higher carbon-number alkanes do not in all cases have a linear characteristic. See Graph 3-11.

53

P-T plot at constant mixture composition
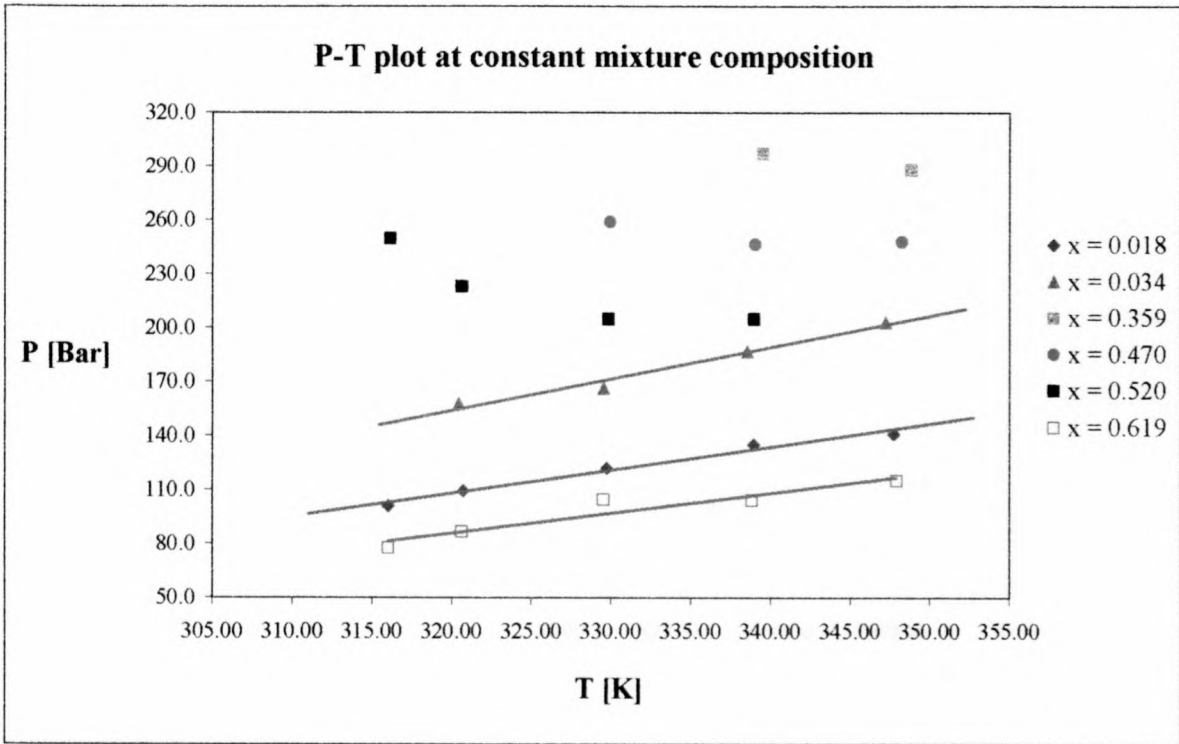
Graph 3-11 P-T plot of the CO_2- nC_{20} system, where x represents $x_{nC20\ mass}$

It can be seen that at compositions away from the critical composition, which was determined to be in the region of $x_{mass\ n-C20}$ = 0.3 for 339 and 348 K, the P-T plot of the data still exhibit a linear relationship but that this starts to change as the critical composition is approached. The behaviour of the near-critical concentration isopleths can be attributed to the shape of the mixture critical line. As mentioned in section 3.1.1, it has been reported that that the system CO_2 – $n-C_{16}$ exhibits type IV behaviour, and has a mixture critical curve with a shape similar to Figure 3-4 (b).

A possible explanation for the behaviour of the P-T plots is thus: The phase boundaries studied in this work fall in a temperature range where the mixture critical curve has a slightly negative slope (e.g. in Figure 3-5 line 3). The mixture critical pressure, or the maximum pressure of the phase boundaries, therefore decreases with an increase in temperature, hence there will be a decrease in all the pressures in the proximity of the mixture critical point. The fact that the pressures of the isopleths further away from the critical composition still increase indicates a flattening of the phase envelope.

54

P-T plot at constant mixture composition

P [Bar]

T [K]

- ◆ x = 0.020
- ▩ x = 0.028
- ▲ x = 0.617
- ● x = 0.685
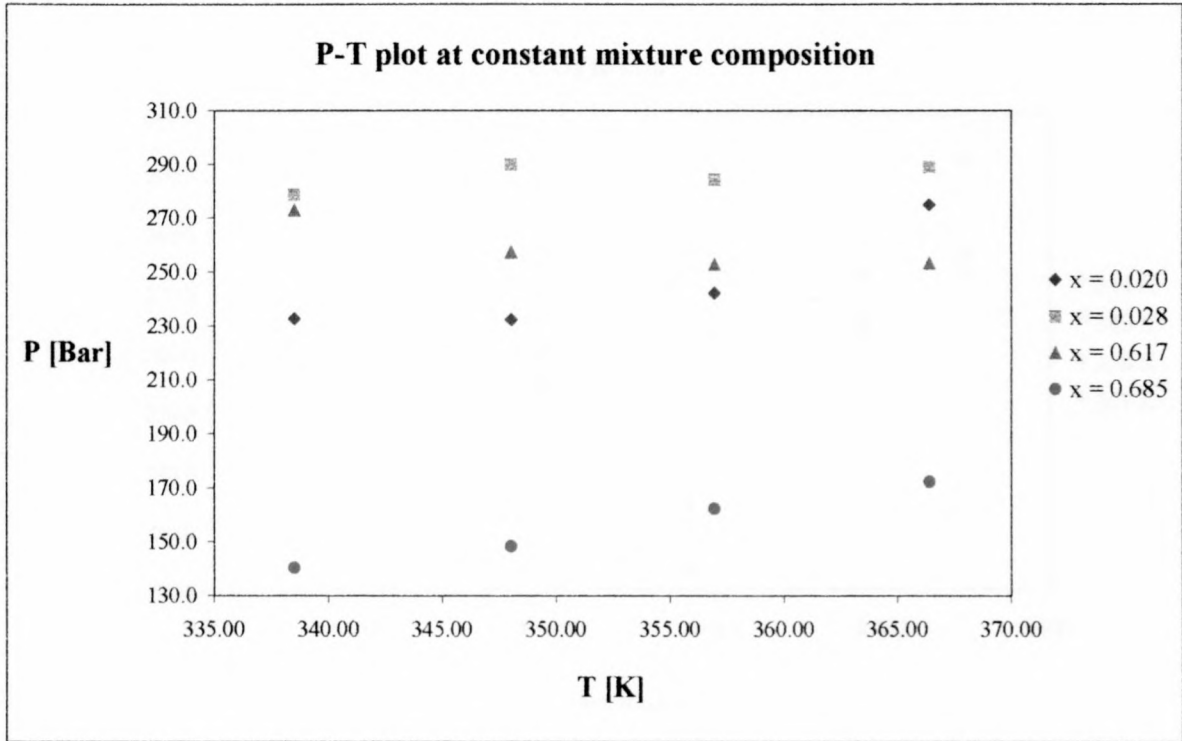
Graph 3-12 P-T plot of the CO_2- nC_{28} system, where x represents $x_{nC28\ mass}$

The decrease in maximum pressure with an increase in temperature was observed in all the carbon dioxide – n-alkane systems where the alkane carbon-number was larger than sixteen. See Graph 3-12 x = 0.617.

- *$CO_2 – n-C_{36}$ System*

An interesting phenomenon was observed at very low heavy component concentrations in the CO_2 – n-C_{36} system. A decrease in the phase boundary pressure up to a heavy component mass fraction of 0.014 was noted. At concentrations higher than this value, an increasingly higher pressure was needed to force the components into a single phase. See Graph 3-13. (The data points at the low heavy component concentration were omitted from Graph 3-8 to promote the clarity of the graph.) It is not known whether the other systems also exhibit this type of behaviour at very low heavy component concentrations, as no measurements were made at such low compositions.

55
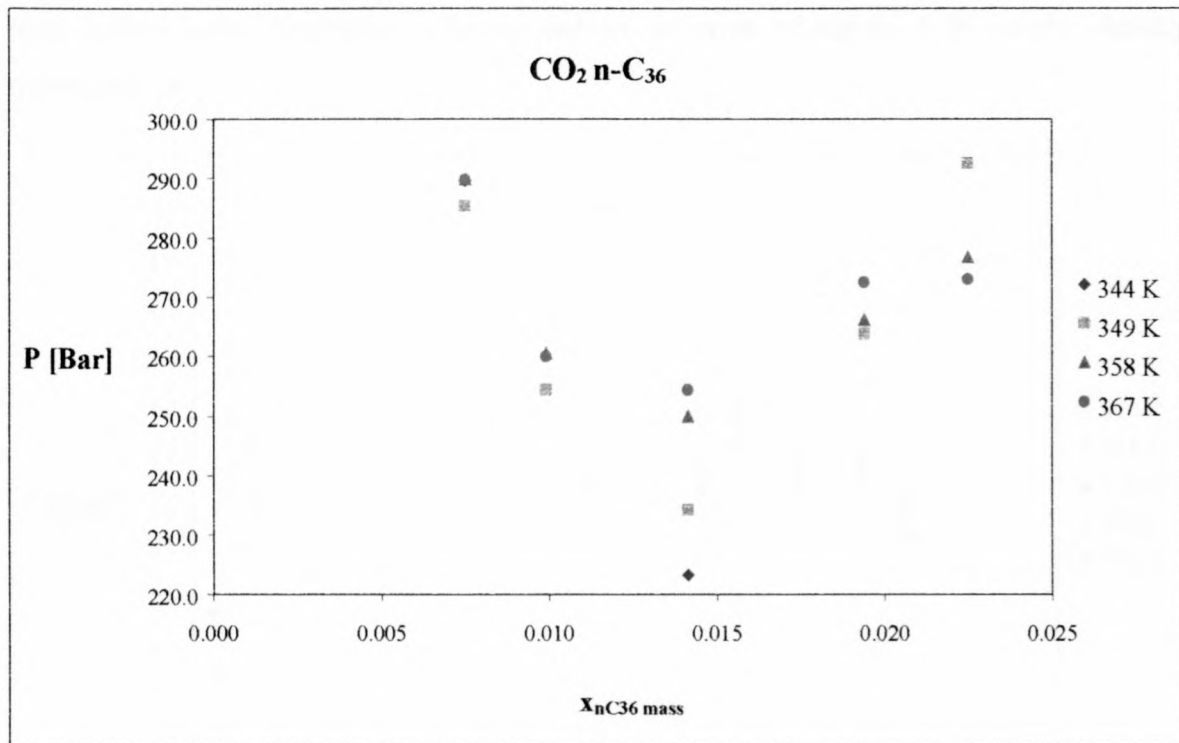
Graph 3-13 Vapour composition of the CO_2 – n-C_{36} System

This type of phase boundary behaviour suggests the existence of vapour-vapour immiscibility at very low n-C_{36} concentrations in the CO_2 – n-C_{36} system in addition to the liquid-vapour phase equilibrium that was measured at the higher alkane concentrations. This is typical type IV behaviour, with a closed vapour-vapour immiscibility envelope at low heavy component concentrations and an open liquid-vapour equilibrium region at higher concentrations. See Figure 3-4 (d).

CO_2 – n-Alkane Mixture Densities

Only the CO_2 – n-C_{20} to CO_2 – n-C_{36} densities at the phase boundaries were investigated. These systems were all studied in the high-pressure cell. The densities for the CO_2 – n-C_{12} and CO_2 – n-C_{16} systems were not measured. The accuracy of the calculated densities is dependant on the accuracy of the mass loaded into the cell, the total cell volume determination and the measurement of the piston displacement. The cell content was weighed to an accuracy of 0.01g and the measurement of the piston displacement is accurate to 0.02 mm. The high-pressure cell volume was determined by measuring the amount of water needed to fill the cell. It is the least accurate of the factors contributing to the determination of the cell, with an accuracy of 0.5 cm³. A 1.3 % error (0.5 cm³) in the

56

total cell volume determination, can lead to an error of up to 4 % in the density determination.
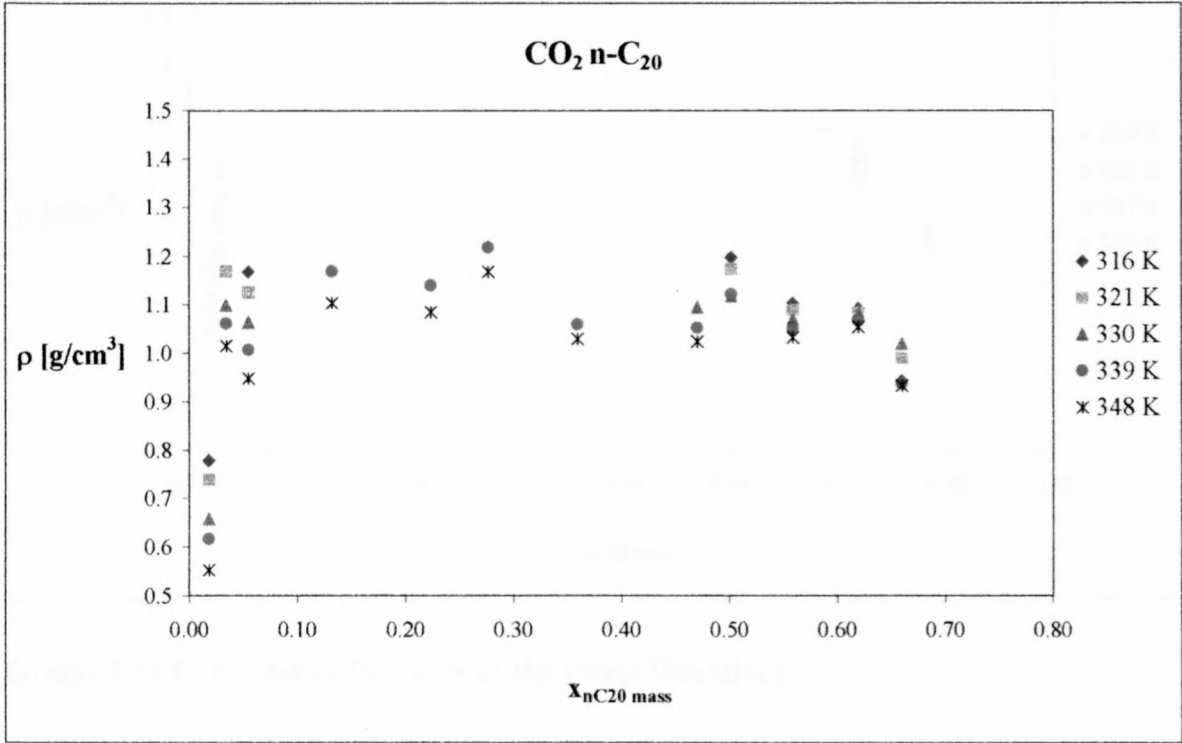
Graph 3-14 CO$_2$ – n-C$_{20}$ Densities at the Phase Boundary
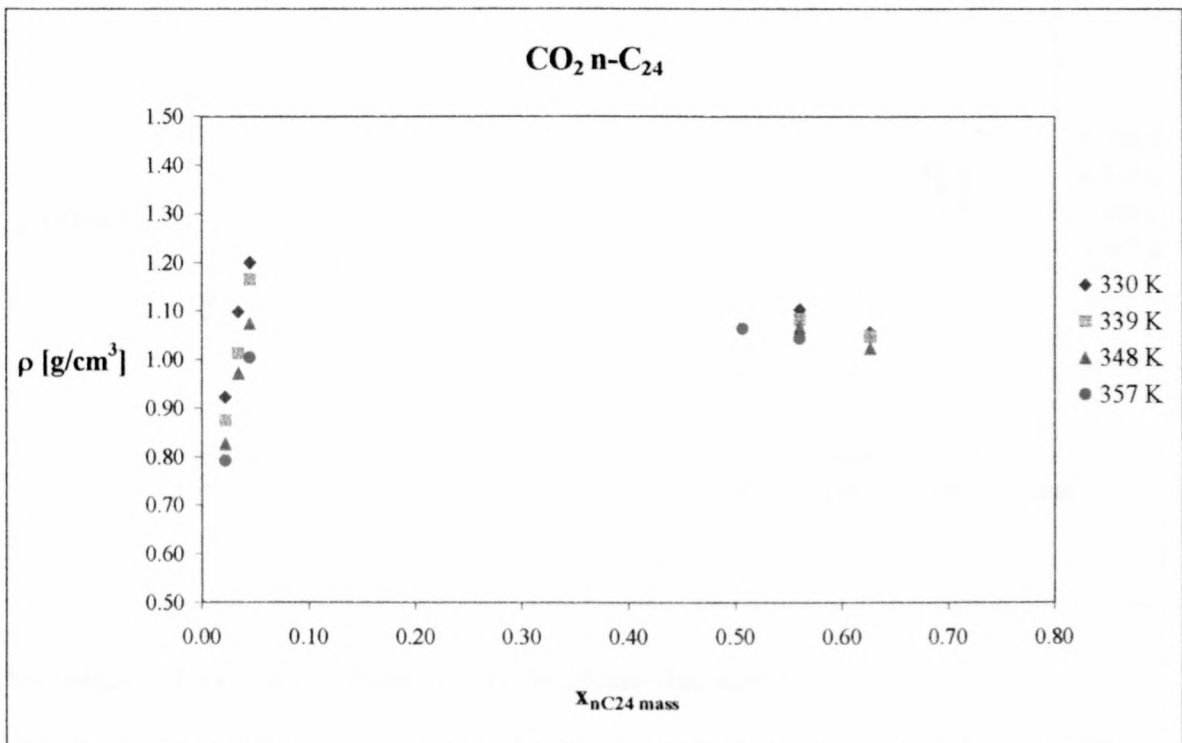
Graph 3-15 CO$_2$ – n-C$_{24}$ Densities at the Phase Boundary

57
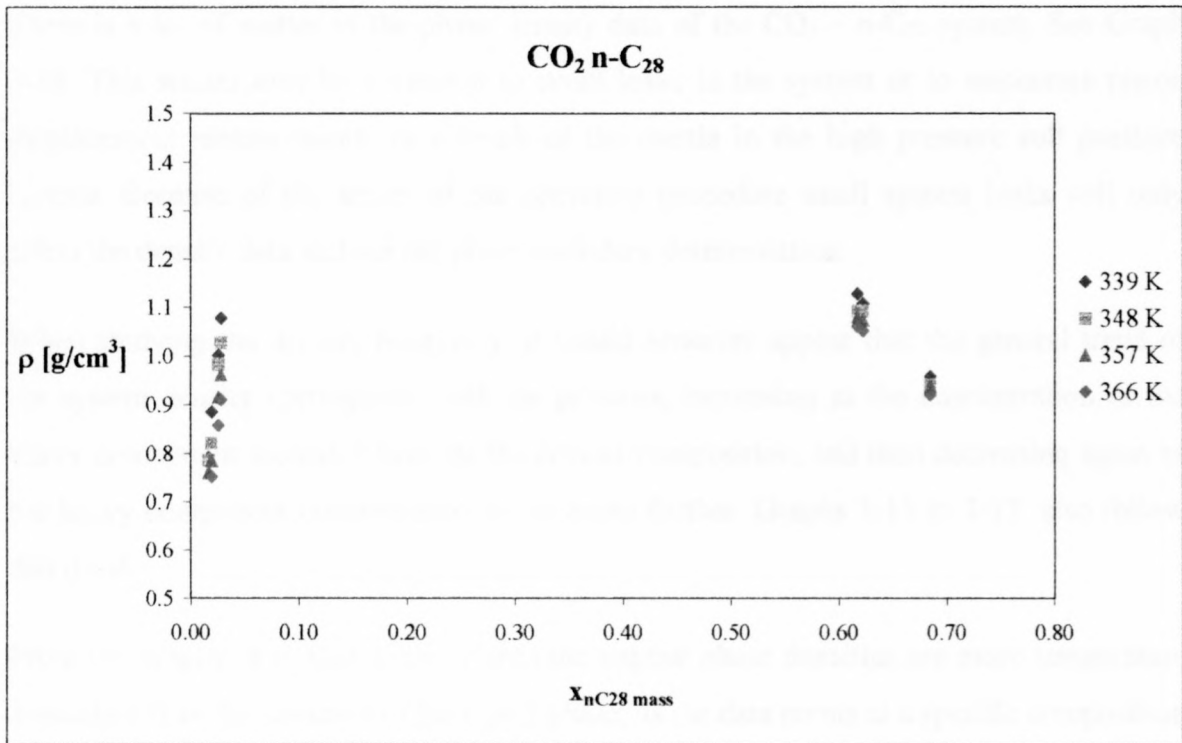
Graph 3-16 CO₂ – n-C₂₈ Densities at the Phase Boundary
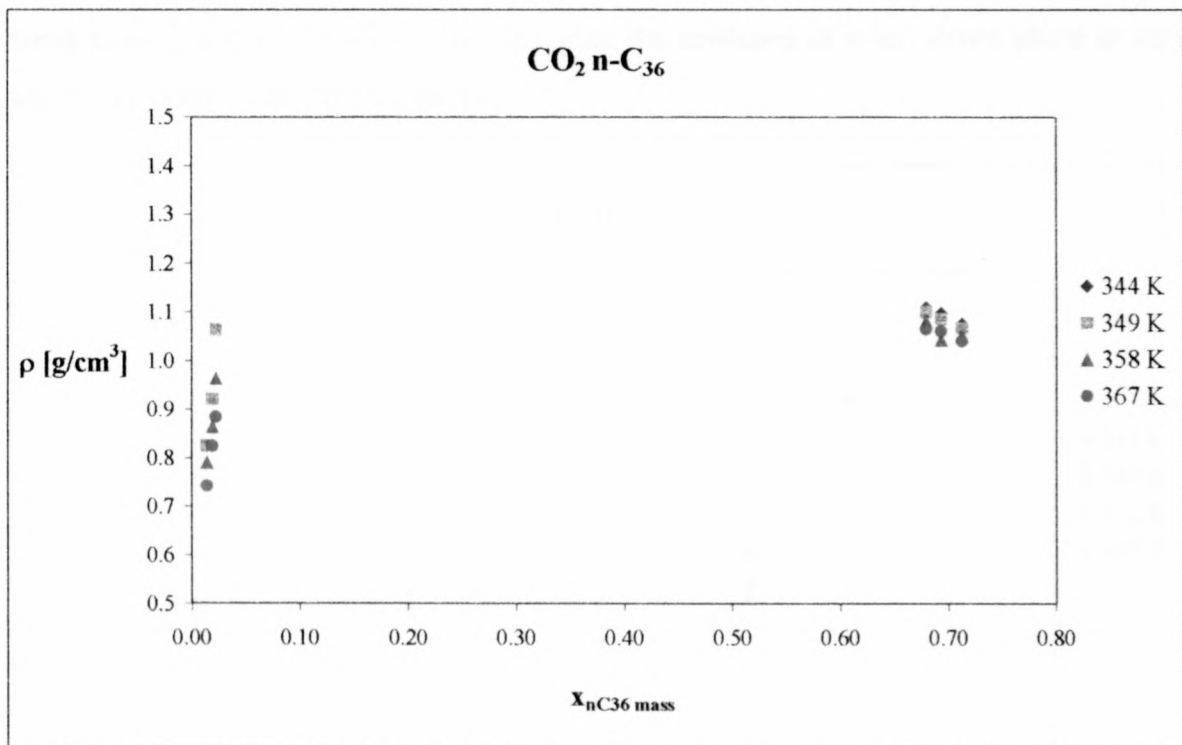
Graph 3-17 CO₂ – n-C₃₆ Densities at the Phase Boundary

Graphs 3-14 to 3-17 are plots of the CO_2-alkane systems' density at the phase boundaries. The graphs all have the same scale to facilitate the comparison of the data.

58

There is a lot of scatter in the phase density data of the $CO_2 - n\text{-}C_{20}$ system. See Graph 3-14. This scatter may be attributed to small leaks in the system or to inaccurate piston displacement measurements as a result of the inertia in the high pressure cell pressure control. Because of the nature of the operating procedure small system leaks will only affect the density data and not the phase boundary determination.

When studying the density behaviour, it would however appear that the general trend of the system density corresponds with the pressure, increasing as the concentration of the heavy component increases towards the critical composition, and then decreasing again as the heavy component concentration is increased further. Graphs 3-15 to 3-17 also follow this trend.

From the graphs, it is also apparent that the vapour phase densities are more temperature dependent than the densities of the liquid phase, as the data points at a specific composition are more spread-out.

On the plot of the vapour phase densities of the $CO_2 - n\text{-}C_{36}$ system, Graph 3-18, the same trend as in Graph 3-13 is observed, indicating the existence of a less dense phase at very low heavy component concentrations.
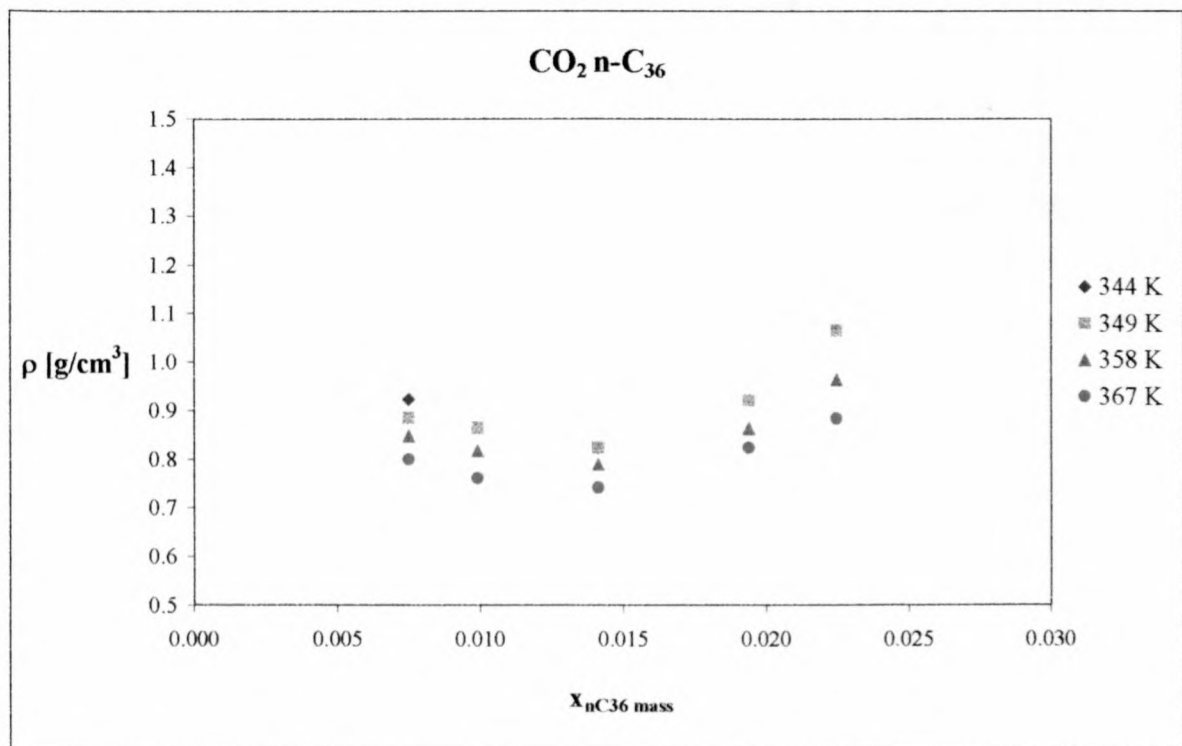
Graph 3-18 Vapour Densities of the $CO_2 - n\text{-}C_{36}$ System

Ethane – n-Alkane Phase Diagrams

The ethane – n-alkane systems were studied in order to measure the phase equilibria of systems with a higher heavy component solubility in the supercritical solvent. The heavy component solubilities were so high that all the phase boundaries could be determined in the view cell.

The following graphs contain the measured ethane – n-alkane phase boundaries:
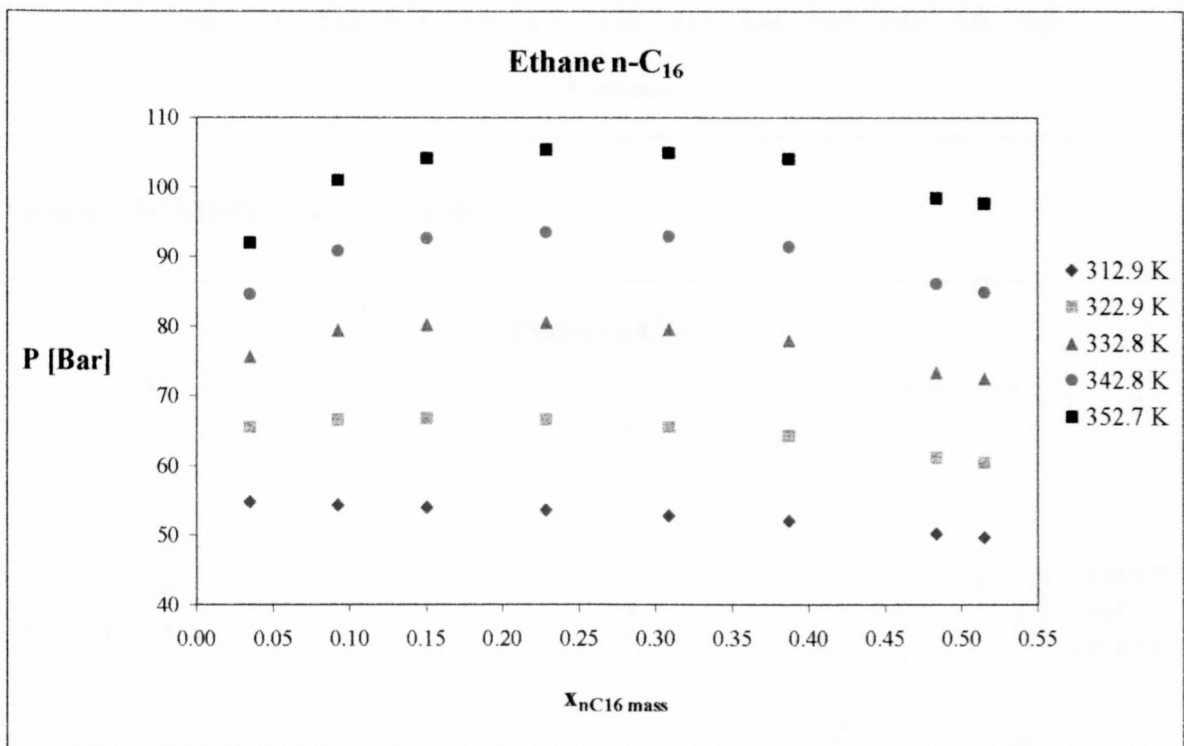
Graph 3-19 Ethane – n-C_{16} System
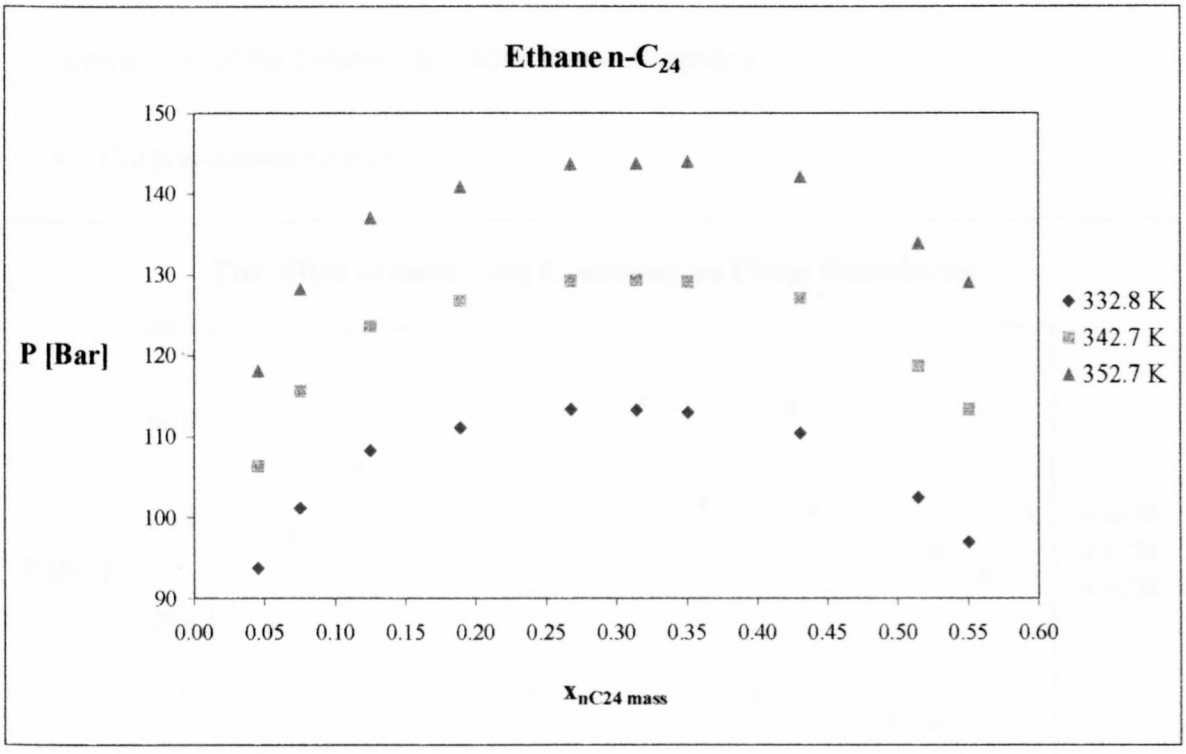
Graph 3-20 Ethane – n-C_{24} System
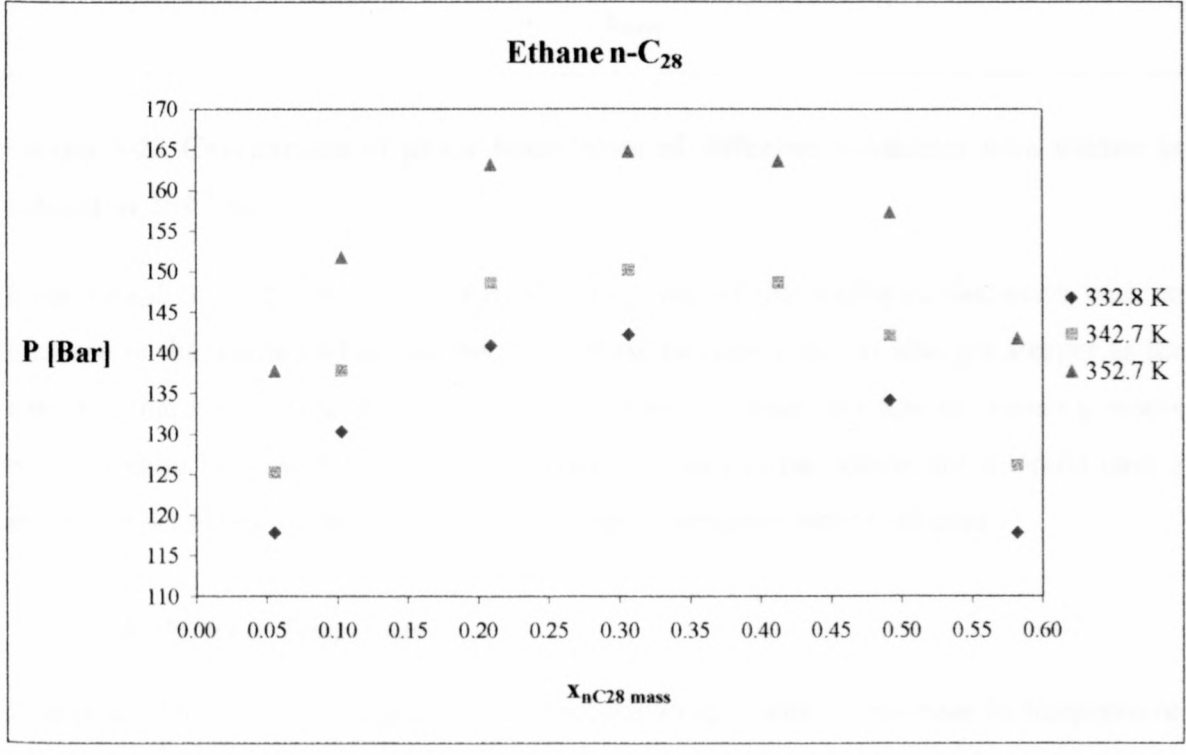
Graph 3-21 Ethane – n-C_{28} System

61

Discussion of the Ethane – n-Alkane Phase Diagrams

- *Carbon-Number effect*

The effect of increasing C-number on Phase Boundaries
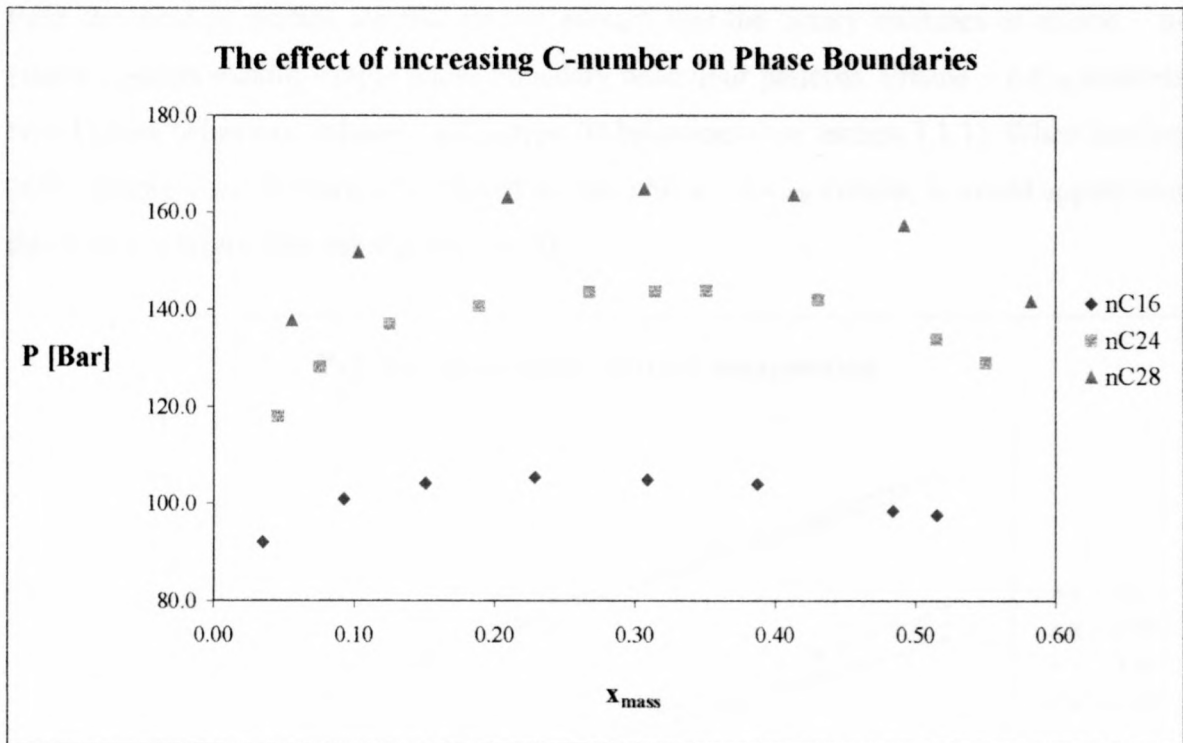
Graph 3-22 Comparison of phase boundaries of different n-Alkanes with ethane as solvent at 352.7 K

From Graph 3-22 it can be seen that the solubility of the n-alkanes decreases with an increase in the solute carbon-number. The phase boundary curves also get steeper as the carbon-number increases. For low carbon-numbers, a small increase in system pressure would greatly increase the fraction of alkane dissolved in the solute, but it would have a much smaller effect on the solubility of the higher carbon-number n-alkanes.

- *The Effect of Temperature*

It appears that the P-$x_{mass\ n\text{-}alkane}$ curves become steeper with an increase in temperature. This effect is clearly on the P-x_{mass} plot of the ethane – n-C_{16} system. See Graph 3-19.

A linear relationship between temperature and pressure was observed over the entire composition range for all the ethane – n-alkane systems. See Graph 3-23. Unlike with the

62

CO_2 – n-alkane systems no decrease in the maximum phase boundary pressure with an increase in temperature was observed.

Because the solute and solvent are of the same homologous chemical species, n-alkanes, their chemical properties are still similar enough that the binary mixtures of ethane – n-alkane systems exhibit simple phase boundary behaviour patterns. Ethane – $n-C_{16}$ exhibits type I phase behaviour, ethane – $n-C_{24}$ type III behaviour (see section 3.1.1). When looking at the simple phase behaviour exhibited by the ethane – $n-C_{28}$ system, it would appear that this binary mixture also belongs to type III.
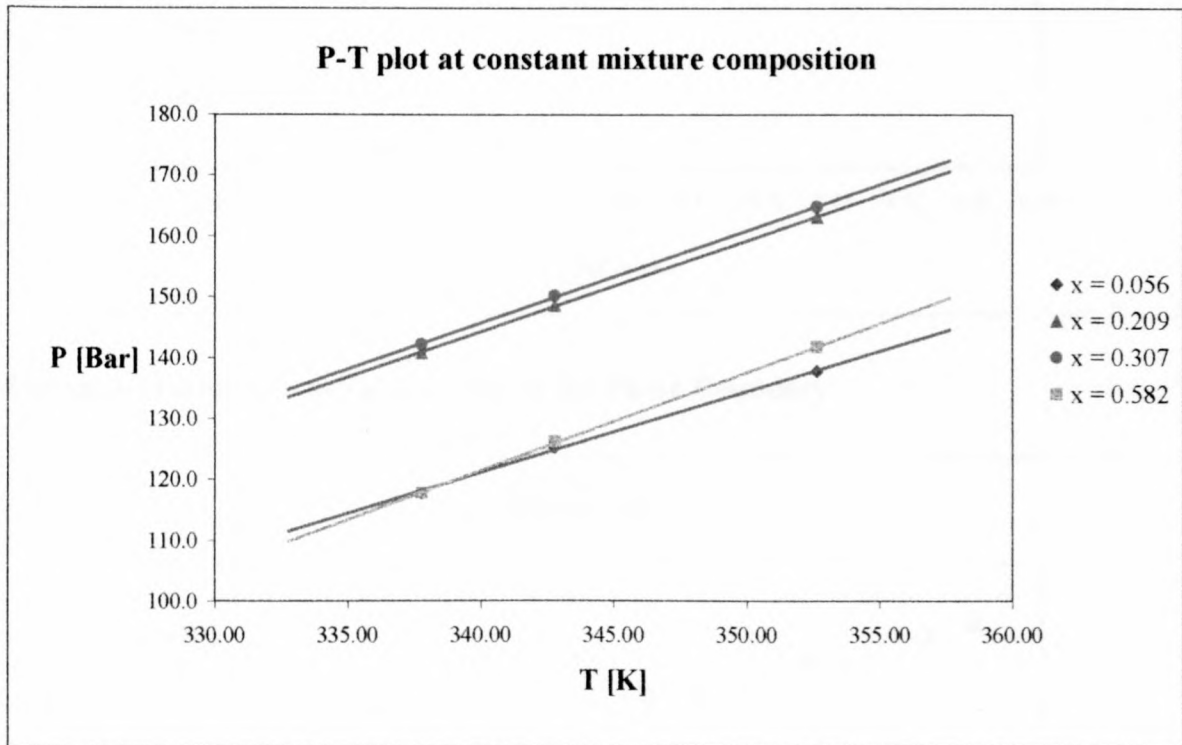
Graph 3-23 P-T plot of the ethane- nC_{28} system, where x represents $x_{nC28 \text{ mass}}$

Ethane – n-Alkane Mixture Densities

The accuracy of the calculated density of the ethane – n-alkane systems is again dependent on the accuracy of the measurement of the mass loaded into the cell, measured to an accuracy of 0.01 g, the measurement of the piston displacement, an accuracy of 0.02 mm, and the determination of the cell volume, with an accuracy 1 cm^3. Because of the large cell volume, a 1 cm^3 error in the total volume determination only results in a 0.76 % error in the actual cell volume, and a 1 % error in the density calculation.

63

The following graphs contain plots of the ethane – n-alkane mixture densities.
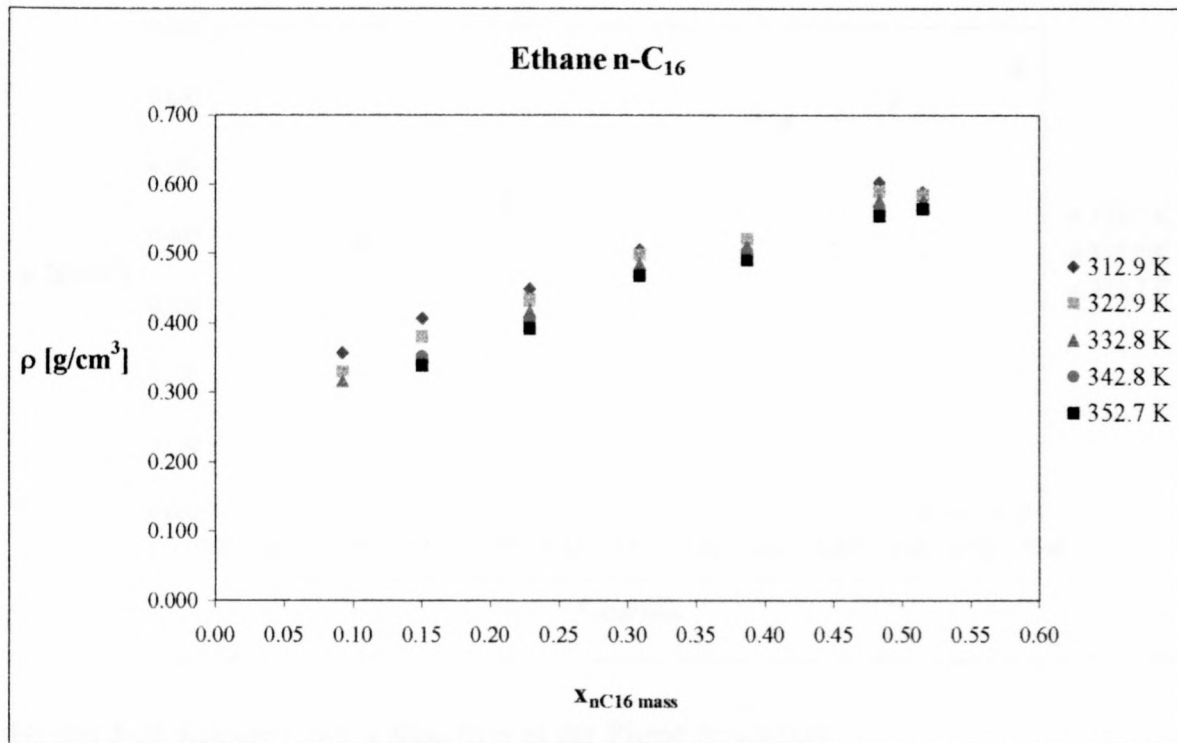
Graph 3-24 Ethane – n-C$_{16}$ Densities at the Phase Boundary
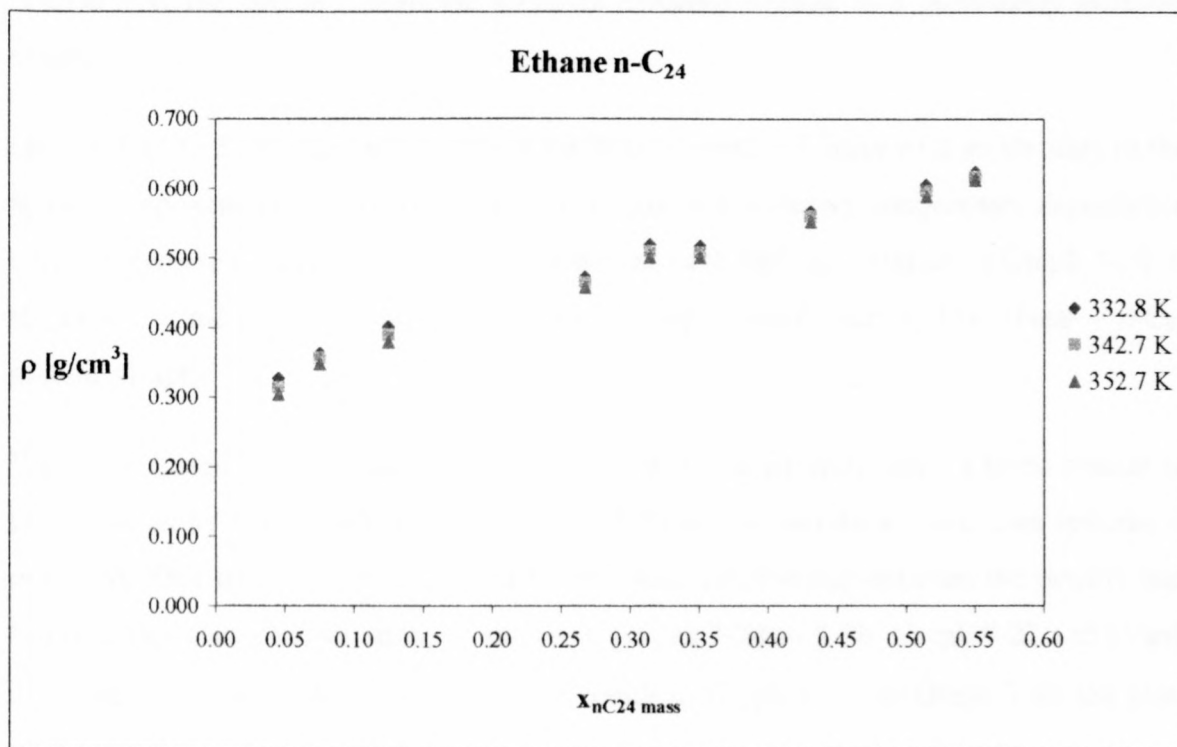
Graph 3-25 Ethane – n-C$_{24}$ Densities at the Phase Boundary

64

Ethane n-C$_{28}$

ρ [g/cm^3]

X$_{nC28\ mass}$

- ◆ 332.8 K
- ▪ 342.7 K
- ▲ 352.7 K
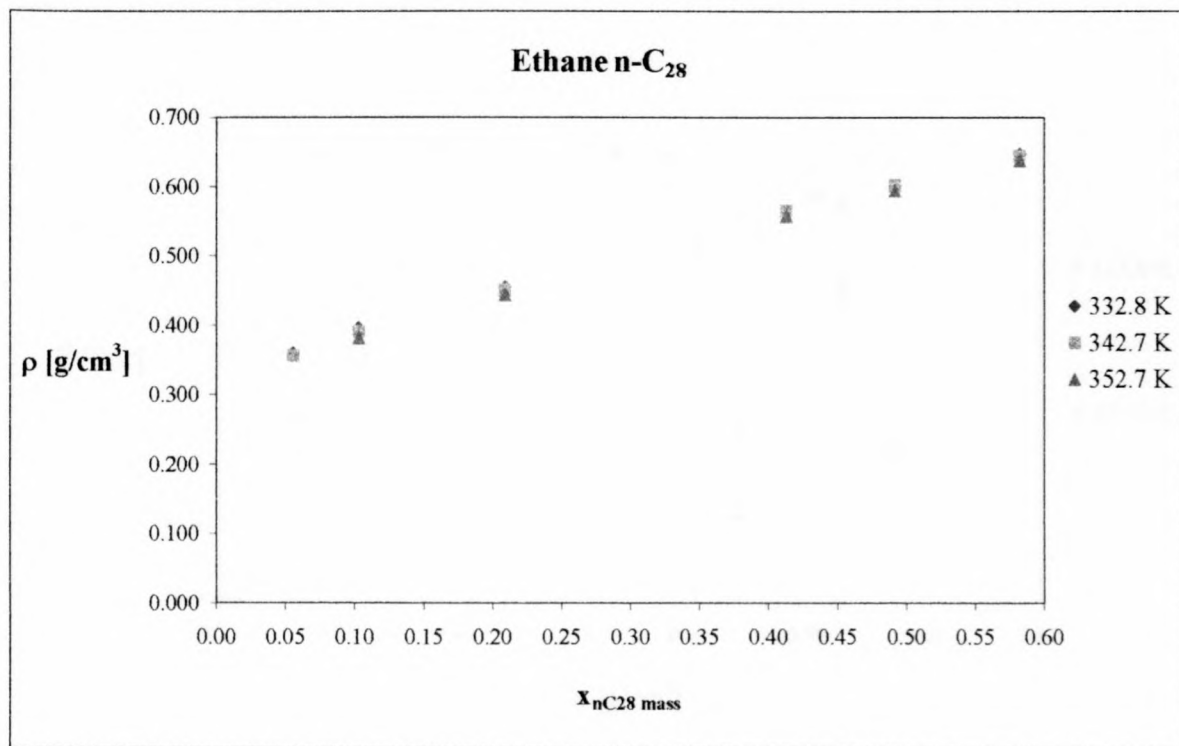
Graph 3-26 Ethane – n-C$_{28}$ Densities at the Phase Boundary

When these graphs are compared to graphs 3-14 to 3-17 of the CO$_2$ – n-alkane densities, it is clear that the ethane – n-alkane mixtures densities behave in a completely different manner.

Graphs 3-24 to 3-26 show an increase in the binary mixture density with an increase in the heavy component concentration. It also indicates a decreasing temperature dependence with an increase in carbon-number. The densities vary with temperature in Graph 3-24 of the ethane – n-C$_{16}$ system, but fall virtually on top of each other in the ethane – n-C$_{28}$ system, Graph 3-26.

When the system pressure and densities are plotted against each other, a trend similar to that reported by Nieuwoudt in (Nieuwoudt, 1994) for the n-Butane – n-alkane systems is observed. This trend can be attributed to the linear relationship between the density and heavy component concentration, as shown in graphs 3-24 to 3-26. Graph 3-27 and Graph 3-28, the P-ρ plots, follow exactly the same trends as Graph 3-19 and Graph 3-20, the plots of the change in phase boundary pressure with heavy component mass fraction.

65
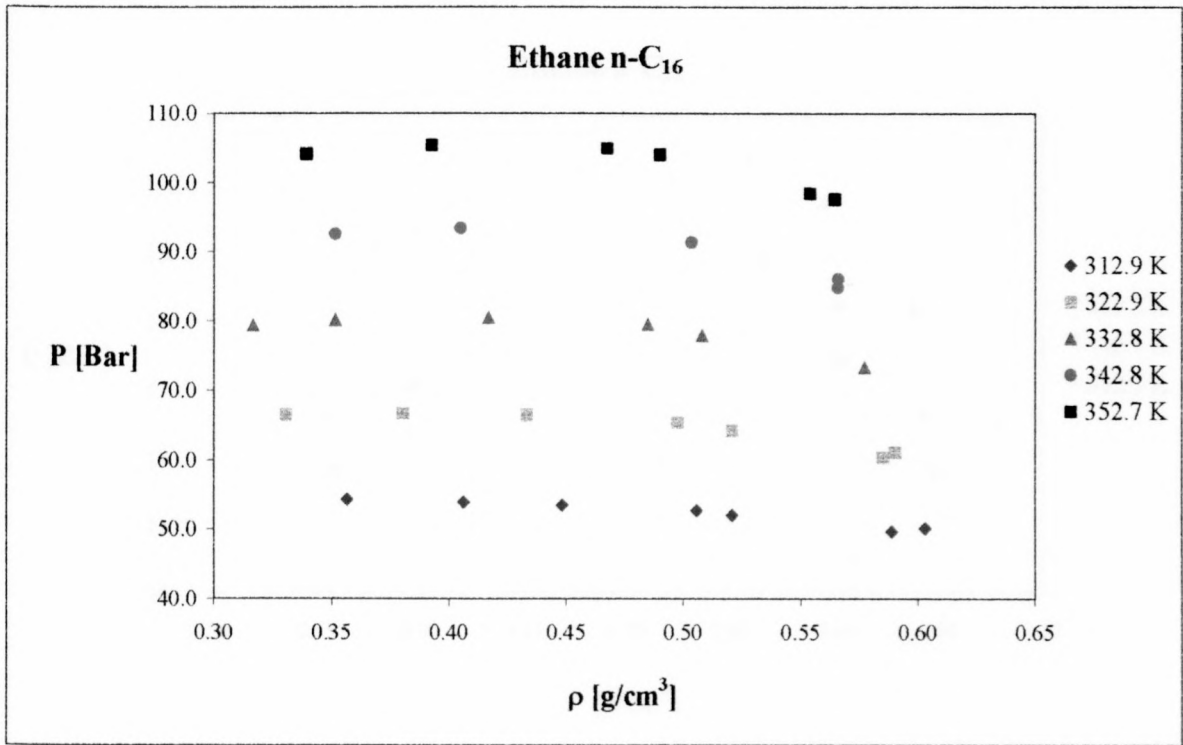
Graph 3-27 P-ρ Plot of the ethane – n-C$_{16}$ system
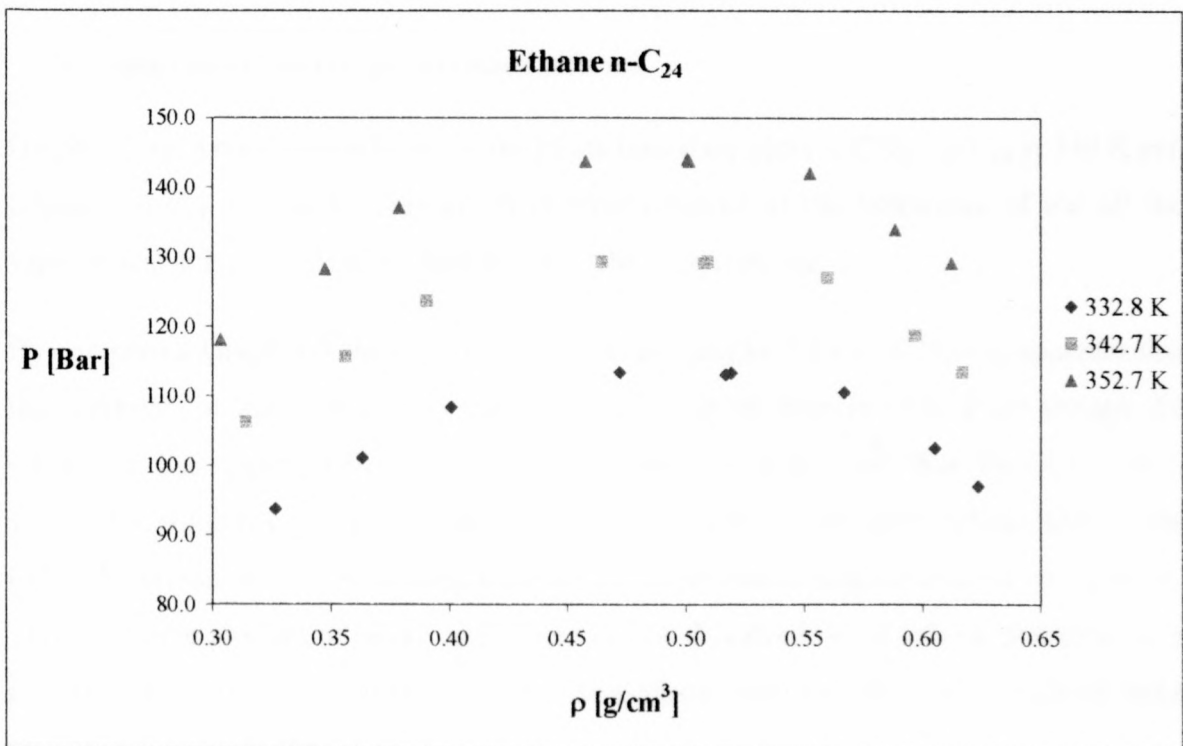
Graph 3-28 P-ρ Plot of the ethane – n-C$_{24}$ system

66
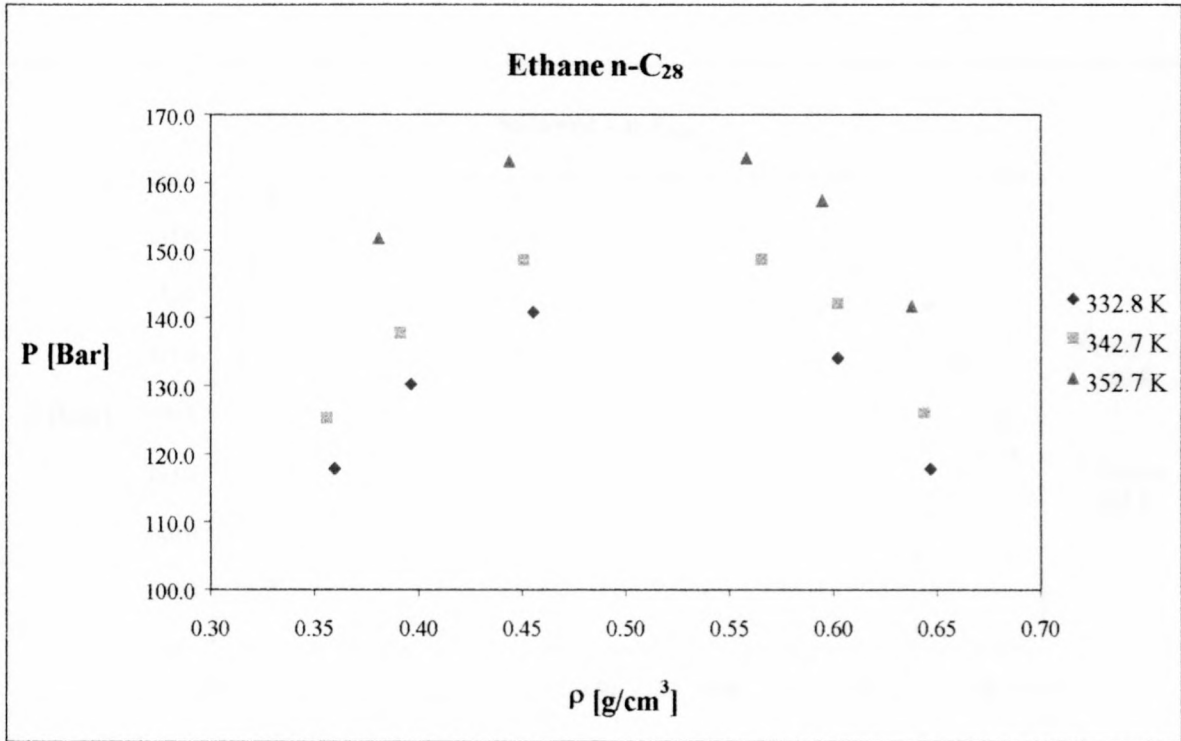
Graph 3-29 P-ρ Plot of the ethane – n-C$_{28}$ system

Comparison of the two supercritical solvents

Graph 3-30 is a comparison between the phase boundary plots of CO_2 – n-C$_{24}$ at 348 K and ethane – n-C$_{24}$ at 352 K. This graph is representative of the behaviour of the all the supercritical solvent – n-alkane systems at all the temperatures.

By comparing Graph 3-3 through to Graph 3-8 and graphs 3-19 to 3-21, it is apparent that the solubility of the n-alkanes is much higher in ethane than in CO_2. Even though the ethane – n-C$_{24}$ system in Graph 3-30 is at a temperature 4 K higher than the CO_2 – n-C$_{24}$ system the solubility of the n-alkane is still higher in the supercritical ethane than in the CO_2. The pressures needed to force the binary mixture into a single phase are much lower. Thus, a similar amount of heavy component can be dissolved in the solvent at much lower pressures if ethane is used as the solvent. The n-alkanes will therefore dissolve much more readily in the ethane than in the CO_2.
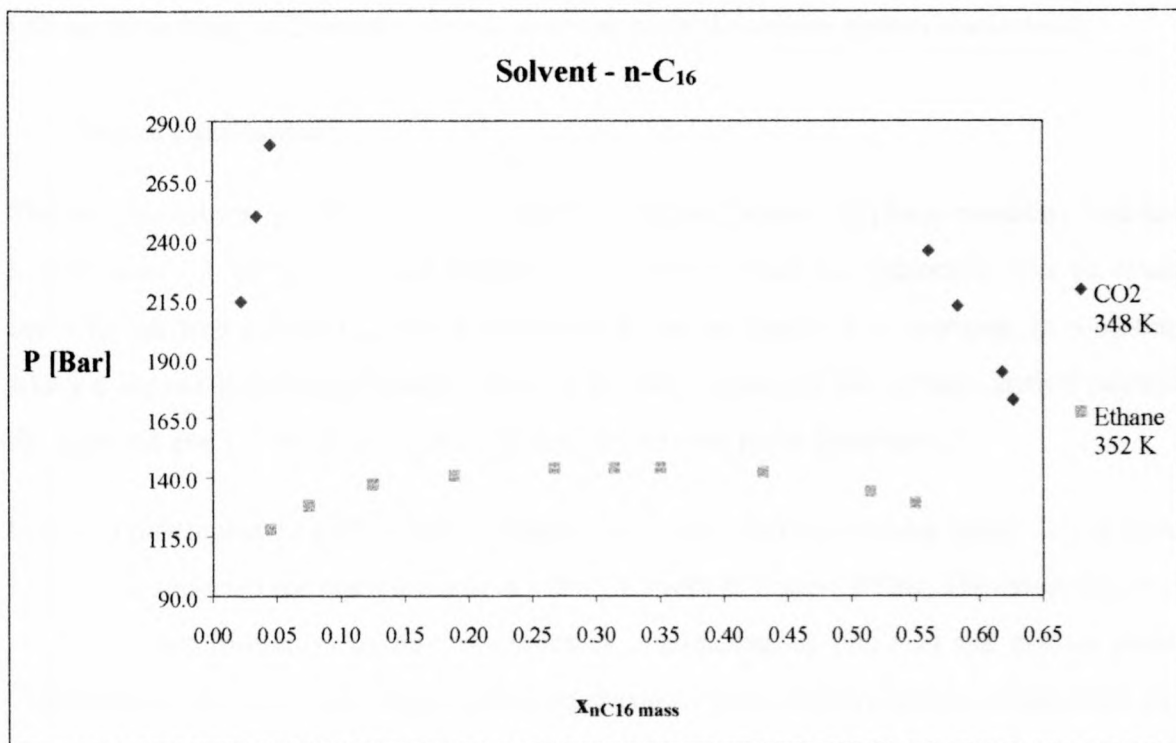
Graph 3-30 Phase boundary plot of binary mixtures n-C$_{24}$ as solute. The CO$_2$ system is at 348 K and ethane system at 352 K.

The ethane – n-alkane phase boundary curves are also much flatter than the phase boundaries of the n-alkane mixtures with CO$_2$. The solubility of the heavy component can therefore be manipulated much more easily when ethane is used as solvent. A small reduction in system pressure would result in a marked decrease in the n-alkane solubility. In an extraction system, this fact will have important implications in the ease of solvent recovery and plant capital and operating costs. If supercritical ethane is used as a solvent, only a small pressure difference between the extraction and solute-recovery sections is necessary. If the solute is recycled in the system, the use of ethane would therefore lead to lower compression costs.

If the supercritical solvents were going to be used in an application where only the light n-alkanes need to be extracted from a mixture of n-alkanes, as in the deoiling of paraffinic waxes, a solvent with a high light component selectivity is required. When ethane is used as a solvent, a small pressure increase at a specific temperature will greatly increase the solubility of the heavy n-alkanes, thus reducing the light component selectivity. However, when CO$_2$ is to achieve the same degree of solubility a much greater pressure increase is

needed before the solubilities of the components are increased to the same extent. Using CO_2 as the solvent will therefore result in better control over the system's selectivity.

Critical Opalescence

The mixture critical point is a point on the P-x diagram where the phase boundary line has a maximum i.e. $dP/dx = 0$ and $d^2P/dx^2 = 0$. At this point no distinction can be made between the two phases that were present at lower pressures. For example: in a system where a vapour-liquid equilibrium is present at lower pressures, the mixture critical point is the pressure and composition where the bubble and dew point lines meet.

Critical opalescence is a phenomenon that occurs at the mixture critical point. Travers and Usher first reported the phenomenon in 1906 (Travers & Usher, 1906). The opalescence is caused by the formation of micro-bubbles in a homologous phase at the critical point. These bubbles have specific light scattering characteristics, light reflected off the fluid has a bluish-white appearance and when it is transmitted through the medium, it will appear reddish-orange in colour. The opalescence can also be observed to a lesser degree in the near critical region. If the phase boundary diagram is very flat, opalescence can occur over a wide range of mixture compositions around the critical point.
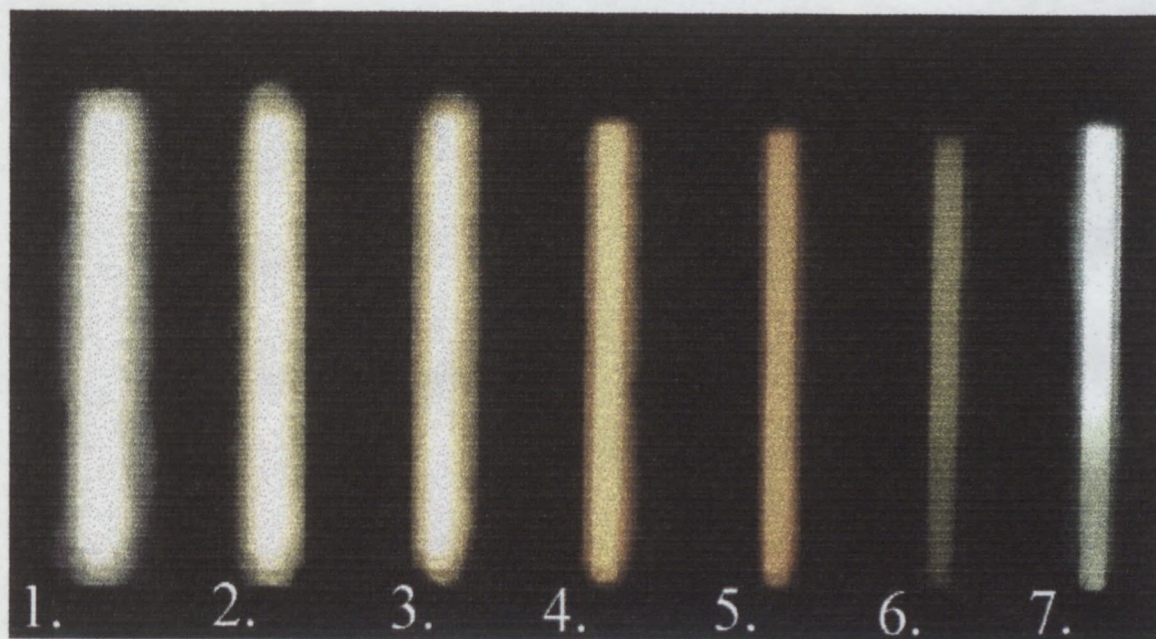
Figure 3-12 Composite photo of phase transition of the $CO_2 - n-C_{16}$ system, near the mixture critical point, taken in the view cell.

Figure 3-12 contains a series of photographs taken of the phase transition with the overall composition of the cell contents very close to the mixture critical composition. The photo progresses from single phase on left, to two phases on the right. The 5th image was taken near the mixture critical point, 165 bar, 313.15 K, 0.313 $x_{mass\ n-C16}$. The critical opalescence effect can clearly be seen in this image. The light source is behind the cell and light is transmitted through the medium, resulting in the orangey colour of the mixture.
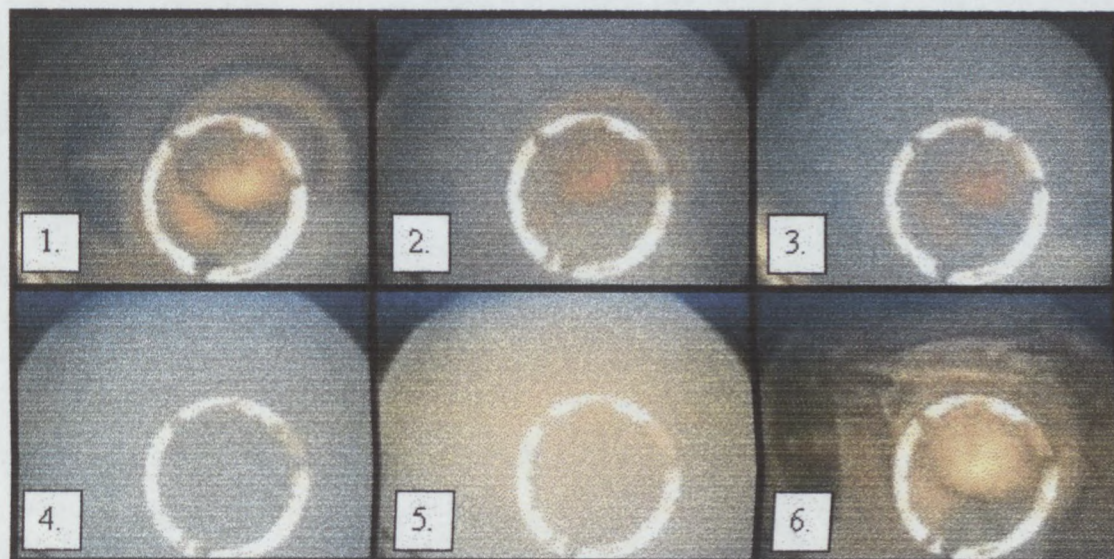
Figure 3-13 Composite photo of phase transition of the CO_2 – n-C_{20} system, near the mixture critical point, taken in the high-pressure cell.

The high-pressure cell experimental set-up is such that light is reflected off the piston through the medium, with the resulting bluish appearance near the critical point. Figure 3-13 is a composite image of the phase transitions detected near the mixture critical point of the CO_2 – n-C_{20} system, 300 bar, 348K and $x_{mass\ n-C20}$ 0.34. The series of images progresses sequentially from a single phase to two phases as a result of a decrease in the system pressure. Critical opalescence was observed in image 4, with the mixture having a bluish colour. (The bright ring visible in all the images is caused by the reflection the light from the light source off the sight glass.)

3.5 CONCLUSIONS

The view cell was found to be a suitable design for the study of binary phase equilibrium boundaries. However, it was found that the solubility of n-alkanes in CO_2 decreased to such a degree with the increase in carbon number that a phase equilibrium cell with a higher maximum operating pressure was needed to study the phase transitions.

By comparing the measured data with the limited published data available for these systems, it was found that the experimental method used to study the phase transitions provided suitable results.

A decrease in the solubility with an increase in the carbon-number of the heavy alkane was observed when using both the supercritical CO_2 and ethane as solvents. The effect of the heavy component carbon-number was however much greater with CO_2 as solvent.

The linear relationship between the pressure and temperature of the phase boundaries for a constant composition as reported in the past, should be applied with care when working with CO_2 – n-alkane systems, as it was found that this trend does not apply at mixture compositions close to the critical point. However, the linear relationship was observed in the ethane – n-alkane systems and at compositions away from the critical point in the CO_2 – n-alkane systems.

Completely different density behaviour was observed for the CO_2 – n-alkane and ethane – n-alkane systems. With the carbon-dioxide systems, there is an increase in mixture density with an increasing heavy component concentration up to a maximum value, the density then decreases with a further increase in heavy component concentration. The ethane – n-alkane systems showed a linear increase in mixture density with an increase in heavy component concentration.

With the exception of the system ethane – $n\text{-}C_{16}$, which belongs to type I, all of the ethane systems investigated exhibited type III phase behaviour. The CO_2 – n-alkane systems studied, with the exception of CO_2 – $n\text{-}C_{12}$, all belonged to the type IV phase boundary group.

From the comparison of the results of the two supercritical solvents, it became clear that for applications in supercritical extraction of alkanes, it is necessary to choose the solvent carefully with respect to the overall solubility, influencing the operating pressure of the system, and the selectivity of the solvent, influencing the ease with which the solubility of a specific component can be manipulated. The solubility of the n-alkanes is much higher in supercritical ethane, but a greater degree of control over the selectivity of the component dissolution can be achieved when using supercritical CO_2.

4 HIGH PRESSURE PHASE EQUILIBRIA MODELLING

4.1 INTRODUCTION

The method used to calculate fluid phase equilibria, using equations of state, is described in most thermodynamic textbooks (Smith et al., 1996). Only a brief summary of the procedure will be given here.

The use of chemical potential as a criterion of phase equilibria can easily be deduced from classical thermodynamics

$$\mu_i^\alpha = \mu_i^\beta \qquad (4.1.1)$$

From the definition of the fugacity of a species, an alternative criterion for phase equilibrium can be derived:

$$f_i^\alpha = f_i^\beta \qquad (4.1.2)$$

Where

$$f_i^\alpha = \phi_i^\alpha x_i P \qquad (4.1.3)$$

$$\phi_i^\alpha x_i P = \phi_i^\beta y_i P \qquad (4.1.4)$$

It can also be shown that the fugacity coefficient may be calculated from the following relationship:

$$\ln \phi = z - 1 - \ln z - \int_\infty^v P - \frac{RT}{v} dv \qquad (4.1.5)$$

and

$$\ln \phi_i = \frac{\partial (n \ln \phi)}{\partial n_i} \bigg|_{T,P,n_j} \qquad (4.1.6)$$

73

In order determine the fugacity coefficient of a chemical species, it is necessary to first establish the PVT relationship of that species. The various equations of state attempt to model this relationship.

4.2   INTRODUCTION TO EQUATIONS OF STATE

A wide variety of equations of state, EOS, and mixing rules are available today. EOS from two main categories were used in this work:

The first group of EOS developed from classical thermodynamics, where empirical functions are used to represent the attractive and repulsive forces in a fluid. These equations are normally cubic in nature. Van der Waals developed the first useful equation of state of this kind. There is a wide variety of cubic equations of state that were developed out of the original approach used by Van der Waals, these equations are collectively known as the Van der Waals Type Equations of State.

The second approach in developing the equations of state is to quantify the various forces present in pure fluids or fluid mixtures fundamentally. Statistical mechanical principles are used to develop equations to represent the various attractive and repulsive forces present. This approach often leads to very complicated equations that are not cubic in volume or compressibility. This has the effect that these EOS are very computationally intensive and severely limits their applications. It is often necessary to simplify these equations before they can be used in practice. These types of EOS will be referred to in this work as the Statistical Mechanical Equations of State.

4.3   VAN DER WAALS TYPE EQUATIONS OF STATE

4.3.1   Van der Waals Equation of State

The Van der Waals equation of state was published in 1873, and formed the basis of many of the modern equations of state. It is based on spherical molecules with attractive and repulsive intermolecular forces depending on the relative distance between the molecules (Brunner, 1994).

74

$$P = \frac{RT}{v-b} - \frac{a}{v^2} \qquad (4.3.1)$$

The parameters a and b represent the attractive and repulsive forces respectively. Both these parameters can be written in terms of the chemical species' critical point:

$$v_c = 3b$$
$$P_c = \frac{a}{27b^2} \qquad (4.3.2)$$
$$T_c = \frac{8a}{27Rb}$$

The Van der Waals equation is able to give a qualitative representation of the PVT behaviour of most substances, but is not accurate enough for the present requirements.

4.3.2   Soave-Redlich-Kwong (SRK) Equation of State

Since the development of the Van Der Waals EOS, a large number of similar-type EOS have been proposed. The Redlich-Kwong (RK) equation of state was the first such an equation to model the vapour phase properties successfully. The Van der Waals repulsive term remained unchanged, but the attractive term was modified to have an explicit temperature dependence (Redlich & Kwong, 1949).

$$P = \frac{RT}{v-b} - \frac{aT^{-0.5}}{v(v+b)} \qquad (4.3.3)$$

The main disadvantage of the RK equation was the fixed temperature dependence of the attractive term. It is very probable that different chemical species would exhibit different temperature dependencies. Wilson and later Soave proposed the use of an alpha function to force the EOS to reproduce the vapour phase more accurately.

The Soave-Redlich-Kwong EOS is as follows (Soave, 1972):

$$P = \frac{RT}{v-b} - \frac{a[T]}{v(v+b)} \qquad (4.3.4)$$

$$b = 0.08664 \frac{RT_c}{P_c} \qquad (4.3.5)$$

The temperature dependent function a(T):

$$a = a_c \alpha(T) \qquad (4.3.6)$$

$$a_c = 0.42748 \frac{R^2 T_c^2}{P_c} \qquad (4.3.7)$$

The alpha function is described as the following:

$$\alpha = \left[1 + m(1 - T_r^{0.5})\right]^2$$
$$m = 0.48 + 1.574\omega - 0.175\omega^2 \qquad (4.3.7)$$

The alpha function attempts to incorporate the molecule's deviation from the ideal spherical model using the acentric factor of the chemical species. The acentric factor, ω, is defined as a function of the species' vapour pressure at a specific temperature:

$$\omega = -\log(P_{vap})\big|_{T_r = 0.7} - 1.0 \qquad (4.3.8)$$

By using the acentric factor the EOS now contains information about the behaviour of the molecules away from the critical point; this will provide some information on the intermolecular forces at low operating pressures.

The SRK equation of state still has some shortcomings however. It predicts a constant critical density of 0.333. This value is approximately correct for small molecules, but inaccurate for long chain molecules. It is also well known that the SRK equation is unable to model liquid densities very well (Reid et al., 1987).

4.3.3   Modified Peng Robinson Equation of State

The Peng Robinson equation of state was another successful modification of the Van der Waals EOS. The equation's general form can be written as (Peng & Robinson, 1976):

$$P = \frac{RT}{v - b} - \frac{a[T]}{v(v + b) + b(v - b)} \qquad (4.3.9)$$

Where

$$b = 0.077796 \frac{RT_c}{P_c} \tag{4.3.10}$$

and

$$a[T] = a_c \alpha[T] \tag{4.3.11}$$

$$a_c = 0.457235 \frac{R^2 T_c^2}{P_c} \tag{4.3.12}$$

The form of the temperature dependence of the $\alpha[T]$ is similar to that used in the Redlich-Kwong EOS:

$$\alpha[T] = \left[1 + m\left(1 - T_R^{0.5}\right)\right]^2 \tag{4.3.13}$$

Where m is considered a function of the component's acentric factor. Peng and Robinson developed a polynomial function in ω to represent this relationship. Stryjek and Vera proposed a similar functional relationship for $m(\omega)$, which would provide a better fit of the experimental data at high and low T_r values (Zabaloy & Vera, 1998). They called this equation the Stryjek-Vera Modification of the Peng-Robinson Equation of State, or the PRSV (Stryjek & Vera, 1986 a; Stryjek & Vera, 1986 b). Their functional relationship for m has the following form:

$$m = m_o + m_1\left(1 + T_R^{0.5}\right)\left(0.7 - T_R\right) \tag{4.3.14}$$

$$m_o = 0.378893 + 1.4897153\omega - 0.17131848\omega^2 + 0.0196554\omega^3 \tag{4.3.15}$$

The coefficient m_1 is an adjustable parameter characteristic of each pure compound. It has however been recommended that for T_r values higher than 0.7, m_1 should be set equal to zero for all compounds other than water and lower alcohols.

Reported values for m_1 for alkanes could only be found up to octadecane (nC_{18}) (Stryjek & Vera, 1986 b). Nieuwoudt (Nieuwoudt, 1994) found that setting $m_1 = 0$ in all cases still provided a reasonable fit of the experimental alkane vapour pressure data. The equations may therefore still be applied to alkane systems without the value of the parameter m_1 being known. Because of this, and since all the experimental work with CO_2 has been

carried out at temperatures above its critical temperature, equation 4.3.14 can be reduced to $m=m_0$.

Zabaloy and Vera (Zabaloy & Vera, 1998) reported that the Peng Robinson EOS structure is superior to the structures of the Van der Waals and SRK EOS. However, as in the case of the Van der Waals and SRK EOS, the PR EOS still has the inherent problem that it predicts a constant $Z=0.307$ regardless of the component.

4.3.4 Patel Teja Equation of State

The Patel Teja, PT, EOS was developed in order to move away from the fixed critical compressibility of the previous EOS as discussed in sections 4.3.2 and 4.3.3. The proposed EOS had the following form (Patel & Teja, 1982):

$$P = \frac{RT}{v-b} - \frac{a[T]}{v(v+b)+c(v-b)} \qquad (4.3.16)$$

According to Patel and Teja (Patel & Teja, 1982), it is necessary to treat the critical compressibility as an empirical parameter and not as the true component critical compressibility. The proposed equation of state was therefore constrained to satisfy the following conditions:

$$\left(\frac{\partial P}{\partial v}\right)_{T_c} = 0$$

$$\left(\frac{\partial^2 P}{\partial v^2}\right)_{T_c} = 0 \qquad (4.3.17)$$

$$\frac{P_c v_c}{RT_c} = \zeta_c$$

Where ζ_c is the empirical "critical compressibility".

When the constraints are applied, equation 4.3.16 yields the following:

$$a[T] = a_c \alpha[T] \qquad (4.3.18)$$

$$a_c = \Omega_a \left(\frac{R^2 T_c^2}{P_c}\right) \qquad (4.3.19)$$

$$b = \Omega_b \left(\frac{RT_c}{P_c} \right) \qquad\qquad (4.3.20)$$

$$c = \Omega_c \left(\frac{RT_c}{P_c} \right) \qquad\qquad (4.3.21)$$

With Ω_a and Ω_c equal to

$$\Omega_c = 1 - 3\zeta_c \qquad\qquad (4.3.22)$$

$$\Omega_a = 3\zeta_c^2 + 3(1 - 2\zeta_c)\Omega_b + \Omega_b^2 + 1 - 3\zeta_c \qquad\qquad (4.3.23)$$

and Ω_b is the smallest positive root of the following cubic equation:

$$\Omega_b^3 + (2 - 3\zeta_c)\Omega_b^2 + 3\zeta_c^2\Omega_b - \zeta_c^3 = 0 \qquad\qquad (4.3.24)$$

The α function was chosen to have the same form as that used by Peng Robinson and Soave.

$$\alpha[T] = \left[1 + m\left(1 - T_R^{0.5}\right) \right]^2 \qquad\qquad (4.3.25)$$

The values for m and ζ_c have been correlated with the component acentric factor ω:

$$m = 0.452413 + 1.30982\omega - 0.295937\omega^2 \qquad\qquad (4.3.26)$$

$$\zeta_c = 0.329032 - 0.076799\omega + 0.0211947\omega^2 \qquad\qquad (4.3.27)$$

From equation 4.3.27 it can be seen that the critical compressibility used in the Patel Teja, PT, EOS is component specific. This EOS therefore does not have the same problem inherent to the Van der Waals, SRK and PR EOS where a constant critical compressibility for all components was used. However, the compressibility used in this equation is still not equal to the true compressibility of the component.

4.3.5 Mixing and Combining Rules

The great advantage of using equations of state for phase equilibria calculations is the ease with which they can be applied to mixtures. The same equation of state used for pure fluids

may be used for mixtures if a satisfactory method exists to determine the mixture parameters. This is commonly achieved by using mixing and combining rules that relate the pure component parameters to that of the mixture (Wei & Sadus, 2000).

The most widely used mixing rules are the Van der Waals one-fluid prescriptions. These rules are based on the assumption that the radial distribution function of the component molecules are equal and that they explicitly contain a contribution from interactions between dissimilar molecules. These mixing rules were used in this work.

$$a = \sum_i \sum_j x_i x_j a_{ij} \qquad (4.3.28)$$

$$b = \sum_i \sum_j x_i x_j b_{ij} \qquad (4.3.29)$$

And for the case of the Patel Teja Equation (section 4.3.4) with an additional c parameter:

$$c = \sum_i \sum_j x_i x_j c_{ij} \qquad (4.3.30)$$

a_{ii}, b_{ii} and c_{ii} are the pure component parameters of component i and a_{ij}, b_{ij} and c_{ij} the cross parameters that are determined by the combining rules.

The mixing rule reported for the c_{ii} parameter deviates from the original mixing rule used by Patel and Teja (Patel & Teja, 1982). The rule as reported here was used by Crause (Crause, 2000) to model the supercritical phase solvent – n – alkane phase equilibria.

Other mixing rules have been developed to improve the EOS performance with strongly polar substances. These mixing rules incorporate factors such as density dependence and local composition, others are derived from the excess Gibbs and Helmholz energies. As these mixing rules were not used in this work, they are not discussed further in this section. The reader is referred to other sources such as (Brunner, 1994; Heidemann & Fredenslund, 1987) and (Wei & Sadus, 2000) for a more detailed discussion of these mixing rules.

There are several combining rules in existence for the determination of the cross parameter values. Wei and Sadus (Wei & Sadus, 2000) refer to three main types of combining rules, the Lorentz rule, the Van der Waals combining rule and the geometric mean rule.

The equation of state parameters in this work are determined by the Van der Waals combining rule:

$$a_{ij} = \left(1 - k_{ij}\right)\sqrt{a_i a_j} \qquad (4.3.31)$$

$$b_{ij} = \left(1 - l_{ij}\right)\left(\frac{b_i + b_j}{2}\right) \qquad (4.3.32)$$

And for the Patel Teja equation (section 4.3.4):

$$c_{ij} = \left(1 - l_{ij}\right)\left(\frac{c_i + c_j}{2}\right) \qquad (4.3.33)$$

It should be noted that the same value l_{ij} is used in both equations 4.3.32 and 4.3.33. The original PT EOS did not include the l_{ij} interaction parameter in the combining rule of the c_{ii} parameter. The binary interaction parameters k_{ij} and l_{ij} are fitted to the experimental mixture data.

When no interaction parameters are known, they may be set to zero and the EOS employed in a purely predictive manner.

4.4 STATISTICAL MECHANICAL EQUATIONS OF STATE

A different approach to the development of the EOS is to attempt to improve the theoretical basis of the terms in the equations of state. Researchers would approach the molecules as having a certain characteristic e.g. a hard spherical body, or a consisting of a series of hard spheres forming chains etc, then through statistical mechanics develop a theoretical equation of state representing the attractive and repulsive forces in such a fluid.

This approach often leads to complex equations of state. The ability of one of these equations of state to model the phase equilibria measured in this work was investigated.

4.4.1 Cubic Simplified Perturbed Hard-Chain Equation of State

The Perturbed Hard Chain Equation of State was originally developed by Beret and Prausnitz (Beret & Prausnitz, 1975). They incorporated the perturbed hard sphere theory,

which is valid for small spherical molecules, and Prigogine's theory on chain molecules, which is only valid at high (liquid) densities.

The Perturbed Hard Chain Theory, PHCT, incorporated the fact that the rotational and vibrational degrees of freedom of a chain molecule were, similarly to the translational degree of freedom, influenced by the system density. In the case of spherical molecules, only the translational degree of freedom is dependent on the system density.

The PHCT has three adjustable parameters: the molecular size, representing the repulsive forces, the molecular potential energy, representing the attractive forces, and the degrees of freedom of the molecule, indicating the molecular motions affected by density.

Donohue and Prausnitz (Donohue & Prausnitz, 1987) provided a slightly modified form of the PHCT and expanded it for application in fluid mixtures. The mixing theory is basically a one fluid theory, but with corrections for nonrandomness in the molecular distribution.

The PHCT was however severely limited by its complexity. In 1987 Kim et al. (Kim et al., 1986) proposed the three parameter Simplified Perturbed Hard Chain Theory, SPHCT. They replaced the attractive portion of the PHCT with a theoretical but simpler expression derived by Lee, Lombardo and Standler. This modification greatly simplified the PHCT: The attractive portion of the PHCT has 63 terms, 27 constants and 10 different mixing rules, while the SPHCT only has one term, one constant and three mixing rules. However, the SPHC Equation of State is still a seventh order polynomial in volume, and the densities have to be determined iteratively (Nieuwoudt, 1994).

Recently Wang and Guo (Wang & Guo, 1993) simplified the PHCT even further and derived a statistical mechanical equation of state that was cubic in volume, the Cubic Simplified Perturbed Hard-Chain Equation of State, CSPHC EOS. They modified the attractive portion of the SPHCT by reformulating the coordination number model for mixtures, and they replaced the complex expression for the repulsive portion of the equation of state with a more simple simulated expression.

The end result of the simplifications was a cubic equation of state with three adjustable pure component parameters. It was found that for n-alkanes these parameters were linear functions of chain length. The functionality was only tested up to n-Eicosane, but

Nieuwoudt extrapolated the data for use in the n-Butane – n- Tetrapentacontane systems with satisfactorily results (Nieuwoudt, 1994).

Of interest, for this study, is that it was found that the error generated by the CSPHS EOS in the prediction of the bubble point pressure and vapour phase composition increased with an increase in the n-alkane chain length. However, it was also found that even with no binary interaction parameters, the EOS was able to accurately represent the VLE data of the ethane – n-C_{20} system (Wang & Guo, 1993).

Wang and Guo also reported that density independent mixing rules were sufficient for non-polar mixtures (Wang & Guo, 1993). The Cubic Simplified Perturbed Hard-Chain Equation of State for mixtures was determined to be as follows:

$$z = 1 + c\left(\frac{1.11574b}{v - 0.44744b}\right) - Z_m \frac{a_m}{v + a_m} \qquad (4.4.1)$$

Where $Z_m = 36$

$$c = \sum_i x_i c_i \qquad (4.4.2)$$

$$b = 4\tau v^* \qquad (4.4.3)$$

$$v^* = \sum_i x_i v_{ij}^* \qquad (4.4.4)$$

$$v_{ij}^* = \frac{N_A \sigma_{ij}^3 s_j}{2^{0.5}} \qquad (4.4.5)$$

Where σ_{ij} is defined as:

$$\sigma_{ij} = 0.5(\sigma_i + \sigma_j) \qquad (4.4.6)$$

N_A is Avogadro's number, 6.023×10^{23}, and $\tau = 0.7405$.

$$a_m = \sum_i \sum_j x_i x_j v_{ij}^* \left[\exp\left(\frac{T_i^*}{2T}\right) - 1\right] \qquad (4.4.7)$$

83

$$T_j^* = \frac{\sum_i x_i c_i T_{ij}^*}{\sum_i x_i c_i}$$ (4.4.8)

$$T_{ij}^* = \frac{\in_{ij} q_i}{c_i k}$$ (4.4.9)

$$\in_{ij} = (1 - k_{ij})(\in_i \in_j)^{0.5}$$ (4.4.10)

k is Boltzmann's constant 1.381e-23 J/K and k_{ij} is the binary interaction coefficient that may be adjusted to fit the EOS to the published data.

The PHCT and hence the SPHC and CSPHC EOS employ the principle that the properties of chainlike and large molecules can be evaluated more accurately by considering segmental and rather than molecular interactions. In a mixture, a small molecule will only 'see' a part of a large chainlike molecule and will not experience interaction with the entire molecule. A chainlike molecule is therefore divided into s_i number of segments with σ_i being the diameter of a segment. The segmental interactions are represented by a square well potential function with $\in_i^*$ being the potential well depth. The intermolecular interaction energy is then equal to $\in_i * s_i$. This energy can also be defined as $\in_i q_i$, where $\in_i$ is the characteristic energy per unit external surface area and q_i is the external surface area of the molecule (Kim et al., 1986).

The optimum values for v_i^*, T_i^* and c_i are determined by fitting the equation of state to the pure component data. Wang and Guo found that the energy and size parameters ($\in_i$ and σ_i) could be determined from $\in_i/k = 59.9$ K and $N_A\sigma_i^3/2^{0.5} = 0.009232$ L/mol for n-alkanes and $\in_i/k = 123.3$ K and $N_A\sigma_i^3/2^{0.5} = 0.009940$ L/mol for CO_2 (Wang & Guo, 1993).

4.5 MODELLING THE MEASURED PHASE EQUILIBRIUM DATA

The predictive ability of the various equations of state to represent the measured phase equilibrium data of the supercritical solvent – n-alkane mixtures is very poor. The EOS were therefore fitted to the data by modifying the binary interaction parameters in the equation of state mixing rules.

As the interaction parameters are used to reduce the difference between the model predictions and the actual values, a smaller interaction parameter indicates a better inherent ability of the equation of state to represent the data.

4.5.1 Fitting the Van der Waals Type EOS

The Van der Waals type EOS, as used in this work, all have two binary interaction coefficients, k_{ij} and l_{ij}. There are several possible methods by which these parameters can be modified to fit the EOS to the experimental data.

Depending on which phase the most accurate data are needed for, the EOS may be fitted to either the heavy or lighter phase. Alternatively both phases may be fitted, for example by fitting the k_{ij} value to the lighter phase and the l_{ij} value to the heavy phase, weighting the interaction parameters by an arbitrary function or by even using different parameter values for the different phases (Brunner, 1994).

It should, however, be noted that while the interaction parameters do help to represent the data, they do not change the nature of the various equations of state. If an equation of state is fundamentally unable to represent the data, no combination of parameter values will be able to force an accurate fit of the experimental data.

It is also important to note that when more than two parameters are used the effects of the parameter values are not exclusive, and that various combinations of different values for the parameters may represent the data with virtually the same deviations.

A computer program developed by Crause (Crause, 2000) was used to fit the Van der Waals type EOS to the experimental data in this work. The fitting was done by repeatedly solving the flash algorithm with the various EOS at the various phase boundary pressures reported in section 3.4.4. The vapour and liquid equilibrium compositions determined at each pressure were then compared with the experimentally determined compositions. The total error for the whole system was determined by one of three error functions:

The sum of the absolute error:

$$\sum \left(w_l \left| x_{\exp t} - x_{calc} \right| + w_v \left| y_{\exp t} - y_{calc} \right| \right) \qquad (4.5.1)$$

The sum of the error fraction:

$$\sum\left(w_l \left| \frac{x_{expt} - x_{calc}}{(x_{expt} + x_{calc})/2} \right| + w_v \left| \frac{y_{expt} - y_{calc}}{(y_{expt} + y_{calc})/2} \right| \right) \tag{4.5.2}$$

The sum of the relative squared error:

$$\sum\left(w_l \left(\frac{x_{expt} - x_{calc}}{x_{expt}} \right)^2 + w_v \left(\frac{y_{expt} - y_{calc}}{y_{expt}} \right)^2 \right) \tag{4.5.3}$$

Where w_l and w_v are weights assigned by the user to the errors in the vapour and liquid phase prediction. It is therefore possible for the user to fit the EOS more to the one phase than the to other.

The EOS is fitted to the data by changing the interaction parameters in order to reduce the calculated error. In the program, the maximum absolute value that the interaction parameters may attain was set at 0.15. The any equation that needs an interaction parameter greater than this value in order to fit the equilibrium data, is considered to be unsuitable to model the system (Crause, 2000).

In some cases, it was found that a better fit of the experimental data could be achieved by manually changing the interaction parameters in the program and not relying on any of error reduction procedures. This can be attributed to the fact that due to the nature of the flash algorithm the program is only able to reduce the error in the liquid and vapour phase concentrations predictions at a specific pressure, where as by manually fitting the data it is possible to reduce the total area between the predicted and experimental phase boundary curve.

4.5.2   Fitting the Cubic Simplified Perturbed Hard-Chain Equation of State

As seen in section 4.4.1, the CSPHC EOS only has one binary interaction parameter. It is therefore a much simpler task to find the optimum k_{ij} value.

The CSPHC EOS was fitted manually to the experimental phase equilibrium data. By comparing the phase boundary plot generated by the EOS to the experimentally determined

plot it was a simple task to reduce the error visually. A computer program developed by Nieuwoudt (Nieuwoudt, 1994) was used to execute the repeated flash algorithms in order to generate a phase boundary diagram at the same temperature as the experimentally determined diagram. The interaction parameter was then manually changed until the area between the experimental and calculated boundary plots had been minimized.

4.6 MODELLING OF EXPERIMENTAL DATA

The Soave-Redlich-Kwong, Modified Peng Robinson, the Patel Teja and the Cubic Simplified Perturbed Hard-Chain Equations of State were used to model the experimental data discussed in section 3.4.4. Because of the differences in the chemical properties of the solvents and in the types of phase behaviour exhibited by the two solvent systems, the modelling of the supercritical CO_2 and ethane systems will be discussed individually.

The ability of the EOS to model the data must be evaluated according to the following criteria:

- The primary criterion is the ability of the EOS to fit the experimental data.
- The size of the interaction parameters. A smaller interaction parameter indicates a better inherent ability to represent the system.
- The ease with which the interaction parameters can be correlated and used to predict parameters for use at other temperatures or with other systems. Traditionally it has been reported that the interaction parameters are independent of temperature, pressure and concentration, but many researchers have reported interaction parameter temperature dependencies (McHugh & Krukonis, 1994; Nieuwoudt, 1994; Kordas et al., 1994). In the past, researchers have developed general interaction coefficient correlations based on the dependence on the alkane acentric factor and the operating temperature.

87

4.6.1 CO_2 – n-Alkane Systems

Representation of the experimental data

It was found that the CPHC equation was unable to model the supercritical CO_2 – n-alkane systems.
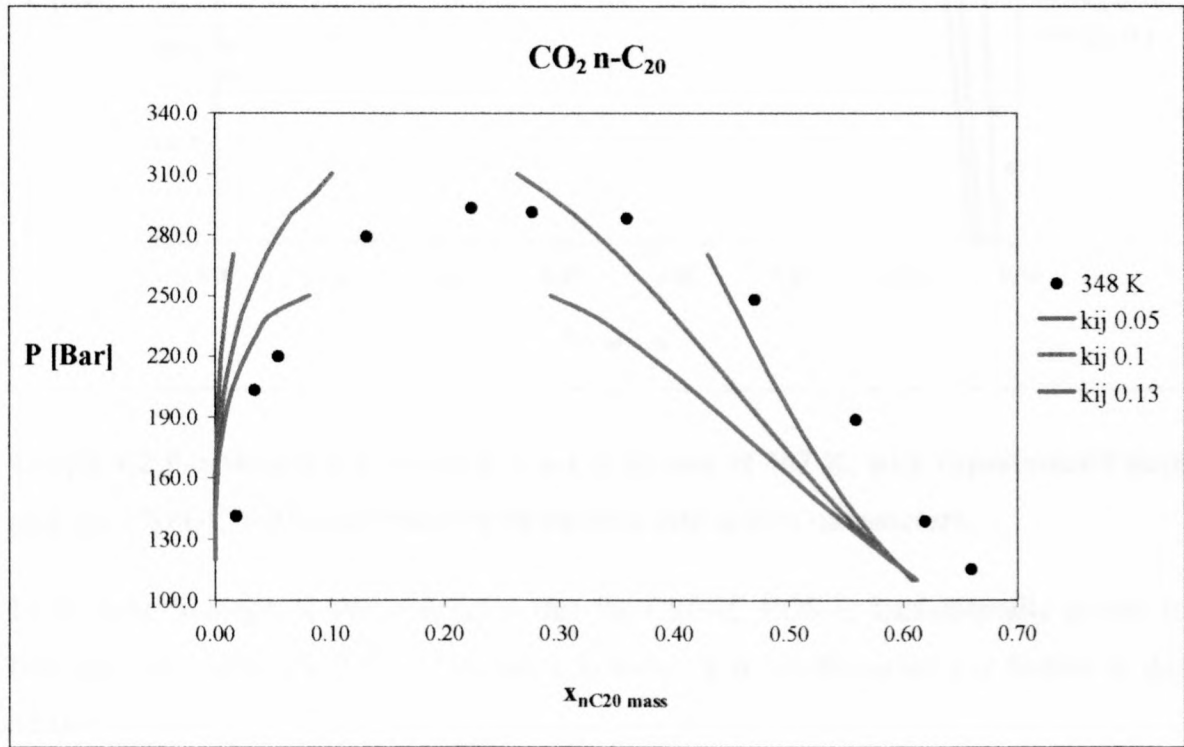
Graph 4-1 P-x Diagram of the CO_2 – n-C_{20} system at 348 K, with experimental data and the CSPHC EOS predictions with various interaction parameters.

It is obvious from the shape of the phase boundaries in Graph 4-1, that the CSPHC EOS predicts a different phase boundary trend than that was determined experimentally. No value of the interaction parameter will force the EOS to fit the data. The failure of the EOS to predict the phase behaviour of the CO_2 – n-alkane systems was also observed in the higher carbon number systems, where it was relatively easy to fit the other EOS to the data. In the CO_2 – n-C_{36} system the CSPHC EOS predicts solubility of virtually zero for the heavy alkane in the solute, even at high pressures. See Graph 4-2.
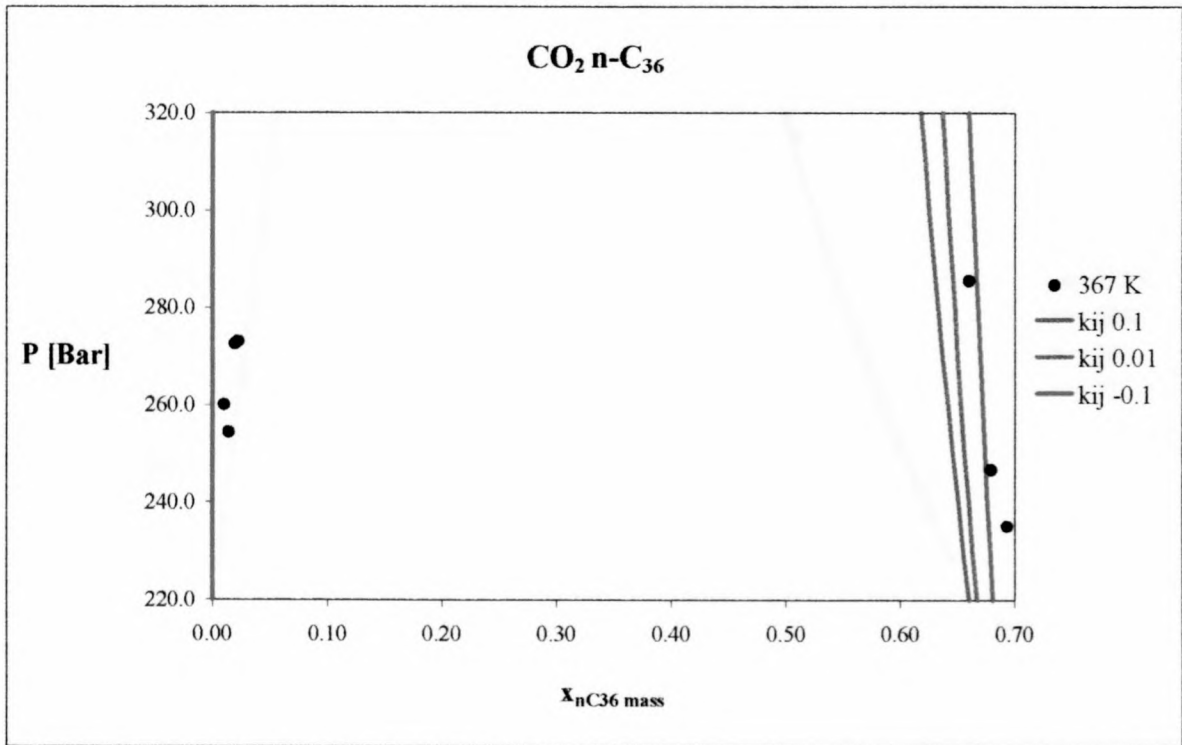
Graph 4-2 P-x Diagram of the CO_2 – n-C_{28} system at 367 K, with experimental data and the CSPHC EOS predictions with various interaction parameters.

From these findings, it was concluded that the CSPHC EOS is fundamentally unable to represent the supercritical CO_2 – n-alkane systems. It is not discussed any further in this section.

As mentioned above, it was found that it was a relatively simple task to fit the equations of state to the experimental data in the regions far away from the mixture critical point. The phase boundaries of the systems CO_2 – nC_{24} to CO_2 – nC_{36} were measured at pressures far below the mixture critical pressure, and it can be seen from Graph 4-3 that all of the EOS provide a virtually identical fit of the experimental data.

However, with the systems where the mixture critical point was reached, it was obvious that the models are not able to represent the data with a high degree of accuracy in this region. In Graph 4-4 it appears as if the PT EOS provides the best fit of the CO_2 – n-C_{20} system at 339K. At this temperature the SRK EOS does not predict a mixture critical point at all. The PR EOS on the other hand is able to represent the mixture critical pressure, but is very inaccurate in its prediction of the liquid phase compositions.

89
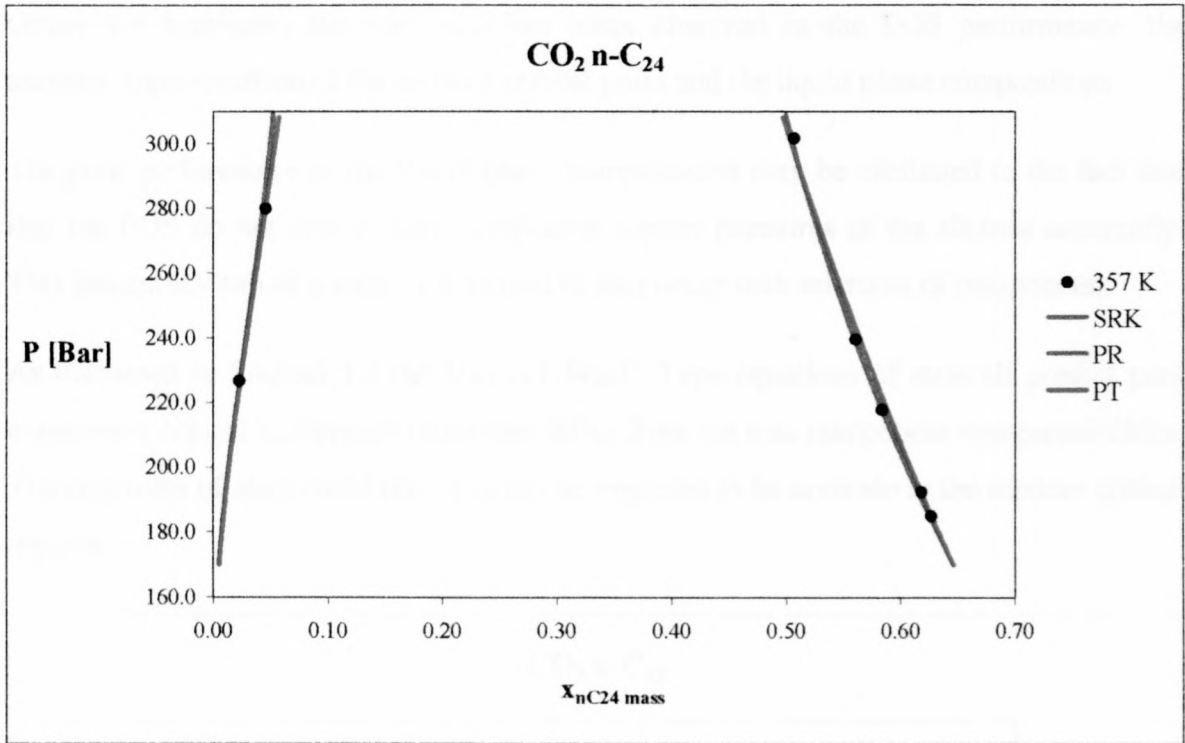
Graph 4-3 P-x Diagram of the CO_2 – n-C_{24} system at 357 K with : SRK k_{ij} 0.102, l_{ij} 0.0766; PR k_{ij} 0.0899, l_{ij} 0.0928; PT k_{ij} 0.0447, l_{ij} 0.15
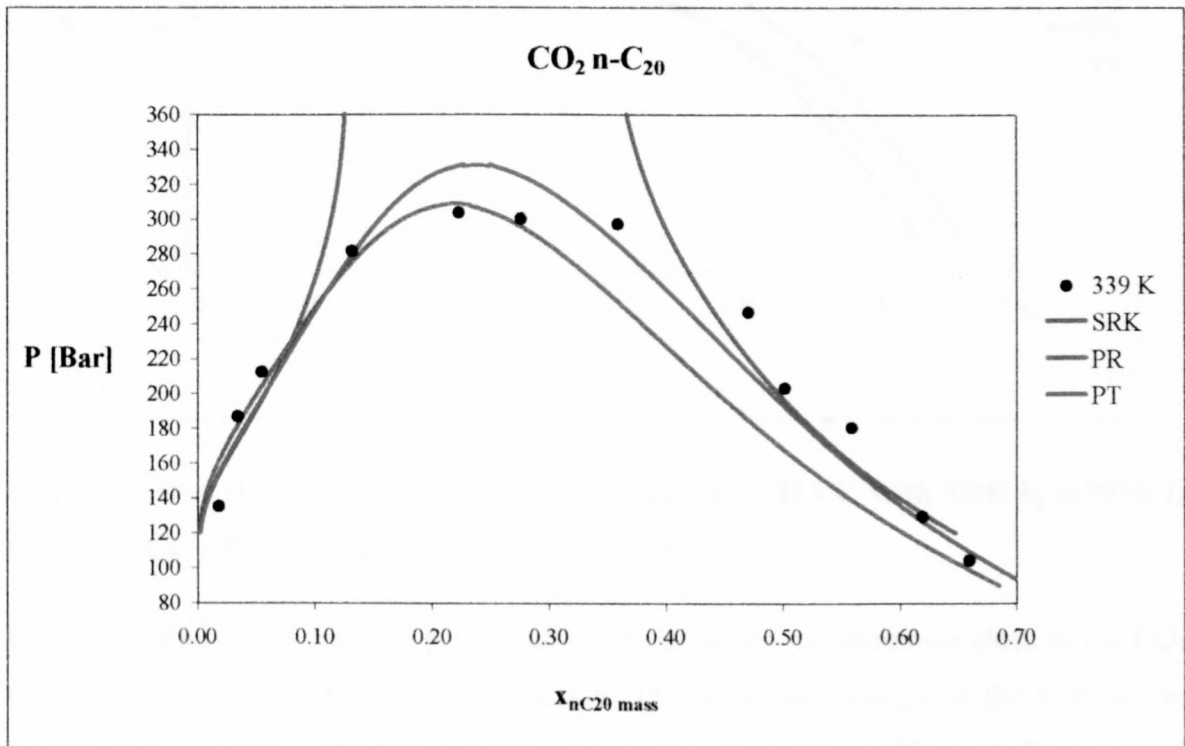
Graph 4-4 P-x Diagram of the CO_2 – n-C_{20} system at 339 K with SRK k_{ij} 0.0979, l_{ij} 0.0562; PR k_{ij} 0.082, l_{ij} 0.12; PT k_{ij} 0.0459, l_{ij} 0.12

Graph 4-4 highlights the main problem areas observed in the EOS performance: the accurate representation of the mixture critical point and the liquid phase compositions.

The poor performance in the liquid phase compositions may be attributed to the fact that that the EOS do not predict pure component vapour pressures of the alkanes accurately. This inaccuracy can of course be expected to also occur with mixtures of components.

As discussed in Section 4.3 the Van der Waals Type equations of state all predict pure component critical compressibilities that differ from the true component compressibilities. The equations of state could therefore not be expected to be accurate in the mixture critical regions.
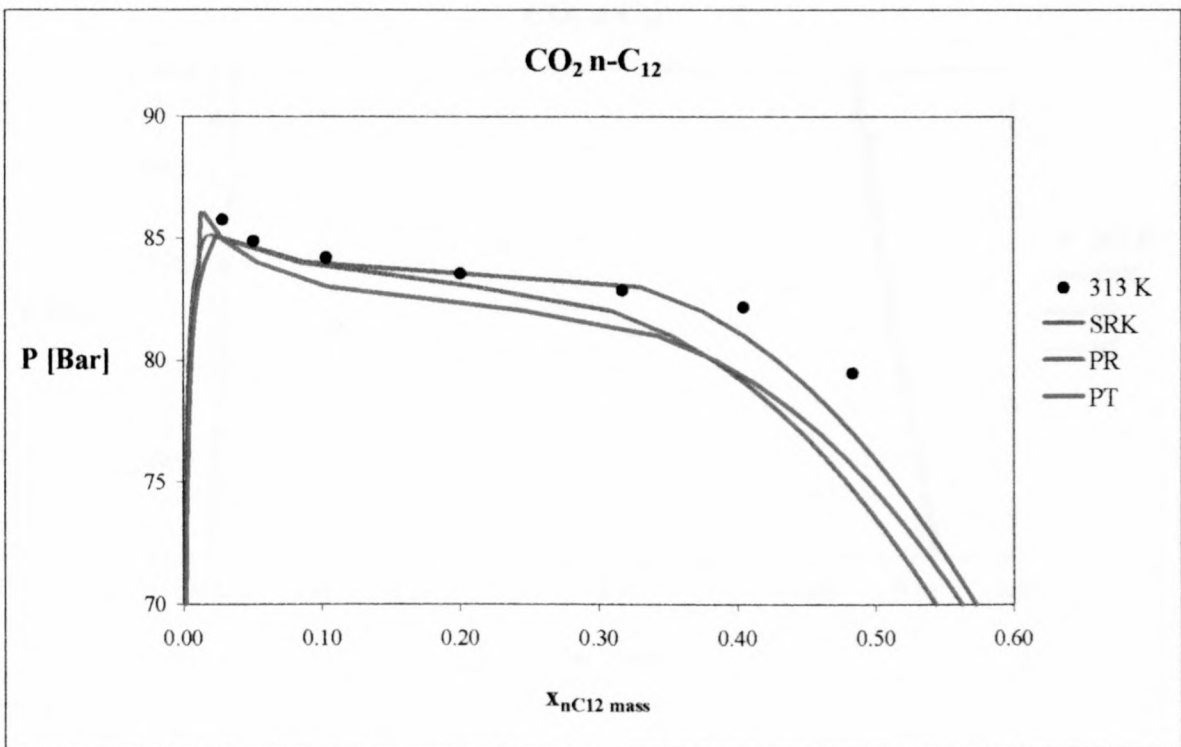
Graph 4-5 P-x Diagram of the CO_2 – n-C_{12} system at 313 K with SRK k_{ij} 0.0976, l_{ij} 0.0269; PR k_{ij} 0.082, l_{ij} 0.039; PT k_{ij} 0.055, l_{ij} 0.025

It was also found that the EOS performed poorly at system temperatures close to the CO_2 critical temperature of 304K. See Graph 4-5. The poor performance of the EOS at the temperatures near the solvent T_c is as a direct consequence of the EOS's inability to model the pure component critical points

The performance of the various equations of state in modelling the experimental data can be summarised as follows:

- $CO_2 - n\text{-}C_{36}$ *System:*

The phase boundaries of this system were determined in a region well away from the mixture critical point. Virtually no difference in the performance of the various EOS could be observed. See Graph 4-6. It was, however, found that none of the EOS predicted the type IV phase behaviour observed at the low heavy-component concentrations of this system. See Graph 4-7 and the discussion of the $CO_2 - n\text{-}C_{36}$ system in section 3.4.4.
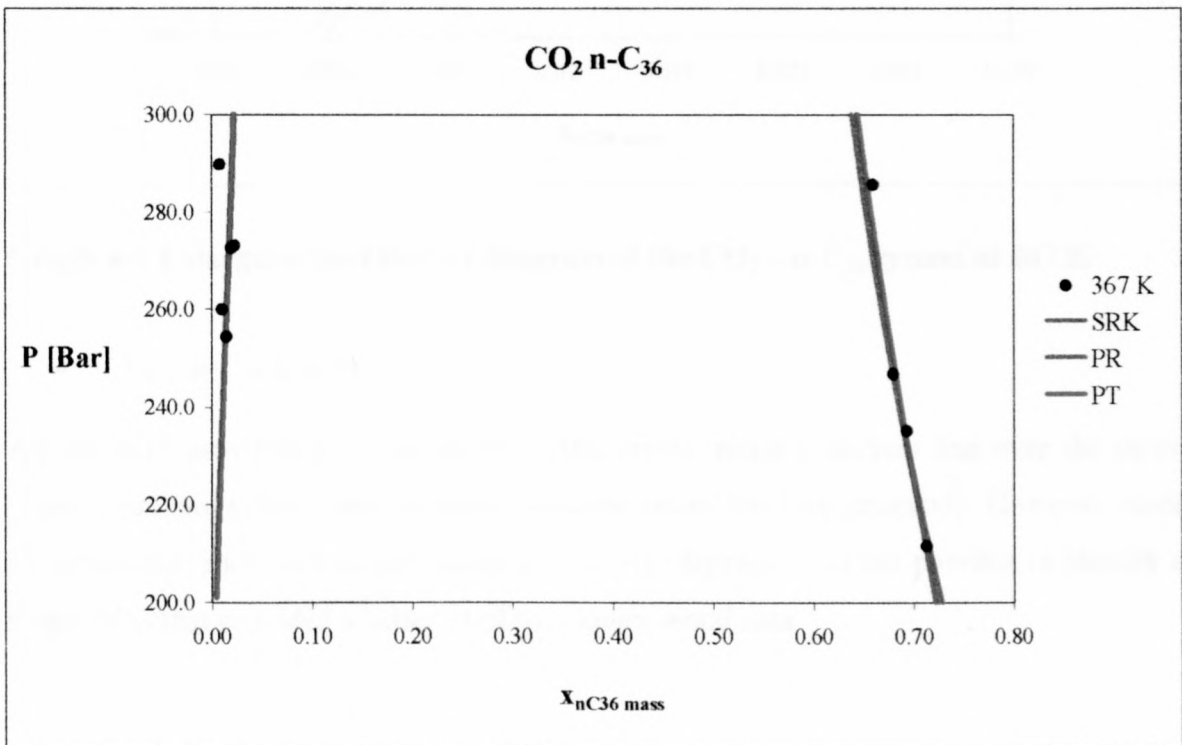
Graph 4-6 P-x Diagram of the $CO_2 - n\text{-}C_{36}$ system at 367 K with SRK k_{ij} 0.0858, l_{ij} 0.0185; PR k_{ij} 0.07, l_{ij} 0.04; PT k_{ij} 0.0193, l_{ij} 0.125
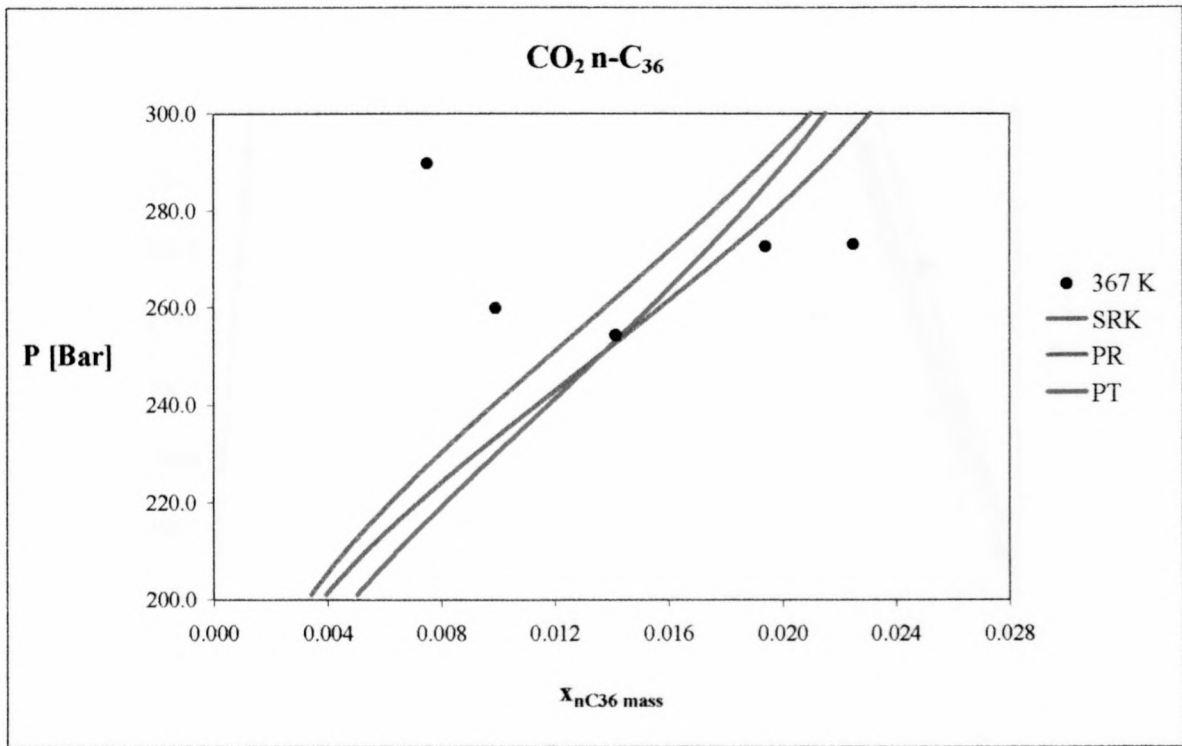
Graph 4-7 Enlargement of the P-x Diagram of the CO_2 – n-C_{36} system at 367 K

- *CO_2 – n-C_{28} System*

All the EOS provided an excellent fit of the vapour phase boundary line over the entire temperature range, but fitted the liquid phase boundary line less accurately. However, since all the models showed this inaccuracy to a similar degree it was not possible to identify a single EOS that provided a better fit of the experimental data.
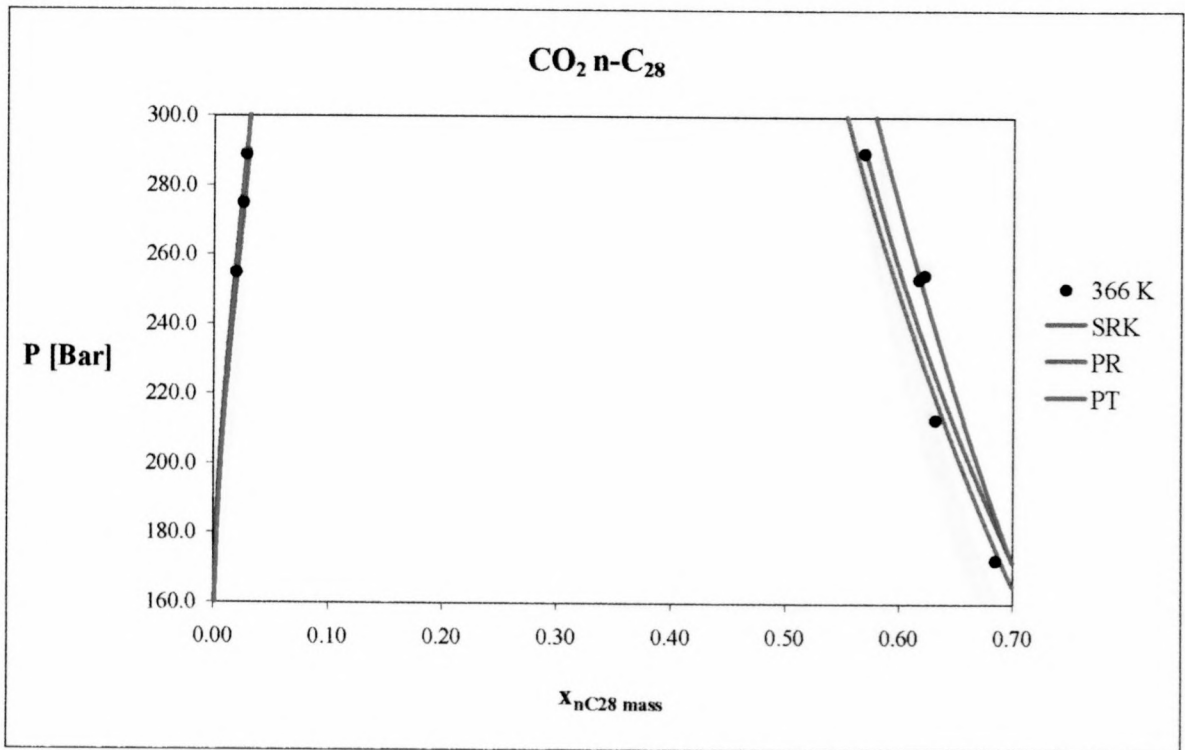
Graph 4-8 P-x Diagram of the CO_2 – n-C_{28} system at 366 K with SRK k_{ij} 0.0968, l_{ij} 0.0598; PR k_{ij} 0.083, l_{ij} 0.09; PT k_{ij} 0.0382, l_{ij} 0.15
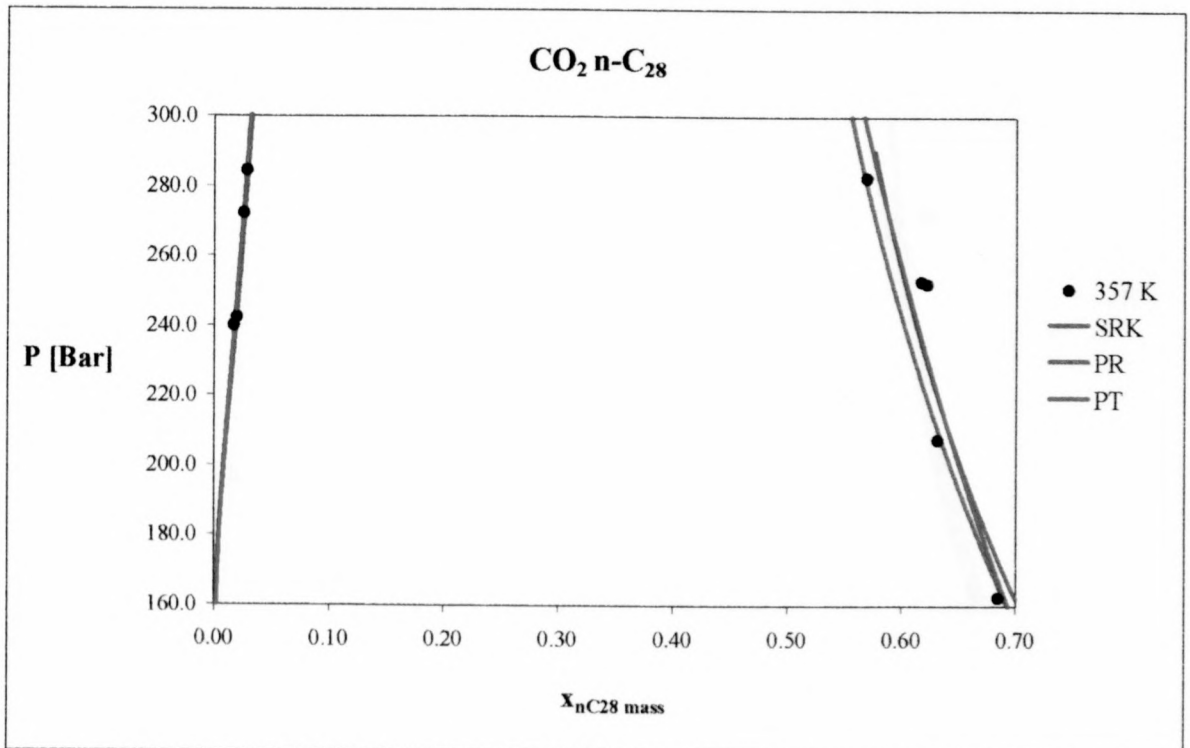
Graph 4-9 P-x Diagram of the CO_2 – n-C_{28} system at 357 K with SRK k_{ij} 0.0981, l_{ij} 0.0557; PR k_{ij} 0.083, l_{ij} 0.08; PT k_{ij} 0.0381, l_{ij} 0.15
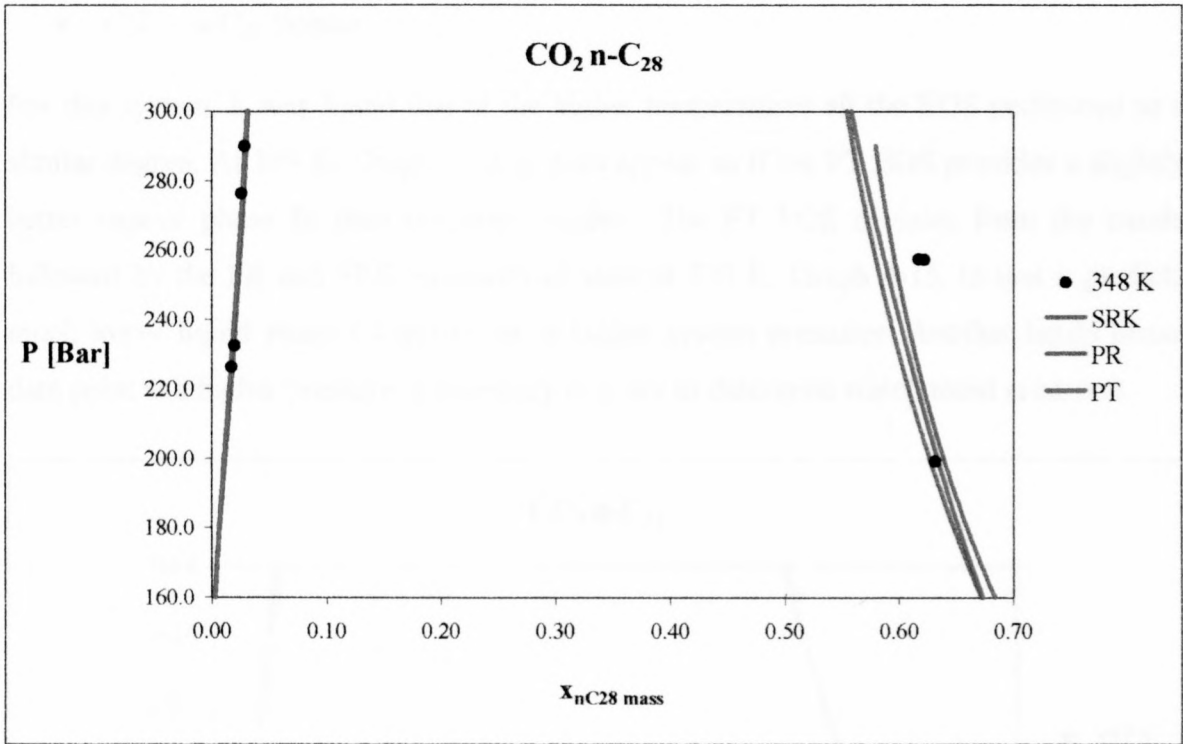
Graph 4-10 P-x Diagram of the CO_2 – n-C_{28} system at 348 K with SRK k_{ij} 0.0981, l_{ij} 0.0557; PR k_{ij} 0.083, l_{ij} 0.08; PT k_{ij} 0.0382, l_{ij} 0.15
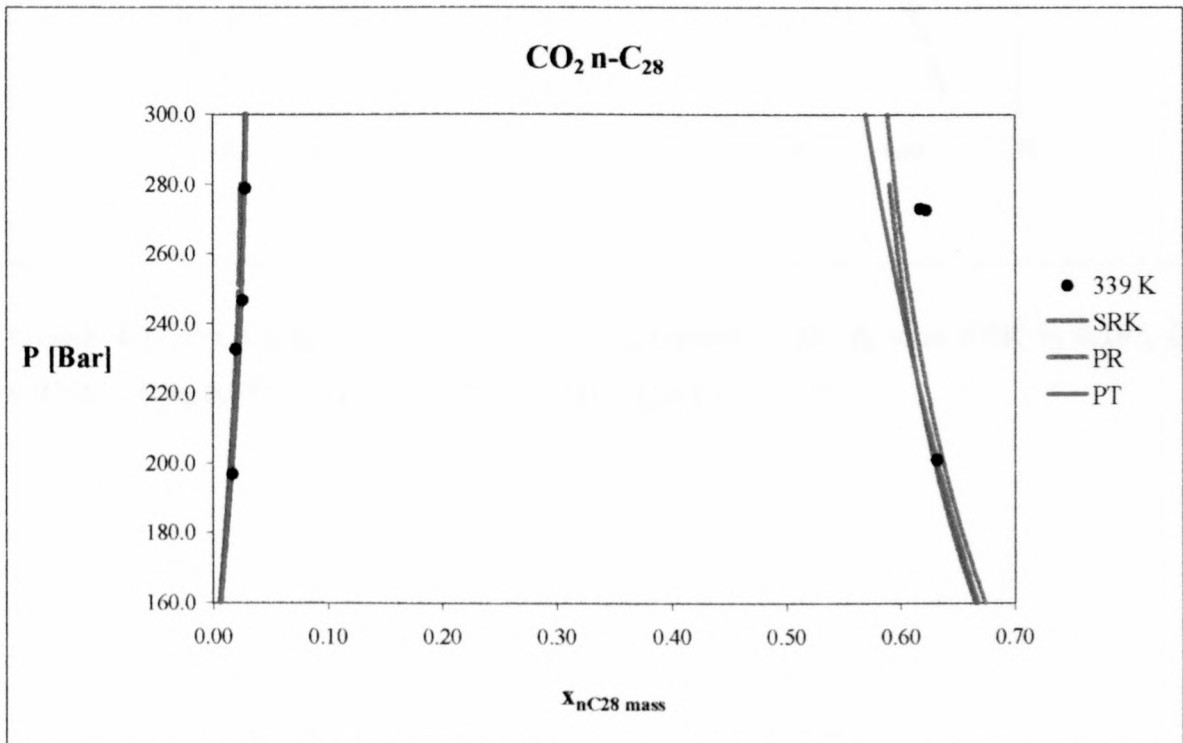
Graph 4-11 P-x Diagram of the CO_2 – n-C_{28} system at 339 K with SRK k_{ij} 0.0981, l_{ij} 0.0557; PR k_{ij} 0.081, l_{ij} 0.05; PT k_{ij} 0.034, l_{ij} 0.12

- *$CO_2 - n\text{-}C_{24}$ System*

For this system, it was found that at the higher temperatures all the EOS performed to a similar degree. At 339 K, Graph 4-14, it does appear as if the PT EOS provides a slightly better vapour phase fit than the other models. The PT EOS deviates from the trends followed by the PR and SRK equations of state at 330 K, Graph 4-15, in that it predicts much lower liquid phase compositions at higher system pressures. Another liquid phase data point at a higher pressure is necessary in order to determine which trend is correct.
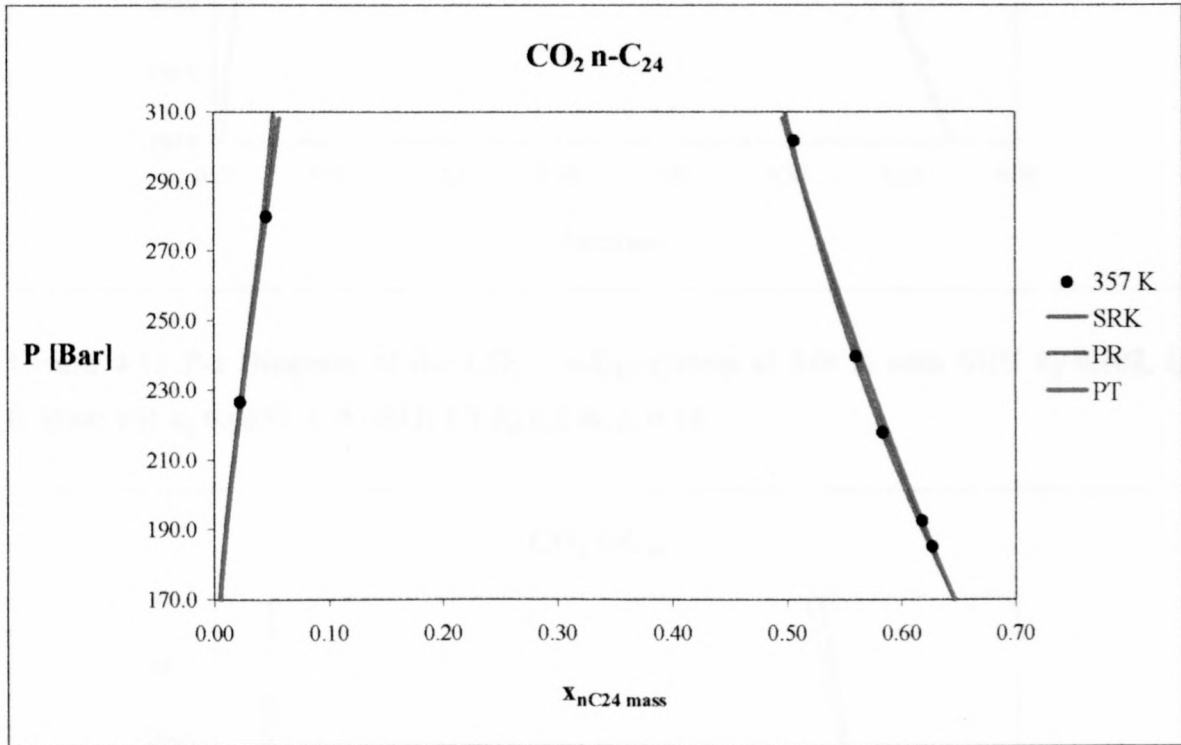
Graph 4-12 P-x Diagram of the $CO_2 - n\text{-}C_{24}$ system at 357 K with SRK k_{ij} 0.102, l_{ij} 0.0766; PR k_{ij} 0.0899, l_{ij} 0.0925; PT k_{ij} 0.0447, l_{ij} 0.15
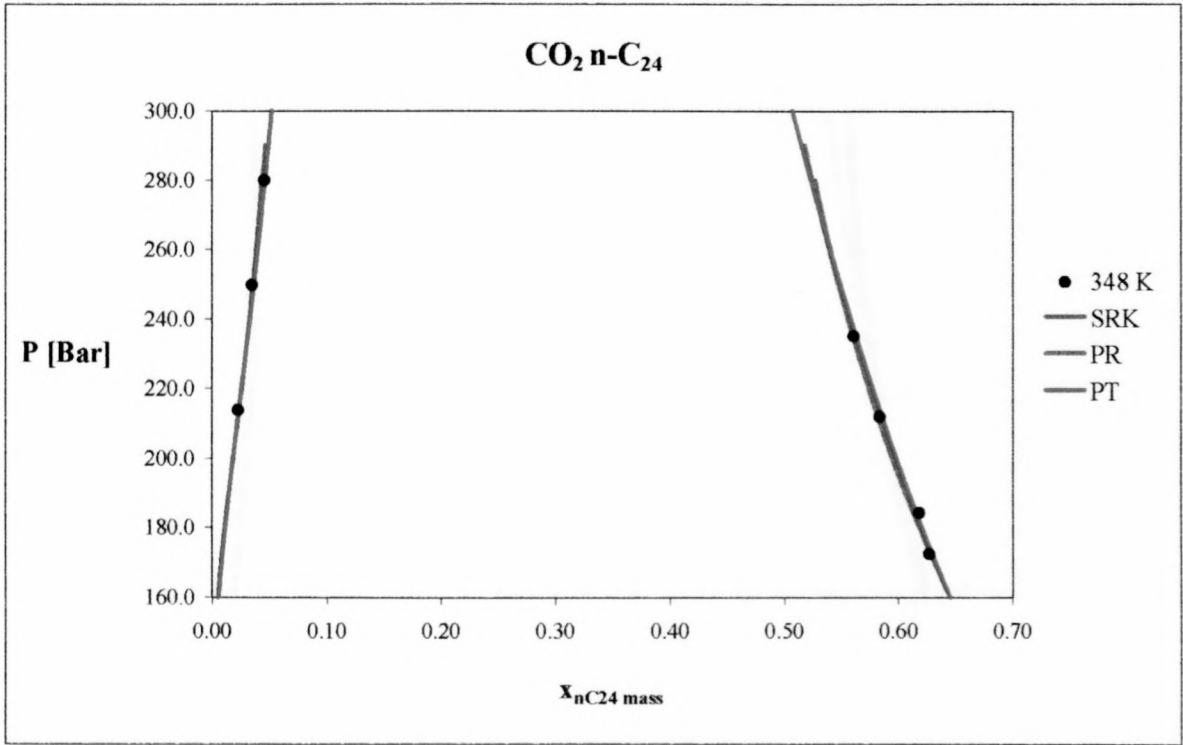
Graph 4-13 P-x Diagram of the CO_2 – n-C_{24} system at 348 K with SRK k_{ij} 0.102, l_{ij} 0.0694; PR k_{ij} 0.0895, l_{ij} 0.0832; PT k_{ij} 0.046, l_{ij} 0.14
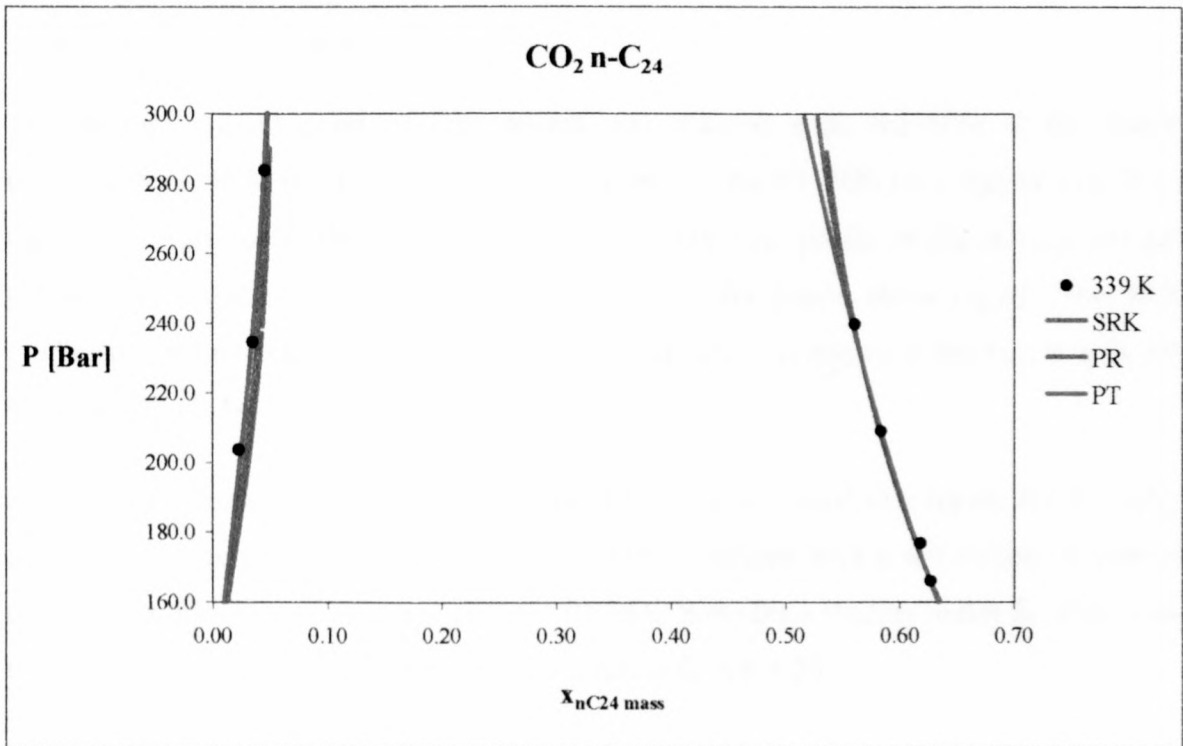
Graph 4-14 P-x Diagram of the CO_2 – n-C_{24} system at 339 K with SRK k_{ij} 0.097, l_{ij} 0.0375; PR k_{ij} 0.0858, l_{ij} 0.0585; PT k_{ij} 0.0459, l_{ij} 0.125
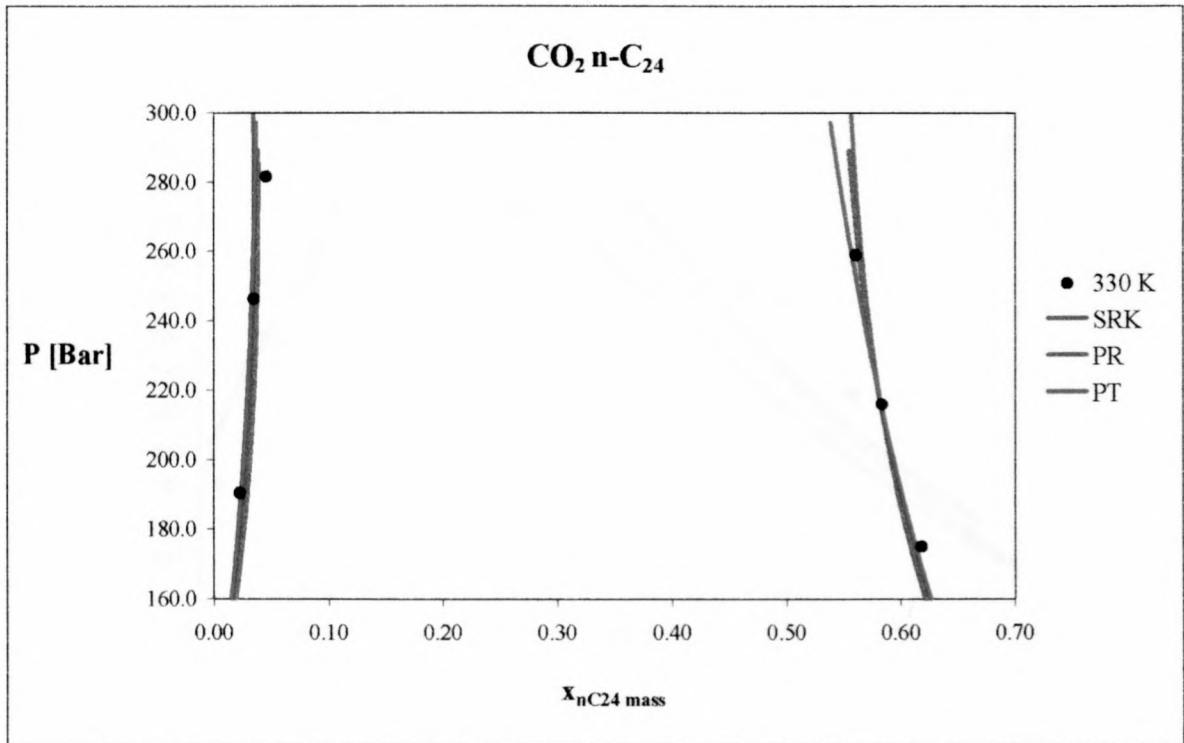
Graph 4-15 P-x Diagram of the CO_2 – n-C_{24} system at 330 K with SRK k_{ij} 0.101, l_{ij} 0.0494; PR k_{ij} 0.0852, l_{ij} 0.0499; PT k_{ij} 0.0470, l_{ij} 0.119

- *CO_2 – n-C_{20} System*

The mixture critical point of this system was reached experimentally at the higher temperatures, 348 K and 339 K. At these temperatures, the PT EOS provided the best fit of the data. It was found that even though the PT EOS over-predicted the mixture critical pressure it was more accurate than the PR EOS in the liquid phase region. The SRK predicted a completely different type of phase behaviour at higher pressures. See Graph 4-16 and Graph 4-17.

At the lower temperatures, the experimental data were measured in a region further away from the mixture critical point, here all the EOS preformed with a satisfactory degree of accuracy. It does however appear as if the PT EOS provides a slightly better fit of the data than the other two EOS. See Graph 4-18 through to Graph 4-20.
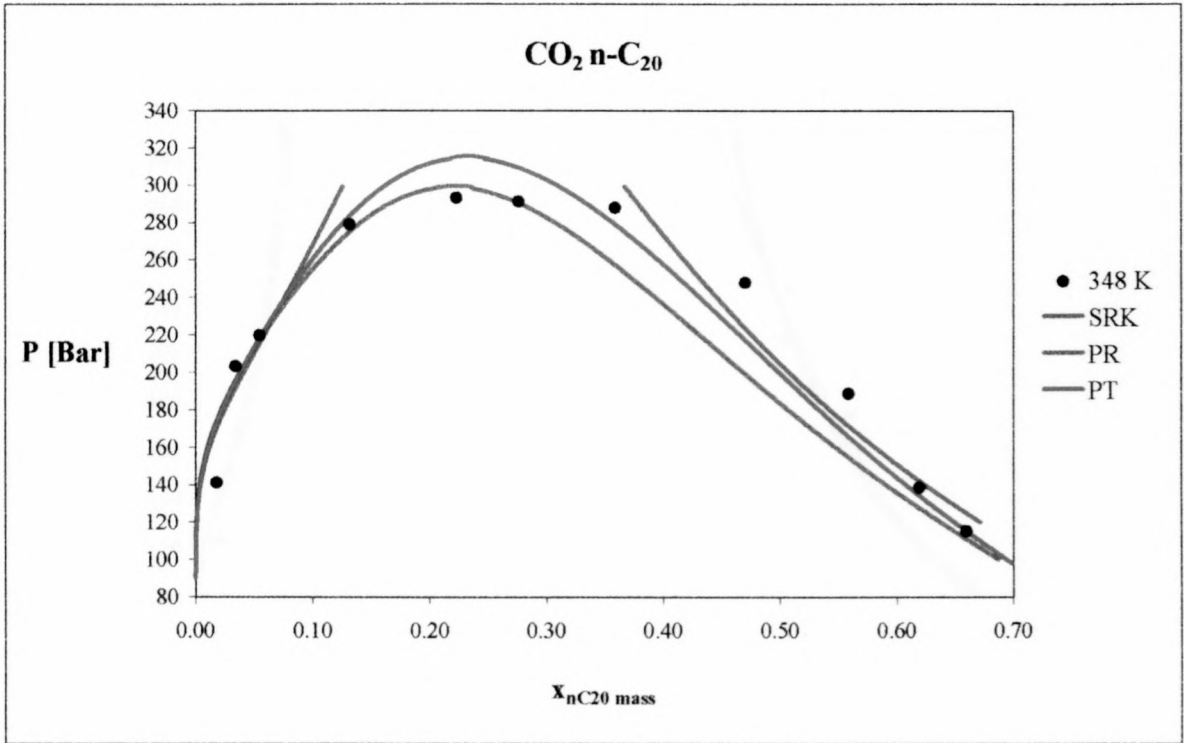
Graph 4-16 P-x Diagram of the CO_2 – n-C_{20} system at 348 K with SRK k_{ij} 0.0979, l_{ij} 0.0720; PR k_{ij} 0.0798, l_{ij} 0.1195, PT k_{ij} 0.0449, l_{ij} 0.149
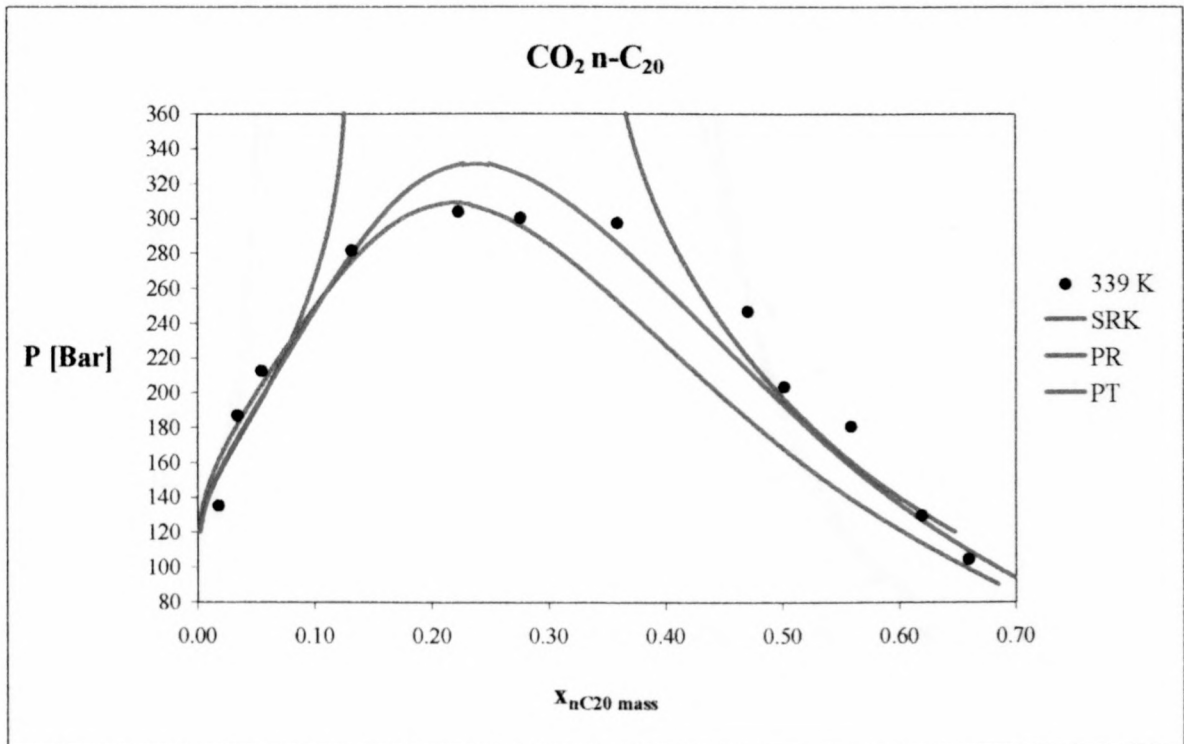
Graph 4-17 P-x Diagram of the CO_2 – n-C_{20} system at 339 K with SRK k_{ij} 0.0979, l_{ij} 0.0562; PR k_{ij} 0.0820, l_{ij} 0.12, PT k_{ij} 0.0459, l_{ij} 0.12
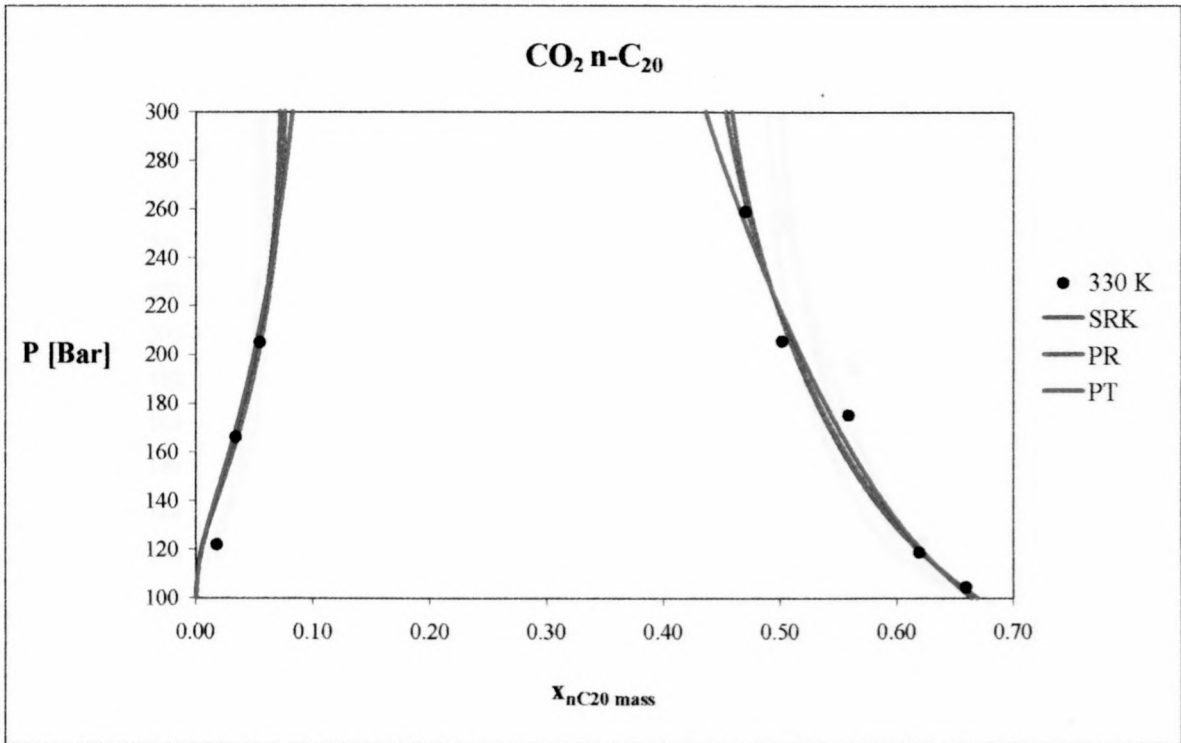
Graph 4-18 P-x Diagram of the CO_2 – n-C_{20} system at 330 K with SRK k_{ij} 0.104, l_{ij} 0.0646; PR k_{ij} 0.0922, l_{ij} 0.072, PT k_{ij} 0.0565, l_{ij} 0.115
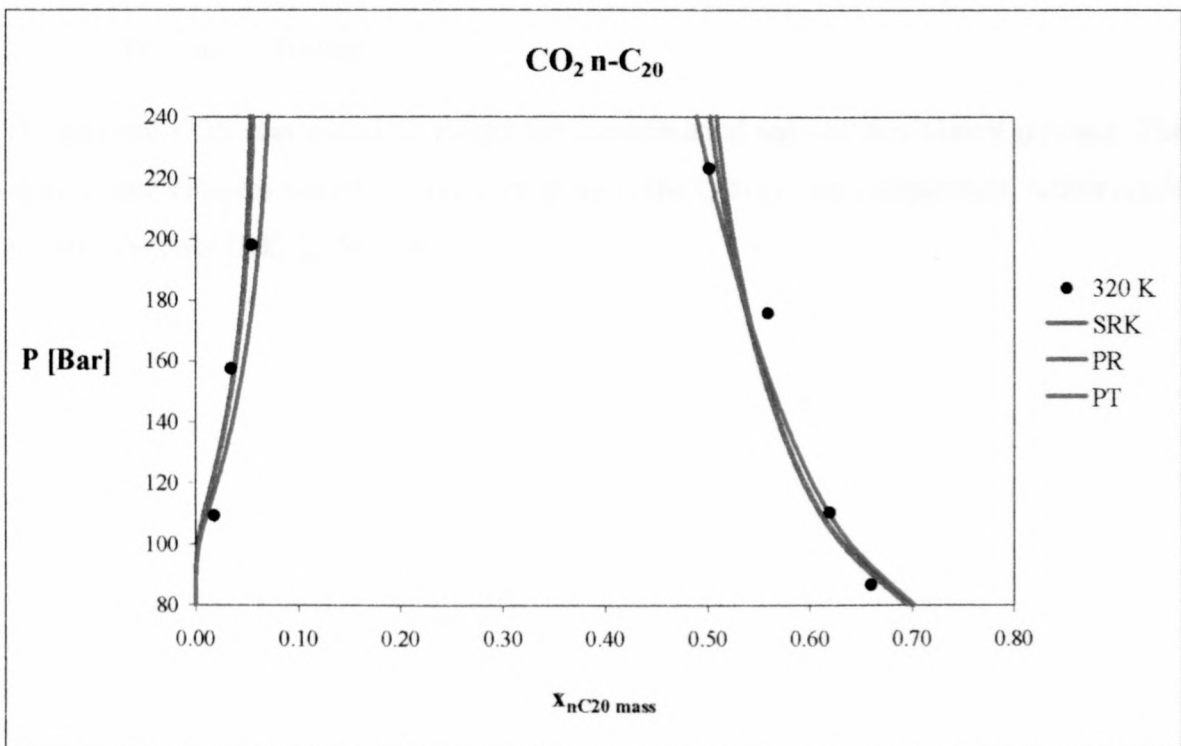
Graph 4-19 P-x Diagram of the CO_2 – n-C_{20} system at 320 K with SRK k_{ij} 0.105, l_{ij} 0.06; PR k_{ij} 0.0931, l_{ij} 0.0686, PT k_{ij} 0.049, l_{ij} 0.079
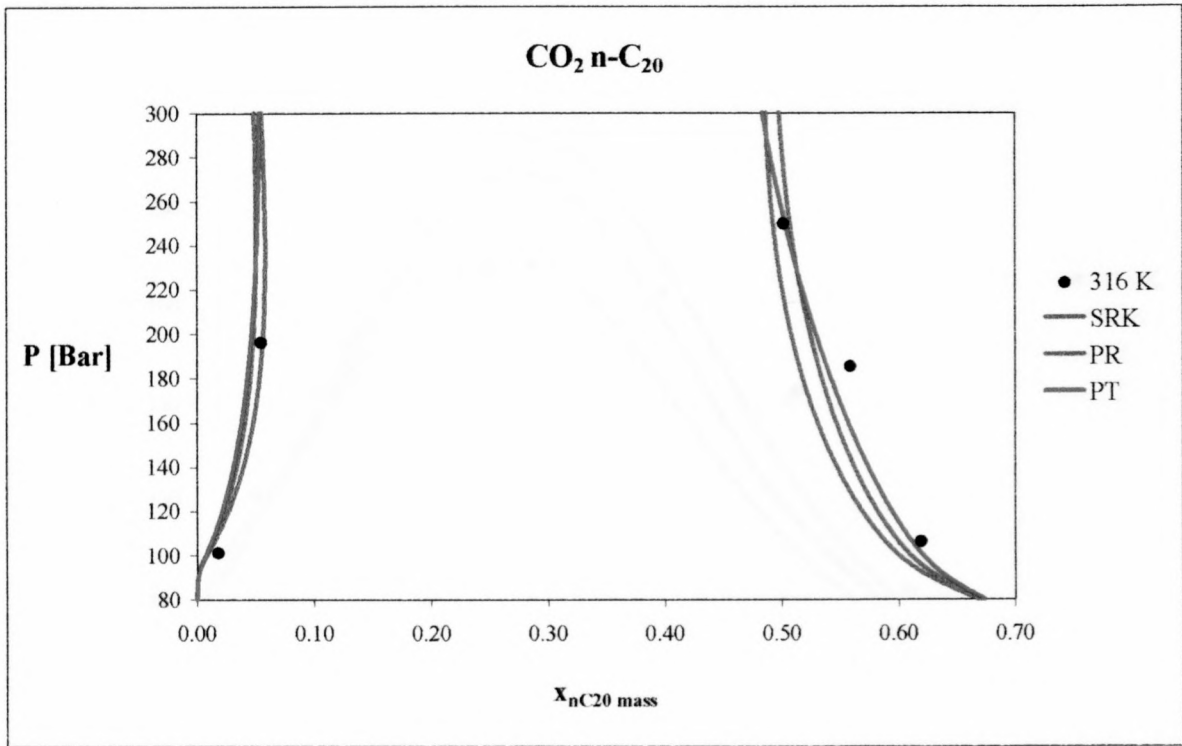
Graph 4-20 P-x Diagram of the CO_2 – n-C_{20} system at 316 K with SRK k_{ij} 0.1, l_{ij} 0.055; PR k_{ij} 0.0931, l_{ij} 0.0686, PT k_{ij} 0.0573, l_{ij} 0.098

- *CO_2 – n-C_{16} System*

No suitable EOS was found to model the experimental data of this binary mixture. The system temperatures were however very close to the CO_2 critical temperature, which could explain the poor EOS performance.
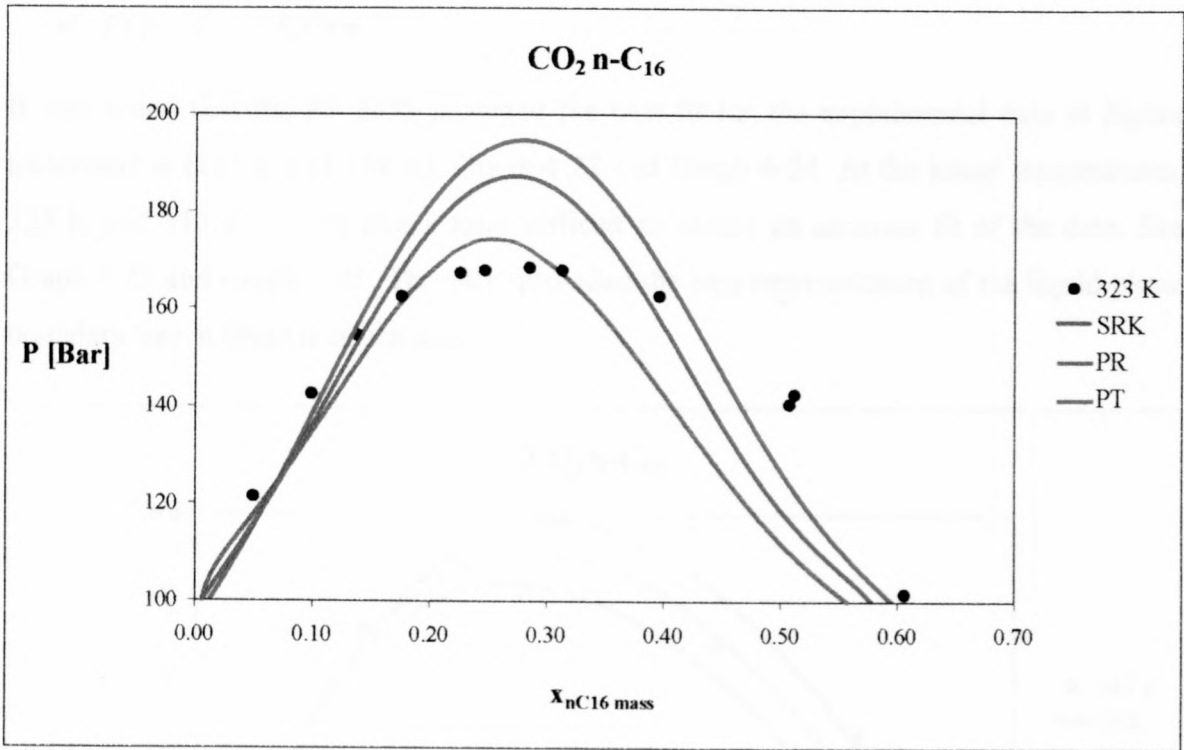
Graph 4-21 P-x Diagram of the CO_2 – n-C_{16} system at 323 K with SRK k_{ij} 0.094, l_{ij} 0.03; PR k_{ij} 0.084, l_{ij} 0.025, PT k_{ij} 0.052, l_{ij} 0.04
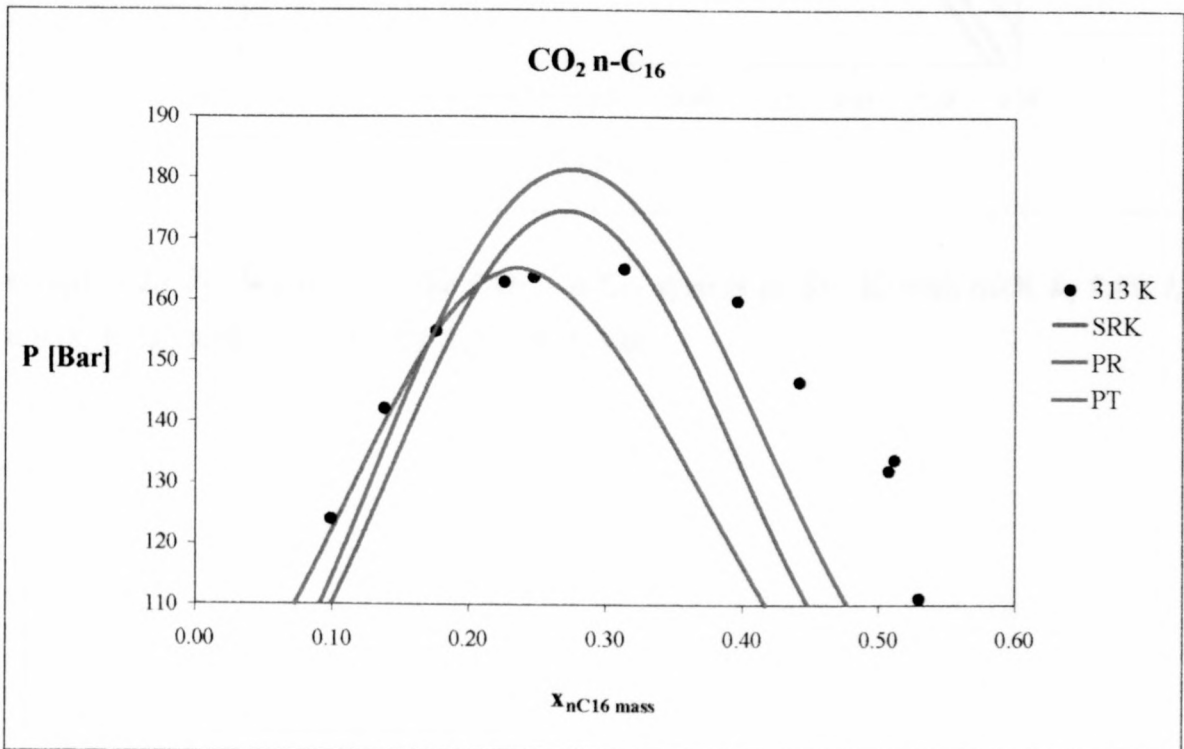
Graph 4-22 P-x Diagram of the CO_2 – n-C_{16} system at 313 K with SRK k_{ij} 0.0945, l_{ij} 0.07; PR k_{ij} 0.0815, l_{ij} 0.025, PT k_{ij} 0.05, l_{ij} 0.04

102

- $CO_2 - n\text{-}C_{12}$ *System*

It was found that the PR EOS provided the best fit for the experimental data at higher temperatures (333 K and 343 K). Graph 4-23 and Graph 4-24. At the lower temperatures, 323 K and 313 K, it was much more difficult to obtain an accurate fit of the data. See Graph 4-25 and Graph 4-26. The SRK provided the best representation of the liquid phase boundary line at these temperatures.
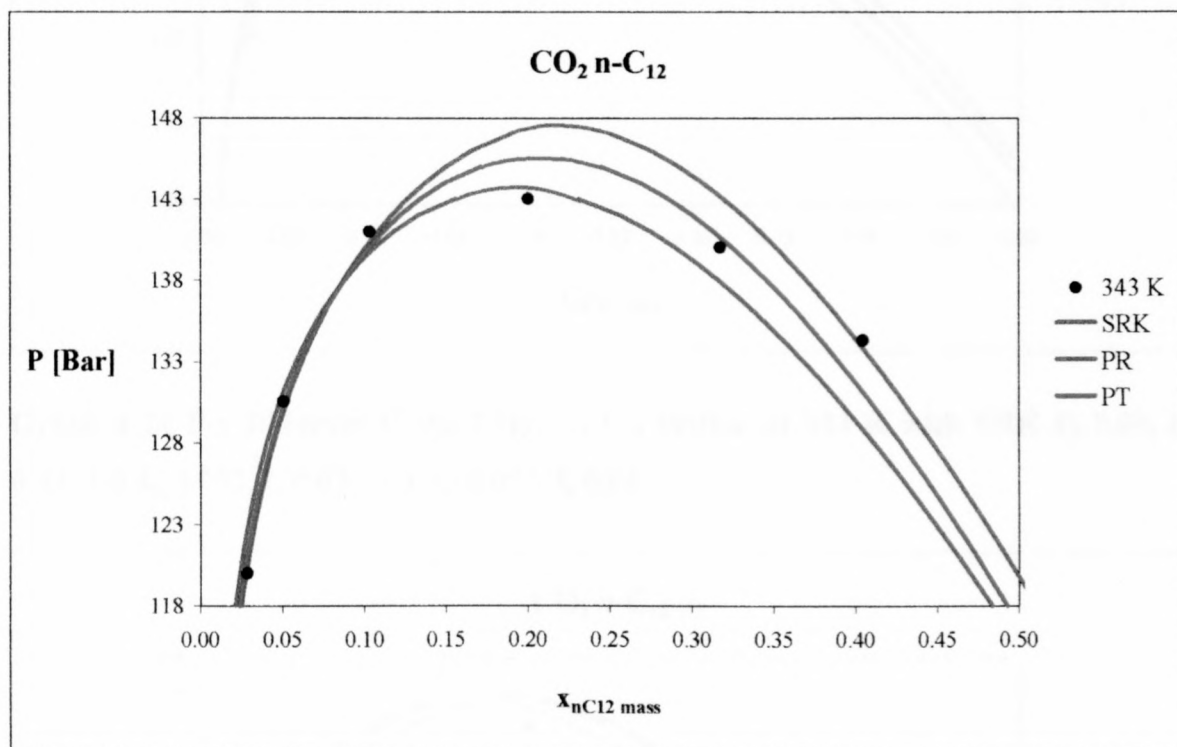
Graph 4-23 P-x Diagram of the CO_2 – n-C_{12} system at 343 K with SRK k_{ij} 0.09, l_{ij} 0.035; PR k_{ij} 0.087, l_{ij} 0.035, PT k_{ij} 0.058, l_{ij} 0.06
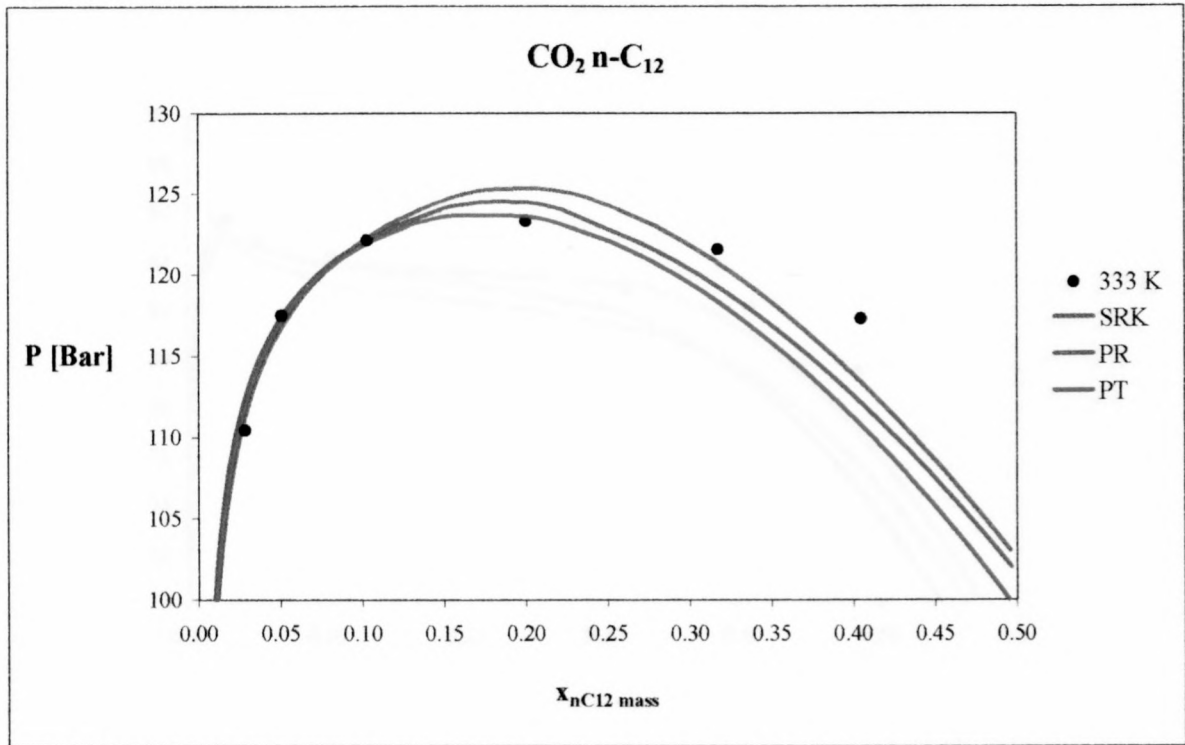
Graph 4-24 P-x Diagram of the CO_2 – n-C_{12} system at 333 K with SRK k_{ij} 0.09, l_{ij} 0.03; PR k_{ij} 0.082, l_{ij} 0.035, PT k_{ij} 0.052, l_{ij} 0.06
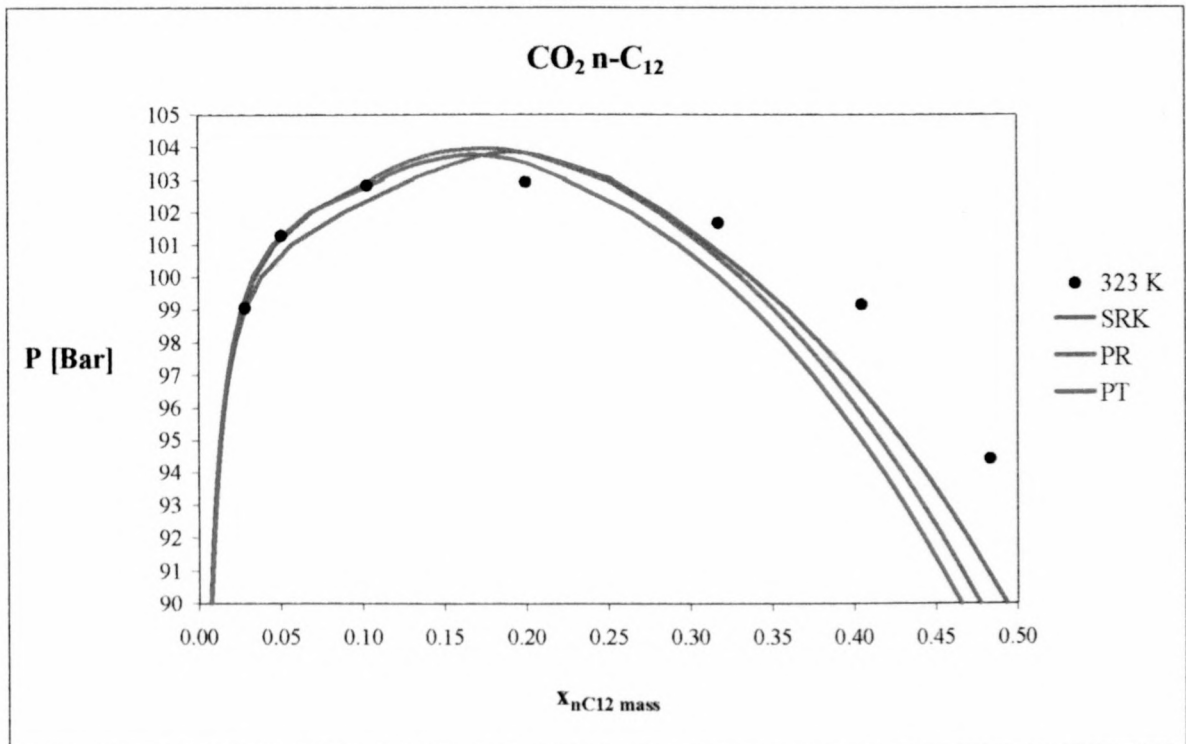
Graph 4-25 P-x Diagram of the CO_2 – n-C_{12} system at 323 K with SRK k_{ij} 0.094, l_{ij} 0.015; PR k_{ij} 0.082, l_{ij} 0.035, PT k_{ij} 0.056, l_{ij} 0.053
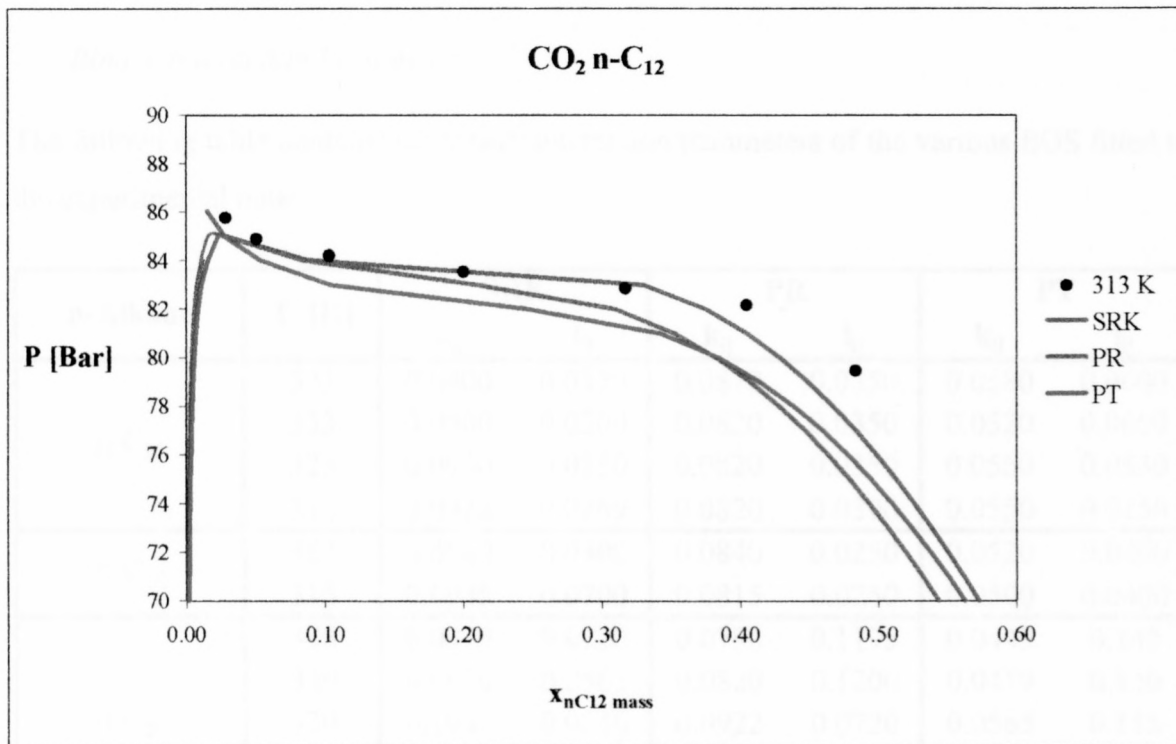
Graph 4-26 P-x Diagram of the CO₂ – n-C₁₂ system at 313 K with SRK k_{ij} 0.0976, l_{ij} 0.0269; PR k_{ij} 0.082, l_{ij} 0.039, PT k_{ij} 0.055, l_{ij} 0.025

Binary Interaction Parameters

The following table contains the binary interaction parameters of the various EOS fitted to the experimental data:

| n-Alkane	T [K]	SRK		PR		PT	
		k_{ij}	l_{ij}	k_{ij}	l_{ij}	k_{ij}	l_{ij}
n-C_{12}	343	0.0900	0.0350	0.0870	0.0350	0.0580	0.0600
	333	0.0900	0.0300	0.0820	0.0350	0.0520	0.0600
	323	0.0940	0.0150	0.0820	0.0350	0.0560	0.0530
	313	0.0976	0.0269	0.0820	0.0390	0.0550	0.0250
n-C_{16}	323	0.0940	0.0300	0.0840	0.0250	0.0520	0.0400
	313	0.0945	0.0700	0.0815	0.0250	0.0500	0.0400
n-C_{20}	348	0.0979	0.0720	0.0798	0.1195	0.0449	0.149
	339	0.0979	0.0562	0.0820	0.1200	0.0459	0.120
	330	0.1040	0.0646	0.0922	0.0720	0.0565	0.115
	321	0.1050	0.0600	0.0931	0.0686	0.0490	0.079
	314	0.1000	0.0550	0.0931	0.0686	0.0573	0.098
n-C_{24}	357	0.102	0.0766	0.0899	0.0925	0.0447	0.150
	348	0.102	0.0694	0.0895	0.0832	0.0460	0.140
	339	0.097	0.0375	0.0858	0.0585	0.0459	0.125
	330	0.101	0.0494	0.0852	0.0499	0.0470	0.119
n-C_{28}	366	0.0968	0.0598	0.0830	0.0900	0.0382	0.150
	357	0.0981	0.0557	0.0830	0.0800	0.0381	0.150
	348	0.0981	0.0557	0.0830	0.0800	0.0382	0.150
	339	0.0981	0.0557	0.0810	0.0500	0.0340	0.120
n-C_{36}	367	0.0858	0.0185	0.0700	0.0400	0.0193	0.126
	358	0.0898	0.0270	0.0700	0.0300	0.0221	0.119
	349	0.0799	-0.0021	0.0682	0.0222	0.0151	0.093
	344	0.0753	-0.0130	0.0652	0.0137	0.0115	0.081

Table 4-1 Interaction Parameters determined for the CO_2 – n-alkane Systems

It can be seen that the PT EOS generally has the smallest k_{ij} values for all the systems, followed by the PR and then the SRK EOS. The SRK l_{ij} values on the other hand are generally the smallest. It is striking that the PT EOS has much larger l_{ij} values than the other EOS. In fact the interaction parameter repeatedly reached the maximum value imposed by the program used to fit the data, and it is suspected that the parameters would even have been larger had they not been limited.

The large PT l_{ij} values are applied in the combining rules of both the b and c values. (Refer to sections 4.3.4 and 4.3.5). It is possible that the b and c values are not affected in a similar manner by the mixture components and that the same interaction parameter cannot be applied to both of them. Trying to force the l_{ij} to incorporate the component interactions for both b and c may have resulted in the large parameter values. This must however still be verified.

The PT k_{ij} interaction parameters were the only parameters where a clear carbon number effect could be discerned. The interaction parameters decrease with an increase in the n-alkane acentric factor, or carbon number. A similar trend was reported by Kordas et al (Kordas et al., 1994), they developed a generalised correlation for a translated modified Peng Robinson equation of state with only one interaction parameter.
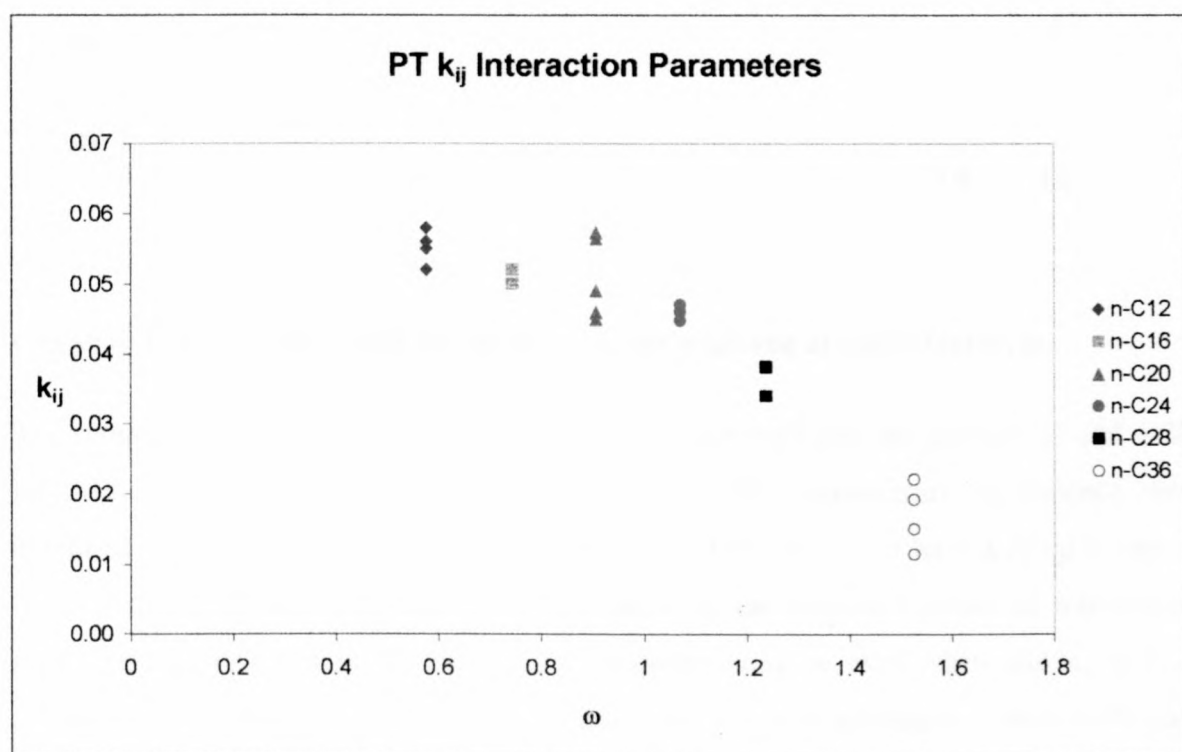
Graph 4-27 PT k_{ij} interaction parameters vs. the n-alkane acentric factor, ω.

No such trend could be discerned from the l_{ij} parameters. From the l_{ij} interaction parameter – acentric factor plot of the PT system, Graph 4-28, it appears as if the parameter values increase with an increase in the heavy component acentric factor to a maximum value and then decreases again. The PR and SRK l_{ij} values also display this type of behaviour. It should be remembered that a limit of 0.15 had imposed on the parameters, which

suppressed the true extent of the parameter increase. In order to confirm this trend, interaction parameters are needed for higher carbon-number n-alkane systems where no limits have been imposed on the maximum interaction parameter value.
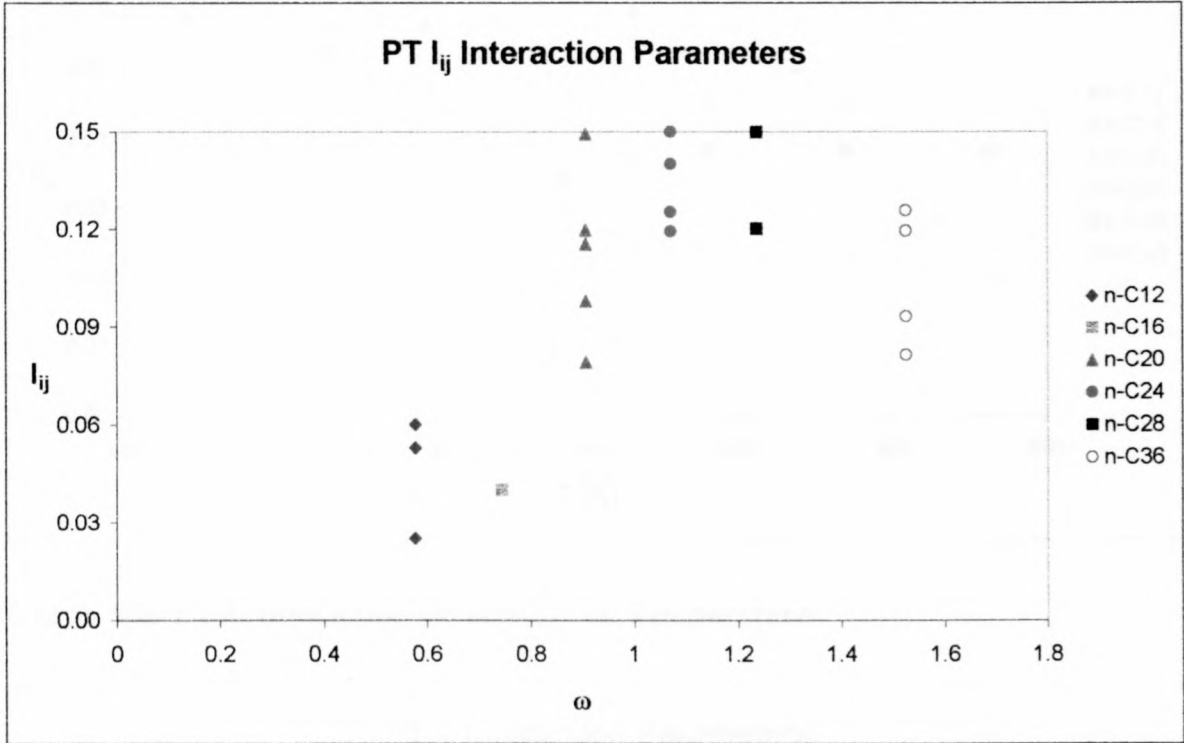
Graph 4-28 PT l_{ij} interaction parameters vs. the n-alkane acentric factor, ω.

The spread in the interaction parameters for the various n-alkanes in graphs 4-27 and 4-28 indicate a temperature dependence in the values. This temperature dependence was exhibited by interaction parameters for all the EOS They appear to have a roughly linear relation to the system temperature, and because of the limited number of interaction parameters available, a linear functional relationship may be used when making a first estimate of an interaction parameter at a different system temperature. Graph 4-29 and Graph 4-30 are typical of the interaction parameter – temperature relationships.
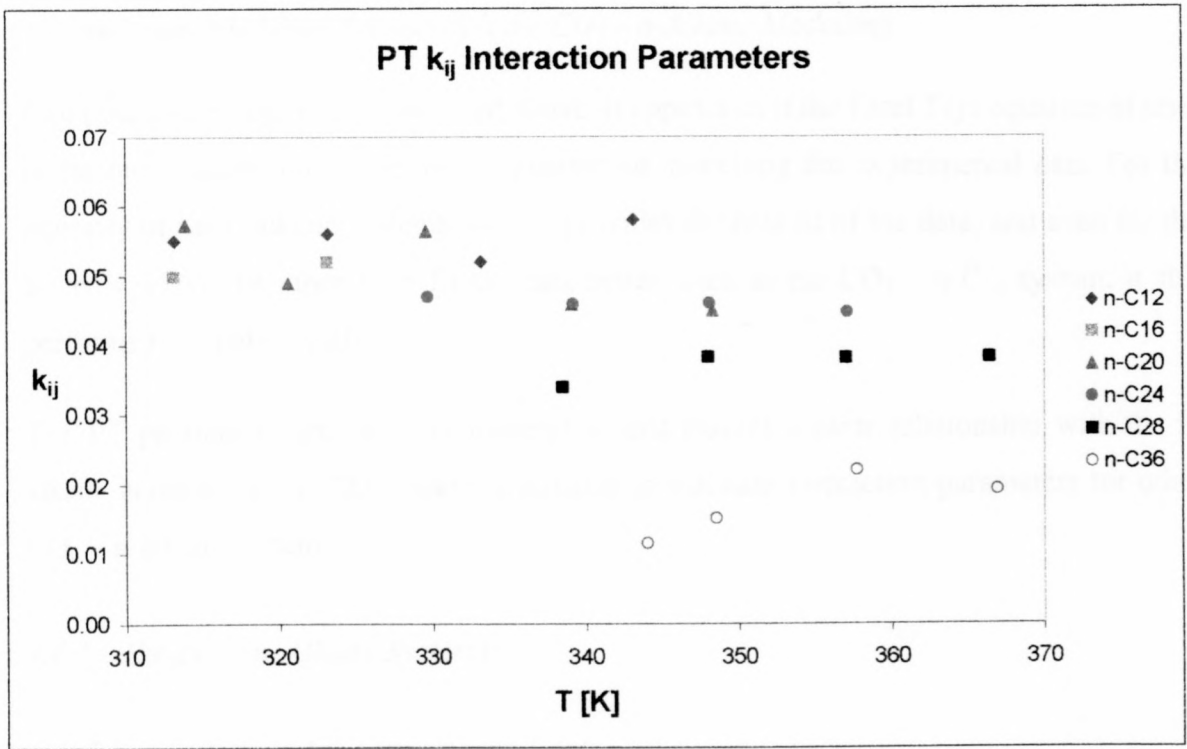
Graph 4-29 PT k_{ij} interaction parameters vs. Temperature
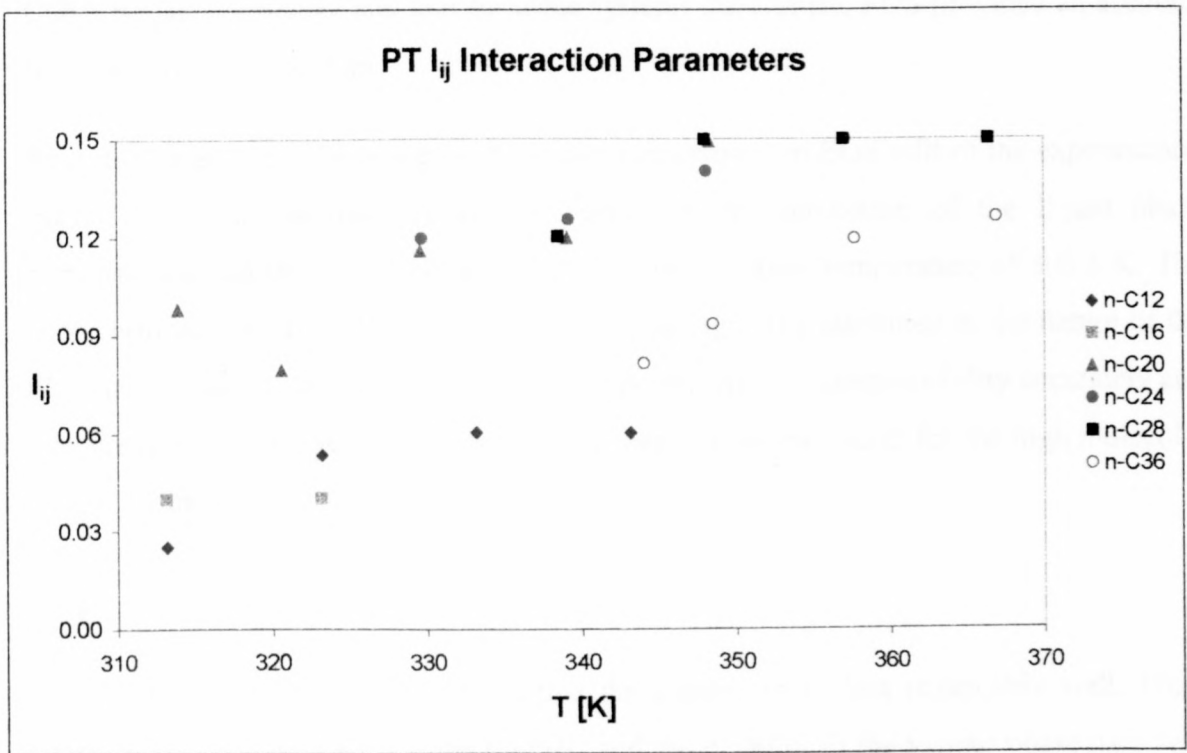
Graph 4-30 PT l_{ij} interaction parameters vs. Temperature.

From the modelling results discussed above, it appears as if the Patel Teja equation of state is the most successful of the three equations in modelling the experimental data. For the majority of the n-alkane systems, the PT provides the best fit of the data, and even for the systems where the other EOS fit the data better, such as the CO_2 – n-C_{12} system, it still performs reasonably well.

The PT parameters are the only parameters that exhibit a clear relationship with the n-alkane acentric factor. This makes it possible to estimate interaction parameters for other CO_2 – n-alkane systems.

4.6.2   Ethane – n-Alkane Systems

Representation of the experimental data

It was found that the EOS represented the ethane – n-alkanes systems much better than the CO_2 – n-alkane systems, and that for these systems the CSPHC EOS provided an accurate fit of the experimental data.

As in the case of the CO_2 systems the greatest inaccuracy in EOS's fit of the experimental data is found in the mixture critical region, in the prediction of the liquid phase compositions and the fitting of data near the ethane critical temperature of 305.3 K. The poor performance of the EOS in these regions can again be attributed to the nature of the EOS, in that they do not predict the pure component critical compressibility accurately and they are not able to give accurate pure component vapour pressures for the high molecular weight alkanes.

- *Ethane – n-C_{28} System*

At high temperatures, all the EOS fitted the experimental data reasonably well. From Graph 4-31 it can be seen that the CSPHC and the PT EOS fit the vapour phase data very well and that the SRK EOS gives a reasonable prediction of the liquid phase compositions.

At the lower temperatures, the performances of the various EOS are not as good. See graphs 4-32 and 4-33, P-x diagrams of the system at 342.8 K and 337.8 K.
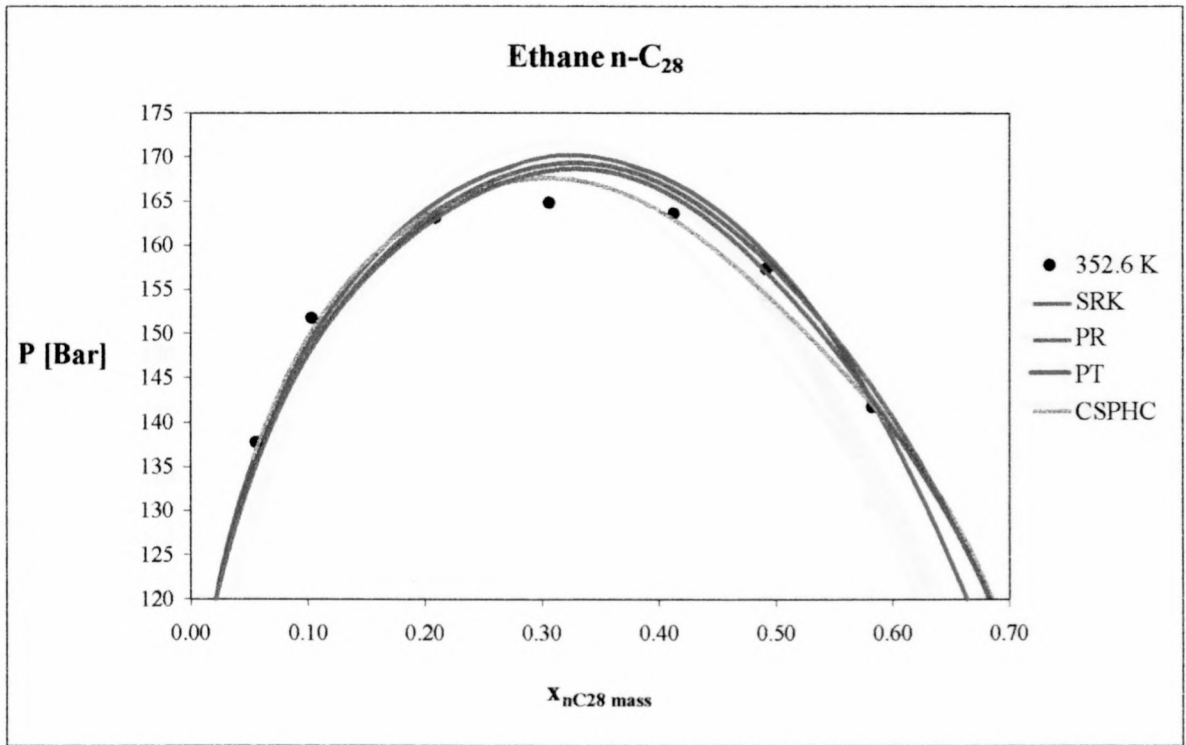
Graph 4-31 P-x Diagram of the ethane – n-C$_{28}$ system at 352.6 K with SRK k_{ij} 0.035, l_{ij} 0.00583; PR k_{ij} 0.026, l_{ij} 0.0138, PT k_{ij} –0.036, l_{ij} 0.12 and CSPHC k_{ij} 0.08
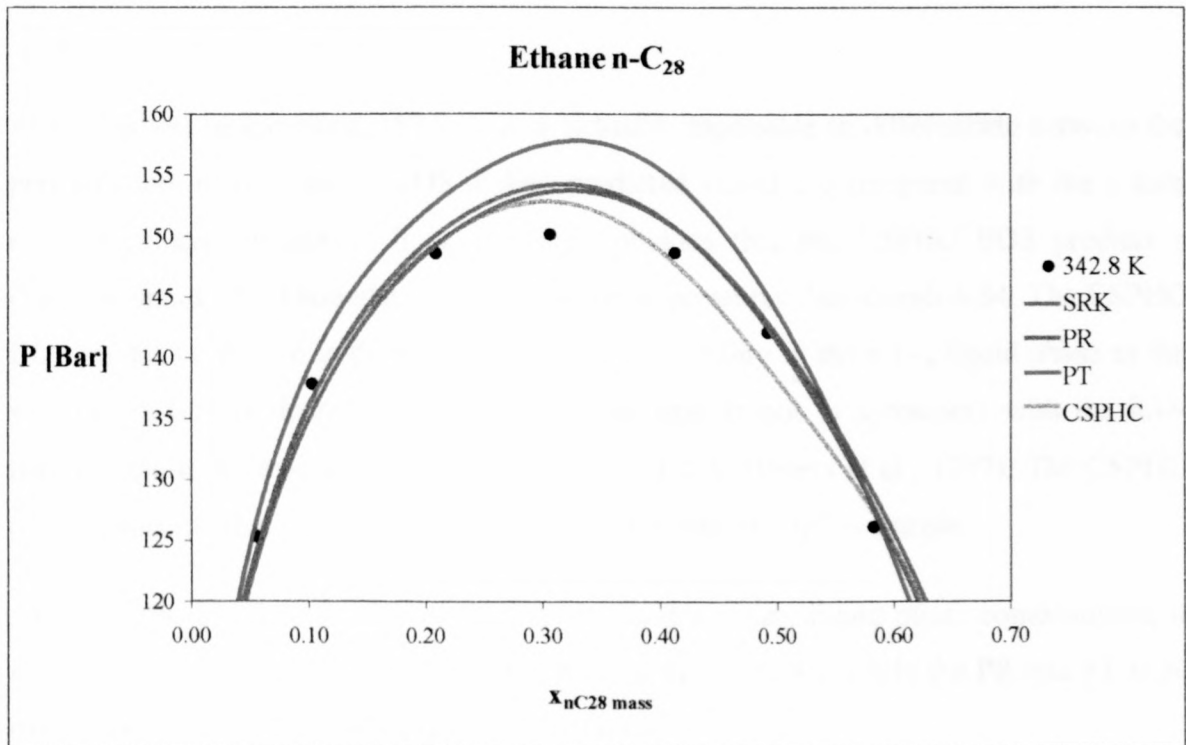
Graph 4-32 P-x Diagram of the ethane – n-C$_{28}$ system at 342.8 K with SRK k_{ij} 0.0345, l_{ij} 0.00568; PR k_{ij} 0.025, l_{ij} 0.0198, PT k_{ij} –0.0349, l_{ij} 0.124 CSPHC k_{ij} 0.08
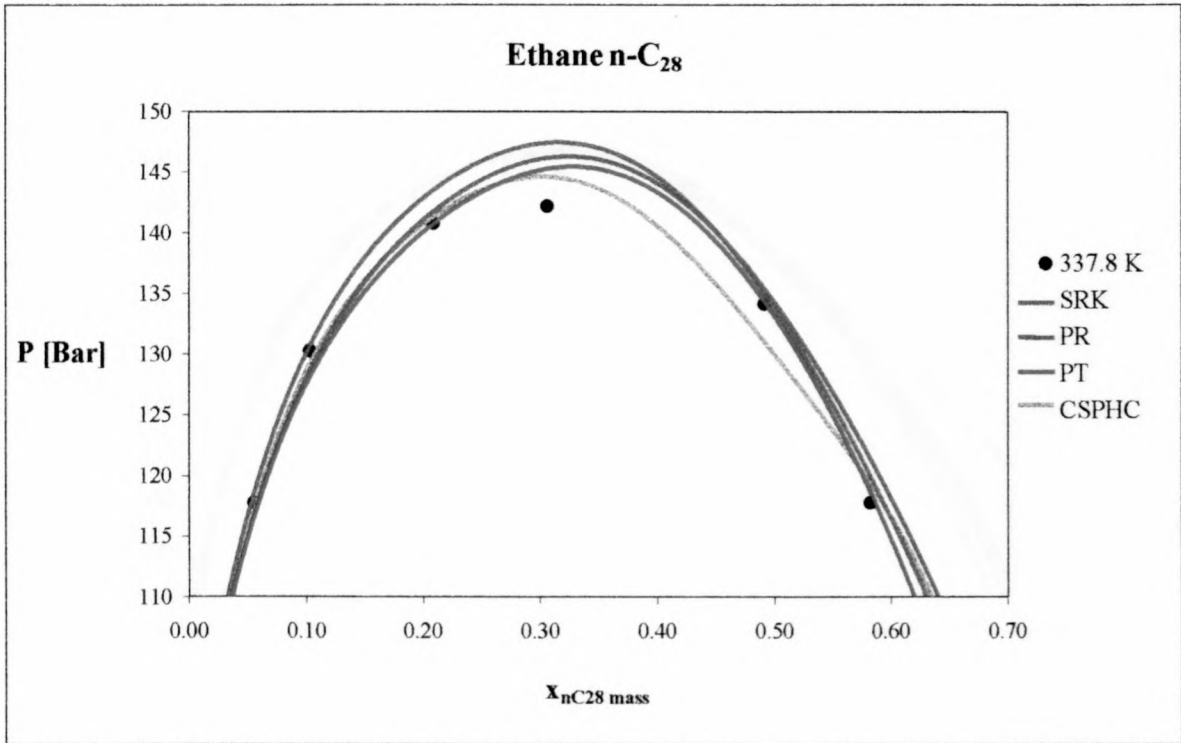
Graph 4-33 P-x Diagram of the ethane – n-C_{28} system at 337.8 K with SRK k_{ij} 0.035, l_{ij} 0.00559; PR k_{ij} 0.025, l_{ij} 0.0239, PT k_{ij} –0.034, l_{ij} 0.122 and CSPHC k_{ij} 0.08

- *CO_2 – n-C_{24} System*

At the highest temperature, 352.7 K, it is virtually impossible to differentiate between the performances of the various EOS if their predicted values are compared with the values determined experimentally. It is, however, obvious that the CSPHC EOS predicts a different liquid phase boundary trend at the lower pressures. See Graph 4-34. The CSPHC EOS predicts a sudden in decrease in the ethane solubility in the n-C_{24} liquid phase as the system pressure is decreased. This sudden decrease is not in agreement with the low-pressure phase behaviour observed by Peters at 350 K (Peters et al., 1987). The CSPHC predicts this trend at other temperatures and for the ethane – n-C_{16} system.

At 342.7 and 332.8 K the SRK EOS has the most accurate liquid phase compositions, it also predicts the mixture critical pressure accurately at 332.8 K while the PR and PT EOS overestimate this value. See Graph 4-35 and 4-36.
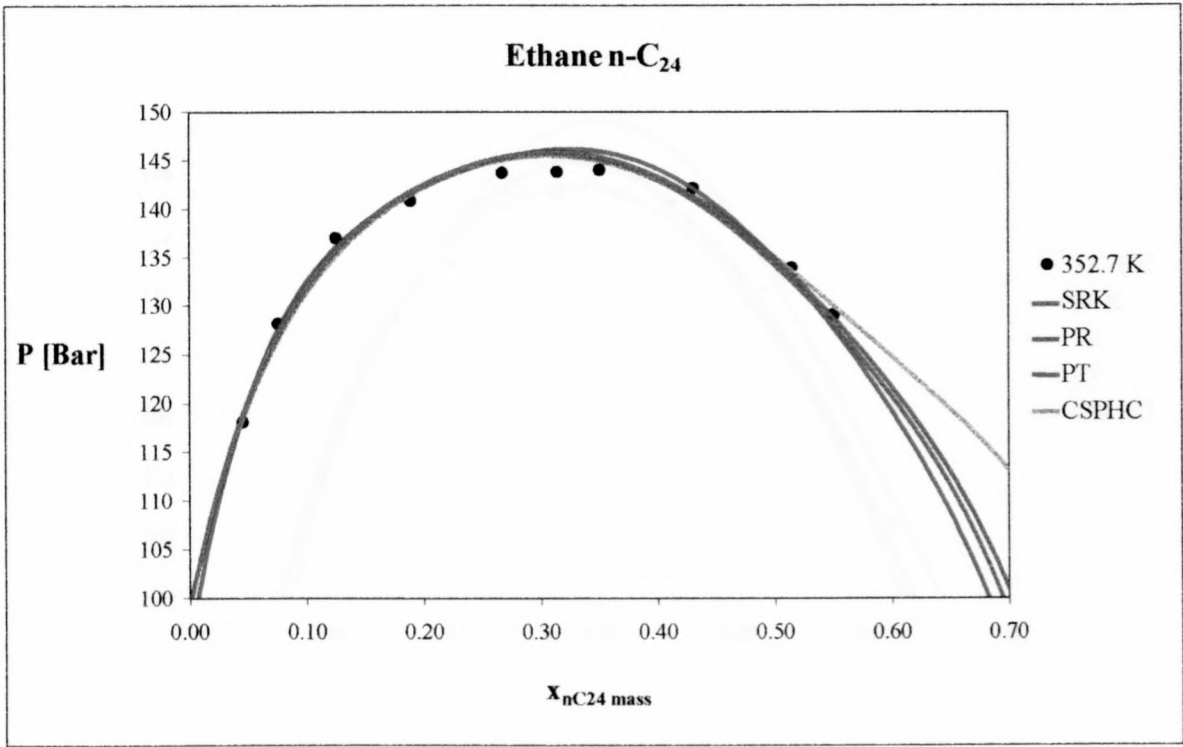
Graph 4-34 P-x Diagram of the ethane – n-C$_{24}$ system at 352.7 K with SRK k_{ij} 0.0333, l_{ij} -0.00253; PR k_{ij} 0.0235, l_{ij} 0.0085, PT k_{ij} –0.035, l_{ij} 0.09 and CSPHC k_{ij} 0.086
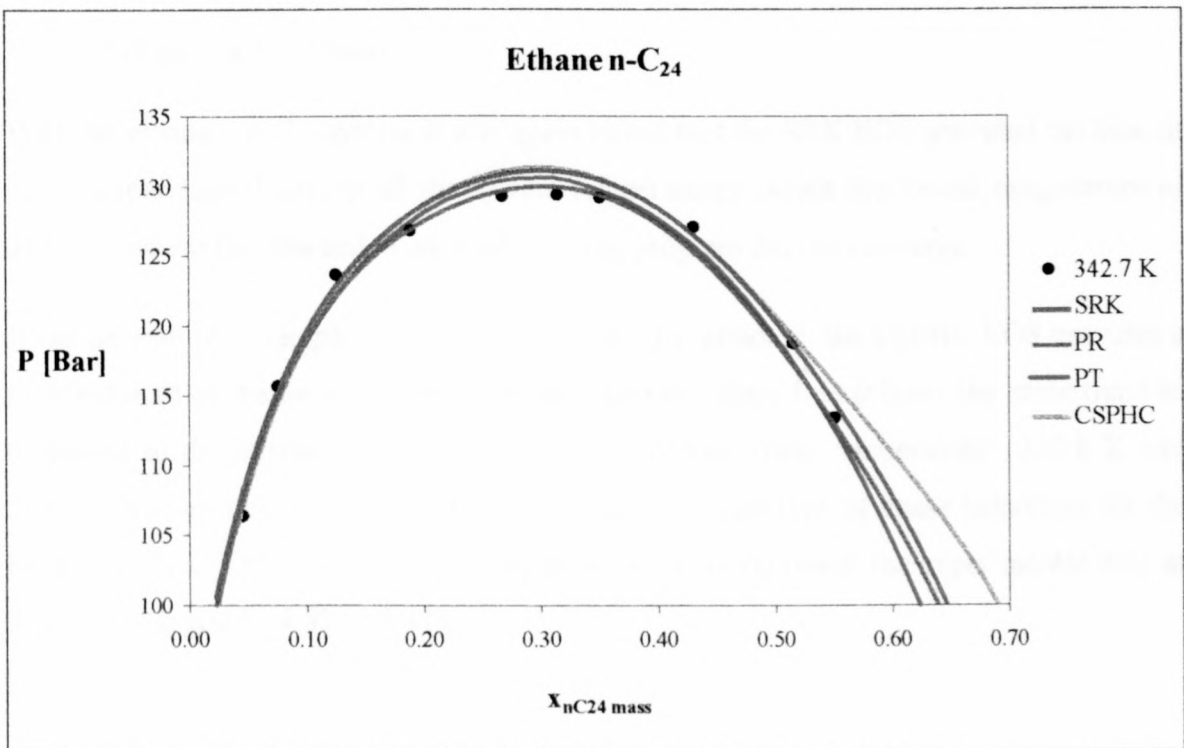
Graph 4-35 P-x Diagram of the ethane – n-C$_{24}$ system at 342.7 K with SRK k_{ij} 0.0329, l_{ij} -0.00246; PR k_{ij} 0.0237, l_{ij} 0.0058, PT k_{ij} –0.0346, l_{ij} 0.086 CSPHC k_{ij} 0.084
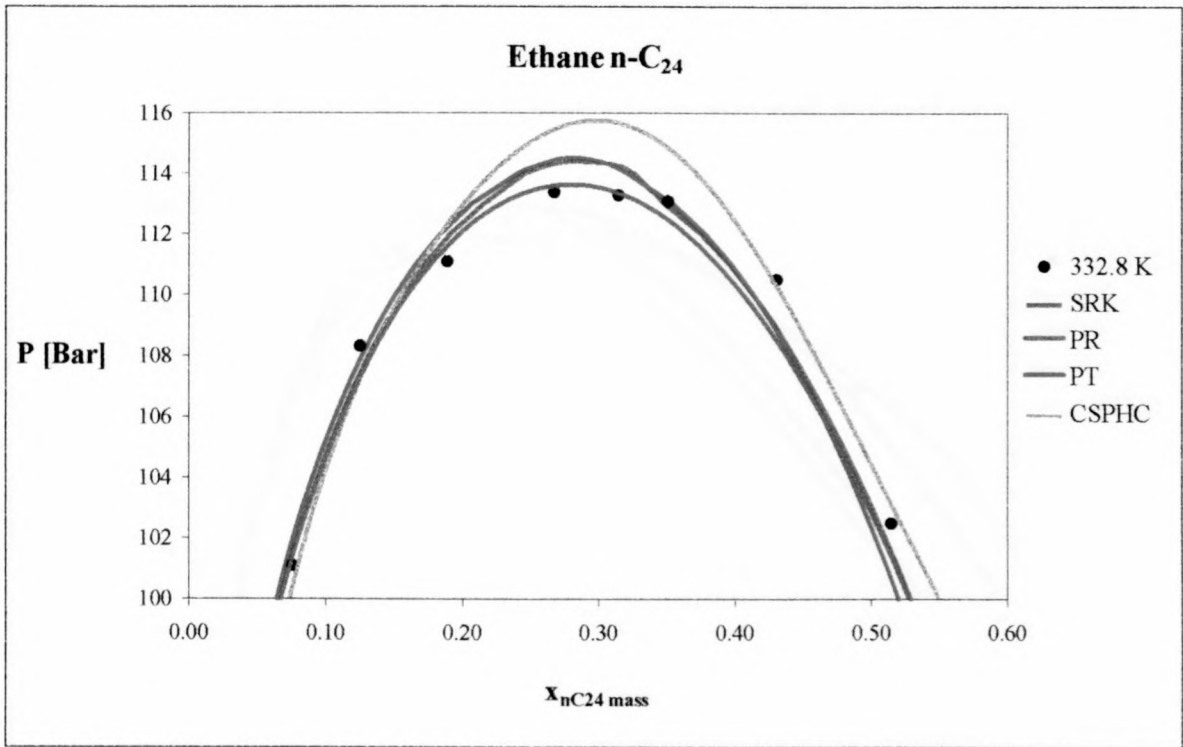
Graph 4-36 P-x Diagram of the ethane – n-C$_{24}$ system at 332.8 K with SRK k_{ij} 0.031, l_{ij} -0.00369; PR k_{ij} 0.0232, l_{ij} 0.005, PT k_{ij} –0.035, l_{ij} 0.082 CSPHC k_{ij} 0.084

- *Ethane – n-C$_{16}$ Systems*

With the ethane – n-C$_{16}$ system it was again found that the SRK EOS provided the best fit of the experimental data at all the system temperatures except the lowest temperature of 312.9 K, where the interaction parameter-fitting program did not converge.

It can be seen from Graph 4-37 and Graph 4-38, that although the CSPHC EOS provides a reasonable fit of the experimental data, the phase boundary line follows the same trend as discussed in the ethane – n-C$_{24}$ system above. At the lower temperatures, 332.8 K and 322.9 K it is also clear that this EOS predicts an incorrect type of phase behaviour for the binary mixture. The CSPHC EOS completely failed to represent the experimental data at 312.9 K. See graphs 4-39 to 4-41.
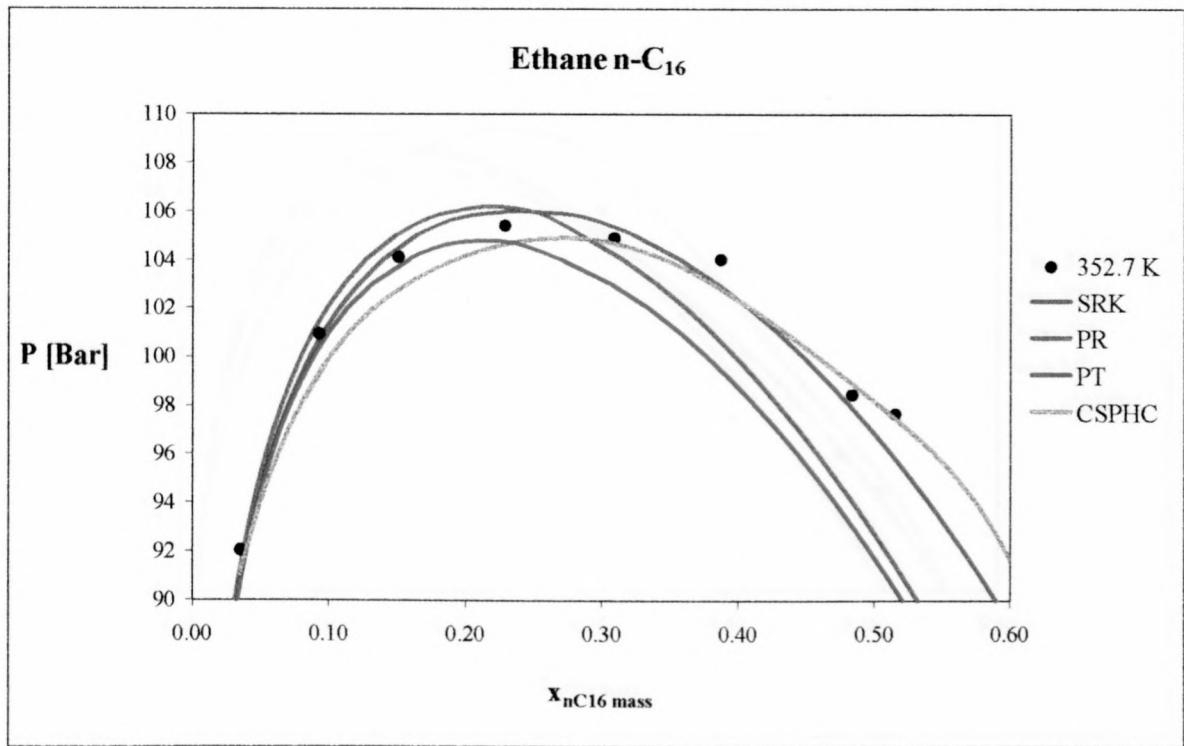
Graph 4-37 P-x Diagram of the ethane – n-C$_{16}$ system at 352.7 K SRK k_{ij} 0.025, l_{ij} -0.0037; PR k_{ij} 0.0002, l_{ij} -0.0082, PT k_{ij} –0.0464, l_{ij} 0.024, CSPHC k_{ij} 0.085
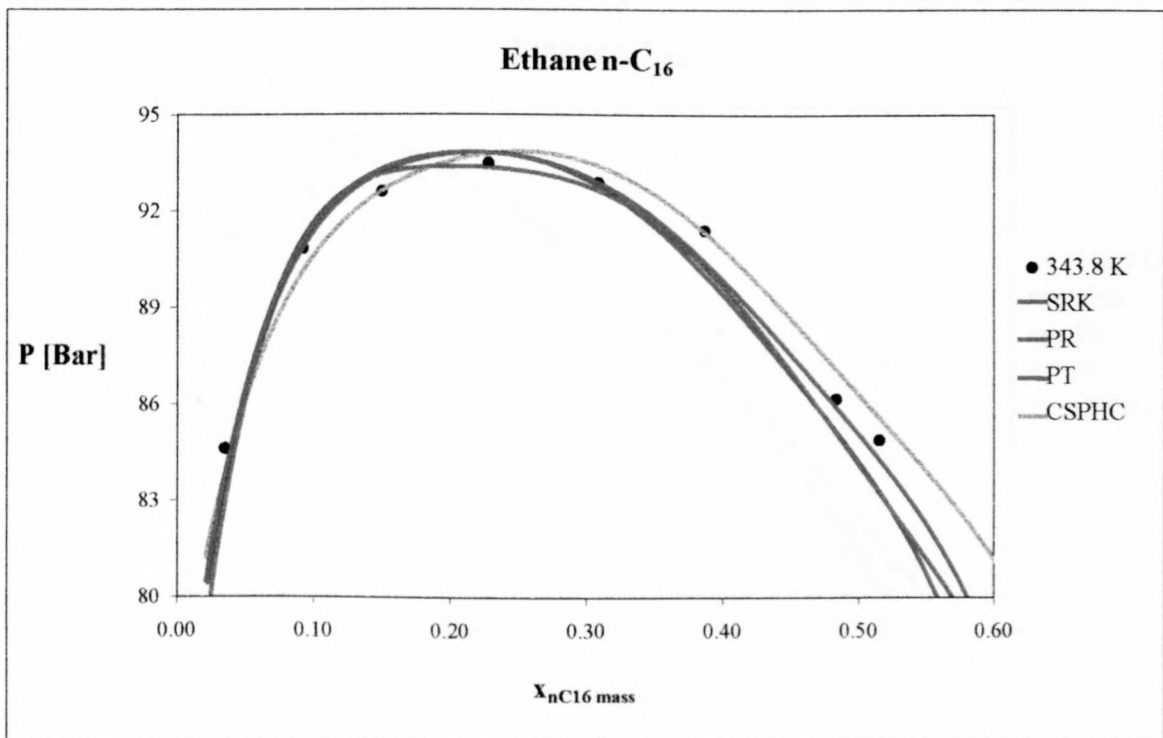
Graph 4-38 P-x Diagram of the ethane – n-C$_{16}$ system at 343.8 K with SRK k_{ij} 0.025, l_{ij} -0.0448 PR k_{ij} 0.0153, l_{ij} -0.0344, PT k_{ij} –0.0289, l_{ij} 0.007, CSPHC k_{ij} 0.075
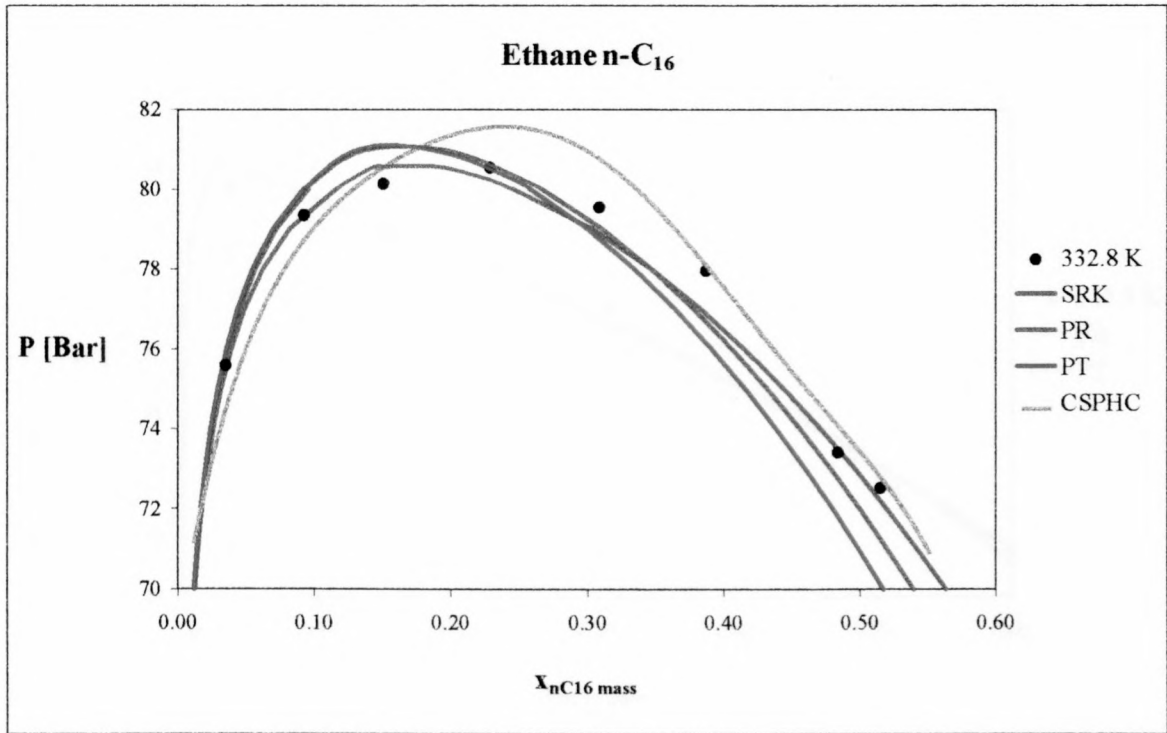
Graph 4-39 P-x Diagram of the ethane – n-C$_{16}$ system at 332.8 K with SRK k_{ij} 0.025, l_{ij} -0.057 PR k_{ij} 0.0134, l_{ij} -0.0386, PT k_{ij} –0.0346, l_{ij} 0.002, CSPHC k_{ij} 0.065
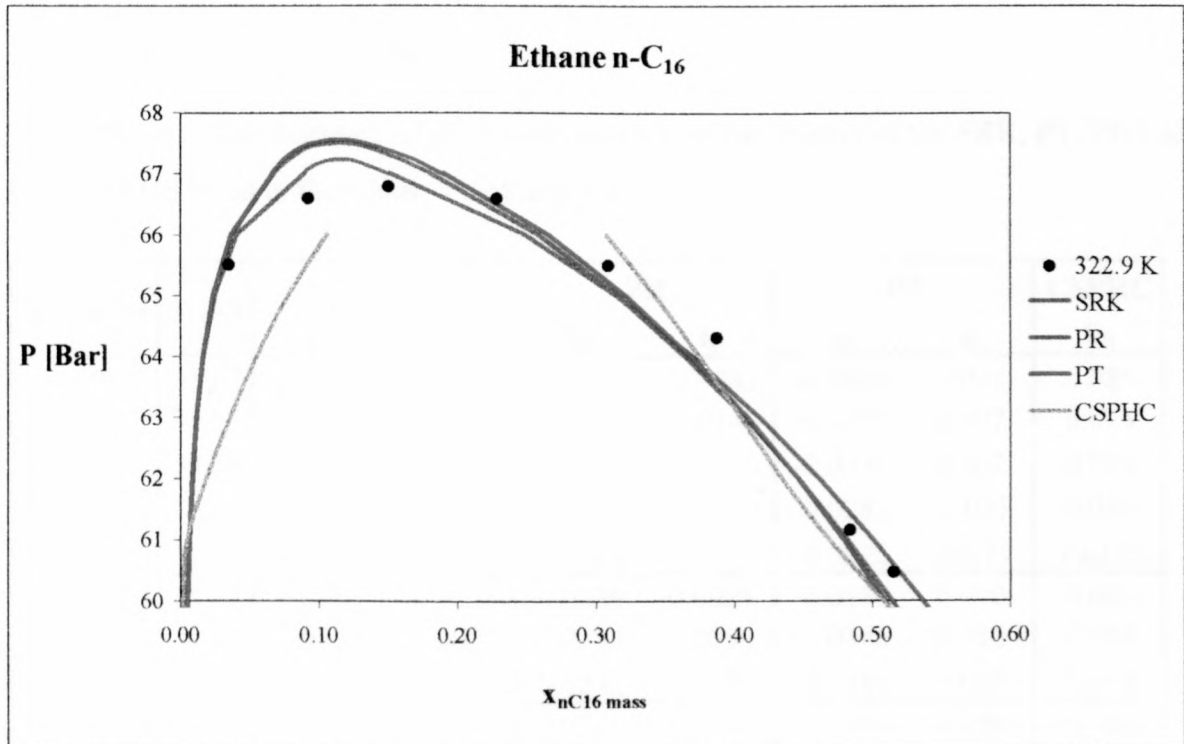
Graph 4-40 P-x Diagram of the ethane – n-C$_{16}$ system at 322.9 K with SRK k_{ij} 0.025, l_{ij} -0.074 PR k_{ij} 0.0147, l_{ij} -0.058, PT k_{ij} –0.0282, l_{ij} -0.021, CSPHC k_{ij} 0.055
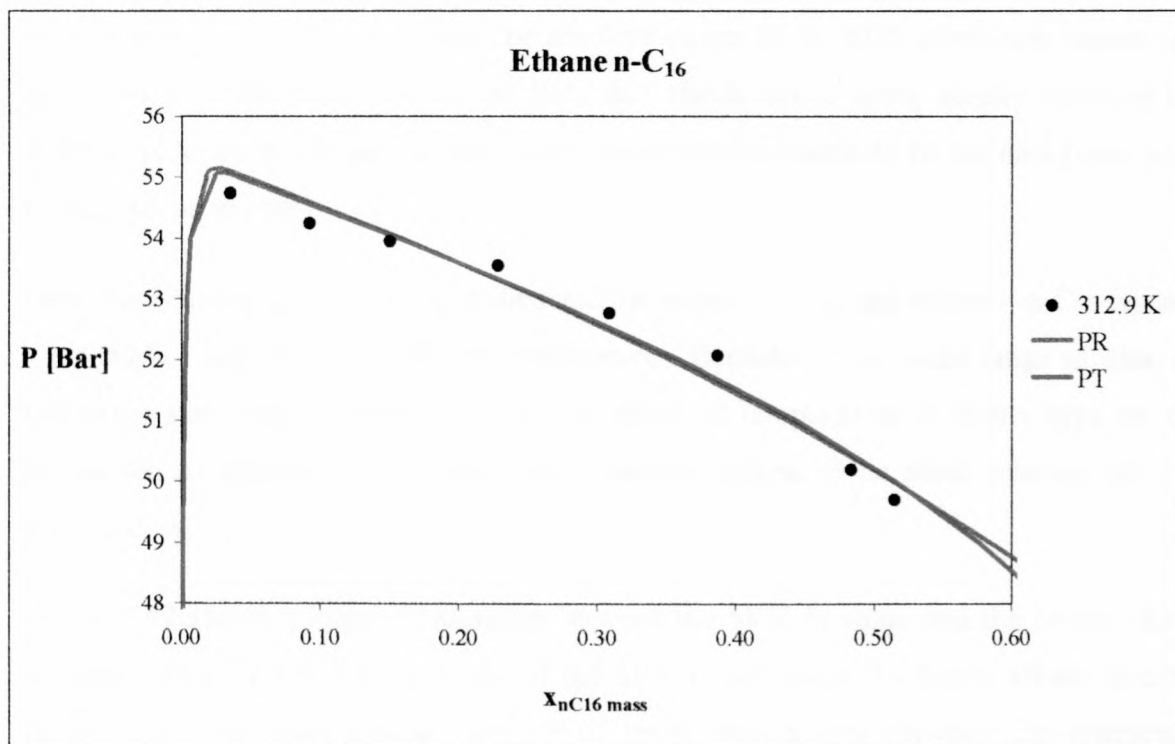
Graph 4-41 P-x Diagram of the ethane – n-C$_{16}$ system at 322.9 K with PR k_{ij} 0.0189, l_{ij} -0.1041, PT k_{ij} –0.0222, l_{ij} 0.073

Binary Interaction Parameters

The following table contains all the binary interaction parameters of the SRK, PT, PR and CSPHC EOS fitted to the ethane – n-alkane data:

n-Alkane	T [K]	SRK		PR		PT		CSPHC
		k_{ij}	l_{ij}	k_{ij}	l_{ij}	k_{ij}	l_{ij}	k_{ij}
n-C$_{16}$	352.7	0.0250	-0.0370	0.0002	-0.0082	-0.0464	0.024	0.085
	342.8	0.0250	-0.0448	0.0153	-0.0344	-0.0289	0.007	0.075
	332.8	0.0250	-0.0570	0.0134	-0.0386	-0.0346	0.002	0.065
	322.9	0.0250	-0.0740	0.0147	-0.0580	-0.0282	-0.021	0.055
	312.9	Failed		0.0189	-0.1041	-0.0222	-0.073	Failed
n-C$_{24}$	352.7	0.0333	-0.0025	0.0235	0.0085	-0.0350	0.090	0.086
	342.7	0.0329	-0.0025	0.0237	0.0058	-0.0346	0.086	0.084
	332.8	0.0310	-0.0037	0.0232	0.0050	-0.0350	0.082	0.084
n-C$_{28}$	352.6	0.0350	0.00583	0.0260	0.0138	-0.0360	0.120	0.080
	342.8	0.0345	0.00568	0.0250	0.0198	-0.0349	0.124	0.080
	337.8	0.0350	0.00559	0.0250	0.0239	-0.0340	0.122	0.080

Table 4-2 Interaction Parameters determined for the ethane – n-alkane Systems

From Table 4-2 it can be seen that the absolute values of the EOS interaction parameters are all of a similar size. There is no EOS that stands out as being ideally suited to the system (very small interaction parameters) or inherently unable to fit the data (very large interaction parameters).

Only three binary mixtures were studied and the ethane – n-C_{24} and ethane – n-C_{28} systems were studied only at three different temperatures. Because of the small range of data, no definitive statements can be made on the effect of temperature or solute type on the interaction parameter values. There does, however, appear to be some relation between these factors.

Graph 4-42 shows a linear relationship between the SRK k_{ij} value and the heavy alkane acentric factor. Graph 4-43 is a plot of the SRK l_{ij} value and the heavy alkane acentric factor. This plot also indicates a type of linear relationship between the interaction parameter and the acentric factor. The spread in the data can, in part, be attributed to the temperature effect, but when Graph 4-47 is studied, it can be seen that the heavy component type influences the degree of temperature dependence. The l_{ij} value appears to have a linear relationship with temperature, but the heavy alkane type influences the slope of the line.

All the EOS k_{ij} and l_{ij} parameters exhibit this type of relationship with the heavy alkane type and temperature, with the exception of the PT and CSPHC k_{ij} parameters, where the alkane type only influences the degree of temperature dependence. See graphs 4-44 and 4-45.
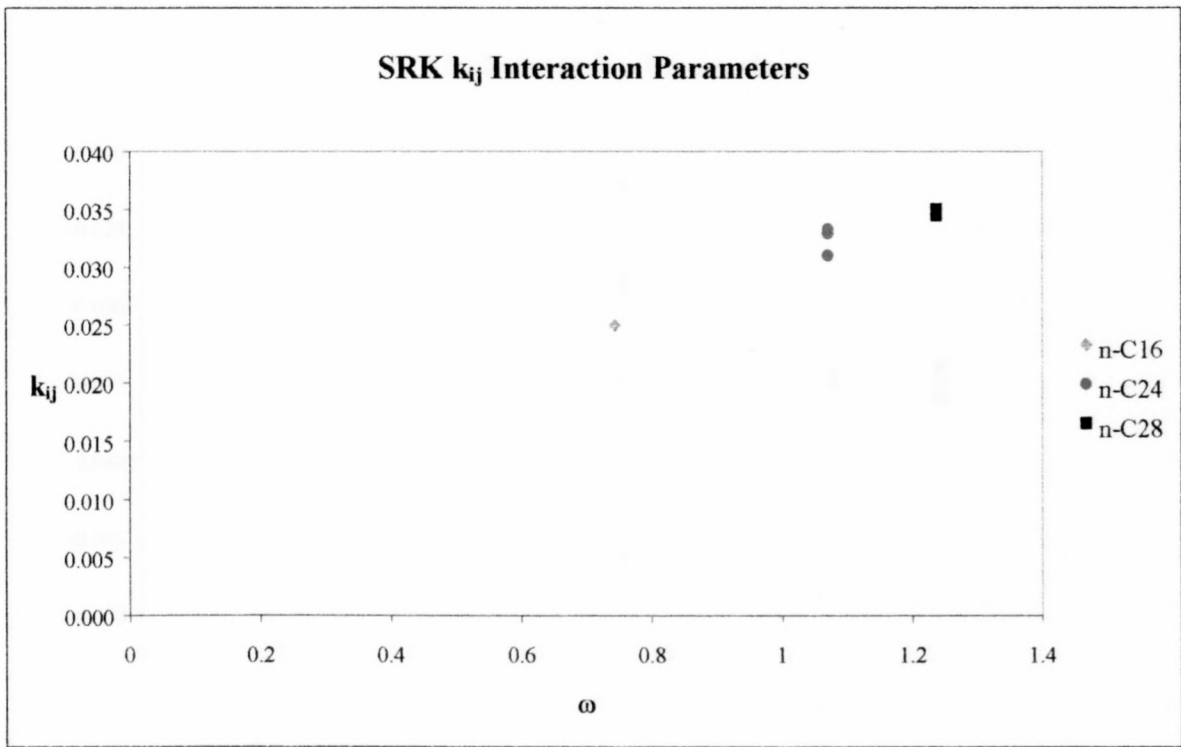
Graph 4-42 SRK k_{ij} interaction parameters vs. the n-alkane acentric factor, ω.
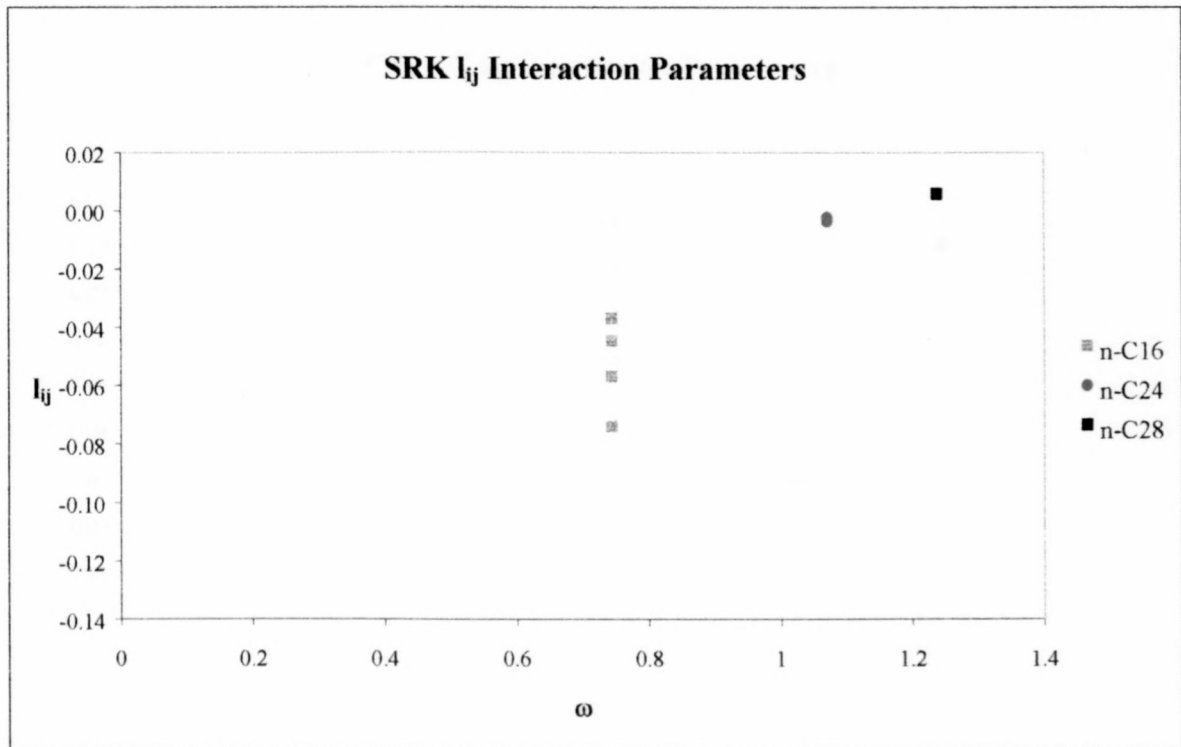
Graph 4-43 SRK l_{ij} interaction parameters vs. the n-alkane acentric factor, ω.

119
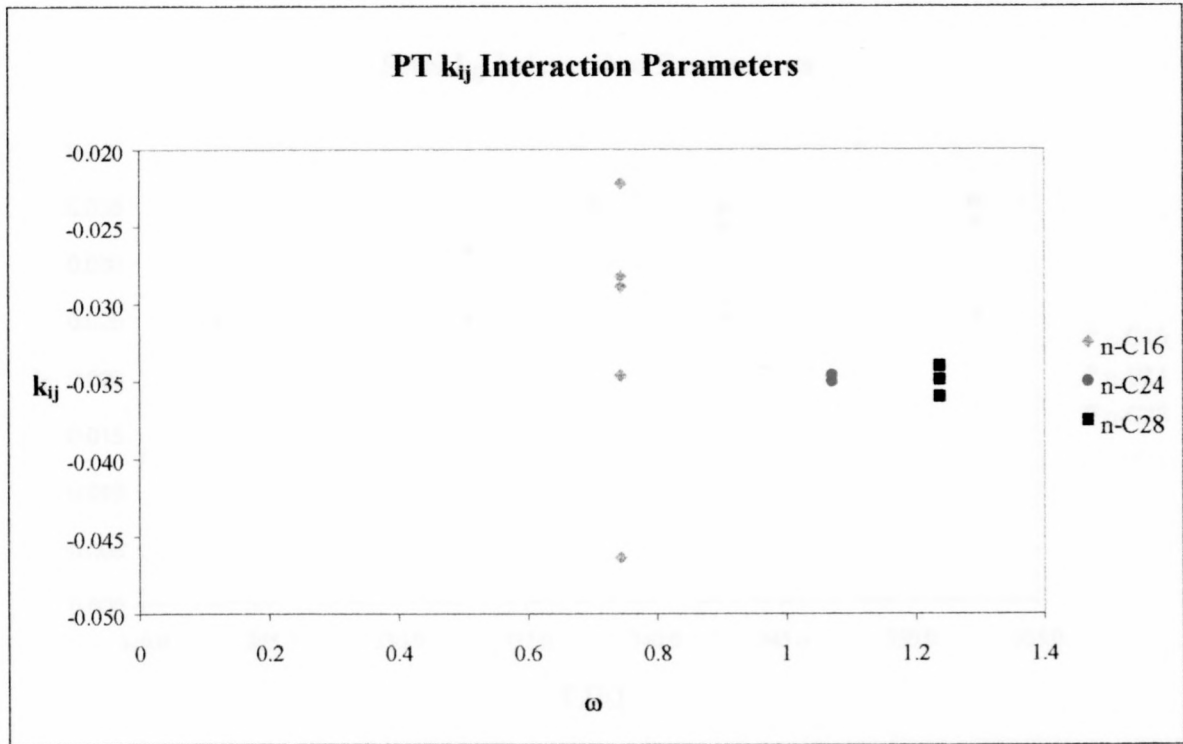
Graph 4-44 PT k_{ij} interaction parameters vs. the n-alkane acentric factor, ω.
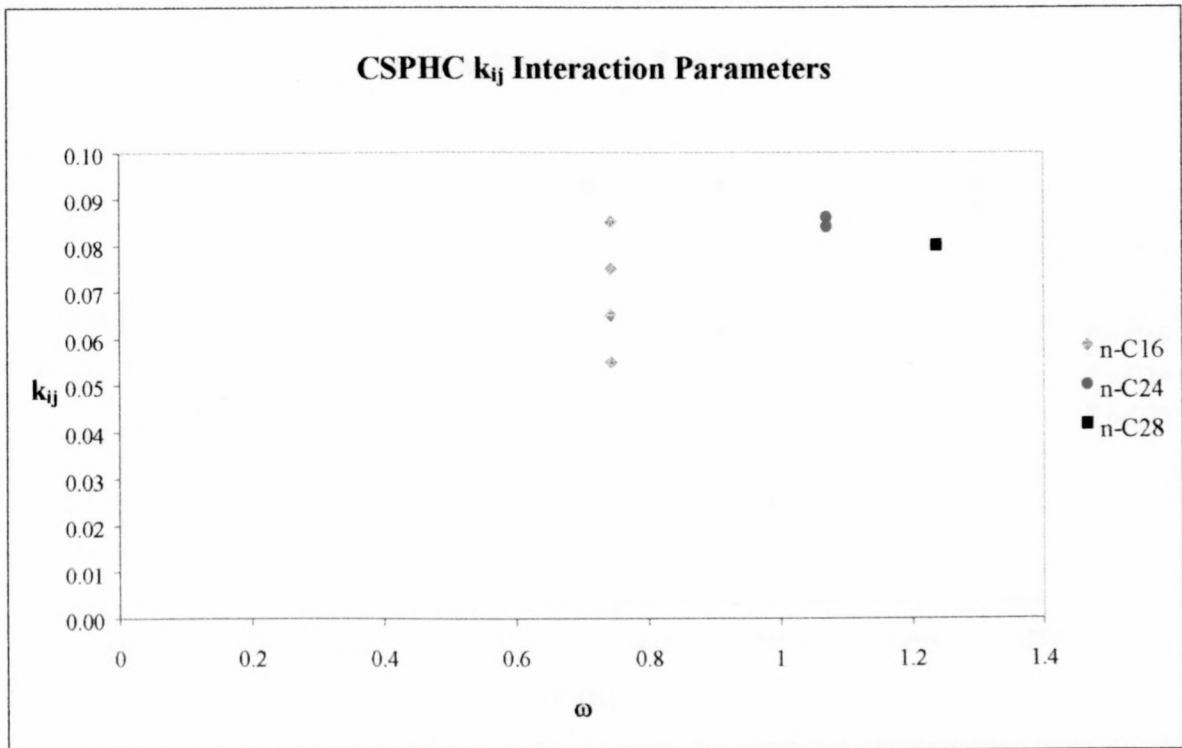
Graph 4-45 CSPHC k_{ij} interaction parameters vs. the n-alkane acentric factor, ω.
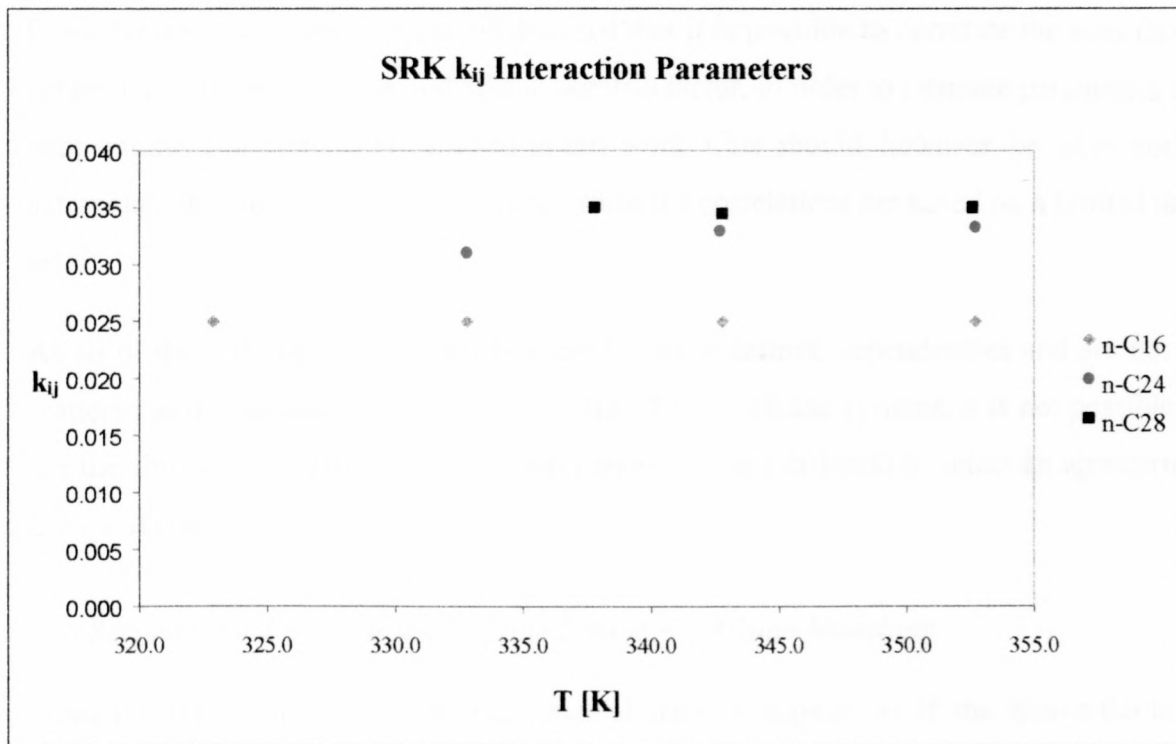
Graph 4-46 SRK k_{ij} interaction parameters vs. temperature.
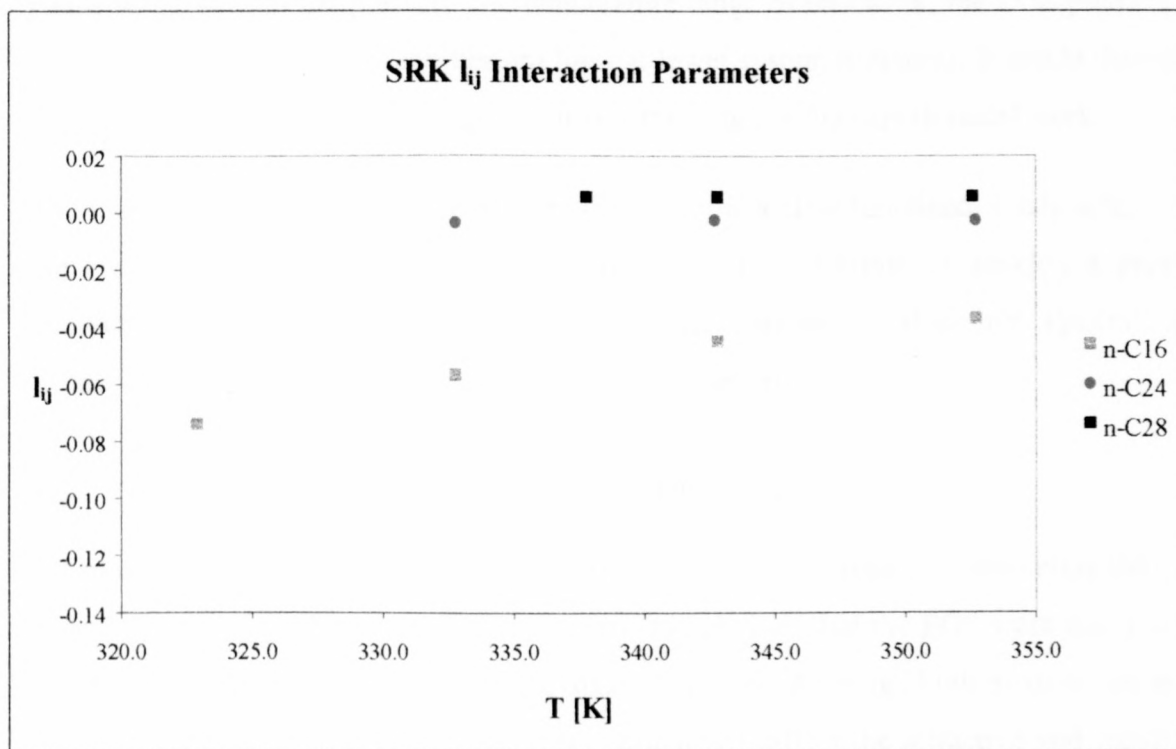
Graph 4-47 SRK l_{ij} interaction parameters vs. temperature.

From the discussion above it can be deduced that it is possible to correlate the interaction parameters with temperature and alkane acentric factor, in order to estimate parameters for temperatures and systems not studied in this work. Care should, however, be taken not to extrapolate the data over too wide a range since the correlations are based on a limited data set.

As all of the different EOS parameters exhibit these definite dependencies and are not as scattered as the parameters determined for the CO_2 – n-alkane systems, it is not possible to use the ability to correlate the interaction parameters as a criterion to select an appropriate EOS to model this system.

Recommended EOS for use with the Ethane – n-Alkane Modelling

From the representation of the experimental data, it appears as if the Soave-Redlich-Kwong equation of state is the most successful in predicting the experimentally determined phase boundaries. Although the CSPHC EOS is successful in accurately representing the phase boundaries in the pressure and temperature range of this work, the EOS predicts an incorrect trend in the phase equilibrium lines at lower system pressures. It would therefore be unwise to apply this EOS in regions outside the range of the experimental work.

The interaction parameters of the SRK EOS also show a clear functional relationship with the system temperature and solute type. It is therefore possible to develop a general interaction parameter correlation to estimate the parameter values for systems and temperatures that have not been investigated experimentally.

4.6.3   Comparison of the CO_2 and Ethane Systems

When comparing the performance of the various equations of state in representing the CO_2 – n-alkane and the ethane – n-alkane systems it is obvious that the EOS were much more successful in representing the ethane – n-alkanes systems. Although both mixtures are non-polar, the CO_2 has a quadrupolar moment, which will affect the attractive and repulsive forces in the binary mixtures. The Van der Waals Type EOS do not make allowance for this force and hence do not perform as well when applied to the CO_2 systems.

The interaction parameters of the EOS when used for the CO_2 – n-alkane systems are larger than the ethane – n-alkane parameters. (Table 4-1 and Table 4-2) Since the different

systems were studied at similar temperatures and with similar heavy n-alkanes, the size difference can be attributed to the fact that the EOS need a much larger correction to represent the CO_2 systems because they are not able to give an accurate representation of the various forces present in the CO_2 binary mixture.

4.7 CONCLUSIONS

It was found that the Patel-Teja equation of state was the most successful in representing the CO_2 – n-alkane systems. The k_{ij} interaction parameter seems to have a roughly linear relationship with temperature and the solute acentric factor. The l_{ij} parameter also exhibits the roughly linear relationship with temperature, but seems to increase to a maximum value and then decrease with increasing solute acentric factor.

The Soave-Redlich-Kwong equation of state may be used to model the ethane – n-alkane systems. There also seems to exist a definite functional relationship between the binary interaction parameters, the system temperature and the solute acentric factor.

It was also found that the Cubic Simplified Perturbed Hard-Chain equation of state predicted inaccurate phase boundary trends for both the CO_2 and the ethane systems. It completely failed to model the CO_2 – n-alkane phase equilibria. Although it was successful in representing the ethane – n-alkane systems within the temperature and pressure range of this work, it became obvious that the system predicted an incorrect trend at lower pressures. The EOS can therefore not be used with confidence outside the scope of this work thus limiting its usefulness.

The Van der Waals Type EOS is unable to accurately represent the attractive and repulsive forces present in the CO_2 – n-alkane systems. The EOS did not perform as well with these systems as with the systems where supercritical ethane was used as solvent, and large interaction coefficients were needed to force the EOS to fit the data.

The traditional problem areas of the equations of state were also highlighted. The fact that the EOS are inaccurate in their representation of pure component critical points and n-alkane vapour pressures resulted in inaccuracies in the representation of the mixture critical points, liquid phase concentrations and the poor performance at system temperatures near the solvent critical temperature.

Although these fundamental problems were also encountered with the PT and SRK equations of state, they will still be suitable for use in the modelling of supercritical extraction columns, where the operating range is far removed from the mixture critical point and the solvent critical temperature. A high degree of accuracy in the liquid equilibrium line is not crucial to the extraction system operation.

4.8 RECOMMENDATIONS

In order to develop general interaction coefficient correlations more experimental data over a wider operating and system range are needed. It is necessary to increase the temperature range over which the data are studied and, especially in the case of the ethane – n-alkane systems, the number of binary systems studied.

In order to find an EOS that will give an accurate representation of the supercritical solvent – n-alkane systems it is necessary to investigate and improve the EOS's performance in the prediction of the pure component vapour pressures and critical points. The presence of other forces, such as the quadrupole moment in CO_2, must also be incorporated in the EOS.

5 CONCLUSIONS AND RECOMMENDATIONS

- It was found that a synthetic method of measuring phase equilibria would be most suited to the investigation of supercritical fluid – n – alkane mixtures. A variable volume view cell with a circulation unit was designed and developed for this study. The unit has a maximum pressure limit of 300 bar and a maximum operating pressure of 280 bar at 353 K.

- The phase transitions can be detected visually or indirectly by monitoring the change in overall density. It was found that by visually observing the phase transition of the supercritical solvent – n-alkane mixtures, the phase boundary could be accurately determined to within 0.1 bar.

- The phase equilibria and densities of binary mixtures of supercritical solvents ethane and CO_2 with n-alkanes, n-C_{12} to n-C_{36} were measured. It was found that the solubilities of the n-alkanes were much higher in supercritical ethane than in CO_2, but that the use of CO_2 will ensure a much better control over the alkane selectivity in an extraction process.

- The n-alkane solubilities in the supercritical ethane are so high because the solvent and solutes are chemically very similar. (Ethane and the n-alkanes belong to the same homologous series). The similar chemical properties of the mixture components also result in the ethane – n-alkane systems displaying much simpler types of phase behaviour than the CO_2 – n-alkane systems, and have the effect that the ethane and CO_2 systems follow entirely different density trends. The ethane systems' saturated density increases with increasing n-alkane concentration, whereas the CO_2 systems have a maximum density value at lower n-alkane concentrations.

- It was found that the CO_2 – n-alkane systems did not exhibit a linear relationship between temperature and pressure for a constant composition at system concentrations near the mixture critical point. Care should therefore be taken when extrapolating experimental data in this region.

- Out of the various equations of state investigated the Patel Teja EOS provided the best representation of the CO_2 – n-alkane systems and the Soave-Redlich-Kwong EOS was the most successful in modelling the ethane – n-alkane systems.

- The binary interaction parameters used to fit the EOS to the experimental data, for both the PT and SRK EOS, display functional relationships with the system temperature and n-alkane acentric factor. This will enable the extrapolation of the interaction parameters for use at other temperatures and n-alkane systems.

- The EOS inability to model the pure component critical points correctly and the n-alkane vapour pressures were highlighted during the attempts to model the experimental data. The inherent flaws in the EOS resulted in the poor performance of the models at system temperatures near the solvent critical temperature, at conditions close to the mixture critical point and in the prediction of the liquid phase compositions.

- It was also found that the equations of state investigated did not successfully represent all the interactions present in the CO_2 – n-alkane systems. The effect of the quadrupole moment the CO_2 has not been accounted for. This resulted in the poor performance of the EOS in modelling the CO_2 systems compared with their ability to represent the ethane – n-alkane systems.

This project was successful measuring high accuracy phase equilibria of supercritical solvents and n-alkanes, but it was found that the ability of the present equations of state to model the data was lacking. It is recommended that an in depth study be made of the various equations of state in existence today, focussing on their ability to predict pure component properties accurately and to represent the various intermolecular forces present in a mixture. An attempt must be made to either find a more suitable equation of state, or to modify an existing equation to improve its performance at high pressures and with heavy molecular weight components.

In order to apply the Patel Teja and Soave-Redlich-Kwong equations of state in the simulation of a supercritical wax fractionation process, general interaction parameter correlations first have to be developed. It is necessary to expand the database of

interaction parameters to include a broader range of operating temperatures and n-alkane systems.

REFERENCES

Beret, S., Prausnitz, J.M., *Perturbed Hard-Chain Theory: An Equation of State for Fluids Containing Small or Large Molecules.* **AIChE Journal,** 21, (6), 1975, 1123-1132.

Bertucco, A., Barolo, M., Elvassore, N., *Thermodynamic Consistency of Vapor-Liquid Equilibrium Data at High Pressure.* **AIChE Journal,** 43, (2), 1997, 547-554.

Breman, B. B., Beenackers, A.A.C.M., Rietjens, E.W.J., Stege, R.J.H., *Gas-Liquid Solubilities of Carbon Monoxide, Carbon Dioxide, Hydrogen, Water, 1-Alcahols (1<=n<=6), and n-Paraffins (2<=n<=6) in Hexadecane, Octacosane, 1-Hexadecanol, Phenanthrene, and Tetraethylene Glycol at Pressures up to 5.5 MPa and Temperatures from 293 to 553 K.* **J. Chem. Eng. Data,** 39, 1994, 647-666.

Brunner, G., *Mass separation with super-critical gases (gas extraction).* **International Chemical Engineering,** 30, (2), 1990, 191-205.

Brunner, G., **Gas Extraction An Introduction to Fundamentals of Supercritical Fluids and the Application to Separation Processes.** Darmstadt, Steinkopff, 1994.

Bruno, T. J., Ely, J.F., **Supercritical Fluid Technology: Reviews in modern theory and applications.** Boca Raton, CRC Press, 1991.

Charoensombut-Amon, T., Martin, R.J., Kobayashi, R., *Application of a Generalized Multiproperty Apparatus to Measure Phase Equilibrium and Vapor Phase Densities of Supercritical Carbon Dioxide in n-Hexadecane Systems up to 26 MPa.* **Fluid Phase Equilibria,** 31, 1986, 89-104.

Chordia, L., Robey, R., *Industrial Applications of Supercritical Fluids.* **5th International Symposium on Supercritical Fluids,** Atlanta, USA, 2000,

Crause, J. C., Nieuwoudt, I., *Fractionation of Paraffin Wax Mixtures.* **5th International Symposium on Supercritical Fluids,** Atlanta, U.S.A., 2000,

Crause, J. C., 2000, *Personal Communication* Department of Chemical Engineering, University of Stellenbosch,

de Haan, A. B., de Graaw, J., *A process for the fractionation of alkanes with supercritical carbon dioxide.* **2nd International Symposium on Supercritical Fluids,** Boston, USA, 1991,

Dohrn, R., Brunner, G, *High-Pressure Fluid-Phase Equilibria: Experimental Methods and Systems Investigated (1988-1993).* **Fluid Phase Equilibria,** 106, 1995, 213-282.

Donohue, M. D., Prausnitz, J.M., *Perturbed Hard Chain Theory for Fluid Mixtures: Thermodynamic Properties for Mixtures in Natural Gas and Petroleum Technology.* **AIChE Journal,** 24, (5), 1987, 849-860.

D'Souza, R. D., Patrick, J.R., Teja, A.S., *High Pressure Phase Equilibria in the Carbon Dioxide - n-Hexadecane and Carbon Dioxide - Water Systems.* **The Canadian Journal of Chemical Engineering,** 66, 1988, 319-323.

Elliott, J., Lira, C.T., **Introductory Chemical Engineering Thermodynamics.** Upper Saddle River, Prentice Hall PTR, 1999.

Fall, D. J., Fall, J.L., Luks, K.D., *Liquid-Liquid-Vapor Immiscibility Limits in Carbon Dioxide + n-Paraffin Mixtures.* **J. Chem. Eng. Data,** 30, 1985, 82-88.

Fornari, R. E., Allesi, P., Kikic, I., *High Pressure Phase Equilibria: Experimental Methods and Systems Investigated (1978-1987).* **Fluid Phase Equilibria,** 57, 1990, 1-33.

Gasem, K. A. M., Robinson, R.L., *Solubilities of Carbon Dioxide in Heavy Normal Paraffins (C20-C44) at Pressures to 9.6 MPa and Temperatures from 323 to 423 K.* **J. Chem. Eng. Data.,** 30, 1985, 53-56.

Heidemann, R. A., Fredenslund, A., *Vapour-Liquid Equilibria in Complex Mixtures.* **I.Chem.E.Symposium Series No. 104,** 1987, A273-A321.

Hickey, R. F., White, C.M., Levander, C.J., McIlvried, H.G., Quiring, M.S., Rosebeary, P.R., *Fischer-Tropsch Catalyst Wax Separation.*

Huang, S. H., Lin, H.M., Chao, K.C., *Solubility of Carbon Dioxide, Methane, and Ethane in n-Eicosane.* **J. Chem. Eng. Data,** 33, 1988 a, 145-147.

Huang, S. H., Lin, H.M., Chao, K.C., *Solubility of Carbon Dioxide, Methane, and Ethane in n-Octacosane.* **J. Chem. Eng. Data,** 33, 1988 b, 143-145.

Huie, N. C., Luks, K.D., James, P.K., *The Phase Behaviour of Systems Carbon Dioxide-n-Eicosane and Carbon Dioxide-n-Decane-n-Eicosane.* **Journal of Chemical Engineering Data,** 18, (3), 1973, 311-313.

Humphrey, J. L., Rocha, J.A., Fair, J.R., *The essentials of extraction.* **Chemical Engineering,** (September 17), 1984, 76-91.

Kaul, B. K., Prausnitz, J.M., *Solubilities of Heavy Hydrocarbons in Compressed Methane, Ethane, and Ethylene: Dew-Point Temperatures for Gas Mixtures Containing Small and Large Molecules.* **AIChE Journal,** 24, (2), 1978, 223-231.

Kim, C. H., Vimalchand, P.M. Donohue, Sandler, S.I., *Local Composition Model for Chainlike Molecules: A New Simplified Version of the Perturbed Hard Chain Theory.* **AIChE Journal,** 32, (10), 1986, 1726-1734.

Kordas, A., Konstantinos, T., Stamataki, S., Tassios, D., *A Generalized correlation for the interaction coefficients of CO_2 - hydrocarbon binary mixtures.* **Fluid Phase Equilibria,** 93, 1994, 141-166.

Krukonis, V., Brunner, G., Perrut, M., *Industrial operations with supercritical fluids: Current processes and perspectives on the future.* **3rd International Symposium on Supercritical Fluids,** Strasbourg, France, 1994, Institut National Polytechnique.

Krukonis, V. J., *Supercritical Fluid Processing: Current Research and Operations.* **International Symposium on Supercritical Fluids,** Nice, France, 1988, Instutut National Polytechnique.

McHugh, M., Krukonis, V., **Supercritical fluid extraction : principles and practice.** Second Edition, Stoneham, Butterworth-Heinemann, 1994.

McHugh, M. A., Seckner, A.J., Yogan, T.J, *High-Pressure Phase Behaviour of Binary Mixtures of Octacosane and Carbon Dioxide.* **Ind. Eng. Chem. Funadam.,** 23, 1984, 493-499.

Nieuwoudt, I., *The Fractionation of High Molecular Weight Alkane Mixtures with Supercritical Fluids.* PhD (Engineering), University of Stellenbosch, Stellenbosch, 1994

Patel, N. C., Teja, A.S., *A New Cubic Equation of State for Fluids and Fluid Mixtures.* **Chemical Engineering Science,** 37, (3), 1982, 463-473.

Peng, D. Y., Robinson, D.B., *A new two constant equation of state.* **Ind. Eng. Fundam.,** 15, 1976, 59-64.

Peters, C. J., Van Der Kooi, H.J., De Swaan Arons, J., *Measurement and calculations of phase equilibria for (ethane+tetracosane) and (p,Vm,T) for liquid tetracosane.* **J. Chem. Thermodynamics,** 19, 1987, 395-405.

Peters, C. J., Spiegelaar, J., De Swaan Arons, J., *Phase Equilibria in Binary Mixtures of Etane + Docosane and Molar Volumes of Liquid Docosane.* **Fluid Phase Equilibria,** 41, 1988, 245-256.

Peters, C. J., de Roo, J.L., Lichtenthaler, R.N., *Measurements and calculations of phase equilibria in binary mixtures of ethane + eicosane.* **Fluid Phase Equilibria,** 69, 1991, 51-66.

Pilat, S., Godlewicz, M., *Method of separating high molecular weight mixtures.* U.S. Patent 2,188,013, Jan. 23. 1940.

Redlich, O., Kwong, J.N.S., *On the thermodynamics of solutions. V. An Equation of State. Fugacities of Gaseous Solutions.* **Chemical Reviews,** 44, 1949, 233-244.

Reid, R. C., Prausnitz, J.M., Sherwood, T.K., **The Properties of Gases and Liquids.** Fourth Edition, McGraw Hill, 1987.

Roebers, J. R., Thies, M. C., *An Equilibrium View Cell for Measuring Phase Equilibria at Elevated Temperatures and Pressures.* **Ind. Eng.Res.,** 29, 1990, 1568-1570.

Schmitt, W. J., Reid, R.C., *The Solubility of Paraffinic Hydrocarbons and their Derivatives in Supercritical Carbon Dioxide.* **Chem. Eng. Comm.,** 64, 1988, 155-176.

Schwarz, C., 2000, *Personal Communication* Department of Chemical Engineering, University of Stellenbosch,

Sequeira Jr., A., **Lubricant Base Oil and Wax Processing.** New York, Marcel Dekker, 1994.

Smith, J. M., Van Ness, H.C., Abbot, M.M., **Introduction to Chemical Engineering Thermodynamics.** Fifth Edition, New York, The McGraw-Hill Companies, Inc., 1996.

Soave, G., *Equilibrium constants for the modified Redlich-Kwong equation of state.* **Chem. Eng. Sci.,** 27, 1972, 1197.

Spee, M., Schneider, G.M., *Fluid Phase Equilibrium Studies on Binary and Tertiary Mixtures of Carbon Dioxide with Hexadecane, 1-Dodecanol, 1,2-Octanediol and Dotriacontane at 393.2 K and at pressures up to 100 MPa.* 1991,

Stryjek, R., Vera, J.H., *An Improved Equation of State.* **Equations of State - Theories and Applications,** American Chemical Society, 560-570, 1986 a

Stryjek, R., Vera, J.H., *PRSV: An Improved Peng-Robinson Equation of State for Pure Compounds and Mixtures.* **The Canadian Journal of Chemical Engineering,** 64, 1986 b, 323-333.

Travers, M. W., Usher, F. L., *On the Behaviour of Certain Substances at their Critical Temperatures.* **Proc. Roy. Soc. A.,** 78, 1906, 247-261.

Tsai, F. N., Huang, S.H., Lin, H.M., Chao, K.C., *Solubility of Methane, Ethane, and Carbon Dioxide in a Mobil Fisher-Tropsch Wax and in n-Paraffins.* **The Chemical Engineering Journal,** 38, 1988, 41-46.

Via, J. C. M. B., C.L., Taylor, L.T., *Supercritical Fluid Fractionation of Low Molecular Weight, High-Density Polyethylene Wax Using Carbon Dioxide, Propane, and Propane-Modified Carbon Dioxide.* **Analytical Chemistry,** 66, (5), 1994, 603-609.

Wang, L. S., Guo, T.M., *A Cubic Simplified Perturbed Hard-Chain Equation of State for Fluids with Chainlike Molecules.* **The Canadian Journal of Chemical Engineering,** 71, 1993, 591-604.

Wei, Y. S., Sadus, R.J., *Equations of State for the Calculation of Fluid Phase Equilibria.* **AIChE Journal,** 46, (1), 2000, 169-196.

Yao, J. S., Tsai, F.N., *Solubilities of Heavy n-Paraffins in Subcritical and Supercritical Carbon Dioxide.* **J. Chem. Eng. Data,** 38, 1993, 171-174.

Zabaloy, M. S., Vera, J.H., *The Peng-Robinson Sequel. An Analysis of the Particulars of the Second and Third Generations.* **Industrial Engineering Chemistry Research,** 37, 1998, 1591-1597.

Appendix A: Detail View Cell Design

A 1 CELL CHAMBER
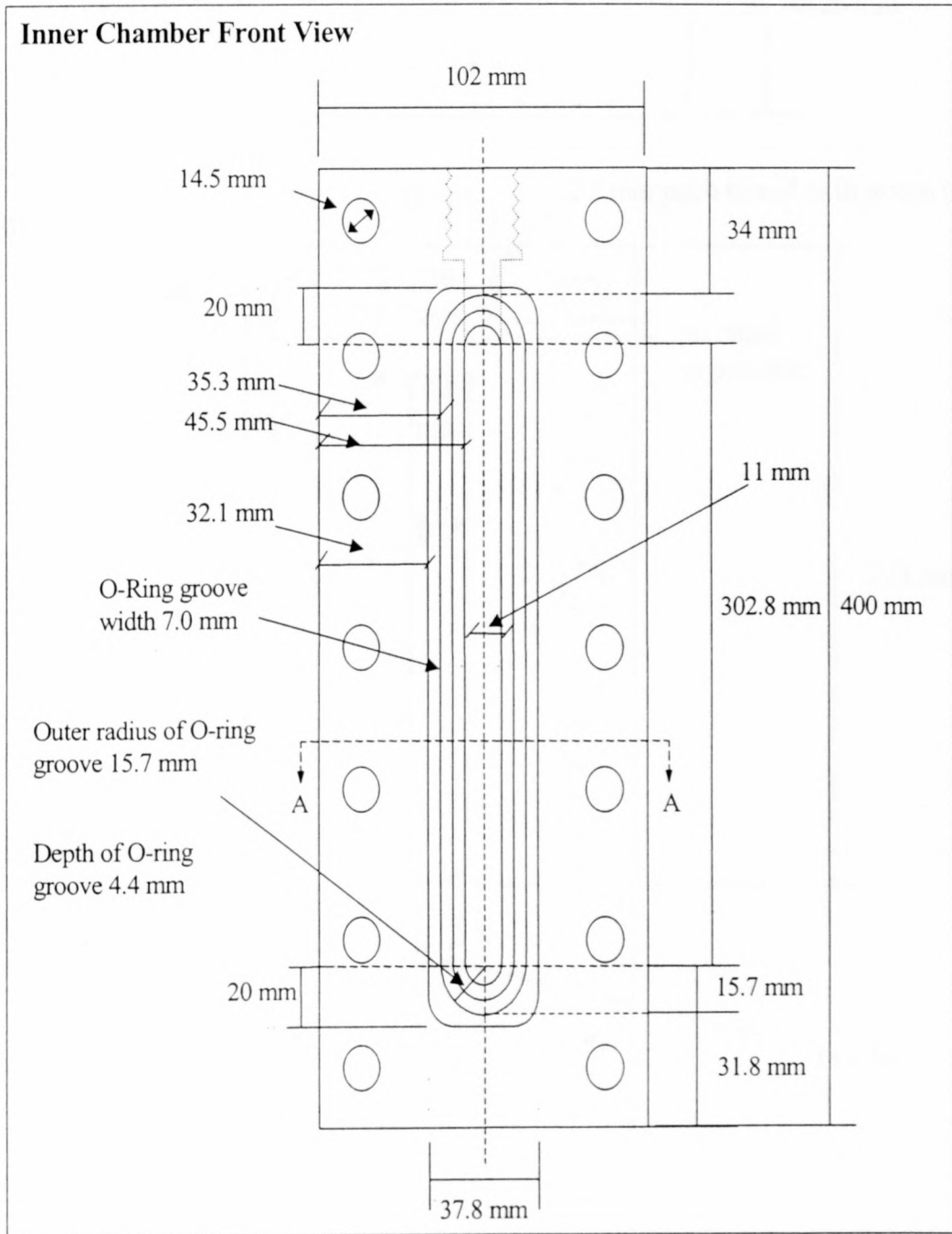
Figure A-1 Cell Inner Chamber (I)

Cut A-A

37.8 mm

11 mm

6.0 mm
4.4 mm

B - B   48.26 mm

Cut B-B

32 mm

2.5 mm pitch thread to fit piston unit

23 mm

30 mm

24 mm

As small as possible

Teflon insert

Drill with 17 mm bit

213 mm

Teflon Insert

30 mm

24 mm   16 mm

11 mm
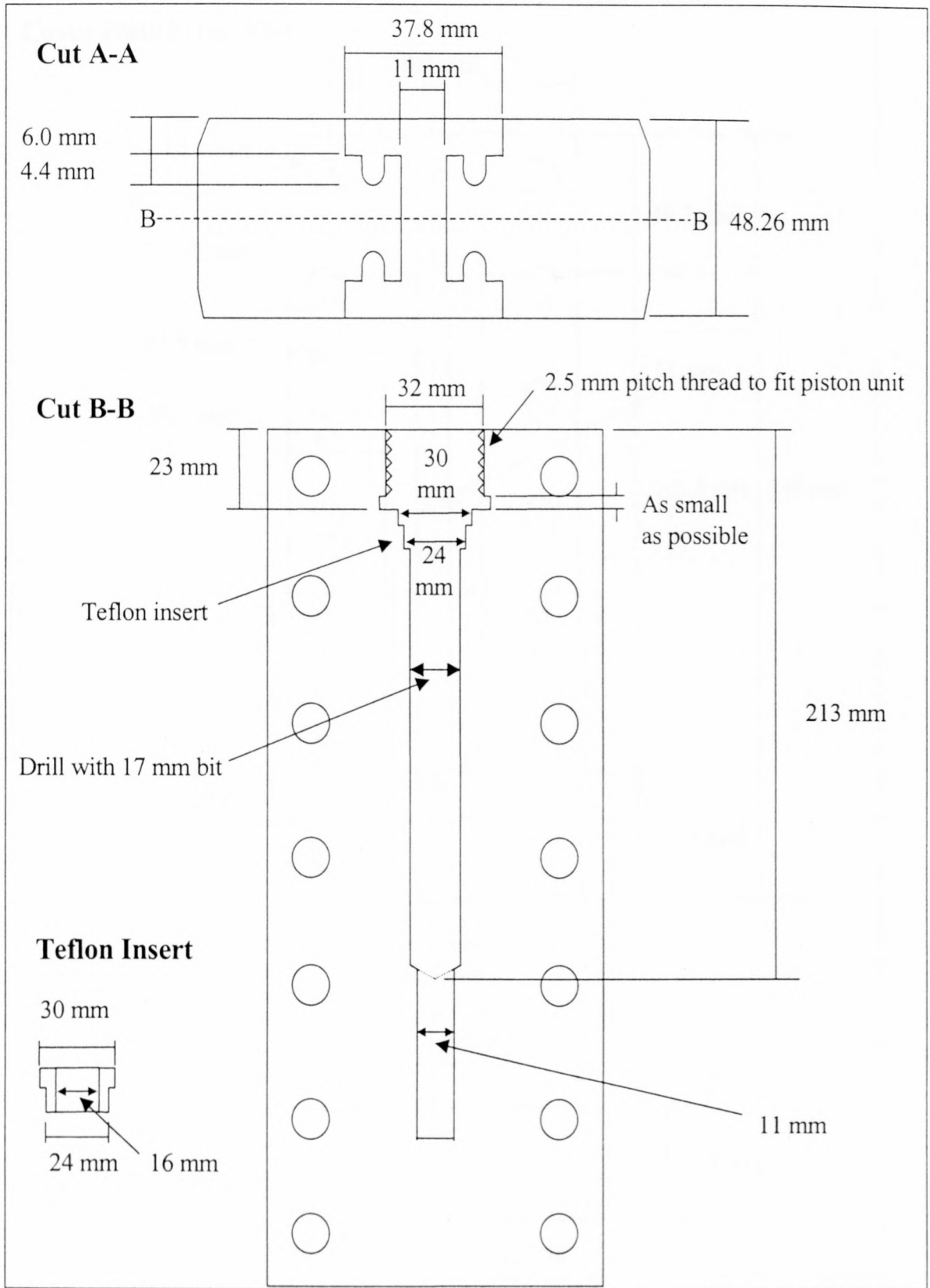
Figure A-2 Cell Inner Chamber (II)

Cover Plate Front View
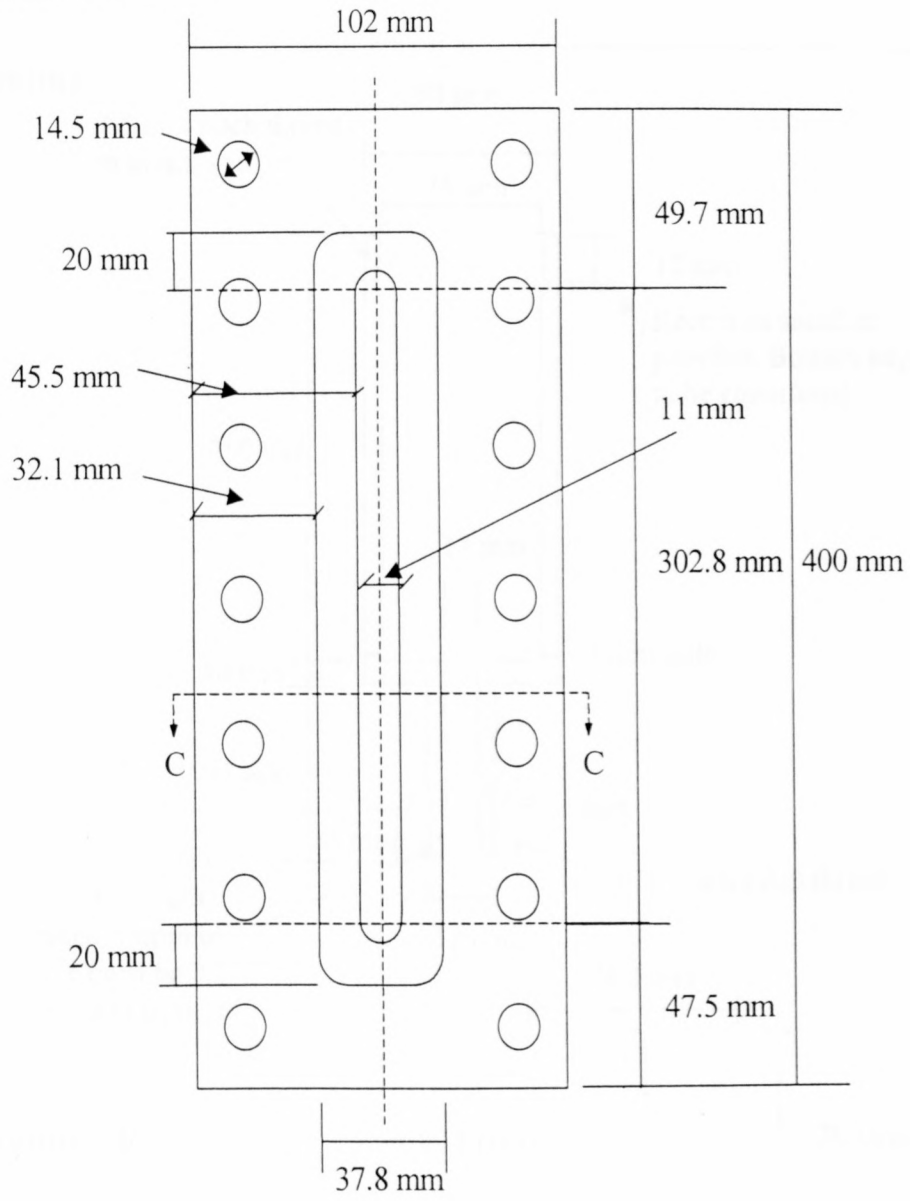
Cut C-C
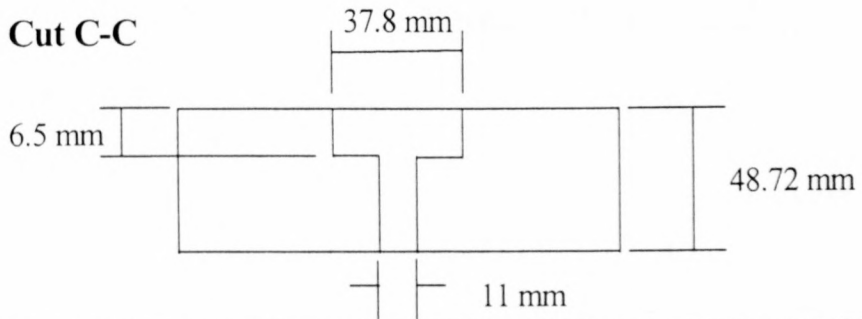
Figure A-3 Cell Cover Plate

A.2 PISTON UNIT

Piston Housing

2.5 mm pitch thread
to match cap

90 mm

75 mm

12 mm

Recess as small as
possible. Bottom edge
to be chamfered

250 mm

17 mm

3 mm hole

10 mm

98 mm

3 mm

25 mm

2.5 mm pitch thread

Width of o-ring groove to
be 3.4 mm. Sharp edges
must be broken. Depth of
o-ring groove must be 2.1
mm. O-ring 4 mm from tip

32 mm

74.4 mm

Piston Housing Lid

Piston

260 mm

75 mm

1/8" NPT

21 mm

28 mm

2.5 mm pitch
thread

320 mm

O-ring Groove cut to
fit O-ring dimentions

16.5 mm

Figure A-4 Piston Unit Design

A.3 PUMP
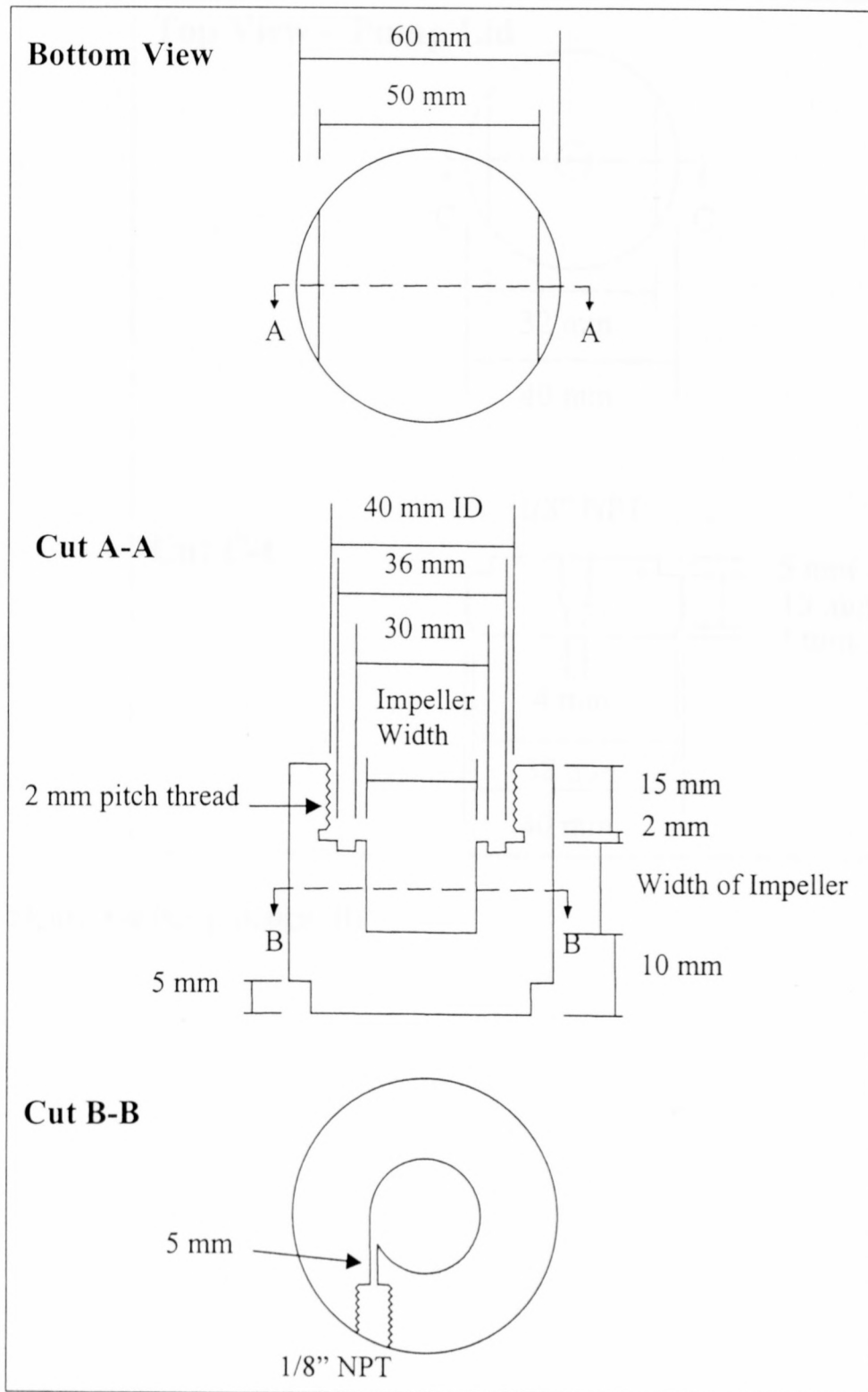
Figure A-5 Pump Design (I)
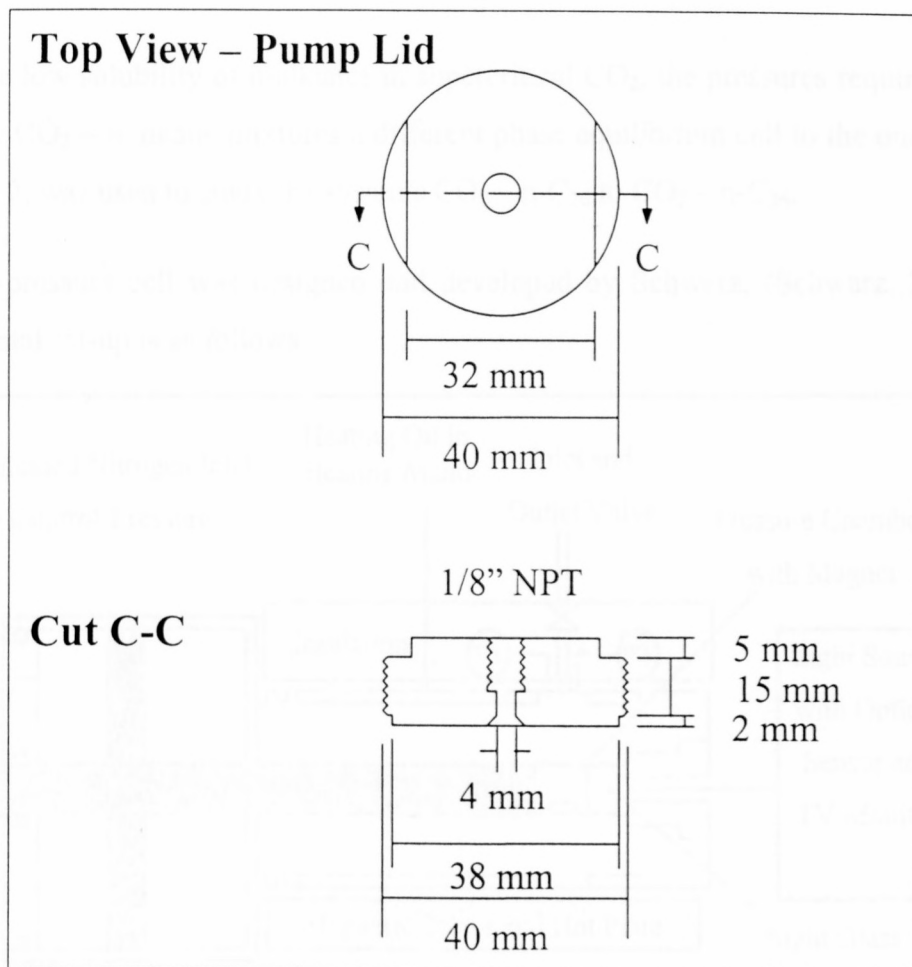
Figure A-6 Pump Design (II)

Appendix B: High Pressure Phase Equilibrium Cell

Due to the low solubility of n-alkanes in supercritical CO_2, the pressures required to force the binary CO_2 – n-alkane mixtures a different phase equilibrium cell to the one discussed in section 2, was used to study the systems CO_2 – n-C_{20} to CO_2 – n-C_{36}.

The high-pressure cell was designed and developed by Schwarz, (Schwarz, 2000). The experimental set-up is as follows:
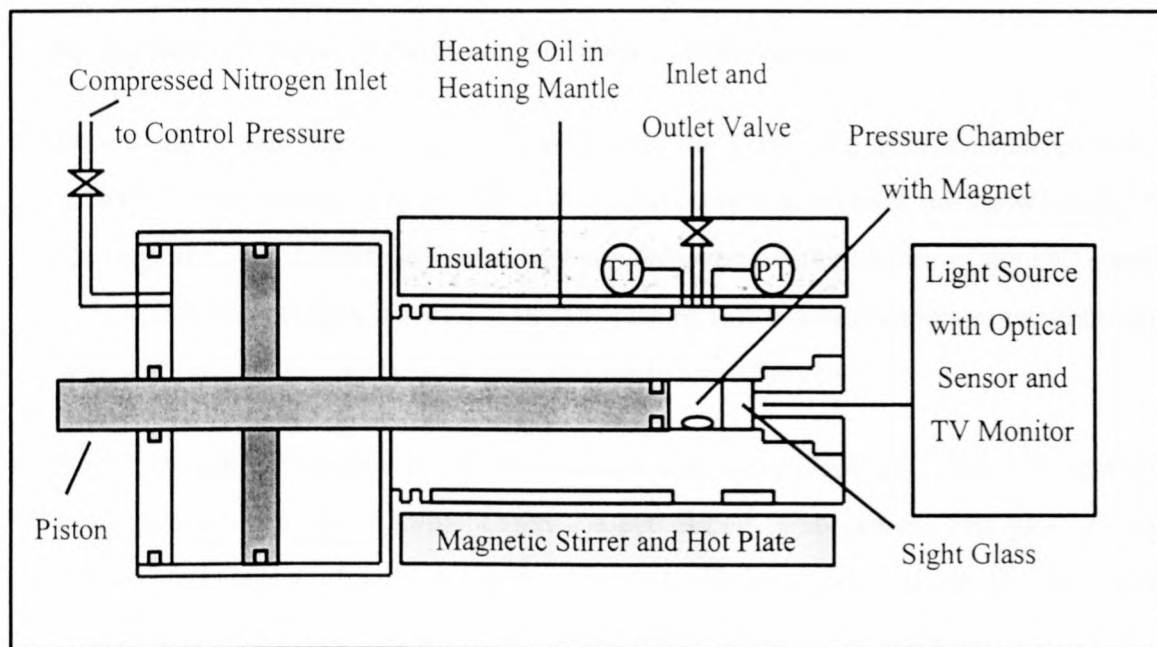
Figure B-1 High-Pressure Cell Design (Schwarz, 2000)

When the piston is extended to its maximum, the cell volume is 38.61 cm³ and a volume reduction of 20 % corresponding to a minimum volume of 8.06 cm³ can be achieved.

The temperature control in this cell is achieved by circulating Dowtherm heating oil from a heating circulator through an outer cell mantle.

The pressure is measured by an ISI NHG pressure transducer (model 171) that was calibrated with a dead weight balance for temperature and total pressure effects. See Appendix E. The piston ratio in the high-pressure cell is much larger than in the view cell, much higher pressures can therefore be achieved while still using standard N_2 cylinder gas to exert the force on the piston.

The sight glass in the high-pressure cell is much smaller than the glass used in the view cell. This enables the high-pressure cell to withstand much higher operating pressures. There is only one sight glass in the cell chamber. Light from a light source in front of the cell sight glass will be reflected off the back of the cell chamber (the piston), enabling the illumination of the cell contents.

This high pressure cell has a maximum working pressure of 310 bar and a design pressure of 500 bar.

Using this high-pressure cell, however, has several disadvantages:

- Due to the small cell volume compared with the view cell, only a small amount of material can be loaded into it. This will magnify any inaccuracies during weighing and loading, and will increase the uncertainty in the overall composition of the cell content. This effect is especially noticeable in the areas of low heavy component concentration, where at times, less than 0.5g of wax was loaded into the cell.

- The temperature control is of this unit is also very difficult. The environmental temperature has a major influence on the actual cell temperature. This has the effect that the data at each 'isotherm' was in fact taken over a range of 3.6 K. The average temperature of a set of data was taken as the temperature of the isotherm.

- It was found that the mixing achieved in this cell was not as good as with the view cell. At certain conditions, it took a couple of hours for the cell contents to reach equilibrium.

- Pressure control in the cell was very difficult because of the inertia of the piston system. There had to be a large pressure difference between the cell content and the pressure exerted by the N_2 before the piston would move. This resulted in the fact that the phase transition pressure range could not be reduced to the extent that it was when using the view cell. See section 2.3.2. With this cell, the phase boundary pressure was determined within a pressure range of 1 bar.

- Because of the high-pressure cell design, it was not as easy to observe the phase transitions as when using the view cell.

Appendix C: Detection of Phase Transition with Change in System Density

As discussed in section 2.1.2 the phase boundary can be detected by monitoring the change in the pressure-volume or pressure-density relationship.

There is a linear relationship between the pressure and volume of the system, but when a phase transition occurs the slope of the linear pressure-volume line changes. As the change in the slope of the line is gradual it is necessary to extrapolate the pressure-volume lines to determine the point of intersect. This point represents the phase boundary pressure.

The change in the length of the rod protruding from the top of the piston unit is a direct function of the change in the cell volume, and hence the density of the cell contents. The change in the rod length was therefore used to determine the phase boundary pressure.
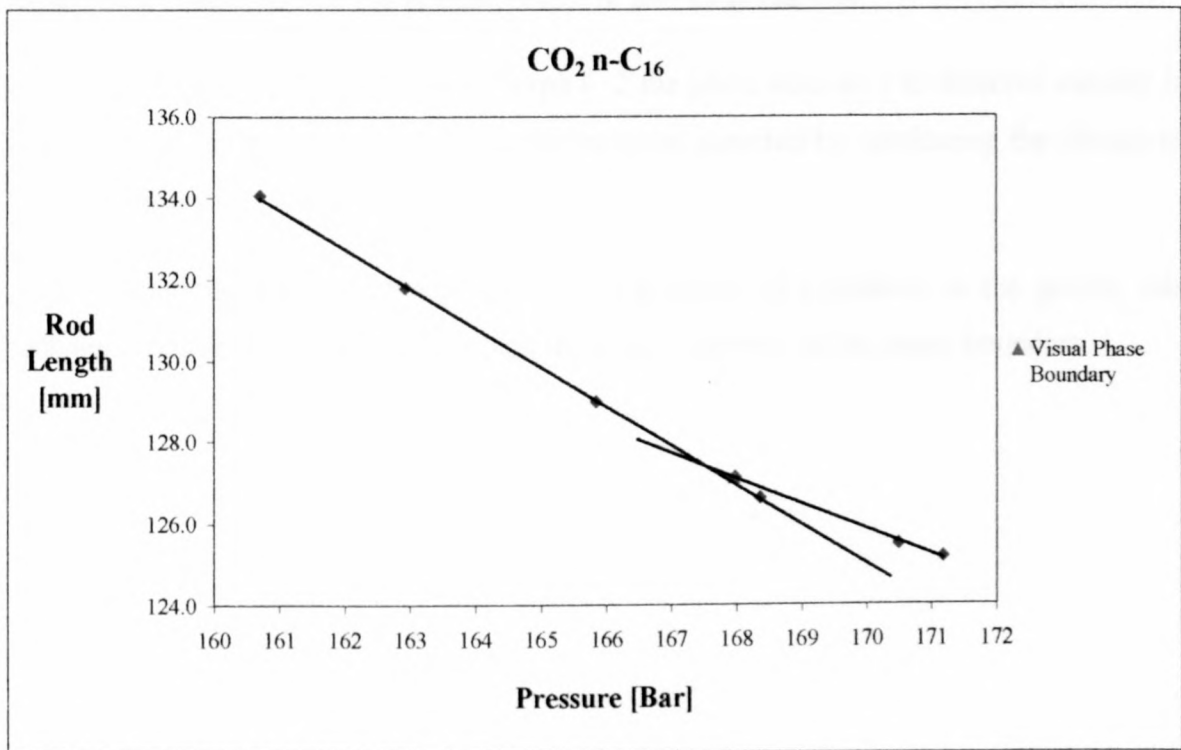
Graph C-1 The CO_2 – n-C_{16} system at 323 K and $z_{nC16\ mass}$ 0.31
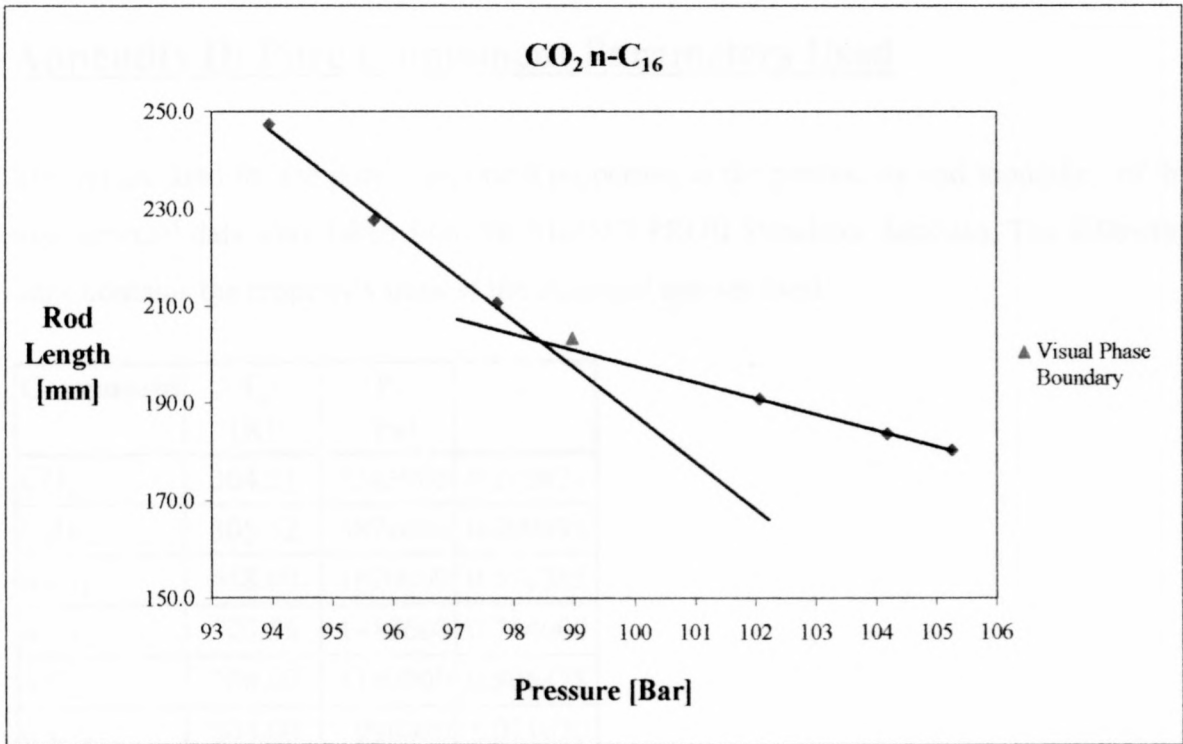
CO$_2$ n-C$_{16}$

Graph C-2 The CO$_2$ – n-C$_{16}$ system at 313 K and $z_{nC16\ mass}$ 0.05

As can be seen from Graph C-1 and Graph C-2 the phase boundary as detected visually is about 0.5 bar higher than the phase transition point detected by monitoring the change in the cell volume.

As the technique used above requires the extrapolation of trendlines on the graphs, this technique was deemed less accurate than the visual detection of the phase boundary.

Appendix D: Pure Component Parameters Used

The values used for the pure component properties in the processing and modelling of the experimental data were taken from the SIMSCI PROII Simulator database. The following table contains the property values of the chemical species used.

Component	T_c [K]	P_c [Pa]	ω
CO_2	304.21	7383000	0.223621
C_2H_6	305.32	4872000	0.099493
n-C_{12}	658.00	1820000	0.576385
n-C_{16}	720.55	1418600	0.744000
n-C_{20}	768.00	1160000	0.906878
n-C_{24}	804.00	980000	1.071020
n-C_{28}	832.00	850000	1.237520
n-C_{36}	874.00	680000	1.525960

Table D-1 Pure component property values used in this work

Appendix E: Pressure Sensor Calibration Data

E.1 VIEW CELL PRESSURE SENSOR

The ISI Digital Melt Pressure Gauge (Model 0251A) used in the view cell was calibrated with a dead weight pressure gauge for temperature and pressure effects.

The following pressure correction correlation was derived:

$$\Delta P = -4.53e-05 * P^2 + 0.019197491P + 0.057886735T - 19.2 \tag{E.1}$$

Where

$$\Delta P = P_{Rdg} - P_{Act} \tag{E.3}$$

With P in Bar and T in K. The pressure in the cell can then be calculated by:

$$P_{Abs} = P_{rdg} - \Delta P + P_{Atm} \tag{E.3}$$

A different pressure meter, of a similar type, was used in the study The CO_2 – n-C_{12} and CO_2 – n-C_{16} systems. The following ΔP correlation was developed for it (P in Bar and T in K):

$$\Delta P = -1.96e-08 * P^2 + 0.037682P + 0.8597T - 57.356 \tag{E.4}$$

Graph E-1 and Graph E-2 are plots of the pressure correction correlations for the two pressure sensors.
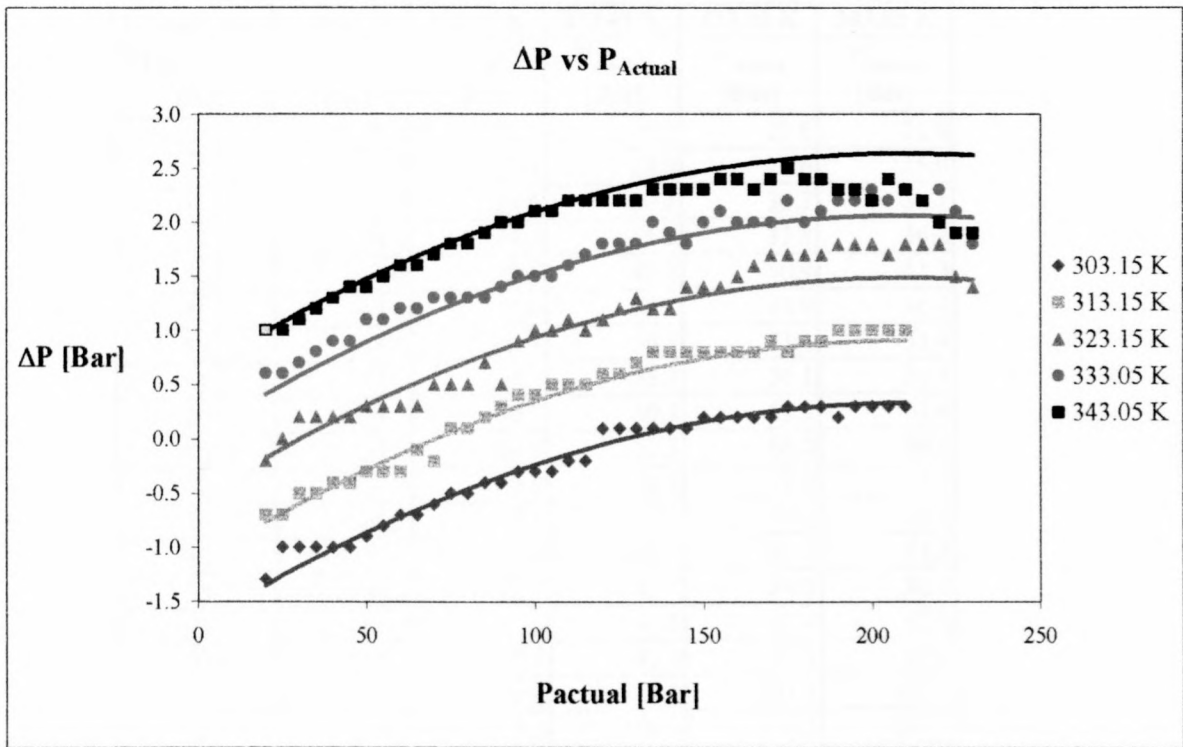
Graph E-1 Pressure Sensor Calibration for View Cell
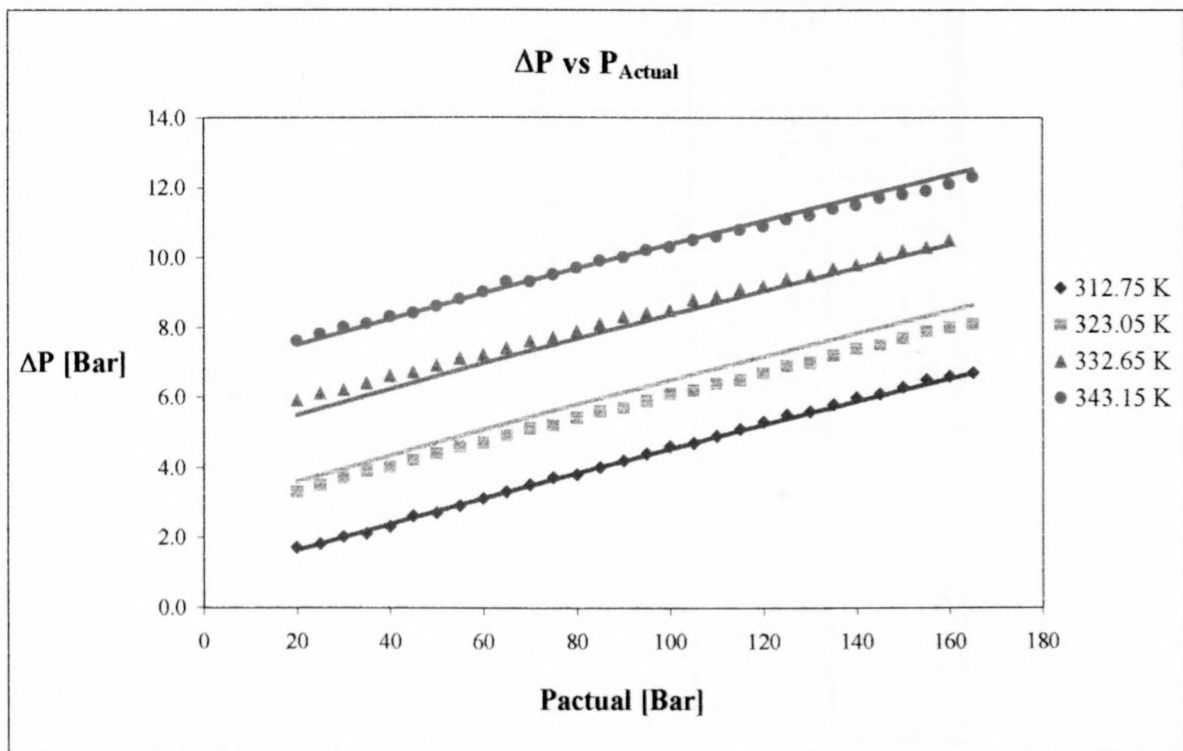
Graph E-2 Pressure Sensor Calibration for View Cell (CO_2 – n-C_{12} and CO_2 – n-C_{16} systems)

Temperature	303.15 K	313.15 K	323.15 K	333.05 K	343.05 K
$P_{dead\ weight}$ [Bar]	$P_{reading}$ [Bar]	$P_{reading}$ [Bar]	$P_{reading}$ [Bar]	$P_{reading}$ [Bar]	$P_{reading}$ [Bar]
20	18.7	19.3	19.8	20.6	21.0
25	24.0	24.3	25.0	25.6	26.0
30	29.0	29.5	30.2	30.7	31.1
35	34.0	34.5	35.2	35.8	36.2
40	39.0	39.6	40.2	40.9	41.3
45	44.0	44.6	45.2	45.9	46.4
50	49.1	49.7	50.3	51.1	51.4
55	54.2	54.7	55.3	56.1	56.5
60	59.3	59.7	60.3	61.2	61.6
65	64.3	64.9	65.3	66.2	66.6
70	69.4	69.8	70.5	71.3	71.7
75	74.5	75.1	75.5	76.3	76.8
80	79.5	80.1	80.5	81.3	81.8
85	84.6	85.2	85.7	86.3	86.9
90	89.6	90.3	90.5	91.4	92.0
95	94.7	95.4	95.9	96.5	97.0
100	99.7	100.4	101.0	101.5	102.1
105	104.7	105.5	106.0	106.5	107.1
110	109.8	110.5	111.1	111.6	112.2
115	114.8	115.5	116.0	116.7	117.2
120	120.1	120.6	121.1	121.8	122.2
125	125.1	125.6	126.2	126.8	127.2
130	130.1	130.7	131.3	131.8	132.2
135	135.1	135.8	136.2	137.0	137.3
140	140.1	140.8	141.2	141.9	142.3
145	145.1	145.8	146.4	146.8	147.3
150	150.2	150.8	151.4	152.0	152.3
155	155.2	155.8	156.4	157.1	157.4
160	160.2	160.8	161.5	162.0	162.4
165	165.2	165.8	166.6	167.0	167.3
170	170.2	170.9	171.7	172.0	172.4
175	175.3	175.8	176.7	177.2	177.5
180	180.3	180.9	181.7	182.0	182.4
185	185.3	185.9	186.7	187.1	187.4
190	190.2	191.0	191.8	192.2	192.3
195	195.3	196.0	196.8	197.2	197.3
200	200.3	201.0	201.8	202.3	202.2
205	205.3	206.0	206.7	207.2	207.4
210	210.3	211.0	211.8	212.3	212.3
215		216.0	216.8	217.2	217.2
220		221.0	221.8	222.3	222.0
225		225.9	226.5	227.1	226.9
230		230.8	231.4	231.8	231.9

Table E-1 View cell pressure sensor calibration data.

Temperature	312.75 K	323.05 K	332.65 K	343.15 K
$P_{dead\ weight}$ [Bar]	$P_{reading}$ [Bar]	$P_{reading}$ [Bar]	$P_{reading}$ [Bar]	$P_{reading}$ [Bar]
20	21.7	23.3	25.9	27.6
25	26.8	28.5	31.1	32.8
30	32.0	33.7	36.2	38.0
35	37.1	38.9	41.4	43.1
40	42.3	44.0	46.6	48.3
45	47.6	49.2	51.7	53.4
50	52.7	54.4	56.9	58.6
55	57.9	59.6	62.1	63.8
60	63.1	64.7	67.2	69.0
65	68.3	69.9	72.4	74.3
70	73.5	75.1	77.6	79.3
75	78.7	80.2	82.7	84.5
80	83.8	85.4	87.9	89.7
85	89.0	90.6	93.1	94.9
90	94.2	95.7	98.3	100.0
95	99.4	100.9	103.4	105.2
100	104.6	106.1	108.5	110.3
105	109.7	111.2	113.8	115.5
110	114.9	116.4	118.9	120.6
115	120.1	121.5	124.1	125.8
120	125.3	126.7	129.2	130.9
125	130.5	131.9	134.4	136.1
130	135.6	137.0	139.5	141.2
135	140.8	142.2	144.7	146.4
140	146.0	147.4	149.8	151.5
145	151.1	152.5	155.0	156.7
150	156.3	157.7	160.2	161.8
155	161.5	162.9	165.3	166.9
160	166.6	168.0	170.5	172.1
165	171.7	173.1	0.0	177.3

Table E-2 View cell pressure sensor calibration data (CO_2 – n-C_{12} and CO_2 – n-C_{16} systems)

E.2 HIGH-PRESSURE CELL CALIBRATION

The ISI NHG pressure gauge (Model 171) in the high-pressure was also calibrated for temperature and pressure effects. The following equation was derived for the pressure deviation:

$$\Delta P = 3.69e - 05 * P^2 + 0.082441T - 22.5904 \qquad (E.5)$$

With P in Bar and T in K. Equations E.3 and E.5 are used to calculate the actual pressure in the cell. The ΔP correlation is shown in Graph E-3.
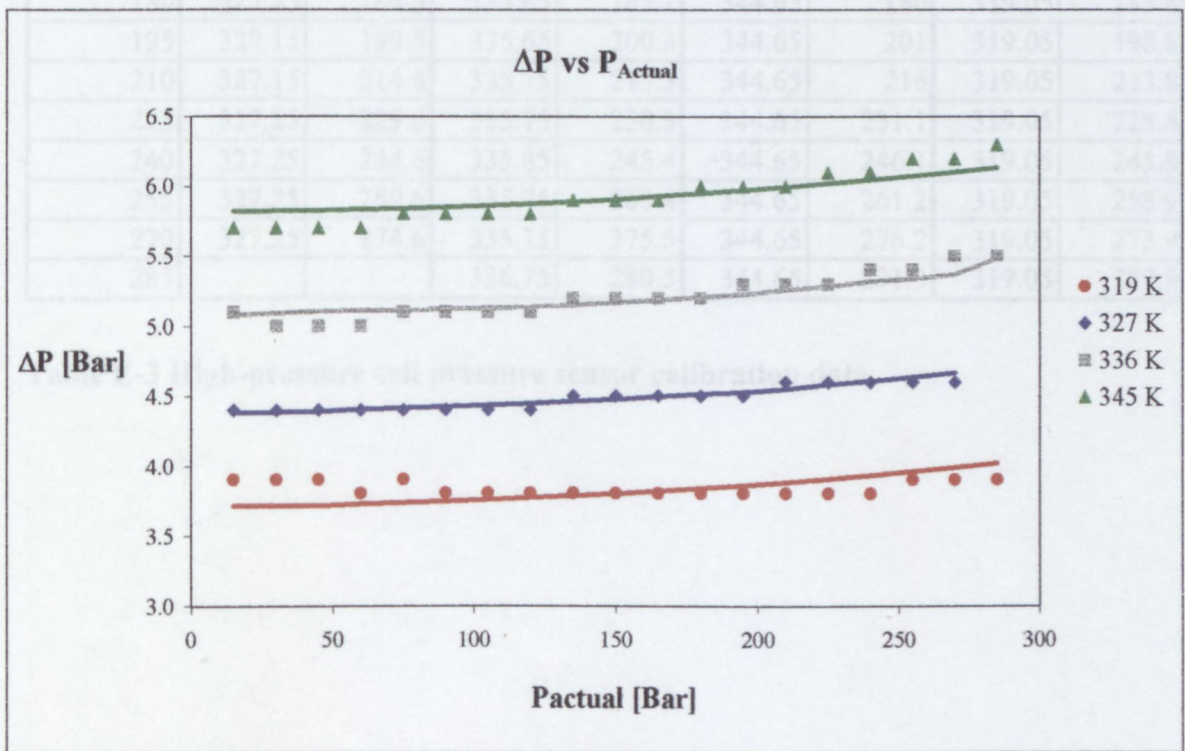
Graph E-3 High-pressure cell pressure sensor calibration data.

P$_{dead\ weight}$ [Bar]	Temp K	P$_{reading}$ [Bar]	Temp K	P$_{reading}$ [Bar]	Temp K	P$_{reading}$ [Bar]	Temp K	P$_{reading}$ [Bar]
15	327.15	19.4	335.65	20.1	344.55	20.7	319.05	18.9
30	327.15	34.4	335.75	35	344.55	35.7	319.05	33.9
45	327.15	49.4	335.85	50	344.55	50.7	318.95	48.9
60	327.25	64.4	335.85	65	344.55	65.7	319.05	63.8
75	327.25	79.4	335.75	80.1	344.55	80.8	319.05	78.9
90	327.25	94.4	335.75	95.1	344.55	95.8	319.05	93.8
105	327.25	109.4	335.65	110.1	344.55	110.8	319.05	108.8
120	327.25	124.4	335.65	125.1	344.55	125.8	319.05	123.8
135	327.25	139.5	335.65	140.2	344.55	140.9	319.05	138.8
150	327.25	154.5	335.65	155.2	344.55	155.9	319.05	153.8
165	327.25	169.5	335.65	170.2	344.65	170.9	319.05	168.8
180	327.25	184.5	335.65	185.2	344.65	186	319.05	183.8
195	327.15	199.5	335.65	200.3	344.65	201	319.05	198.8
210	327.15	214.6	335.75	215.3	344.65	216	319.05	213.8
225	327.25	229.6	335.75	230.3	344.65	231.1	319.05	228.8
240	327.25	244.6	335.85	245.4	344.65	246.1	319.05	243.8
255	327.25	259.6	335.75	260.4	344.65	261.2	319.05	258.9
270	327.25	274.6	335.75	275.5	344.65	276.2	319.05	273.9
285			336.75	290.5	344.65	291.3	319.05	288.9

Table E-3 High-pressure cell pressure sensor calibration data.

Appendix F: Phase Equilibrium Data

F.1 CO_2 – N-ALKANE SYSTEMS

CO_2 - nC_{12} System							
Temperature 313.2 K		Temperature 323.2 K		Temperature 333.2 K		Temperature 343.2 K	
P_{abs} [Bar]	$z_{mass\ nC12}$	P_{abs} [Bar]	$z_{mass\ nC12}$	P_{abs} [Bar]	$z_{mass\ nC12}$	P_{abs} [Bar]	$z_{mass\ nC12}$
85.7	0.028	99.0	0.028	110.4	0.028	120.0	0.028
84.9	0.051	101.3	0.051	117.5	0.051	130.5	0.051
84.2	0.103	102.8	0.103	122.1	0.103	141.0	0.103
83.5	0.200	102.9	0.200	123.3	0.200	143.0	0.200
82.8	0.317	101.7	0.317	121.6	0.317	140.0	0.317
82.2	0.405	99.1	0.405	117.3	0.405	134.3	0.405
79.5	0.483	94.4	0.483				

Table F-1 CO_2 – n-C_{12} Phase Equilibrium Data

CO_2 - nC_{16} System			
Temperature 313.2 K		Temperature 323.2 K	
P_{abs} [Bar]	$z_{mass\ nC16}$	P_{abs} [Bar]	$z_{mass\ nC16}$
99.0	0.050	121.4	0.050
123.9	0.099	142.5	0.099
142.0	0.138	154.5	0.138
154.7	0.176	162.4	0.176
162.8	0.226	167.3	0.226
163.7	0.247	167.9	0.247
165.1	0.313	168.4	0.285
159.8	0.396	168.0	0.313
146.6	0.442	162.6	0.396
132.0	0.507	140.5	0.507
133.8	0.511	142.6	0.511
111.1	0.529	101.5	0.606
95.0	0.588		
85.5	0.606		

Table F-2 CO_2 – n-C_{16} Phase Equilibrium Data

CO$_2$ - nC$_{20}$ System					
Temperature 315.9 K		**Temperature 320.6 K**		**Temperature 329.6 K**	
P_{abs} [Bar]	$z_{mass\ nC20}$	P_{abs} [Bar]	$z_{mass\ nC20}$	P_{abs} [Bar]	$z_{mass\ nC20}$
100.9	0.018	109.1	0.018	121.8	0.018
196.1	0.055	157.4	0.034	166.2	0.034
249.6	0.502	197.9	0.055	205.0	0.055
185.2	0.559	223.1	0.502	258.9	0.470
106.0	0.619	175.6	0.559	205.6	0.502
77.4	0.660	110.3	0.619	175.3	0.559
		86.4	0.660	118.6	0.619
				104.3	0.660

Temperature 339.1 K		**Temperature 348.3 K**	
P_{abs} [Bar]	$z_{mass\ nC20}$	P_{abs} [Bar]	$z_{mass\ nC20}$
135.0	0.018	140.9	0.018
166.2	0.034	203.1	0.034
205.0	0.055	219.7	0.055
258.9	0.470	279.0	0.132
205.6	0.502	293.2	0.224
175.3	0.559	291.2	0.277
		287.9	0.359
		247.9	0.470
		188.6	0.559
		138.5	0.619
		115.0	0.660

Table F-3 CO$_2$ – n-C$_{20}$ Phase Equilibrium Data

CO$_2$ - nC$_{24}$ System							
Temperature 329.7 K		Temperature 339.2 K		Temperature 348.1 K		Temperature 357.1 K	
P$_{abs}$ [Bar]	z$_{mass\ nC24}$	P$_{abs}$ [Bar]	z$_{mass\ nC24}$	P$_{abs}$ [Bar]	z$_{mass\ nC24}$	P$_{abs}$ [Bar]	z$_{mass\ nC24}$
190.4	0.022	203.6	0.022	213.8	0.022	226.6	0.022
246.2	0.035	234.5	0.035	249.7	0.035	279.8	0.046
281.4	0.046	283.7	0.046	279.8	0.046	301.6	0.507
258.9	0.561	239.6	0.561	235.1	0.561	239.5	0.561
216.0	0.583	208.9	0.583	212.0	0.583	217.8	0.583
174.9	0.618	176.8	0.618	184.3	0.618	192.4	0.618
154.8	0.627	166.0	0.627	172.4	0.627	185.0	0.627

Table F-4 CO$_2$ – n-C$_{24}$ Phase Equilibrium Data

CO$_2$ - nC$_{28}$ System							
Temperature 338.5 K		Temperature 348.0 K		Temperature 357.0 K		Temperature 366.4 K	
P$_{abs}$ [Bar]	z$_{mass\ nC28}$	P$_{abs}$ [Bar]	z$_{mass\ nC28}$	P$_{abs}$ [Bar]	z$_{mass\ nC28}$	P$_{abs}$ [Bar]	z$_{mass\ nC28}$
196.8	0.017	226.3	0.017	239.8	0.017	254.8	0.019
232.5	0.019	232.4	0.019	242.2	0.019	274.8	0.026
246.6	0.026	276.2	0.026	272.2	0.026	288.8	0.028
278.7	0.028	289.9	0.028	284.4	0.028	289.5	0.569
272.9	0.617	257.3	0.617	282.5	0.569	253.2	0.617
272.6	0.622	257.1	0.622	252.7	0.617	254.5	0.622
200.9	0.632	199.1	0.632	252.1	0.622	212.9	0.632
140.1	0.685	148.4	0.685	207.4	0.632	172.3	0.685
				162.3	0.685		

Table F-5 CO$_2$ – n-C$_{28}$ Phase Equilibrium Data

CO₂ - nC₃₆ System							
Temperature 338.5 K		Temperature 348 K		Temperature 357 K		Temperature 366.4 K	
P_{abs} [Bar]	$z_{mass\ nC36}$	P_{abs} [Bar]	$z_{mass\ nC36}$	P_{abs} [Bar]	$z_{mass\ nC36}$	P_{abs} [Bar]	$z_{mass\ nC36}$
289.6	0.008	285.4	0.008	289.8	0.008	289.7	0.008
223.2	0.014	254.4	0.010	260.6	0.010	260.0	0.010
0.0	0.660	234.3	0.014	250.0	0.014	254.4	0.014
258.2	0.679	263.8	0.019	266.3	0.019	272.6	0.019
237.4	0.693	292.6	0.022	276.9	0.022	273.1	0.022
201.0	0.713	297.5	0.660	291.3	0.660	285.6	0.660
		254.7	0.679	250.7	0.679	246.8	0.679
		233.7	0.693	231.5	0.693	235.1	0.693
		201.4	0.713	205.3	0.713	211.5	0.713

Table F-6 CO₂ – n-C₃₆ Phase Equilibrium Data

F.2 ETHANE – N-ALKANE SYSTEMS

Ethane - nC$_{16}$ System					
Temperature 312.9 K		Temperature 322.9 K		Temperature 332.8 K	
P_{abs} [Bar]	$z_{mass\ nC16}$	P_{abs} [Bar]	$z_{mass\ nC16}$	P_{abs} [Bar]	$z_{mass\ nC16}$
54.7	0.035	65.5	0.035	75.6	0.035
54.2	0.092	66.6	0.092	79.3	0.092
53.9	0.151	66.8	0.151	80.1	0.151
53.6	0.229	66.6	0.229	80.5	0.229
52.8	0.309	65.5	0.309	79.5	0.309
52.1	0.387	64.3	0.387	78.0	0.387
50.2	0.484	61.2	0.484	73.4	0.484
49.7	0.515	60.5	0.515	72.5	0.515
Temperature 342.8 K		Temperature 352.7 K			
P_{abs} [Bar]	$z_{mass\ nC16}$	P_{abs} [Bar]	$z_{mass\ nC16}$		
84.6	0.035	92.0	0.035		
90.8	0.092	100.9	0.092		
92.6	0.151	104.1	0.151		
93.5	0.229	105.4	0.229		
92.9	0.309	104.9	0.309		
91.4	0.387	104.0	0.387		
86.2	0.484	98.5	0.484		
84.9	0.515	97.7	0.515		

Table F-7 Ethane – n-C$_{16}$ Phase Equilibrium Data

Ethane - nC₂₄ System					
Temperature 332.8 K		Temperature 342.7 K		Temperature 352.7 K	
P_{abs} [Bar]	$z_{mass\ nC24}$	P_{abs} [Bar]	$z_{mass\ nC24}$	P_{abs} [Bar]	$z_{mass\ nC24}$
93.7	0.046	106.4	0.046	118.1	0.046
101.1	0.075	115.7	0.075	128.2	0.075
108.3	0.125	123.6	0.125	137.0	0.125
111.1	0.189	126.8	0.189	140.8	0.189
113.4	0.268	129.3	0.268	143.7	0.268
113.3	0.315	129.4	0.315	143.8	0.315
113.1	0.351	129.2	0.351	144.0	0.351
110.5	0.431	127.1	0.431	142.1	0.431
102.5	0.515	118.7	0.515	133.9	0.515
96.9	0.550	113.4	0.550	129.1	0.550

Table F-8 Ethane – n-C₂₄ Phase Equilibrium Data

Ethane - nC₂₈ System					
Temperature 337.8 K		Temperature 342.8 K		Temperature 352.6 K	
P_{abs} [Bar]	$z_{mass\ nC28}$	P_{abs} [Bar]	$z_{mass\ nC28}$	P_{abs} [Bar]	$z_{mass\ nC28}$
117.7	0.056	125.3	0.056	137.7	0.056
130.2	0.103	137.8	0.103	151.7	0.103
140.8	0.209	148.5	0.209	163.1	0.209
142.2	0.307	150.1	0.307	164.8	0.307
134.1	0.492	148.6	0.413	163.6	0.413
117.7	0.582	142.1	0.492	157.3	0.492
		126.1	0.582	141.7	0.582

Table F-9 Ethane – n-C₂₈ Phase Equilibrium Data

Appendix G: Experimental Data

Cell Information	View Cell	High-Pressure Cell
Total Cell Volume (0 piston displacement)	132.07 cm^3	38.43 cm^3
Piston Length (0 displacement)	233.85 mm	83.52 mm
Piston Diameter	16.52 mm	22.12 mm

Table G-1 Phase Equilibrium Cell Information

Table G-2 CO₂ – n-C₁₂ Experimental Data in View Cell

nC₁₂ before g	nC₁₂ after g	nC₁₂ mass loaded g	CO₂ before g	CO₂ after g	CO₂ mass loaded g	T 60.0 °C P rdg Bar	T 60.0 °C P actual Bar	T 60.0 °C Piston mm	T 70.0 °C P rdg Bar	T 70.0 °C P actual Bar	T 70.0 °C Piston mm
2.5	0.2	2.3	1138.4	1059.9	78.5	118.2	110.4	-	130	120.0	-
4.8	0.3	4.5	1145.3	1061	84.3	125.5	117.5	-	140.9	130.5	-
10.6	0.3	10.3	1150.3	1060.7	89.6	130.3	122.1	-	extrapol	141.0	-
21.4	0.6	20.8	1143.6	1060.5	83.1	131.5	123.3	237.02	extrapol	143.0	-
34.9	0.4	34.5	1138.4	1064.2	74.2	129.7	121.6	224.06	150.7	140.0	239.46
45.8	0.5	45.3	1130	1063.4	66.6	125.3	117.3	225.30	144.8	134.3	236.22
54.4	0.3	54.1	1126.1	1068.3	57.8						

Table G-3 CO₂ – n-C₁₆ Experimental Data in View Cell

nC₁₆ before g	nC₁₆ after g	nC₁₆ mass loaded g	CO₂ before g	CO₂ after g	CO₂ mass loaded g	T 40 P rdg Bar	T 40 P actual Bar	T 40 Piston mm	T 50 P rdg Bar	T 50 P actual Bar	T 50 Piston mm
5.5	0.5	5.0	1137.8	1042.3	95.5	102.5	99.0	203.48	127.6	121.4	231.16
9.9	0.3	9.6	1131.4	1044.1	87.3	128.3	123.9	98	149.4	142.5	112.46
15.4	0.5	14.9	1150.2	1057.3	92.9	147.0	142.0	136.28	161.8	154.5	163.64
18.7	0.3	18.4	1127.4	1041.3	86.1	160.1	154.7	106.8	170.0	162.4	99.82
25.2	0.5	24.7	1138.3	1053.7	84.6	168.5	162.8	121.54	175.0	167.3	145.36
26.4	0.3	26.1	1121.8	1042.3	79.5	169.4	163.7	107.1	175.6	167.9	127.12
29.4	0.4	29.0	1116.7	1044	72.7				176.2	168.4	98.84
34.1	0.5	33.6	1124.9	1051.2	73.7	170.8	165.1	110.32	175.7	168.0	127.14
44.2	0.5	43.7	1127.7	1061.1	66.6	165.4	159.8		170.2	162.6	147.58
52.1	0.6	51.5	1115.4	1050.3	65.1	151.7	146.6	165.76			
55.8	0.5	55.3	1096.4	1042.7	53.7	136.6	132.0	137.52	147.4	140.5	145.9
56.4	0.4	56.0	1095.7	1042.2	53.5	138.5	133.8	133.66	149.5	142.6	142.9
60.7	0.4	60.3	1103.6	1050	53.6	115.0	111.1				
64.5	0.5	64.0	1098.5	1053.6	44.9	98.4	95.0	139.4			
65.5	0.5	65.0	1092.5	1050.2	42.3	88.6	85.5		107.0	101.5	125.26

158

nC$_{20}$			CO$_2$			T oil 70			°C	T oil 80			°C
before g	after g	mass loaded g	before g	after g	mass loaded g	T act °C	P rdg Bar	P actual Bar	Piston mm	T act °C	P rdg Bar	P actual Bar	Piston mm
0.350	0.000	0.350	1182.7	1163.8	18.9	65.8	139.8	135.0	64.70	74.6	146.5	140.9	74.06
20.558	19.981	0.577	1249.2	1233.0	16.2	65.4	191.6	186.8	19.00	74.1	208.8	203.1	20.84
55.128	54.120	1.008	1260.8	1243.4	17.4	64.6	217.2	212.3	25.44	73.5	225.4	219.7	28.38
16.310	14.340	1.970	842.2	829.2	13.0	66.3	286.4	281.4	16.80	75.5	284.8	279.0	18.74
3.550	0.000	3.550	1249.0	1236.6	12.3	65.9	308.5	303.5	19.78	76.1	299.0	293.2	21.62
17.880	14.330	3.550	1272.4	1263.1	9.3	67.7	305.0	300.0	10.94	76.5	297.0	291.2	12.10
7.080	0.000	7.080	1144.1	1131.5	12.6	66.4	302.1	297.1	31.92	75.7	293.7	287.9	33.30
8.500	0.060	8.440	1195.3	1185.8	9.5	65.9	251.4	246.5	27.90	75.1	253.6	247.9	29.10
8.500	0.060	8.440	1133.2	1124.8	8.4	65.8	208.1	203.3	22.56				
8.500	0.060	8.440	1268.3	1261.6	6.7	66.1	185.1	180.3	20.98	75.1	194.2	188.6	21.58
8.400	0.000	8.400	1082.8	1077.6	5.2	65.9	134.2	129.4	16.60	75.1	144.1	138.5	16.98
13.440	0.000	10.140	1120.9	1115.7	5.2	65.7	109.0	104.3	20.56	74.8	120.6	115.0	20.72

Table G-4 CO$_2$ – n-C$_{20}$ Experimental Data in High-Pressure Cell

Table G-5 (first set: 60 °C and 70 °C)

nC24			CO2			60				Toil / 70			
before g	after g	mass loaded g	before g	after g	mass loaded g	T act °C	T P rdg mm	P actual Bar	Piston mm	T act °C	Toil P rdg Bar	P actual Bar	Piston mm
0.66	0.02	0.64	962.56	934.74	27.82	54.7	194.4	190.4	63.88	66	208.4	203.6	68.18
0.75	0.04	0.71	958.79	939.05	19.74	56.9	250.3	246.2	32.00	66.2	239.4	234.5	36.08
0.66	0.02	0.64	1267.93	1254.51	13.42	56.9	285.6	281.4	14.02	66.1	288.7	283.7	14.92
9.28	0.40	8.88	875.85	867.22	8.63	57.1				56.4			
24.58	14.41	10.17	877.80	869.83	7.97	56.6	263.0	258.9	26.34	65.9	244.5	239.6	27.12
9.28	0.40	8.88	839.31	832.97	6.34	56.7	220.0	216.0	18.94	65.9	213.8	208.9	19.58
9.28	0.40	8.88	939.99	934.51	5.48	57.1	178.9	174.9	17.60	65.8	181.6	176.8	18.22
24.58	14.41	10.17	836.34	830.29	6.05	56.7	158.8	154.8	23.52	66.2	170.8	166.0	23.84

Table G-5 (second set: 80 °C and 90 °C)

nC24			CO2			80				T oil / 90			
before g	after g	mass loaded g	before g	after g	mass loaded g	T act °C	Toil P rdg Bar	P actual Bar	Piston mm	T act °C	T oil P rdg Bar	P actual Bar	Piston mm
0.66	0.02	0.64	962.56	934.74	27.82	75.4	219.5	213.8	73.20	83.4	233.1	226.6	77.16
0.75	0.04	0.71	958.79	939.05	19.74	75.2	255.5	249.7	38.32				
0.66	0.02	0.64	1267.93	1254.51	13.42	74.8	285.6	279.8	17.60	83.6	286.4	279.8	20.00
9.28	0.40	8.88	875.85	867.22	8.63	76.1				84.0	308.3	301.6	26.40
24.58	14.41	10.17	877.80	869.83	7.97	74.8	240.8	235.1	27.82	84.3	246.1	239.5	28.78
9.28	0.40	8.88	839.31	832.97	6.34	74.5	217.7	212.0	19.90	84.3	224.3	217.8	20.80
9.28	0.40	8.88	939.99	934.51	5.48	75.3	189.9	184.3	18.82	83.8	198.9	192.4	19.08
24.58	14.41	10.17	836.34	830.29	6.05	74.9	178	172.4	24.80	84.2	191.5	185.0	24.76

Table G-5 CO$_2$ – n-C$_{24}$ Experimental Data in High-Pressure Cell

Table G-6 CO₂ – n-C₂₈ Experimental Data in High-Pressure Cell

nC₂₈ before g	nC₂₈ after g	nC₂₈ mass loaded g	CO₂ before g	CO₂ after g	CO₂ mass loaded g	T act °C (T 70)	P rdg mm Bar (70)	P actual Bar (70)	Piston mm °C (70)	T act °C (Toil 80)	P rdg Bar (80)	P actual Bar (80)	Piston mm °C (80)
14.82	14.33	0.49	904.18	875.63	28.55	65.8	201.6	196.8	79.08	75.4	232	226.3	79.8
14.82	14.33	0.49	856.85	832.20	24.65	65.8	237.4	232.5	57.56	75.3	238.1	232.4	63.2
14.82	14.33	0.49	850.85	832.17	18.68	63.7	251.5	246.6	33.34	74.6	282	276.2	34.3
14.82	14.33	0.49	954.45	937.53	16.92	64.9	283.7	278.7	25.56	74.5	295.7	289.9	27.6
51.02	40.51	10.51	837.13	829.18	7.95								
34.87	26.08	8.79	832.87	827.42	5.45	65.7	277.9	272.9	16.38	75	263.1	257.3	17.4
8.96	0.24	8.72	832.23	826.94	5.29	65.9	277.6	272.6	16.40	74.7	262.9	257.1	16.9
51.02	40.51	10.51	835.74	829.61	6.13	65.5	205.7	200.9	26.82	74.4	204.8	199.1	27.7
51.02	40.51	10.51	832.15	827.31	4.84	65.7	144.9	140.1	25.22	75.2	154	148.4	26.0

nC₂₈ before g	nC₂₈ after g	nC₂₈ mass loaded g	CO₂ before g	CO₂ after g	CO₂ mass loaded g	T act °C (T 90)	P rdg Bar (90)	P actual Bar (90)	Piston mm °C (90)	T act °C (Toil 100)	P rdg Bar (100)	P actual Bar (100)	Piston mm °C (100)
14.82	14.33	0.49	904.18	875.63	28.55	84.3	246.4	239.8	82.94	93.5	262.2	254.8	70.66
14.82	14.33	0.49	856.85	832.20	24.65	84.2	248.8	242.2	67.04	93.7	282.3	274.8	41.78
14.82	14.33	0.49	850.85	832.17	18.68	83.8	278.8	272.2	38.04	92.3	296.3	288.8	33.3
14.82	14.33	0.49	954.45	937.53	16.92	83.2	291.0	284.4	30.66	93.7	297	289.5	33.96
51.02	40.51	10.51	837.13	829.18	7.95	84.1	289.1	282.5	32.98				
34.87	26.08	8.79	832.87	827.42	5.45	83.3	259.3	252.7	17.8	92.9	260.6	253.2	18.42
8.96	0.24	8.72	832.23	826.94	5.29	83.9	258.7	252.1	17.46	93.2	261.9	254.5	18.16
51.02	40.51	10.51	835.74	829.61	6.13	83.7	213.9	207.4	27.96	93.4	220.2	212.9	28.72
51.02	40.51	10.51	832.15	827.31	4.84	83.8	168.7	162.3	26.12	93.4	179.6	172.3	26.92

nC$_{36}$ before g	after g	mass loaded g	CO$_2$ before g	after g	mass loaded g	T act °C	T P rdg mm	75 P actual Bar	°C Piston mm	T act °C	Toil P rdg Bar	80 P actual Bar	°C Piston mm
14.56	14.34	0.22	860.39	831.32	29.07	71.3	295.0	289.6	66.12	74.6	291.2	285.4	69.56
14.56	14.33	0.23	852.24	829.27	22.97		228.5			75.3	260.2	254.4	53.30
0.42	0.07	0.35	853.70	829.30	24.40	70.1		223.2	61.58	75.5	240	234.3	61.58
0.42	0.07	0.35	847.69	830.00	17.69					76	269.6	263.8	34.48
0.42	0.07	0.35	845.71	830.50	15.21					74.6	298.4	292.6	21.54
24.51	15.08	9.43	830.95	826.09	4.86	71.1	263.6	258.2	16.54	75.7	303.4	297.5	17.60
24.31	14.75	9.56	829.98	825.47	4.51	71.1	242.7	237.4	16.22	75.7	260.5	254.7	16.80
24.31	14.75	9.56	829.27	825.04	4.23	70.7	206.3	201.0	15.54	75.4	239.4	233.7	16.58
24.51	15.08	9.43	827.92	824.12	3.80	71.0				75.6	207.1	201.4	15.84

nC$_{36}$ before g	after g	mass loaded g	CO$_2$ before g	after g	mass loaded g	T act °C	Toil P rdg Bar	90 P actual Bar	°C Piston mm	T act °C	Toil P rdg Bar	100 P actual Bar	°C Piston mm
14.56	14.34	0.22	860.39	831.32	29.07	84.4	296.5	289.8	73.48	94.4	297.2	289.7	78.94
14.56	14.33	0.23	852.24	829.27	22.97	85.1	267.2	260.6	57.34	94.3	267.4	260.0	62.90
0.42	0.07	0.35	853.70	829.30	24.40	83.5	256.6	250.0	65.1	92.5	261.8	254.4	70.40
0.42	0.07	0.35	847.69	830.00	17.69	84.5	272.9	266.3	37.9	94.0	280.0	272.6	40.52
0.42	0.07	0.35	845.71	830.50	15.21	83.6	283.5	276.9	25.6	92.8	280.5	273.1	29.38
24.51	15.08	9.43	830.95	826.09	4.86	84.6	298.0	291.3	18.1	93.8	293.1	285.6	18.90
24.31	14.75	9.56	829.98	825.47	4.51	84.9	257.3	250.7	17.39	94.0	254.2	246.8	17.92
24.31	14.75	9.56	829.27	825.04	4.23	85.2	238.0	231.5	17.94	94.5	242.5	235.1	17.34
24.51	15.08	9.43	827.92	824.12	3.80	84.7	211.8	205.3	16.3	93.8	218.8	211.5	16.60

Table G-7 CO$_2$ – n-C$_{36}$ Experimental Data in High-Pressure Cell

Ethane – n-C₁₆ Experimental Data

Band 1 (T bath 40 °C and 50 °C):

nC₁₆ before g	nC₁₆ after g	nC₁₆ mass loaded g	Ethane before g	Ethane after g	Ethane mass loaded g	T act °C	T bath 40 P rdg Bar	40 P actual Bar	°C Piston mm	T act °C	T bath 50 P rdg Bar	50 P actual Bar	°C Piston mm
1.50	0.17	1.33	1113.15	1076.50	36.65	39.8	53.5	54.74		49.7	65	65.50	
4.31	0.46	3.85	1115.21	1077.41	37.80	39.8	53	54.24	162.5	49.7	66.1	66.58	205.48
6.86	0.43	6.43	1118.79	1082.52	36.27	39.8	52.7	53.95	107.76	49.8	66.3	66.78	141.30
10.98	0.35	10.63	1119.61	1083.77	35.84	39.8	52.3	53.55	101.22	49.7	66.1	66.58	118.02
13.82	-0.09	13.91	1114.01	1082.92	31.09	39.7	51.5	52.77	32.88	49.7	65	65.50	39.56
20.21	0.32	19.89	1081.60	1050.12	31.48	41.8	50.8	52.08	77.98	49.7	63.8	64.31	77.98
26.52	0.42	26.10	1115.75	1087.90	27.85	41.8	48.9	50.20	35.08	49.7	60.6	61.16	44.12
29.23	0.38	28.85	1098.63	1071.49	27.14	41.8	48.4	49.71	61.34	49.7	59.9	60.47	64.18

Band 2 (T bath 60 °C and 70 °C):

nC₁₆ before g	nC₁₆ after g	nC₁₆ mass loaded g	Ethane before g	Ethane after g	Ethane mass loaded g	T act °C	T bath 60 P rdg Bar	60 P actual Bar	°C Piston mm	T act °C	T bath 70 P rdg Bar	70 P actual Bar	°C Piston mm
1.50	0.17	1.33	1113.15	1076.50	36.65	59.7	75.8	75.6		69.6	85.5	84.6	
4.31	0.46	3.85	1115.21	1077.41	37.80	59.7	79.6	79.3	231.32	69.7	91.8	90.8	
6.86	0.43	6.43	1118.79	1082.52	36.27	59.7	80.4	80.1	184.20	69.6	93.6	92.6	184.20
10.98	0.35	10.63	1119.61	1083.77	35.84	59.6	80.8	80.5	137.78	69.7	94.5	93.5	152.90
13.82	-0.09	13.91	1114.01	1082.92	31.09	59.7	79.8	79.5	50.66	69.7	93.9	92.9	
20.21	0.32	19.89	1081.60	1050.12	31.48	59.7	78.2	78.0	89.50	69.6	92.4	91.4	93.72
26.52	0.42	26.10	1115.75	1087.90	27.85	59.7	73.6	73.4	53.84	69.6	87.1	86.2	62.36
29.23	0.38	28.85	1098.63	1071.49	27.14	59.7	72.7	72.5	70.66	69.7	85.8	84.9	79.38

Band 3 (T bath 80 °C):

nC₁₆ before g	nC₁₆ after g	nC₁₆ mass loaded g	Ethane before g	Ethane after g	Ethane mass loaded g	T act °C	T bath 80 P rdg Bar	80 P actual Bar	°C Piston mm
1.50	0.17	1.33	1113.15	1076.50	36.65	79.6	93.6	92.0	
4.31	0.46	3.85	1115.21	1077.41	37.80	79.5	102.6	100.9	
6.86	0.43	6.43	1118.79	1082.52	36.27	79.5	105.8	104.1	204.72
10.98	0.35	10.63	1119.61	1083.77	35.84	79.6	107.1	105.4	169.72
13.82	-0.09	13.91	1114.01	1082.92	31.09	79.5	106.6	104.9	66.74
20.21	0.32	19.89	1081.60	1050.12	31.48	79.6	105.7	104.0	106.66
26.52	0.42	26.10	1115.75	1087.90	27.85	79.5	100.1	98.5	71.98
29.23	0.38	28.85	1098.63	1071.49	27.14	79.5	99.3	97.7	80.42

Table G-8 Ethane – n-C₁₆ Experimental Data in View Cell

Table G-9 (top section)

nC$_{24}$ before (g)	after (g)	mass loaded (g)	Ethane before (g)	after (g)	mass loaded (g)	60 T act (°C)	T bath P rdg (Bar)	60 P actual (Bar)	Piston (mm)	70 T act (°C)	T bath P rdg (Bar)	70 P actual (Bar)	Piston (mm)
27.80	26.02	1.78	1059.43	1022.12	37.31	59.6	94.1	93.7	176.02	69.5	107.5	106.4	198.28
29.40	26.20	3.20	1091.65	1052.39	39.26	59.7	101.6	101.1	162.98	69.6	116.9	115.7	174.08
134.07	129.15	4.92	1055.42	1021.03	34.39	59.6	108.9	108.3	75.06	69.6	124.9	123.6	87.40
22.65	14.38	8.27	1114.04	1078.58	35.46	59.7	111.7	111.1	140.40	69.6	128.1	126.8	149.72
13.29	0.35	12.94	1118.52	1083.11	35.41	59.7	114	113.4	95.58	69.6	130.6	129.3	103.30
30.32	14.52	15.80	1115.31	1080.89	34.42	59.7	113.9	113.3	39.01	69.6	130.7	129.4	77.82
33.71	14.60	19.11	1120.57	1085.21	35.36	59.7	113.7	113.1	109.38	69.6	130.5	129.2	117.98
36.22	14.47	21.75	1121.62	1092.88	28.74	59.7	111.1	110.5	33.24	69.6	128.4	127.1	38.50
56.08	27.20	28.88	1062.20	1034.98	27.22	59.6	103	102.5	50.12	69.6	120	118.7	56.28
31.98	0.55	31.43	1060.50	1034.83	25.67	59.7	97.4	96.9	44.84	69.6	114.6	113.4	49.60

Table G-9 (bottom section)

nC$_{24}$ before (g)	after (g)	mass loaded (g)	Ethane before (g)	after (g)	mass loaded (g)	80 T act (°C)	T bath P rdg (Bar)	80 P actual (Bar)	Piston (mm)
27.80	26.02	1.78	1059.43	1022.12	37.31	79.5	119.9	118.1	218.60
29.40	26.20	3.20	1091.65	1052.39	39.26	79.5	130.1	128.2	187.80
134.07	129.15	4.92	1055.42	1021.03	34.39	79.5	139	137.0	101.78
22.65	14.38	8.27	1114.04	1078.58	35.46	79.5	142.8	140.8	62.64
13.29	0.35	12.94	1118.52	1083.11	35.41	79.5	145.7	143.7	110.54
30.32	14.52	15.80	1115.31	1080.89	34.42	79.5	145.8	143.8	84.98
33.71	14.60	19.11	1120.57	1085.21	35.36	79.5	146	144.0	125.28
36.22	14.47	21.75	1121.62	1092.88	28.74	79.5	144.1	142.1	44.10
56.08	27.20	28.88	1062.20	1034.98	27.22	79.6	135.9	133.9	62.52
31.98	0.55	31.43	1060.50	1034.83	25.67	79.5	131	129.1	52.86

Table G-9 Ethane – n-C$_{24}$ Experimental Data in View Cell

nC$_{28}$			Ethane				T bath 65		°C		T bath 70		°C
before	after	mass loaded	before	after	mass loaded	T act	P rdg	P actual	Piston	T act	P rdg	P actual	Piston
g	g	g	g	g	g	°C	Bar	Bar	mm	°C	Bar	Bar	mm
36.42	33.91	2.51	1071.40	1028.80	42.60	64.5	118.7	117.7	202.60	69.7	126.6	125.3	208.54
36.76	31.58	5.18	1070.75	1025.64	45.11	64.5	131.3	130.2	209.34	69.5	139.2	137.8	217.06
11.09	0.12	10.97	1079.25	1037.75	41.50	64.8	141.9	140.8	155.18	69.7	150.0	148.5	160.30
15.80	0.07	15.73	1058.09	1022.52	35.57	64.6	143.3	142.2		69.6	151.6	150.1	
35.70	14.95	20.75	1053.28	1023.79	29.49					69.7	150.1	148.6	32.16
43.09	14.78	28.31	1052.79	1023.54	29.25	64.7	135.2	134.1	63.56	69.6	143.5	142.1	63.56
180.50	144.73	35.77	1047.70	1022.05	25.65	64.6	118.7	117.7	60.60	69.5	127.4	126.1	62.68

nC$_{28}$			Ethane				T bath 80		°C
before	after	mass loaded	before	after	mass loaded	T act	P rdg	P actual	Piston
g	g	g	g	g	g	°C	Bar	Bar	mm
36.42	33.91	2.51	1071.40	1028.80	42.60	79.6	139.7	137.7	
36.76	31.58	5.18	1070.75	1025.64	45.11	79.4	153.8	151.7	233.60
11.09	0.12	10.97	1079.25	1037.75	41.50	79.5	165.2	163.1	169.10
15.80	0.07	15.73	1058.09	1022.52	35.57	79.4	166.9	164.8	
35.70	14.95	20.75	1053.28	1023.79	29.49	79.6	165.7	163.6	37.66
43.09	14.78	28.31	1052.79	1023.54	29.25	79.5	159.4	157.3	69.28
180.50	144.73	35.77	1047.70	1022.05	25.65	79.4	143.7	141.7	67.02

Table G-10 Ethane – n-C$_{28}$ Experimental Data in View Cell

NOMENCLATURE

Symbol	Definition	Units
a	Energy parameter in Van der Waals Type EOS	
a_m	Function defined in equation 4.4.7	
b	Co-volume parameter in Van der Waals Type EOS	
$b/4$	Hard-core molar volume in CSPHC EOS	m^3/mole
c	Patel Teja Parameter	
$3c$	Number of external degrees of freedom per molecule in CSPHC EOS	
f	Fugacity	Pa
F	Degrees of freedom (equation 3.2.1)	
k	Boltzmann's constant (1.381e-23 J/K)	J/K
K	Distribution Coefficient	
k_{ij}	Binary interaction parameter	
l_{ij}	Binary interaction parameter	
m,m_0	Function of acentric factor	
m_1	Function of reduced temperature	
n	Number of components	
N_A	Avogadro's number (6.023e23)	
p	Number of phases	
P	Pressure	Pa
q	Normalised surface area per molecule	m^2/mole
R	Universal Gas Constant	J/mole/K
s	Number of segments per molecule	
T	Temperature	K
T^*	Characteristic temperature for intermolecular interaction	K
v	Molar volume	m^3/mole
v^*	Characteristic volume per mole	m^3/mole
$\bar{v}$	Partial molar volume	m^3/mole
w	Weight assigned to error function	
x	Mol fraction	

Symbol	Definition	Units
ΔP	Pressure correction	Pa
y	Mol fraction	
z	Total mol fraction in appendix E	
z	Compressibility factor	
Z_m	Maximum coordination number	
α	Energy correction term in SRK, PR and PT EOS	
ϕ	Fugacity coefficient of mixture	
ϕ_i	Fugacity coefficient a component in a mixture	
μ	Chemical potential	
ρ	Density	kg/m^3
σ	Hard-core diameter of chain segment	m
τ	Constant in CSPHC EOS (0.7405)	
ω	Acentric factor	
$\Omega_a, \Omega_b, \Omega_c$	Patel Teja parameters	
ζ_c	Patel Teja critical compressibility	
$\in$	Characteristic energy per unit surface area	J
$\in^*$	Characteristic segmental interaction energy	J

Superscripts

α	Phase α	
β	Phase β	
l	Liquid phase	
v	Vapour phase	

Subscripts

Actual	Absolute pressure
ABS	Absolute pressure
c	Pure component critical property
e	Upper limit of data measurements in Equation 3.2.2
i	Lower limits of data measurements in Equation 3.2.2
i,j	Component i or j in a mixture
ii	Pure component parameters
ij	Cross parameters
r	Reduced property
RDG	Gauge pressure
1,2	Component 1 and 2